THE UNIVERSITY of EDINBURGH

This thesis has been submitted in fulfilment of the requirements for a Doctor of Philosophy at the University of Edinburgh. Please note the following terms and conditions of use:

Improved Methodologies for Security of Electricity Supply of Future Power System

Duo Fang

Doctor of Philosophy

THE UNIVERSITY OF EDINBURGH

2020

Abstract

The security of electricity supply has always been important, but it has recently become one of the critical issues for the planning and operation of modern electricity networks. There are several reasons for that, including increased demands and deregulation of electricity markets, resulting in much lower infrastructural investments, which both pushed existing networks to operate closer to their security limits. The increasing penetration levels of variable and inherently non-dispatchable renewable energy resource, as well as the implementation of demand-responsive controls and technologies on the demand side, together with the application of real-time thermal ratings for system components, have introduced an unprecedented level of uncertainties into the system operation. These uncertainties present genuinely new challenges for the maintenance of high system security levels.

The first contribution of this thesis is the development of advanced computational tools to strengthen the decision-making capabilities of system operators and ensure secure and economic operation under high uncertainty levels. It initially evaluates the hosting capacities for wind-based generation in a distribution network subject to operational security limits. In order to analyse the impacts of variations and uncertainties in the wind-based generation, loads and dynamic thermal ratings of network components, both deterministic and probabilistic approaches are applied for hosting capacity assessment at each bus, denoted as "locational hosting capacity", which is of interest to distributed generation (DG) developers. Afterwards, the locational hosting capacities are used to determine the hosting capacity of the whole network, denoted as "network hosting capacity", which is of primary interest to system operators. As the available hosting capacities change after the connection of any DG units, a sensitivity analysis is implemented to calculate the variations of the remaining hosting capacity for any number of DG units connected at arbitrary network buses.

The second contribution of this thesis is a novel optimisation model for the active management of networks with a high amount of wind-based generation and utilisation of dynamic thermal ratings, which employs both probabilistic analysis and

interval/affine arithmetic for a comprehensive evaluation of related uncertainties. Affine arithmetic is applied to deal with interval information, where the obtained interval solutions cover the full range of possible optimal solutions, with all realisations of uncertain variables. However, the interval solutions overlook the probabilistic characteristics of uncertainties, e.g. a likely very low probabilities around the edges of intervals. In order to consider realistic probability distribution information and to reduce overestimation errors, the affine arithmetic approach is combined with probabilistic (Monte Carlo) based analysis, to identify the suitable ranges of uncertainties for optimal balancing of risks and costs.

Finally, this thesis proposes a general multi-stage framework for efficient management of post-contingency congestions and constraint violations. This part of the work uses developed thermal models of overhead lines and transformers to calculate the maximum lead time for system operators to resolve constraint violations caused by post-fault contingency events. The maximum lead time is integrated into the framework as the additional constraint, to support the selection of the most effective corrective actions. The framework has three stages, in which the optimal settings for volt-var controls, generation re-dispatch and load shedding are determined sequentially, considering their response times. The proposed framework is capable of mitigating severe constraint violations while preventing overheating and overloading conditions during the congestion management process. In addition, the proposed framework also considers the costs of congestion management actions so that the effective corrective actions can be selected and evaluated both technically and economically.

Lay Summary

Modern power systems have developed rapidly in the past several years. On the demand side, the amount of load presents a fast increment due to economic growth, and on the generation side, the penetration of renewable energy source is rising steadily because of low generation cost and carbon emission. Those changes have contributed significantly to the benefits of power systems, both economic and environmental. However, the fast development of power systems also results in several challenges, among which security of electricity supply is one of the most severe. The increasing demand puts significant pressure on network facilities and the integration of large amounts of renewable energy source introduces new uncertainties in both power system planning and operation due to its intermittent characteristics.

This thesis aims to develop advanced computational tools to improve the decision-making capabilities of system operators to ensure the secure and economic operation with uncertainties. At first. This thesis uses probabilistic models to evaluate the uncertain parameters in power system planning and operation, which include ambient conditions, variations of wind-based generation and dynamic thermal ratings of network components. Afterwards, the developed uncertain models are used in the evaluation of hosting capacities of distribution networks for wind-based generation and the power flow analysis of networks with high wind penetration. The hosting capacity assessment and probabilistic power flow analysis show that the application of dynamic thermal ratings can provide significant benefits to wind energy integration in both planning stage and operational stage, but will further increase the uncertain level of system operation. Consequently, the operational risks will be higher at the same time, which deserve further attention.

To solve those problems, a new optimization model is developed in this thesis for the secure operation of systems with large amounts of wind energy and dynamic thermal ratings. This proposed model can find the optimal wind curtailment strategies based on the interval information of uncertain input variables with low computational efforts, to maximize system economic performance while maintaining system security.

Probabilistic models of uncertain variables are used to verify the performance of the optimization model.

In the ends, this thesis proposes a novel framework to identify remedial actions when contingency events, e.g. unexpected outages of transmission lines, occur. The unexpected contingency events may result in the overloading conditions and violations of voltage limits. In the proposed framework, the maximum lead time to clear the consequences of contingency events are taken into consideration, and the selection of remedial actions are divided into three stages according to the response times of different approaches. The proposed framework is able to identify the most efficient remedial actions in sequence and prevent the potential damages caused by overheating components when the remedial actions are implemented.

Acknowledgement

Firstly, I would like to thank my supervisor, Dr Sasa Djokic, for his continuous guidance during my PhD study period, especially for his patience and encouragement, which gave me the strong motivation to overcome difficulties in my research. I would also like to thank my second supervisor, Prof. Gareth Harrison, for his instructions and help during hard times.

I also wish to thank my colleagues and friends at the Institute for Energy Systems. They gave me not only a good working environment but also a lovely memorable experience in Edinburgh.

Finally, and most importantly, thank you to my parents (Liangcai Fang and Lijun Xu). Without their support and encouragement, I would not be able to accomplish my PhD research.

Declaration

I declare that this thesis was composed by myself, that the work contained herein is my own, except where explicitly stated otherwise in the text, and that this work has not been submitted for any other degree or professional qualification except as specified.

_____

Duo Fang

Contents

X

List of Figures

List of Tables

Acronyms and Abbreviations

2-pW	Two-parameter Weibull distribution
3-pW	Three-parameter Weibull distribution
AA	Affine arithmetic
AAAC	All aluminium alloy conductor
AC	Alternating current
ACOPF	Alternating current optimal power flow
ACSR	Aluminium conductor steel-reinforced
CCP	Chance constrained programming
C-DEEPSO	Canonical differential evolutionary particle swarm optimization
CM	Congestion management
DC	Direct current
DCOPF	Direct current optimal power flow
DE	Differential evolution
DG	Distributed generation
DNO	Distributed network operator
DTR	Dynamic thermal rating
GND	Generalized normal distribution
HST	Hottest-spot temperature
IA	Interval arithmetic
IGDT	Information gap decision theory
LHC	Locational hosting capacity
LP	Linear programming
LTER	Long-term emergency rating
MAE	Mean absolute error
MAEAAB	Maximum absolute error among all bins
MCS	Monte Carlo simulation
MGND	Finite mixture of generalized normal distribution
MILP	Mixed-integer linear programming

MLT	Maximum lead time
MOM	Method of moments
MvM	Finite mixture of von Mises distribution
MWB	Finite mixture of Weibull distribution
NHC	Network hosting capacity
NR	Normal rating
OHL	Overhead transmission line
OLTC	On-load tap changing
ONAN	Oil natural air natural
OPF	Optimal power flow
OS	Opportunity seeker
OVT	Maximum allowable overloading time
PEM	Point estimation method
P-OPF	Probabilistic optimal power flow
PSO	Particle swarm optimization
QCQP	Quadratic constrained quadratic programming
RA	Risk adverse
RES	Renewable energy source
RMSE	Root-mean-square error
RO	Robust optimisation
SCADA	Supervisory control and data acquisition
SDP	Semidefinite programming
SG	Smart grid
SOCP	Second-order cone programming
SP	Stochastic programming
STER	Short-term emergency rating
STR	Static thermal rating
TOT	Top-oil temperature
WF	Wind farm
WMAE	Weighted mean absolute error
WT	Wind turbine

List of Symbols

A'	Projected area of the conductor per unit length
a_i, b_i, c_i	Cost coefficients of generator i
B_{ij}	Imaginary part of the $ij\,th$ component of the admittance matrix
B^{dc}	Susceptance matrix
b_{ij}	Series susceptance of the branch between bus i and bus j
b'_{ij}	Shunt susceptance of the branch between bus i and bus j
C	Diagonal matrix of random variables sampled at each iteration which follows a Bernoulli distribution with the success probability P
C	Set of considered contingency events
$C(\cdot)$	Copula function
$C_{loadshedding}(\cdot)$	Cost function for load shedding
$C_{redispatch}(\cdot)$	Cost function for generation re-dispatch
D	Diameter of overhead line conductor
e_i	Real part of the voltage at bus i
F	A number aiming to control the amplification of differential variation in C-DEPSO
$f(\cdot)$	Objective function of an optimization problem
f_i	Imaginary part of the voltage at bus i
$f^a(\cdot)$	Affine formulation
$f_M(\cdot)$	PDF of finite mixture model
$\mathcal{G}$	The set of generator indices
$G(\cdot)$	Equality constraints of an optimization problem
G_{ij}	Conductance for the $ij\,th$ component of the admittance matrix
g_{ij}	Series conductance of the branch between bus i and bus j
$H(\cdot)$	Inequality constraints of an optimization problem
H_c	Altitude of the sun

I_i^P	Constant current term of the general ZIP model for the active load
I_i^Q	Constant current term of the general ZIP model for the reactive load
I_{rated}	Current limit provided by DTR
$I^2R(T_c)$	Joule heat gain rate per unit length
K_{angle}	Wind direction factor
K_i, K_U	Ratios of load before and after step change to the rated load
k_f	Thermal conductivity of the air at T_{film}
$\mathcal{L}$	The set of branch indices
$\mathcal{L}_{\mathrm{T}}$	Set of transformer indices
m	Empirically derived exponent used to calculate winding hottest-spot temperature rise over top-oil temperature at rated load
$M_3(\cdot)$	Third-order central moment
$MaxGen$	Maximum number of generations of C-DEEPSO
MB	Memory with size B
mC_p	Heat capacity of an overhead line conductor per unit length
N	Total number of bins
n	Empirically derived exponent used to calculate the variation of top-oil temperature rise
$\mathcal{N}$	The set of bus indices
NP	Population size of C-DEEPSO swarm
N_s	Sampling size
N_{shunt}	Set of shunt capacitor indices
N_{target}	Set of the target bus indices for load shedding
P_i	Probability that the random variable falls within the ith bin (obtained by the integration of the fitted PDF)
$\hat{P}_i$	Probability that the sample data falls within the ith bin
P_{curtw}	Curtailed active power at wind farm w
P_d	Active demand at bus i
$\mathbf{P_g}$	Vector of generator active power outputs

P_{gi}	Active power output of the generator at bus i
p_i^g	The size of DG connected at bus i
P_{gi0}	Initial value of active power output of the generator at bus i during congestion management
P_{gi}^{min} , P_{gi}^{max}	The lower and upper limits of active power output of generator i
$\bar{P}_{gw}$	Upper bound of supplied active power from wind farm w
P_i^l , P_j^l	Active power flow on branch l measured at the *from* bus i and the *to* bus j
P_i^P	Constant power term of the general ZIP model for the active load
P_i^Q	Constant power term of the general ZIP model for the reactive load
P_{lij}	Active power flow on the branch l between bus i and bus j
P_{LSj}	Amount of load shedding at bus j
P_w	Active power output of wind farm w
$\mathbf{Q}$	Uncorrelated sample vector for the sampling with copula function
q_c	Convection heat loss rate per unit length
q_{cn}	Natural convection heat loss per unit length
Q_{di}	Reactive demand at bus i
$\mathbf{Q_g}$	Vector of generator reactive power outputs
Q_{gi}	Reactive power output of the generator at bus i
Q_{gi0}	Initial value of reactive power output of the generator at bus i during congestion management
Q_{gi}^{min} , Q_{gi}^{max}	The lower and upper limits of reactive power output of generator i
Q_i^l, Q_j^l	Reactive power flow on branch l measured at the *from* bus i and the *to* bus j
Q_{lij}	Reactive power flow on the branch l between bus i and bus j
q_r	Radiated heat loss rate per unit length
q_s	Solar heat gain rate per unit length

Q_{se}	Total solar and sky radiated heat flux rate with elevation corrected
Q_w	Reactive power output of wind farm w
$radx$	Radius of the affine form for the uncertain variable x
$Ramp_{DOWN}^i$	Ramp-down rate of the generator at bus i
$Ramp_{UP}^i$	Ramp-up rate of the generator at bus i
S_i^l, S_j^l	Apparent power flow on branch l measured at the $from$ bus i and the to bus j
S_l^{max}	MVA limit of the power flow at branch l
T_a	Ambient temperature
T_c	Conductor surface temperature
T_{cf}	Conductor surface temperature of an overhead line conductor many time constants after the step-change of loading conditions
T_{film}	Temperature of the boundary layer
T_H	Winding hottest-spot temperature
T_{Hf}	Winding hottest-spot temperature of a transformer many time constants after the step-change of loading conditions
t_{ij}	Tap ratio of the transformer between bus i and bus j
u_i, c_{ij}, s_{ij}	Conic variables which are used to replace the multiplication of voltages in SOCP-OPF
u_c	Control variables for post-contingency congestion management model with contingency event c
u_0	Base case control variables for post-contingency congestion management model
ul	Unknown uncertainty level of parameter ξ
$\widehat{ul}$	Maximum value of the unknown uncertainty levels
$\breve{ul}$	Minimum value of the unknown uncertainty levels
V_i^{min}, V_i^{max}	The lower and upper limits of bus voltage magnitude at bus i
V_t	Velocity of the tth-generation solution candidates of C-DEEPSO
V_w	Wind speed
$|\mathbf{V}|$	Vector of bus voltage magnitude

$\lvert V_i \rvert$	Magnitude of voltage at bus i, V_i
W	SDP variables to replace the multiplication of voltages in SDP-OPF
$\mathcal{W}$	Set of wind farm indices
X_{best}	Best solution that ever found by the individuals in C-DEEPSO swarm
x_c	State variables for post-contingency congestion management model with contingency event c
X_{gb}	Best solution ever found by the swarm in C-DEEPSO
X_{gb}^*	Mutated best solution ever found by the swarm in C-DEEPSO
x_{ij}	Series reactance of the branch between bus i and bus j
x_l, x_u, x_o	The lower, upper bounds and forecast value of the uncertain variable x, given by the affine form
X_r	An individual different from all C-DEEPSO solution candidate in the last generation by specific sample rules
X_{r1}, X_{r2}	Two randomly sampled C-DEEPSO solutions
X_{st}	Individual generated by a specific strategy by the DE algorithm
X_t	The tth-generation solution candidates of C-DEEPSO
x_0	Base case state variables for post-contingency congestion management model
$\tilde{x}$	Affine form of an uncertain variable, x
Y	Correlated sample vector for the sampling with copula function
Y	Network admittance matrix
y_i	Value of the fitted CDF function at the middle point of the ith bin
$\hat{y}_i$	Value of the empirical CDF function at the middle point of the ith bin
y_{ik}	Admittance of the branch from bus i to bus k
Z_c	Azimuth of the sun
Z_i^P	Constant impedance term of the general ZIP model for the active load

Z_i^Q	Constant impedance term of the general ZIP model for the reactive load
Z_l	Azimuth of the overhead line conductor
α_e	Temperature coefficient of the conductor resistance
β	Shape parameter for a distribution
β_c	Predefined critical limit (Robustness) which the objective function value should avoid surpassing
β_o	Predefined opportunity value that the objective function should be lower than
γ	Location parameter for a distribution
ε	Emissivity
η	Scale parameter for a distribution
ε_i	Noise symbol due to the ith uncertainty
κ	Concertation parameter of von Mises distribution
μ	Dynamic viscosity of air
$\mu_A(\cdot)$	Membership function of a fuzzy set A
μ_m	The mth moment
ξ	Uncertain parameters
ξ_0	Forecast value of uncertain parameter ξ
ρ_f	Air density
$\boldsymbol{\rho_g}$	Matrix of linear correlation parameters
σ	Standard deviation
τ	Mutation rate set by users for C-DEEPSO
ϕ	Wind attacking angle which is between the wind direction and the conductor axis
$\phi(\cdot)$	PDF of standard normal distribution
$\Phi(\cdot)$	CDF of standard normal distribution
χ	Matrix of the parameters to define a distribution function
θ	Effective angle of irradiance of the sun's rays
$\boldsymbol{\theta}$	Vector of bus votlage angle
θ_i	Angle of the voltage at bus i

θ_i^{min} , θ_i^{max}	The lower and upper limits of bus voltage angle at bus i
τ_w	Winding time constant at hot spot location
ω	Vector of weight factors of the finite mixture model
ω^*	Mutated weight factor in C-DEEPSO
ω_A	Weight on the memory term in C-DEEPSO
ω_C	Weight on the communication term in C-DEEPSO
ω_I	Weight on the inertia in C-DEEPSO
ΔP_{gi}	Variation of active power output of the generator at bus i during congestion management
ΔQ_{gi}	Variation of reactive power output of the generator at bus i during congestion management
$\Delta T_{H,R}$	Winding hottest-spot temperature rise over top-oil temperature at rated load
$\Delta T_{H,i}$, $\Delta T_{H,U}$	Initial and final hottest-spot temperature rise over top-oil temperature
ΔT_H	Winding hottest-spot temperature rise over top-oil temperature
$\Delta T_{to,R}$	Top-oil temperature rise over ambient temperature at rated load and for the considered tap position
$\Delta T_{to,i}$, $\Delta T_{to,U}$	Initial and final top-oil temperature rise
ΔT_{to}	Top-oil temperature rise over ambient temperature
A'	Projected area of the conductor per unit length
a_i, b_i, c_i	Cost coefficients of generator i
B_{ij}	Imaginary part of the $ij\,th$ component of the admittance matrix
B^{dc}	Susceptance matrix
b_{ij}	Series susceptance of the branch between bus i and bus j
b'_{ij}	Shunt susceptance of the branch between bus i and bus j
C	Diagonal matrix of random variables sampled at each iteration which follows a Bernoulli distribution with the success probability P
C	Set of considered contingency events

$C(\cdot)$	Copula function
$C_{loadshedding}(\cdot)$	Cost function for load shedding
$C_{redispatch}(\cdot)$	Cost function for generation re-dispatch
D	Diameter of overhead line conductor
e_i	Real part of the voltage at bus i
F	A number aiming to control the amplification of differential variation in C-DEPSO
$f(\cdot)$	Objective function of an optimization problem
f_i	Imaginary part of the voltage at bus i
$f^a(\cdot)$	Affine formulation
$f_M(\cdot)$	PDF of finite mixture model
$\mathcal{G}$	The set of generator indices
$G(\cdot)$	Equality constraints of an optimization problem
G_{ij}	Conductance for the ij th component of the admittance matrix
g_{ij}	Series conductance of the branch between bus i and bus j
$H(\cdot)$	Inequality constraints of an optimization problem
H_c	Altitude of the sun
I_i^P	Constant current term of the general ZIP model for the active load
I_i^Q	Constant current term of the general ZIP model for the reactive load
I_{rated}	Current limit provided by DTR
$I^2R(T_c)$	Joule heat gain rate per unit length
K_{angle}	Wind direction factor
K_i, K_U	Ratios of load before and after step change to the rated load
k_f	Thermal conductivity of the air at T_{film}
$\mathcal{L}$	The set of branch indices
$\mathcal{L}_{\mathrm{T}}$	Set of transformer indices
m	Empirically derived exponent used to calculate winding hottest-spot temperature rise over top-oil temperature at rated load
$M_3(\cdot)$	Third-order central moment

$MaxGen$	Maximum number of generations of C-DEEPSO
MB	Memory with size B
mC_p	Heat capacity of an overhead line conductor per unit length
N	Total number of bins
n	Empirically derived exponent used to calculate the variation of top-oil temperature rise
$\mathcal{N}$	The set of bus indices
NP	Population size of C-DEEPSO swarm
N_s	Sampling size
N_{shunt}	Set of shunt capacitor indices
N_{target}	Set of the target bus indices for load shedding
P_i	Probability that the random variable falls within the ith bin (obtained by the integration of the fitted PDF)
$\hat{P}_i$	Probability that the sample data falls within the ith bin
P_{curtw}	Curtailed active power at wind farm w
P_d	Active demand at bus i
$\mathbf{P_g}$	Vector of generator active power outputs
P_{gi}	Active power output of the generator at bus i
p_i^g	The size of DG connected at bus i
P_{gi0}	Initial value of active power output of the generator at bus i during congestion management
P_{gi}^{min} , P_{gi}^{max}	The lower and upper limits of active power output of generator i
$\bar{P}_{gw}$	Upper bound of supplied active power from wind farm w
P_i^l, P_j^l	Active power flow on branch l measured at the *from* bus i and the *to* bus j
P_i^P	Constant power term of the general ZIP model for the active load
P_i^Q	Constant power term of the general ZIP model for the reactive load
P_{lij}	Active power flow on the branch l between bus i and bus j
P_{LSj}	Amount of load shedding at bus j
P_w	Active power output of wind farm w

$\mathbf{Q}$	Uncorrelated sample vector for the sampling with copula function
q_c	Convection heat loss rate per unit length
q_{cn}	Natural convection heat loss per unit length
Q_{di}	Reactive demand at bus i
$\mathbf{Q_g}$	Vector of generator reactive power outputs
Q_{gi}	Reactive power output of the generator at bus i
Q_{gi0}	Initial value of reactive power output of the generator at bus i during congestion management
Q_{gi}^{min}, Q_{gi}^{max}	The lower and upper limits of reactive power output of generator i
Q_i^l, Q_j^l	Reactive power flow on branch l measured at the *from* bus i and the *to* bus j
Q_{lij}	Reactive power flow on the branch l between bus i and bus j
q_r	Radiated heat loss rate per unit length
q_s	Solar heat gain rate per unit length
Q_{se}	Total solar and sky radiated heat flux rate with elevation corrected
Q_w	Reactive power output of wind farm w
$radx$	Radius of the affine form for the uncertain variable x
$Ramp_{DOWN}^i$	Ramp-down rate of the generator at bus i
$Ramp_{UP}^i$	Ramp-up rate of the generator at bus i
S_i^l, S_j^l	Apparent power flow on branch l measured at the $from$ bus i and the to bus j
S_l^{max}	MVA limit of the power flow at branch l
T_a	Ambient temperature
T_c	Conductor surface temperature
T_{cf}	Conductor surface temperature of an overhead line conductor many time constants after the step-change of loading conditions
T_{film}	Temperature of the boundary layer
T_H	Winding hottest-spot temperature

T_{Hf}	Winding hottest-spot temperature of a transformer many time constants after the step-change of loading conditions
t_{ij}	Tap ratio of the transformer between bus i and bus j
u_i, c_{ij}, s_{ij}	Conic variables which are used to replace the multiplication of voltages in SOCP-OPF
u_c	Control variables for post-contingency congestion management model with contingency event c
u_0	Base case control variables for post-contingency congestion management model
ul	Unknown uncertainty level of parameter ξ
$\widehat{ul}$	Maximum value of the unknown uncertainty levels
$\breve{ul}$	Minimum value of the unknown uncertainty levels
V_i^{min}, V_i^{max}	The lower and upper limits of bus voltage magnitude at bus i
V_t	Velocity of the tth-generation solution candidates of C-DEEPSO
V_w	Wind speed
$|\mathbf{V}|$	Vector of bus voltage magnitude
$|V_i|$	Magnitude of voltage at bus i, V_i
$\mathbf{W}$	SDP variables to replace the multiplication of voltages in SDP-OPF
$\mathcal{W}$	Set of wind farm indices
X_{best}	Best solution that ever found by the individuals in C-DEEPSO swarm
x_c	State variables for post-contingency congestion management model with contingency event c
X_{gb}	Best solution ever found by the swarm in C-DEEPSO
X_{gb}^*	Mutated best solution ever found by the swarm in C-DEEPSO
x_{ij}	Series reactance of the branch between bus i and bus j
x_l, x_u, x_o	The lower, upper bounds and forecast value of the uncertain variable x, given by the affine form
X_r	An individual different from all C-DEEPSO solution candidate in the last generation by specific sample rules

X_{r1}, X_{r2}	Two randomly sampled C-DEEPSO solutions
X_{st}	Individual generated by a specific strategy by the DE algorithm
X_t	The tth-generation solution candidates of C-DEEPSO
x_0	Base case state variables for post-contingency congestion management model
$\tilde{x}$	Affine form of an uncertain variable, x
$\mathbf{Y}$	Correlated sample vector for the sampling with copula function
Y	Network admittance matrix
y_i	Value of the fitted CDF function at the middle point of the ith bin
$\hat{y}_i$	Value of the empirical CDF function at the middle point of the ith bin
y_{ik}	Admittance of the branch from bus i to bus k
Z_c	Azimuth of the sun
Z_i^P	Constant impedance term of the general ZIP model for the active load
Z_i^Q	Constant impedance term of the general ZIP model for the reactive load
Z_l	Azimuth of the overhead line conductor
α_e	Temperature coefficient of the conductor resistance
β	Shape parameter for a distribution
β_c	Predefined critical limit (Robustness) which the objective function value should avoid surpassing
β_o	Predefined opportunity value that the objective function should be lower than
γ	Location parameter for a distribution
ε	Emissivity
η	Scale parameter for a distribution
ε_i	Noise symbol due to the ith uncertainty
κ	Concertation parameter of von Mises distribution
μ	Dynamic viscosity of air

$\mu_A(\cdot)$	Membership function of a fuzzy set A
μ_m	The mth moment
ξ	Uncertain parameters
ξ_0	Forecast value of uncertain parameter ξ
ρ_f	Air density
$\boldsymbol{\rho_g}$	Matrix of linear correlation parameters
σ	Standard deviation
τ	Mutation rate set by users for C-DEEPSO
ϕ	Wind attacking angle which is between the wind direction and the conductor axis
$\phi(\cdot)$	PDF of standard normal distribution
$\Phi(\cdot)$	CDF of standard normal distribution
χ	Matrix of the parameters to define a distribution function
θ	Effective angle of irradiance of the sun's rays
$\boldsymbol{\theta}$	Vector of bus votlage angle
θ_i	Angle of the voltage at bus i
θ_i^{min} , θ_i^{max}	The lower and upper limits of bus voltage angle at bus i
τ_w	Winding time constant at hot spot location
ω	Vector of weight factors of the finite mixture model
ω^*	Mutated weight factor in C-DEEPSO
ω_A	Weight on the memory term in C-DEEPSO
ω_C	Weight on the communication term in C-DEEPSO
ω_I	Weight on the inertia in C-DEEPSO
ΔP_{gi}	Variation of active power output of the generator at bus i during congestion management
ΔQ_{gi}	Variation of reactive power output of the generator at bus i during congestion management
$\Delta T_{H,R}$	Winding hottest-spot temperature rise over top-oil temperature at rated load

$\Delta T_{H,i}$, $\Delta T_{H,U}$	Initial and final hottest-spot temperature rise over top-oil temperature
ΔT_H	Winding hottest-spot temperature rise over top-oil temperature
$\Delta T_{to,R}$	Top-oil temperature rise over ambient temperature at rated load and for the considered tap position
$\Delta T_{to,i}$, $\Delta T_{to,U}$	Initial and final top-oil temperature rise
ΔT_{to}	Top-oil temperature rise over ambient temperature

1.1   Introduction

The proper evaluation and understanding of the complex interactions between the "supply-side" and "demand-side" play a significant role in the transformation of existing electricity networks into "smart grids" (SGs). From the perspective of SGs, the variations in the amounts of power flows and the changes in the forms of energy exchanges between the supply side and demand side are the most important contributing factors of those interactions. Significant changes in the fundamental principles of power system operation have already taken place on both the supply side and demand side of networks and are expected to be more pronounced in the future. Bi-directional power flows in both direct current (DC) and alternating current (AC) forms have started to replace the unidirectional power flows [1].

Some of the expected SG functionalities, e.g., increased use of network automation and reconfiguration schemes, implementation of advanced components, and flexible management of energy consumption will undoubtedly improve system reliability performance. However, they may also result in the more frequent congestions and voltage deviations, causing interruptions of electricity supply, i.e. in a possible deterioration of power system security. In addition, the increase in transients in SGs due to, e.g., high-speed transfer to alternative supply points, more frequent switching of power electronic devices, as well as conventional capacitor banks may cause the reduction of power quality levels. Off-grid operation of micro-grids may also result in the lower power quality levels within the micro-grids, and elsewhere in the network. Of further concerns are the higher dynamics of bi-directional power flows due to highly dispersed small-scale DG, which will reduce network fault currents and may be disconnected from the network, i.e. exactly when their output is needed. Therefore, additional concerns should be included in system performance analysis when some of these SG functionalities are implemented.

Improvements in the security of supply are often assumed to be one of the fundamental aspects of the SGs, as the threat of supply disruption appears to resonate with many

segments of the public. It is significant to both end-users (electricity customers) and power supply companies, as well as to the other subjects involved with the generation, transmission, distribution, and utilisation of electrical energy, always drawing increasing attention among them. Maintaining the security of supply while improving economic operation and reducing environmental impact, such as CO_2 emissions, have become one of the main themes in SG development [2]. However, the security of supply is threatened by many factors. For instance, many energy supply infrastructures are approaching the end of life in the UK [2]. Although some generation has been substituted by renewable generation such as wind turbines, new challenges are introduced due to the intermittent nature of renewable energy. Besides, the development of SGs will result in increasingly complex electricity networks, introducing more flexible controls, monitoring and communication systems and incorporating various demand-side management [1]. These new technologies will provide more flexible and fast-response controls for system operations. On the other hand, they may put considerable pressure on the delivery of a continuous and high-quality supply of electrical energy.

1.2 Need for advanced computational tools for security analysis of electricity supply systems

Modern society increasingly relies on continuous electricity supply. System operators must maintain the security of electricity supply at all time, or for most of the time, regarding disturbances, such as severe weather events, random faults, and failures of ageing components and infrastructures. An insufficient level of security may result in frequent electricity supply interruptions, which will typically result in direct and indirect damages and costs to systems, as well as tremendous economic losses for customers. For example, the Northeast Blackout in 2003 affected 55 million people (estimated) in Canada and the US, whose economic losses were over $6 billion, as estimated by the US Department of Energy.

From the perspective of system operation, security refers to the degree of risk in its ability to survive imminent disturbances (contingencies) without lengthy interruptions of electricity supply to all customers, or at least majority of customers [3]. A pre-contingency network should be able to transmit the power from generation to

customers without violations of any operating limits, including thermal limits of transmission components, voltage constraints and stability constraints [4][5]. When contingencies occur, the network, however, may not be able to maintain the supply without constraint violations due to re-routed power flows based on the physical characteristics of the reconfigured network. The violation of network operating limits in post-contingency operating conditions will result in activation of protection systems, disconnecting impacted components and further reducing system security. Accordingly, system operators need to implement remedial actions to enhance system stability and mitigate thermal overloading and bus voltage violations.

Over the last few decades, significant development has occurred in electric power systems, which brought new opportunities but also presented new challenges [6]. Firstly, the power system operating conditions are more "stressful" [7]. Electric networks have become one of the most complex human-made systems, the majority of which were designed and built decades ago. However, the constantly increasing electricity demands, because of economic growth, population increase and industrialization process, may outpace the upgrade of network infrastructures. System planners and operators prefer pushing networks closer to their operational security limits to maximize the benefits in the deregulated electricity market while deferring investments to upgrade network infrastructures. Additionally, large-scale investments have been made in the development of renewable generation. As the locations of new generation are generally different from those of the existing centralized generation, both the scale and the direction of power flows in the existing networks can be affected significantly. In addition, the renewable generation is highly variable and unpredictable, and cannot be dispatched as the conventional generation. Therefore, integration of renewable generation with high penetration levels has posed further challenges to network operation.

Secondly, more uncertainties are introduced into system operation. These come from the increasing penetration level of variable renewable energy sources (RES), demand response from flexible loads, as well as the introduction of intra-day electricity markets, which all make the network operating conditions harder to forecast. The system is exposed to more significant deviations from their planned schedule. As a result, system

operators need to perform corrective actions, such as generation re-dispatch to maintain the power balance and system security, as the system is increasingly operated closer to the limits [8].

Moreover, unlike conventional generators, most of the distributed generation (DG) is connected to the network electrically via power electronic interface rather than electromechanically. The increased penetration of that type of DG has resulted in the reduction of both system fault levels and system inertia. In the low-inertia networks, low-frequency electromechanical oscillations among synchronous generators may not be damped effectively, and even small disturbances could lead to system instability [9].

In order to tackle the issues related to maintaining required security levels of electricity supply, it is necessary to develop advanced computational tools for system operators to improve their control and decision-making capabilities, so that the balance between the economic costs and security performance can be achieved.

1.3 Research objectives and main contributions of the thesis

The main research objective is to develop methodologies and incorporate them in a general framework for improving system security and optimisation of network economic benefits, which specifically focus on improving the system operators controls and decision-making capability for ensuring high security levels of electric supply in the presence of the high levels of uncertainties.

Main results of this thesis have been presented in two journal papers [10], [11] and 11 conference papers [12]–[22]. The main contributions are summarized as the following points:

- **Modelling of uncertain parameters in power system operations:** In [14], mixture distributions are applied to model the uncertainties in wind energy resource (wind speeds and wind directions). The usual approach to model wind generation is the use of power curves, which specify the deterministic relationship between the wind speed and power output of a wind turbine.

However, as power curves provided by wind turbine manufacturers are generally obtained in controlled conditions, they ignore the effects of wind dynamics (fluctuations in wind speeds and wind directions), presence of turbulence, as well as site and application specific factors, which cause the deviations from the expected power outputs given by manufacturer power curves. In [14], the deviations are taken into account and modelled by mixture distributions. A more detailed analysis of the relationship between input wind energy conditions (wind speeds and wind directions) and power outputs from wind turbines is presented in [15], [17] and [22]. In [17], a novel model is developed for the evaluation of uncertainties in wind turbine power outputs, based on correlating wind speeds and wind directions, through Gaussian mixture Copula model and vine Copula. In [15] and [22], the outliers in the measured wind turbine data are identified and cleared at first. Then, the equivalent power curve models for individual wind turbines are developed, based on the remaining data. Afterwards, the aggregated wind farm power curve model is obtained, considering different operating states of wind turbines in the wind farm. In addition to evaluating uncertainties related to wind energy, approaches for assessing uncertainties and forecasting variations in demands are presented in [16] and [19].

- **Impact of dynamic thermal ratings (DTR) on hosting capacity for wind-based DG**: A three-stage hosting capacity assessment for wind-based DG in a distribution network with the utilization of DTRs is presented in [20]. DTRs for overhead transmission lines and transformers are estimated with the dynamic thermal models of bare overhead conductors and transformers presented in [23] and [24]. In the first stage, locational hosting capacities (LHC) at each bus are evaluated considering the uncertainties introduced by wind power outputs, DTRs and load variations. In the second stage, optimization-based approaches are presented to assess the hosting capacity for the whole network based on the first-stage LHC results, assuming that DG units are connected at all buses. In the third stage, bus-to-bus LHC sensitivity factors are calculated to estimate the changes in available LHCs for any number of DG units connected at arbitrary buses.

- **A novel optimization model for the operation of networks with high penetration of wind energy generation:** The results of MCS-based optimal power flow analysis presented in [14] show that the application of DTRs can increase wind integration effectively, but will cause potential overloading risks when the wind speed is low. In order to overcome these problems, a novel optimization model, which combines affine arithmetic (AA) and probabilistic optimal power flow (P-OPF), is proposed for the optimal operation of networks with DTR and wind generation [10]. The proposed method provides an improved analysis of underlying uncertainties in the generation, transmission capacity and system demands, which are represented by probability distributions (e.g. for wind speeds, wind directions and wind power generation) and interval values (e.g. demand variations). The combined AA-P-OPF method provides essential information that can be used by system operators to evaluate the trade-off between security and costs and then select the most optimal controls.

- **A multi-stage model for post-contingency congestion management:** A multi-stage OPF-based approach is proposed to manage operational limit violations caused by disturbances, such as fault-caused contingencies in which the maximum lead time (MLT) available for network operators to resolve violated operational limits in post-contingency condition is evaluated based on the dynamic thermal models of overhead lines and power transformers. In the first stage, optimal settings of volt-var controls are determined. The second stage provides optimal generation re-dispatch, supported by fast-start generators. In the third and ultimate stage, optimal load shedding is implemented to mitigate all remaining constraint violations [12], [13], [18], [21].

1.4 Thesis structure

The thesis has seven chapters. The summary of the contents of each chapter is given as follows:

Chapter 1: This chapter gives a general introduction and overview of the thesis. It discusses the motivation and objectives of the research, as well as the summary of the main contributions, presented in the following chapters.

Chapter 2: This chapter presents the theoretical backgrounds and reviews methods and models used in the thesis.

Chapter 3: This chapter evaluates the hosting capacity of distribution networks for variable wind-based distributed generation, also considering variations in DTR and loading conditions. Both deterministic and probabilistic methods are used to determine the locational hosting capacity at individual buses and the hosting capacity of the whole network.

Chapter 4: In this chapter, probabilistic models are developed for dealing with the uncertainties in system operation. Suitable analytical PDFs are used to fit the uncertainties introduced by several sources, including wind speeds, wind directions, and wind power outputs. The MCS-based analysis is used with the developed probabilistic models, and the correlated impacts of DTRs and wind power generation on network operation are analysed.

Chapter 5: This chapter proposes a novel framework for network operation, in which AA and P-OPF are both applied to manage uncertainties represented by probabilistic distribution functions and range intervals.

Chapter 6: This chapter proposes a multi-stage OPF-based model for congestion management (CM). Dynamic thermal models for overhead lines (OHLs) and transformers are applied to calculate the maximum lead time (MLT) available to system operators for implementing remedial actions.

Chapter 7: This chapter gives the main conclusions from the presented work and findings of the research, as well as discussion of the contributions. Some limitations of the presented research and recommendations for future work are also discussed.

Chapter 2
Overview of Approaches for Power System Security Control and Management of Uncertainties

2.1 Introduction

This chapter starts with an overview of power system security and the framework to achieve and maintain system security, in which fundamental functions of power system security are discussed first. Afterwards, the classifications of system operating states are provided, and different control strategies in each state to maintain system security are explained. Subsequently, this chapter presents a literature review of approaches for the management of uncertainties in power systems, in which some commonly used methods are introduced, their advantages and limitations are compared and discussed. Finally, this chapter introduces the general formulation of ACOPF method, which is an important tool to ensure secure and economical operation. As the OPF is generally nonconvex and NP-hard, this chapter presents some approximations and relaxations of ACOPF, which can significantly improve computational efficiency.

2.2 Power system security

A properly designed and operated system should meet several fundamental requirements. The system must be able to balance the total system generation against power consumption and losses. As the energy consumption in a network keeps varying and a large amount of electricity cannot be stored, the adequate spinning reserve should be scheduled to maintain power balance. The quality of power supply, including constancy of frequency and voltage, and the level of reliability, also need to be maintained based on specific requirements in standards. Finally, the system should operate with the lowest or most optimal cost of supplied energy and minimum environmental impact [25]. Apart from above, an equally important aspect of the power system operation is to maintain system security, which involves the practices and measures or actions to keep the system operating when contingency events occur. A contingency is defined as an event which affects the power system, causing the

8

failures, disconnections or removal from operational services of one or more network components, such as generators, transformers or transmission lines.

A critical aspect of system security study is to guarantee the satisfaction of operating limits, e.g. branch power flow and bus voltage limits after contingency events. A particular system state is secure only regarding one or more specific contingency cases and a given set of quantities monitored for limit violations. The outage of one component will cause the redistribution of power flows in the remaining network, which may result in overloading conditions of other transmission components or instability conditions of generating units. The consequences of a single outage may spread in the network and lead to cascading failures, which are regarded as the leading cause for large system blackouts. Most power systems are operated with specific security criteria, such as "N-1 security criterion", which specifies that the system will be able to withstand ae unexpected failure or outage of any single network component at all time and remain in the normal operating condition without constraint violations. System security consists of three primary functions, which are implemented by the system control centre: system monitoring, contingency analysis and corrective action analysis [26][27].

2.2.1 System monitoring

System monitoring provides system operators with real-time information on the status of system components and system operating conditions. Usually, voltages, power flows, frequency, as well as component status information, generation changes and load information, are collected, monitored and transmitted by telemetry systems. The telemetered data are used as the inputs for further security assessment, e.g. to inform system operators of the actual or expected constraint violations in the network. Additionally, system monitoring data, as well as state estimation, can be used to give the best estimates (in the statistical sense) of the current or future system conditions or operating states [27]. Such systems, combined with supervisory control systems that allow system operators to implement control actions remotely, are referred to as supervisory control and data acquisition system, termed as SCADA [25].

2.2.2 Contingency analysis

The second primary security function, contingency analysis, aims to analyse the impacts of the possible faults in the system and alert system operators to any potential constraint violation (or system stability issue). Contingency analysis has three states, i.e. contingency definition, contingency selection and contingency evaluation. In the first state, a list of credible contingencies with high probability to occur is prepared for various network configurations and operating conditions. In the second stage, the contingencies are ranked in rough order of their severity. The severity of specific contingencies is evaluated based on simulations with the high computational speed, such as DC power flow. In the last contingency evaluation stage, a detailed assessment with full AC power flow is performed for successive individual cases in the decreasing order of severity, until the cases with no post-contingency constraint violations are identified and a shortened contingency list is obtained [26].

2.2.3 Corrective action analysis

The third security function is corrective action analysis, aiming to identify the proper or optimal control actions to remediate constraint violations caused by contingencies identified in the list in the previous sub-section.

Electric power system control comprises generating unit control, system generation control and transmission control. Prime mover controls and excitation controls are two main functions of generating unit control. Prime mover controls have the functionalities of rotor speed regulation and control of mechanical energy sources, such as steam turbines. The excitation control aims to regulate generator voltages and reactive power outputs of the generation units. The dispatch of active power generation is determined by system generation control to balance the total system generation against system loads and losses so that the desired frequency and power balance within the whole system can be maintained. The transmission controls include the controls of power and voltage control devices, such as reactive power compensators, OLTC transformers, phase-shifting transformers and HVDC transmission controls [25], as well as controls of network topology, such as optimal transmission switching [28] and network reconfiguration [29].

These control actions contribute significantly to system operation, so that the operational security limits, such as branch power flow and bus voltage limits, can always be satisfied, even if (credible or expected) disturbances occur. However, control objectives can vary significantly in different operating conditions. Under normal operating conditions, the control objective is generally subject to economic benefits, so the system can be operated as affordably and efficiently as possible, with higher utilization of network components. On the other hand, when the system is in abnormal operating conditions (e.g. due to a fault), the control objective is to recover the system to normal operating conditions as soon as possible and to prevent potential larger damages and economic losses [30].

Classification of system operating states

For the purpose of making proper control strategies for different operating conditions, system operating conditions are classified into different operating states. A three-stage framework for operating state classification is initially proposed in [31] and extended to five stages in [32]. System operating states are divided based on the level of system adequacy and system security. The adequacy is assessed based on power balance equations and availability of generating units to supply all loads plus losses, while security is evaluated with respect to the post-fault stable system operation and satisfaction of component and network operational limits. Figure 2.1 [25] depicts these operating states and transitions between the states. Table 2.1 lists the criteria for the state classifications and characteristics of each state.
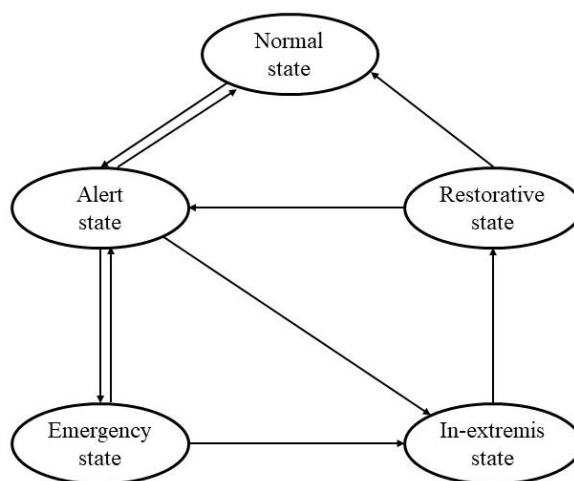
Figure 2.1: Power system operating states

In the normal state, the system can supply all the loads (adequacy) with all security limits satisfied. The network has a sufficient level of security margins, so it can withstand at least one contingency with or without the implementation of corrective control actions. In this state, system operators tend to maximise system economic benefits and minimise environmental impact.

A relatively moderate and frequent disturbance, such as specific weather condition, can reduce system security level. For instance, high temperature can reduce transmission capacities of transmission lines, while snow/ice or wind can cause damages and failures of overhead lines. In such cases, the system will usually transit into the alert state, where both adequacy and security constraints are still satisfied if the constraint violations caused by any contingency can be removed by corrective actions. Proper preventive actions, such as generation shifting, or the increase of reserve generation, or system reconfiguration, can be applied to restore the system from alarm state to the normal state.

If the control actions are not implemented or not efficient when a sufficiently severe disturbance occurs for the system in the alert state, the system will transfer to the emergency state. In this state, system adequacy can still be maintained, but security limits, such as bus voltage limits and short-term emergency ratings of transmission lines, will be violated. In order to prevent more severe consequences, such as cascading failures and blackouts, control actions should be implemented to mitigate violations of system security limits and bring the system back to alert state.

Table 2.1: Classification of system operating states and their characteristics

Operating states	Operational limits satisfied?	System Adequacy?	N-1 security criteria satisfied?	Corrective actions required?
Normal	✓	✓	✓	✗
Alert	✓	✓	✗	✓
Emergency	✗	✓	✗	✓
In-extremis	✗	✗	✗	✓
Restorative	✓	✗	✗	✓

If the above actions are not applied or are ineffective, the system will enter the in-extremis state, in which the cascading failures are likely to happen. To prevent the widespread blackout, control actions, such as load shedding and controlled system splitting, should be applied.

Implementations of in-extremis control actions usually separate the network into several "islands", so that further deterioration (within islands) is prevented. Finally, the system will enter the restorative state, when system operators try to recover the electricity supply by reconnecting separated parts of the system and network facilities, as well as implementing load restoration schemes. These actions will help the system to transfer into the normal or alert state, depending on the circumstances and the considered period of the overall restorative state.

The classification of system operating states can provide system operators with a framework in which control strategies can be developed with specific control objectives and adequate control actions can be implemented effectively in different states.

Preventive vs corrective control

Control actions for power system security have been divided into two general categories: preventive and corrective controls. Preventive controls are implemented before disturbances, aiming to better prepare the network for future contingency events. In contrast, corrective controls are applied in post-disturbance states, to recover the system and return it into the normal/alert state, in such a way that the consequences can be minimized. Preventive control actions include generation rescheduling, network reconfiguration, voltage regulation, reactive power compensation and contracted load curtailment. Corrective actions consist of direct or indirect load shedding, generation shedding or connection of reserve generation, switching of shunt capacitors or reactors, and network splitting. Typically, the best or most optimal control actions are achieved by security-constrained optimization methods [30][33].

2.3   Uncertainty handling in power systems

Mathematically, the term "uncertainty" is defined as the difference between the actual value and the measured, estimated, or calculated value [34]. In modern power systems,

decision makings in both planning and operational stages are subject to different uncertainties. In the UK, RES capacity has increased to around 45 GW by the end of 2018. During 2018, the total renewable energy generation was around 110 TWh, which accounted for around 33.0% of the total electricity generated. Due to the uncertainties in RES, the power outputs of renewable generation are significantly more variable than these of traditional centralised and utility-controlled generation units. The increased penetration of RES has not only introduced new uncertainties, but it has also increased the levels of previously present uncertainties [35][36]. In order to maintain the security of electric power supply, it is essential to analyse characteristics of uncertainties with appropriate models and to manage them with adequate/optimal controls.

In electric power systems, sources of uncertainties can be divided into two categories: technical parameter uncertainties and economic parameter uncertainties [37]. Technical uncertainties can be further classified into two subgroups, operational and topological parameter uncertainties. The uncertainties of operational parameters are the variations in generation outputs, changes of demand, etc. The availability of generation units and outages of network branches are topological parameter uncertainties. The uncertainties of economic parameters can also be subdivided into two groups, macroeconomic parameters, such as economic growth, and microeconomic parameters, which include variations in electricity prices, fuel costs and investment costs.

There are multiple methods to handle uncertainties during the analysis of power systems. The main differences between those methods are in the models used to describe uncertainties. These approaches can be classified into three categories, probabilistic approaches, possibilistic approaches and hybrid approaches [36].

2.3.1 Probabilistic approaches

Probabilistic approaches are commonly used for modelling uncertainties in the power system, where uncertain variables are modelled by specific probability density functions (PDFs). For instance, the variations in wind speed, system loads and solar irradiation can be modelled by Weibull distribution [37][38][39], Gaussian distribution [40] and Beta distribution [41][42][43], respectively.

14

Given a function $Y = F(X)$, where X represents the set of uncertain variables following specific PDFs, and y represents the output, the probabilistic information of the output can be determined by three widely used approaches: Monte Carlo simulation (MCS), scenario-based analysis (SBA), and point estimation method (PEM) [44].

The MCS is a broad class of methods relying on repeated random sampling to obtain numerical results. The general steps of MCS are given as follows, in which N_s denotes the sampling size; $Mean_Y$ and Std_Y are the mean value and standard deviation of Y for the uncertainties.

1. Initialize N_s, Set $i = 1$
2. Sample $X_{e,i}$ according to specific distributions and compute $Y_{e,i} = F(X_{e,i})$
3. $i = i + 1$. if $i > N_s$ continue, otherwise, go to step 2.

4. Calculate the mean and standard deviation as $Mean_Y = \frac{\sum_{i=1}^{N_s} Y_{e,i}}{N_s}$ and $std_Y = \sqrt{\frac{\sum_{i=1}^{N_s}(Y_{e,i} - Mean_Y)^2}{N_s}}$

The sampling size N_s should be large enough to ensure the convergence criteria of MCS is satisfied. In the following research presented in this thesis, the convergence criterion is that the distribution characteristics (means, variances, etc.) of MCS results will not change significantly if the sampling size is further increased. The samples are generated by inverse transform sampling which generates random numbers from the uniform distribution between 0 and 1 initially, and then feed them through the inverse cumulative distribution functions (CDF) of typical distributions to obtain samples.

In [39] and [45], MCS is applied to deal with uncertainties in demands and RES outputs in distribution networks during the planning stage. References [48] and [49] use MCS to handle uncertain parameters in optimal scheduling and dispatch problems introduced by RES outputs, demand variations, as well as power demand of electric vehicles. In [48] and [49], MCS is used to manage uncertain wind power outputs and load variations in transmission expansion planning. The MCS approach has been widely used in many fields of power system research due to its simplicity. However, the accuracy of MCS results is highly dependent on the number of sampling and may be reduced as the number of uncertain parameters increases. Thus, to achieve results

with a high level of accuracy on a large-scale problem with many uncertain variables, a very large number of trials may be required, which will result in significant computational requirements.

The SBA is another category of approaches to managing uncertain variables in power systems. In these methods, a group of scenarios X_i, $i = 1, 2, ..., K$ for uncertain variables are selected and assigned with probabilities P_i, $i = 1, 2, ..., K$ based on the corresponding PDFs. Then the mean value of the output can be determined by:

$$Mean_Y = \sum_{i=1}^{K} P_i F(X_i) \tag{2.1}$$

SBA is an efficient approach to deal with stochastic programming (SP), which is an approach to model optimisation problems that involve uncertainty [50]. The most widely used SP model is the two-stage program [51]. The decision-maker takes actions in the first stage, then the random events get realised, which affect the outcome of the first-stage decision. After that, recourse decisions are made in the second stage to compensate for the negative effects which may be caused by first-stage decisions. The optimal solutions of this recourse model consist of a single first-stage decision and a collection of second-stage decisions corresponding to the realisations of uncertain variables. The mathematic formulation of the two-stage model is presented as [52]:

$$\min_{x_1} f(x_1) + \mathbb{E}[Q(x_1, \xi)]$$
$$s.t. G(x_1) = 0 \tag{2.2}$$
$$H(x_1) \leq 0$$

where x_1 represents the vector of the first-stage decision variables and ξ represents the vector of the random variables. $f(x_1)$, $G(x)$ and $H(x)$ represents the first-stage objective function, equality constraints and inequality constraints, respectively. $\mathbb{E}[Q(x_1, \xi)]$ is the expected value of the recourse cost and $Q(x_1, \xi)$ is given by:

$$Q(x_1, \xi) = \min_{x_2} q(x_2, \xi)$$
$$s.t. G_q(x_1, x_2, \xi) = 0 \tag{2.3}$$
$$H_q(x_1, x_2, \xi) \leq 0$$

where x_2 is the second-stage decision variables, G_q and H_q are the equality and inequality constraints in the second stage.

In most applications, the closed form of solutions to the optimisation model presented by (2.2) and (2.3) is not available due to the implicit formulation of objective functions and constraints with random variables. SBA can be applied to formulate the computationally tractable approximation. Representing the random variables ξ with K scenarios $\xi_i, i = 1, \ldots, K$ and corresponding probabilities $P_i, i = 1, \ldots, K$, the two-stage model can be reformulated as:

$$\min_{x_1, x_2} f(x_1) + \sum_{i=1}^{K} P_i q(x_{2i}, \xi_i)$$
$$s.t. \, G(x_1) = 0$$
$$H(x_1) \leq 0$$
$$G_q(x_1, x_{2i}, \xi_i) = 0, i = 1, 2, \ldots, K$$
$$H_q(x_1, x_{2i}, \xi_i) \leq 0, i = 1, 2, \ldots, K$$

(2.4)

Two-stage SP has been applied for day-ahead planning, reserve management and electricity market trading [53]–[56]. Similar to MCS, the increase of scenario numbers can improve the accuracy of the achieved results but will increase the computational burden. Consequently, the trade-off between the accuracy (loss of the information) and the reduction of the computational burden should be made carefully through scenario reduction [57]–[60].

The PEM works based on the moments of uncertain inputs. For the problem $Y = F(X)$ in which the length of uncertain vector X is n, the main steps to estimate the mean value and standard deviation of Y with two-point estimation method are given as follows [61]:

1. Set $E(Y) = 0, E(Y^2) = 0, k = 1$
2. Calculate the locations and probabilities of concentrations, $\epsilon_{k,i}$ and $P_{k,i}$:

$$\epsilon_{k,i} = \frac{1}{2} \frac{M_3(X_k)}{\sigma_{X_k}^3} + (-1)^{i+1} \sqrt{n + \frac{1}{2} \left(\frac{M_3(X_k)}{\sigma_{X_k}^3} \right)^2}, i = 1, 2$$

(2.5)

$$P_{k,i} = \frac{(-1)^i \epsilon_{k,3-i}}{2n \sqrt{n + \frac{1}{2}\left(\frac{M_3(X_k)}{\sigma_{X_k}^3}\right)^2}}, i = 1,2 \tag{2.6}$$

where X_k is the kth component of the uncertain variable X and $M_3(X_k)$ denotes the third-order central moment of X_k.

3. Calculate the concentration points $X_{k,i}$:

$$X_{k,i} = Mean_{X_k} + \epsilon_{k,i} \times std_{X_k}, i = 1,2 \tag{2.7}$$

where $Mean_{X_k}$ and std_{X_k} are the mean and standard deviation of X_k

4. Calculate $E(Y)$ and $E(Y^2)$ as:

$$E(Y) = E(Y) + \sum_{i=1}^{2} P_{k,i}F(x, \mathbf{X}_i) \tag{2.8}$$

$$E(Y^2) = E(Y^2) + \sum_{i=1}^{2} P_{k,i}F^2(x, \mathbf{X}_i) \tag{2.9}$$

where $\mathbf{X}_i$ is the uncertain vector in which the kth component is replaced by the concentration points calculated in Step 2, given as:

$$\mathbf{X}_i = [X_1, X_2, \dots X_{k,i}, \dots, X_n], i = 1,2 \tag{2.10}$$

5. $k = k + 1$ if $k \geq n$ continue, otherwise go to Step 2.

6. Calculate the mean and standard deviation of Y by:

$$Mean_Y = E(Y) \tag{2.11}$$

$$std_Y = \sqrt{E(Y^2) - E^2(Y)} \tag{2.12}$$

PEM estimates the moments of outputs with only $2n$ function calculations. Compared with MCS and SBA, it is less computationally expensive. Some applications of PEM in power systems are provided by[62]–[66]

In this thesis, the MCS method is used to generate samples for uncertain wind speeds and directions, power outputs of wind turbines as well as load variations, which is discussed in Chapter 4 and Chapter 5.

2.3.2 Possibilistic method

Possibilistic methods apply the fuzzy set theory proposed by [67] to model the uncertain variables, in which the uncertain parameters are presented by fuzzy sets.

Assuming that U is a collection of objects denoted by x and the deterministic set A can be represented by the characteristic function φ_A shown as (2.13), which maps U into two-element set $\{0,1\}$ as:

$$\varphi_A(x) = \begin{cases} 0, x \notin A \\ 1, x \in A \end{cases}, \forall x \in U \tag{2.13}$$

Similarly, a fuzzy set A in U can be represented by a set of ordered pairs denoted as $A = \{(x, \mu_A(x)) | x \in U\}$ in which μ_A is a membership function given as (2.14), mapping U into the closed interval [0, 1]. The value of the membership function would be 0 if the object x is out of the set and the value would be 1 if x is exactly in the set. However, if the object x is possibly in the set, the value of the membership function would be between 0 and 1. Triangle fuzzy membership function, which is in general use to represent the load uncertainty, can be given as [68]:

$$\mu_A(x) = \begin{cases} \dfrac{x - d - a}{a}, & x \in [(d - a), d] \\ \dfrac{(d + b) - x}{b}, & x \in [d, d + b] \\ 0, & otherwise \end{cases} \tag{2.14}$$

where d is the most probable value of the uncertain parameter, a and b represent the inferior dispersion and superior dispersion, respectively.

For the given problem $Y = F(X)$ in which the uncertain variables X are modelled by fuzzy sets, the fuzzy set of the output can be determined by α-cut method [68]. The values of α are between 0 and 1. Applying α-cuts to the fuzzy set A, the interval A^α, which includes all the individuals of A whose membership function value is larger than α can be represented as:

$$A^\alpha = \{x \in U | \mu_A(x) \geq \alpha\} \tag{2.15}$$

or

$$A^\alpha = \left[\underline{A^\alpha}, \overline{A^\alpha}\right] \tag{2.16}$$

where $\underline{A^\alpha}$ and $\overline{A^\alpha}$ are the lower and upper bounds of the interval.

Then the calculation of fuzzy sets follows interval arithmetic [69]. Given two intervals $[a,b]$ and $[c,d]$ which are defined as $[a,b] = \{x | a \le x \le b\}$ and $[c,d] = \{x | c \le x \le d\}$, interval arithmetic operations are defined by:

$$
\begin{aligned}
[a,b] + [c,d] &= [a + c, b + d] \\
[a,b] - [c,d] &= [a - d, b - c] \\
[a,b] \cdot [c,d] &= [\min(ac, ad, bc, bd), \max(ac, ad, bc, bd)] \\
\frac{[a,b]}{[c,d]} &= \left[\min\left(\frac{a}{c}, \frac{a}{d}, \frac{b}{c}, \frac{b}{d}\right), \max\left(\frac{a}{c}, \frac{a}{d}, \frac{b}{c}, \frac{b}{d}\right)\right]
\end{aligned}
\tag{2.17}
$$

After obtaining the fuzzy set for the output, the defuzzification needs to be implemented to translate the fuzzy number to a real value. Multiple defuzzification methods can be used including the centroid method, maximum defuzzification technique, weighted average defuzzification technique [70], etc.

In power system analysis, the fuzzy numbers can be used to model uncertainties, such as load and generation, and then the fuzzy power flow analysis can be solved with interval arithmetic method [71]. The fuzzy logic has been applied to deal with uncertainties in power plant maintenance scheduling [72], unit commitment [73] and economic dispatch [74]–[76] with RES.

2.3.3 Other uncertainty handling approaches in power systems

Apart from the methods presented above, there are some methods which can be used when both probabilistic and possibilistic information are not available. Interval arithmetic (IA) is one of these approaches, wherein the ranges of output variables based on the known ranges of input variables [69][77]. Interval power flow calculation is introduced by [78] and interval analysis has been used to deal with power system uncertainties in electricity market decision makings [79], unit commitment [80] and distribution network reconfiguration [81]. However, as IA assumes that the unknown values of the uncertain inputs can vary independently within the given intervals, the range estimated by IA tend to be much wider than the exact range of the results. In order to overcome this problem, affine arithmetic (AA), which takes into account the dependency between computed and input variables, is proposed for interval computation. This method is used to determine the optimal wind curtailment strategies

for networks with high wind penetration in this thesis, which is discussed in Chapter 5.

Robust optimisation (RO) [82] is another technique to manage interval uncertainties. It aims to find the solution which is feasible for any realisation of the uncertainties in the given sets, even if the worst scenario occurs. Given a network with uncertainties which include RES and load variations, RO is able to find the solution which provides the optimal scheduling of network control actions with the realization of the worst cases. Then the network can stand any realization of uncertain variables without constraint violations and provide a reasonable economic or environmental performance (objective function) [40], [83], [84].

Chance-constrained programming (CCP) [85] is another formulation of stochastic programming discussed above, which can also be considered as a subclass of robust optimization methods. The robustness guaranteed in chance-constrained programming is probabilistic and constraint violations are allowed with usually very low pre-defined probability. Solution techniques to CCP are versatile. For a linear problem, assuming that the uncertain variables follow Gaussian distribution, the CCP can be transformed into a formulation of a second-order cone programming (SOCP), which is solvable in polynomial time using well-known methods of convex optimization [86]. However, solving chance constrained nonlinear optimization problems is still a challenging task, as it is difficult to evaluate the distributions of outputs from a nonlinear system, although the distributions of inputs are known. The additional check of the satisfaction of these chance constraints is either using MCS [87] or SBA [88][89], which can become time-consuming as the pre-defined constraint violation probability is low or when it is based on complicated multivariate integrations, which are highly non-convex [90]. To deal with these challenging problems, convex relaxation proposed by [91]–[93] might be a potential option.

When the information on uncertainties is to a large extent missing, information gap decision theory (IGDT) [94] can be applied, which only needs the nominal values for uncertain parameters. Given a decision-making model under uncertain conditions presented as (2.18):

$$\min_{x} f(x, \xi)$$
$$s.t. \, G(x, \xi) = 0 \qquad (2.18)$$
$$H(x, \xi) \leq 0$$

The optimisation problem can be solved initially assuming that the uncertain parameters would not deviate from the nominal values. Then the question which would arise when the realised uncertain parameters are different from the predicted values is: whether the uncertainty will entail positive or negative outcomes? Two different IGDT strategies, risk adverse (RA) and opportunity seeker (OS), can address this problem. RA strategy is to find the decisions which can avoid the potential failures, while OS strategy aims to find the decisions that could be beneficial from the realizations of uncertainties [95].

In IGDT-based approaches, the enveloped bound model described as (2.19) is one of the commonly used to describe uncertain variables:

$$U(ul, \xi_0) = \left\{ \xi : \left| \frac{\xi - \xi_0}{\xi_0} \right| \leq ul \right\}, ul \geq 0 \qquad (2.19)$$

where ul is the unknown uncertainty level of parameters ξ, ξ_0 is the forecast value of the uncertain parameter and $U(ul, \xi_0)$ is the set of all values of ξ whose deviation from the nominal value ξ_0 will never be larger than $ul\xi_o$.

The RA strategy tries to select the decisions which can make the objective function "immune" against the deviations of uncertain parameters. The most robust decision is obtained if the objective function "sustains" with respect to the maximum radius of uncertainty. The decision-making policy can be formulated as the bilevel optimisation model:

$$\max_{x} ul$$
$$s.t. \, G(x, \xi) = 0 \qquad (2.20)$$
$$H(x, \xi) \leq 0$$

where $\widehat{ul}$ is given by the maximum value of the unknown uncertainty levels:

$$\widehat{ul} = \max_{ul} ul$$
$$s.t. \, f(x, \xi) \leq \beta_c \qquad (2.21)$$

in which β_c is the predefined critical limit (Robustness) which the objective function value should avoid surpassing.

In contrast to RA strategy, decision-makers who apply OS strategy are generally optimistic about the uncertain events that may bring about positive outcomes. In this strategy, the decision variables are selected, assuming that the positive outcomes can occur with a slight deviation of uncertain variables. The mathematical formulation of OS strategy is given as follows:

$$\min_{x} \breve{u}l$$
$$s.t.\, G(x, \xi) = 0 \qquad\qquad (2.22)$$
$$H(x, \xi) \leq 0$$

where $\breve{u}l$ is calculated by:

$$\breve{u}l = \min_{ul} ul$$
$$s.t.\, f(x, \xi) \leq \beta_o \qquad\qquad (2.23)$$

in which β_o is the opportunity value that the objective function should be lower than. Applications of IGDT in energy systems are reviewed by [96].

2.3.4 Summaries of approaches for management of uncertainties in power systems

The attributes of the commonly used uncertain management approaches in power systems are listed as Table 2.2.

In probabilistic approaches, the uncertainties are described by distribution functions. The information from these distributions, such as expectation and variance of the output, is determined by sampling or scenario-based methods, which are easy to implement but require a significant number of sampling and computational efforts to achieve results with a high level of accuracy.

Possibilistic methods model uncertain inputs with fuzzy numbers and calculate the fuzzy sets of outputs according to fuzzy logic. Although they convert the ambiguous uncertain information into effective numerical expressions, the applications may be restricted due to the complicated implementation.

Hybrid approaches, combining probabilistic and possibilistic methods, are capable of dealing with uncertainties described by different models but are also subject to the disadvantages of both methods.

Interval arithmetic, robust optimization and IGDT-based methods can be applied when the information on uncertainties (e.g. their probability distributions) is severely missing. Nevertheless, the main disadvantage of these approaches is that their results are too conservative when the uncertain events are finally realized. Furthermore, interval arithmetic suffers from "the curse of dimension", which may result in "error explosion" when applied to problems with many uncertain variables.

Chance constrained programming, which applies probabilistic information instead of intervals, can avoid the conservativeness of the solutions. However, obtaining the tractable equivalent reformulation of CCP is still challenging, especially when the constraints with uncertain variables are nonlinear, as it is usually the case.

Table 2.2: Summary of attributes of uncertain management approaches in power system

Method	Uncertainty representation	Advantages	Disadvantages
Probabilistic	PDFs	Easy to implement	High computational burden and approximate results
Possibilistic	Fuzzy sets	Convert ambiguous information to numerical expression	Complex to implement
Hybrid	PDFs & fuzzy sets	Deal with multiple types of uncertainties	Shortcomings of both probabilistic and possibilistic methods
IA	Intervals	Applicable when uncertain information is severely missing; Robust solutions are obtained	Too conservative; Error explosion
RO	Intervals		Too conservative
IGDT	Forecast values and bounded models		
CCP	PDFs	Conservativeness is controlled	Complicated formulation hard to solve

Considering the strengths and shortcomings of those methods, the selection of proper uncertain management approaches should be made carefully based on the types of uncertain variables. Additionally, further research efforts should be invested in the development of uncertain handling methods with higher robustness, less computational burden and simplicity of implementation.

2.3.5 Hybrid probabilistic-possibilistic approaches

In some cases, some uncertain parameters are modelled by PDFs while the others are modelled by fuzzy membership functions. To handle uncertainties in a way that some are modelled probabilistically while the others are represented possibilistically, the hybrid methods are required. Possibilistic-Monte Carlo approach and Possibilistic-scenario based approach have been introduced in [97] and [98].

2.4 Optimal power flow

Optimal power flow (OPF) problem was firstly formulated by [99] in 1962. It plays an essential role in the analysis of power systems. Typically, it is solved on a "year-by-year" basis in system planning studies and on a "day-ahead" basis for electricity market analysis. Moreover, OPF is at the heart of the economically efficient and secure operation of networks [100].

2.4.1 General formulation of OPF

The OPF problem aims to find the optimal operating point $x \coloneqq \{\mathbf{P}, \mathbf{Q}, |\mathbf{V}|, \boldsymbol{\theta}\}$ for an objective function, subject to both equality and inequality constraints. The general formulation of alternating current optimal power flow (ACOPF) problem is given by:

$$\underset{x}{\text{Min}} \, f(x) \tag{2.24}$$

$$s.t. \, G(x) = 0 \tag{2.25}$$

$$H(x) \leq 0 \tag{2.26}$$

where equation (2.24) represents the objective function, such as generation cost minimisation of active power loss minimisation. The equations (2.25) and (2.26) represent the equality constraints and inequality constraints, respectively. In ACOPF problem, the equality constraints include the AC power flow equations, while the inequality constraints consist of the security limits of power system operation,

including bus voltages, thermal ratings of branches and minimum/maximum generator power outputs.

Equality constraints of OPF – AC power flow equations

Given an electrical grid with a set of network buses $\mathcal{N}$ and network branches $\mathcal{L}$, the relationships between branch flows and bus voltages are given by AC power flow equations shown as (2.27) and (2.28).

$$P_{gi} - P_{di} = |V_i| \sum_{j\in\mathcal{N}} |V_j| \left(G_{ij} \cos(\theta_i - \theta_j) + B_{ij} \sin(\theta_i - \theta_j)\right), \forall i \in \mathcal{N} \quad (2.27)$$

$$Q_{gi} - Q_{di} = |V_i| \sum_{j\in\mathcal{N}} |V_j| \left(G_{ij} \sin(\theta_i - \theta_j) - B_{ij} \cos(\theta_i - \theta_j)\right), \forall i \in \mathcal{N} \quad (2.28)$$

where: P_{gi} and Q_{gi} are active and reactive power outputs of the generator at bus i, P_{di} and Q_{di} are active and reactive demands at bus i, $|V_i|, \theta_i$ and $|V_j|, \theta_j$ represent bus voltage magnitudes and voltage angles at bus i and bus j respectively, G_{ij} and B_{ij} are the conductance and the susceptance for the $ij\ th$ component of the admittance matrix Y, determined by:

$$Y_{ij} = \begin{cases} \sum_{(l,i,k)\in\mathcal{L}_i \cup \mathcal{L}_i^R} y_{ik}, & if\ i = j \\ -y_{ij}, & if\ i \neq j \\ 0, & Otherwise \end{cases} \quad (2.29)$$

where for each branch $(l, i, k) \in \mathcal{L}$, i and k are the *from* and *to* buses respectively, and l is the branch id, $\mathcal{L}_i$ and $\mathcal{L}_i^R$ are the subsets of branch ids with which the *from* end and the *to* end of the branch are bus i respectively.

Equations (2.27) and (2.28) define the relationship between the $4|\mathcal{N}|$ variables $x \coloneqq \{\mathbf{P_g, Q_g}, |\mathbf{V}|, \boldsymbol{\theta}\}$ at each bus. To solve those equations, the buses in the networks are divided into three categories, PV, PQ and slack bus. The buses at which generators with automatic voltage regulation are installed are defined as PV buses. For a PV bus, its active power injection and voltage magnitude are specified. PQ buses are usually load buses, or buses in which generators do not have voltage regulation capabilities. For the PQ bus, its active and reactive power injections are known. The slack bus aims to set the reference for voltage magnitudes, voltage angles and frequency of the system.

Slack bus will balance power flows and compensate transmission losses and has a predefined voltage magnitude and voltage angle, usually 1.0 pu and 0°.

Inequality constraints – operational security limits

In the OPF problem, the inequality constraints consist of the physical and operational limits of the electric power system. Violations of these limits will reduce system security levels, as it will likely result in the activation of related protection systems (e.g. overloading), So operations beyond these limits may lead to cascade failures of components and blackout. Consequently, system operators should ensure that the limits are always satisfied.

Security limits presented as (2.30) include bus voltage limits and thermal limits of branches. These limits constrain the electricity transferred between nodes during the steady-state operating conditions. Operation beyond branch thermal limits will trigger the protection, and the corresponding overloading components will be tripped to prevent their damage due to overheating. Similarly, the steady-state voltage at each bus should be maintained within the specified voltage margin, as the violations of bus voltage limits may lead to damages, tripping or poor operation of equipment connected at the buses.

$$
\begin{cases}
P_{gi}^{min} \leq P_{gi} \leq P_{gi}^{max}, \forall i \in \mathcal{G} \\
Q_{gi}^{min} \leq Q_{gi} \leq Q_{gi}^{max}, \forall i \in \mathcal{G} \\
V_i^{min} \leq |V_i| \leq V_i^{max}, \forall i \in \mathcal{N} \\
\theta_i^{min} \leq \theta_i \leq \theta_i^{max}, \forall i \in \mathcal{N} \\
\left(P_{lij}\right)^2 + \left(Q_{lij}\right)^2 \leq (S_l^{max})^2, \forall (l,i,j) \in \mathcal{L}
\end{cases}
\tag{2.30}
$$

where $\mathcal{G}$ is the set of generator indices. P_{lij} and Q_{lij} denote active and reactive power flows on the branches l.

Objective functions

In modern power system operation, two common objectives for OPF problems are minimisation of fuel cost of power generation and minimisation of active power losses. The objective functions for fuel cost minimisation and active power losses are formulated as follows:

$$f_c = \sum_{i \in \mathcal{G}} a_i P_{gi}^2 + b_i P_{gi} + c_i \ (\$/h) \tag{2.31}$$

where a_i, b_i and c_i are the cost coefficients of generator i.

$$f_l = \frac{1}{2}\sum_{(l,i,j) \in \mathcal{L}}[g_{ij}\left(|V_i|^2 - |V_j|^2\right) + 2b_{ij}|V_i||V_j|\sin(\theta_j - \theta_i)] \tag{2.32}$$

where g_{ij} and b_{ij} are the series conductance and susceptance of branch l.

2.4.2 Approximation and convex relaxation of ACOPF

The ACOPF problem is non-convex due to nonlinear terms $|V_i|^2$ and $V_iV_j^*$, where V_j^* is the conjugate of V_j , as well as inequality constraints, So its solution can be NP-hard due to the nonconvexity. Significant research effort in previous literature has been invested in developing accurate approximations of ACOPF.

The DC optimal power flow (DCOPF), which has been widely used in power system planning, is linear programming (LP) problem, for which the solution techniques are highly efficient and reliable, even for large-scale networks. Integer variables, such as the connection of generators and switching status/control of branches, can be integrated into the optimization problem conveniently and DCOPF is extended to mixed-integer linear programming (MILP), which are suitable for many applications, such as optimal transmission reconfiguration [101]–[103], unit commitment [104] and system expansion planning [105].

In spite of DCOPF method, more accurate approximation of ACOPF have also been researched and significant research effort has been invested into convex relaxation. Nonconvexity of ACOPF is mainly caused by the AC power flow equations, as well as the inequality constraints on voltage magnitudes and power flows. By using proper reformulation, the non-convex formulation can be transferred into a convex programming problem, whose global optimum can be guaranteed. The solution of convex relaxed reformulation provides a lower bound for the solutions of the original problem. If the gap between two solutions is zero, the globally optimal solution to the original problem can be recovered from the solution to the relaxed problem [106]. Additionally, if the relaxed problem is infeasible, it can be guaranteed that the original problem is not feasible as well. Convex relations of ACOPF are based on second-order

28

cone programming (SOCP), quadratically constrained quadratic programming (QCQP) and semidefinite programming (SDP) [107], [108].

DC optimal power flow

DCOPF is a common simplification of the full ACOPF in which reactive power is neglected. This simplification is based on three assumptions [25]:

- Voltage magnitudes at all buses are close to the nominal values, $|V_i| = 1.0$ pu;
- Voltage angle differences between the *from* and *to* ends of any branches are close to 0, such that $\sin(\theta_i - \theta_j) \approx \theta_i - \theta_j$, $\cos(\theta_i - \theta_j) \approx 1$;
- Transmission line series resistance and shunt admittance are ignored so that the transmission losses do not exist.

Following these assumptions, the optimal variable set is reduced to $x := \{\mathbf{P_g}, \boldsymbol{\theta}\}$. The simplified DCOPF is given by:

$$\underset{x}{\text{Min}}\, f(x) \tag{2.33}$$

$$s.t.\, P_{gi} - P_{di} = \sum_{j \in \mathcal{N}} B_{ij}^{dc} \theta_j\,, \forall i \in \mathcal{N} \tag{2.34}$$

$$P_{li,j} = \frac{1}{x_{ij}}(\theta_i - \theta_j), \forall (l, i, j) \in \mathcal{L} \tag{2.35}$$

$$\begin{cases} P_{gi}^{min} \le P_{gi} \le P_{gi}^{max}, \forall i \in \mathcal{G} \\ \theta_i^{min} \le \theta_i \le \theta_i^{max}, \forall i \in \mathcal{N} \\ P_{lij}^{min} \le P_{lij} \le P_{lij}^{max}, \forall (l, i, j) \in \mathcal{L} \end{cases} \tag{2.36}$$

where B^{dc} represents the susceptance matrix; x_{ij} is the series reactance of branch l.

DCOPF suffers from several disadvantages, which limit its application in the control of modern power systems. Firstly, it is not applicable in applications in which the R/X ratio of branches is large so that the resistances and losses cannot be ignored, conflicting with the third assumption above. Secondly, the DCOPF solution may not be feasible (nonlinear power flow equations are not satisfied) and the operators need to tighten some constraints in DCOPF and resolve it, which reduces computational

29

efficiency significantly. The tightening of constraints typically relies on heuristic methods that are hard to apply for large-scale networks. Thirdly, the solution of the DCOPF is not optimal for the original problem and therefore the "quality" of the solution cannot be guaranteed.

SOCP relaxation of ACOPF

In the SOCP-ACOPF, new variables u_i, c_{ij} and s_{ij} are introduced for each bus $i \in \mathcal{N}$ and each branch $l \in \mathcal{L}$ to replace the quadratic terms, $|V_i|^2$ and $V_i V_j^*$, [109], [110]:

$$u_i := |V_i|^2, c_{ij} := |V_i||V_j| \cos(\theta_i - \theta_j), s_{ij} := -|V_i||V_j| \sin(\theta_i - \theta_j) \qquad (2.37)$$

The new introduced variables, termed as conic variables, follow the equality constraints (2.38) and (2.39) which are nonconvex:

$$u_i u_j = c_{ij}^2 + s_{ij}^2, \forall(l, i, j) \in \mathcal{L} \qquad (2.38)$$

$$\theta_j - \theta_i - \text{atan}\left(\frac{s_{ij}}{c_{ij}}\right) = 0, \forall(l, i, j) \in \mathcal{L} \qquad (2.39)$$

In order to have a convex SOCP formulation, the equality constraints (2.38) are relaxed into convex inequality constraints as (2.49) and the voltage angle constraints (2.39) are dropped. The relaxed ACOPF needs to satisfy the following constraints:

$$P_{gi} - P_{di} = G_{ii} u_i + \sum_{(l,i,j) \in \mathcal{L}_i \cup \mathcal{L}_i^R} \left(G_{ij} c_{ij} - B_{ij} s_{ij}\right), \forall i \in \mathcal{N} \qquad (2.40)$$

$$Q_{gi} - Q_{di} = -B_{ii} u_i - \sum_{(l,i,j) \in \mathcal{L}_i \cup \mathcal{L}_i^R} \left(B_{ij} c_{ij} + G_{ij} s_{ij}\right), \forall i \in \mathcal{N} \qquad (2.41)$$

$$P_{lij} = g_{ij}\left(c_{ii} - c_{ij}\right) + b_{ij} s_{ij}, \forall(l, i, j) \in \mathcal{L} \qquad (2.42)$$

$$Q_{lij} = -b_{ij}\left(c_{ii} - c_{ij}\right) + g_{ij} s_{ij}, \forall(l, i, j) \in \mathcal{L} \qquad (2.43)$$

$$P_{lij}^2 + Q_{lij}^2 \leq S_l^{max}, \forall(l, i, j) \in \mathcal{L} \qquad (2.44)$$

$$\left|V_i^{min}\right|^2 \leq c_{ii} \leq |V_i^{max}|^2, \forall i \in \mathcal{N} \qquad (2.45)$$

$$P_{gi}^{min} \leq P_{gi} \leq P_{gi}^{max}, \forall i \in \mathcal{G} \qquad (2.46)$$

$$Q_{gi}^{min} \leq Q_{gi} \leq Q_{gi}^{max}, \forall i \in \mathcal{G} \qquad (2.47)$$

$$c_{ij} = c_{ji}, s_{ij} = -s_{ji}, \forall(l, i, j) \in \mathcal{L} \qquad (2.48)$$

$$c_{ij}^2 + s_{ij}^2 \leq c_{ii}c_{jj}, \forall(l,i,j) \in \mathcal{L} \tag{2.49}$$

where (2.40) and (2.41) are the reformulated AC power flow equations and (2.42) - (2.44) represent the power flows on each branch as well as branch flow limits. It should be noted that (2.44) are convex quadratic as both active and reactive power flow P_{lij} and Q_{lij} are linear with respect to conic variables. Equation (2.45) represents the bus voltage magnitude limits.

It should be noted that this formulation is based on the relaxation of constraints (2.38) and (2.39). This relaxation is exact for OPF of a radial network and the optimal voltage angles can be easily recovered by (2.39). However, this relaxation may result in infeasible solutions to the original problems when applied to mesh networks, as the sum of voltage angle differences across the lines in a mesh network should always be equal to zero. To deal with this problem, multiple approaches have been proposed to reformulate the arctangent constraints (2.39) so that these constraints can be included while maintaining the convexity. The author in [111] proposes a sequential conic procedure based on a Taylor series approximation, resulting in an ACOPF approximation. Two conic quadratic constraints based on rectangular coordinates are introduced in [110] to replace the arctangent functions.

SDP relaxation of ACOPF

All the constraints of OPF can be formulated as linear functions of the entries of the quadratic matrix $\mathbf{VV}^*$, where $\mathbf{V}$ is the vector of bus voltage, $[V_i, ..., V_{\mathcal{N}}]^T$, and $\mathbf{V}^*$ is the conjugate transpose of the vector $\mathbf{V}$. Similar to the SOCP formulation, the non-convex constraints of ACOPF can be relaxed to convex if the term $\mathbf{VV}^*$ is replaced with a new matrix variable $\mathbf{W}$. In order to maintain the equivalence between $\mathbf{VV}^*$ and $\mathbf{W}$, two additional constraints need to be introduced: 1) the new matrix $\mathbf{W}$ should be positive semidefinite $\mathbf{W} \succeq 0$, and 2) the rank of the matrix $\mathbf{W}$ should be equal to 1, $rank\{\mathbf{W}\} = 1$. The constraint $rank\{\mathbf{W}\} = 1$ is nonconvex. Ignoring this constraint, the SDP relaxation can be shown as [112]:

$$\min f(x) \text{ over } x = \{\mathbf{P_g}, \mathbf{Q_g}, \mathbf{W}\} \tag{2.50}$$

$$s.t. P_{gi} - P_{di} = \sum_{(l,i,j)\in\mathcal{L}_i\cup\mathcal{L}_i^R} \text{Re}\{(W_{ii} - W_{ij})y_{ij}^*\}, \forall i \in \mathcal{N} \tag{2.51}$$

$$Q_{gi} - Q_{di} = \sum_{(l,i,j)\in\mathcal{L}_i\cup\mathcal{L}_i^R} \text{Im}\{(W_{ii} - W_{ij})y_{ij}^*\}, \forall i \in \mathcal{N} \tag{2.52}$$

$$|V_i^{min}|^2 \le W_{ii} \le |V_i^{max}|^2, \forall i \in \mathcal{N} \tag{2.53}$$

$$P_{gi}^{min} \le P_{gi} \le P_{gi}^{max}, \forall i \in \mathcal{G} \tag{2.54}$$

$$Q_{gi}^{min} \le Q_{gi} \le Q_{gi}^{max}, \forall i \in \mathcal{G} \tag{2.55}$$

$$|(W_{ii} - W_{ij})y_{ij}^*| \le S_l^{max}, \forall (l,i,j) \in \mathcal{L} \tag{2.56}$$

$$\mathbf{W} \succeq 0 \tag{2.57}$$

If this SDP relaxation provides a rank-1 optimal solution $\mathbf{W}^*$, then the relaxation is exact, and the bus voltages can be recovered.

2.5 Conclusions

This chapter first discussed the three primary functions of power system security, system monitoring, contingency analysis and corrective action analysis, followed by a classification of system operating states and a brief introduction to control strategies for different states. Then, different approaches to manage uncertainties in power systems were introduced and briefly discussed. According to the different models applied to describe uncertainty parameters, these approaches were divided into three groups: probabilistic methods, possibilistic methods and hybrid methods. In order to make proper decisions for maintaining system security considering economic and environmental aspects, for operating conditions with high levels of uncertainty, the OPF problem is an essential tool. This chapter presented the general formulation of the OPF problem. Moreover, considering the practical requirements on the robustness and computational efficiency of the solutions, a commonly used approximation, DCOPF, and two potential convex relaxation formulations, SOCP and SDP, were introduced.

Chapter 3
Assessment of Distribution Network Hosting Capacity for Wind-Based Renewable Generation

3.1 Introduction

In order to address rising concerns about the climate change and provision of affordable and sustainable energy supply, there was recently a significant increase of installations of various renewable-based electricity generation sources in distribution networks, which are anticipated to increase further in the future. Although renewable-based DG units are typically with smaller rated powers, their aggregate impact in a local distribution network will be stronger as their numbers increase. As the number of DG units increases, they will also start to reverse power flows at specific periods of time, e.g. at minimum loading conditions and/or when DG outputs are high, when part of the network with DG will be a net active power exporter during these times. However, at the times of maximum demand and/or when DG outputs are low, the network will be a net importer of active power.

Connection of a high amount of DG presents a number of challenges to distribution network operators (DNOs), as the existing electricity networks can accommodate increasing connections of DG only to a certain limit. This limit, which is usually denoted as a "hosting capacity" (HC), is typically determined with respect to specific technical or operational network constraints, including thermal limits, voltage constraints, power quality limits, etc. The concept of HC can be further interpreted in terms of an HC of an individual bus and HC of the whole network. For example, a DG owner who is planning to connect one or more DG units in a specific part of the distribution network will be interested in information on the maximum connectable DG power at one or more individual buses in the network, which is denoted as the "locational hosting capacity" (LHC). On the other hand, DNOs are under significant pressure to allow for increased DG connections and they are interested not only in LHC but also in the overall maximum power of multiple DG units that can be connected in the whole network, which is denoted as the "network hosting capacity" (NHC).

Various studies have been carried out to investigate the potential approaches for HC assessment. EPRI developed a "streamlined HC" method [113] to calculate HC of a feeder, taking into account sizes, types and locations of DG and feeder physical characteristics, as an intermediate step between the quick estimations and extensive analytical studies. Assessment of HC is performed with analytical methods (e.g. [114]), probabilistic methods (e.g. Monte Carlo based sampling in [115]) and optimisation-based methods (e.g. [116][117]). Both active and reactive management strategies, such as power curtailment [118], reactive power compensation [119], voltage control by OLTC transformers [120], or control of DG power factor [121], are used to maximise HC for DG in distribution systems. In [122] and [123], an optimisation model is developed to include uncertainties introduced by renewable DG, in which the objective function is to maximise the DG capacity connected into the network. Similarly, [124] - [125] presented multi-objective stochastic programming models for HC assessment under uncertainties. In [126], two objective functions focusing on economic aspects are considered: 1) the cost of the purchased energy from the upstream network and 2) operation and maintenance costs of DGs. In [127], two objective functions relative to technical aspects are used: 1) the maximization of the total installed DG capacity and 2) the minimization of active losses.

In a given network, LHC and NHC will vary with numbers and locations of connected DG units. Generally, maximum LHC at any network bus can be allocated when there is no other DG connected ("first-come-first-served" approach). Maximum available LHC will reduce to a different extent after connecting additional DG units. In this chapter, deterministic and probabilistic approaches are applied for HC allocation, considering variations of demands, DG outputs and DTRs of network components. The HC assessment has three steps, where maximum LHC of individual buses is calculated first, assuming the connection of a single DG unit in the network. Afterwards, results for maximum LHC are used to calculate NHC, assuming that DG units are connected at all network buses. This step gives minimum LHC from proportional allocation of available NHC. Finally, bus-to-bus LHC-sensitivity factors are calculated to determine how available LHC changes for any number of DG units connected at arbitrary network buses.

3.2 Dynamic thermal rating of overhead lines

DTR can provide actual current-carrying capacities of network components, based on their real-time operating conditions, and in that way, allow for the higher utilisation of network components. The increase in the uncertainty levels of power system operation, more competitive energy markets, as well as more frequent cross-regional power exchanges, have all pushed the existing networks to operate closer to their technical limits, which in itself presents a range of new challenges to network operation. Rather than investing in network upgrading and re-enforcing, the application of DTRs can be a more effective option to mitigate potential system congestions, both economically and technically.

The application of DTR has potential benefits for renewable energy integration, especially wind-based generation. Transmission and distribution overhead lines with DTR control system are able to facilitate the integration of higher wind energy sources when the wind speed is high, as the corresponding wind-cooling impact on line conductors is more intensive. The implementation of DTR can therefore increase wind energy delivery, reduce wind energy curtailment, and improve the reliability and security of systems with high wind penetration [128][129][130] [131].

For an overhead transmission/distribution line (OHL), the thermal rating is defined with respect to the maximum operating temperature at which the line conductors can maintain line security/safety clearance and prevent annealing of conductors. Traditionally, OHLs were operated with static thermal rating (STR), which is calculated concerning the assumed ambient conditions. In ER P27 [132], the recommended wind speed for STR estimation is 0.5 m/s, while the ambient temperature is 9°C, 20°C and 2°C for spring/autumn, summer and winter, respectively. On the other hand, the DTR implies that the thermal rating of an overhead line is dynamically changing with environmental conditions and the calculation of DTR for OHL can be done based on the thermal model of bare overhead conductors.

The thermal model of the bare overhead conductor presented by IEEE standard 738-2012 [23] is described by the following heat balance equation.

$$q_c + q_r + mC_p \frac{dT_c}{dt} = q_s + I^2 R(T_c) \tag{3.1}$$

where the left-hand side of the equation is the heat loss rate per unit length and the right-hand-side is the heat gain rate per unit length; q_c and q_r denote convection heat loss rate per unit length (W/m) and radiated heat loss rate per unit length (W/m) respectively; mC_p is the heat capacity of the conductor (J/(m°C)); T_c represents the conductor surface temperature (°C). On the right-hand side of the equation, q_s is the rate of solar heat gain per unit length (W/m) and $I^2 R(T_c)$ is the rate of joule heat gain per unit length (W/m); $R(T_c)$ is the AC resistance of the conductor at the temperature of T_c (Ω/m).

After setting $\frac{dT_c}{dt}$ to be zero, the steady-state heat balance equation can be obtained:

$$q_c + q_r = q_s + I^2 R(T_c) \tag{3.2}$$

For given ambient data and set value of the maximum allowed operating temperature, the maximum allowable steady-state current of the conductor can be calculated by:

$$I = \sqrt{\frac{q_c + q_r - q_s}{R(T_c)}} \tag{3.3}$$

3.2.1 Convection heat loss rate - q_c

The convection heat loss rate is significantly affected by the wind condition. Natural convection heat loss which occurs when there is no wind is given by:

$$q_{cn} = 3.645 \rho_f^{0.5} D^{0.75} (T_c - T_a)^{1.25} \tag{3.4}$$

where ρ_f is the air density (kg/m^3), D is the diameter of the conductor (m), and T_a is the ambient temperature (°C), respectively.

The forced convection heat loss rate at low wind speeds and high wind speeds are presented as follows. At any speed, the convection heat loss rate is calculated with two equations below and the larger value is selected.

$$q_{c1} = \left[1.01 + 1.35 \left(\frac{D \rho_f V_w}{\mu_f} \right)^{0.52} \right] k_f K_{angle} (T_c - T_a) \tag{3.5}$$

$$q_{c2} = 0.754 \left(\frac{D\rho_f V_w}{\mu_f}\right)^{0.6} k_f K_{angle}(T_c - T_a) \tag{3.6}$$

where V_w is the wind speed (m/s), μ_f is the dynamic viscosity of air (kg/(m·s)). k_f is the thermal conductivity of air (W/(m· °C)).) at the temperature of the boundary layer of the conductor and the air, T_{film}, where:

$$T_{film} = \frac{T_c + T_a}{2} \tag{3.7}$$

K_{angle} is the wind direction factor which reflects the impact of wind direction on wind cooling effect:

$$K_{angle} = 1.194 - \cos(\phi) + 0.194 \cos(2\phi) + 0.368 \sin(2\phi) \tag{3.8}$$

where ϕ is the wind attacking angle which is between the wind direction and the conductor axis.

3.2.2 Radiated heat loss rate - q_r

The radiated heat loss rate is significantly dependent on the difference in temperature between conductor surface and its surrounding, which is assumed to be at ambient temperature.

$$q_r = 17.8D\varepsilon \left[\left(\frac{T_c + 273}{100}\right)^4 - \left(\frac{T_a + 273}{100}\right)^4\right] \tag{3.9}$$

where ε is the emissivity.

3.2.3 Conductor heat capacity – mC_p

Conductor heat capacity is defined as the product of specific heat and mass per unit length. For the non-homogeneous stranded conductor such as aluminium conductor steel-reinforced (ACSR), the heat capacity can be calculated approximately as follows:

$$mC_p = \sum m_i C_{pi} \tag{3.10}$$

where m_i is the mass per unit length of ith conductor material (kg/m) and C_{pi} is the specific heat capacity of ith conductor material $(J/(kg°C))$.

3.2.4 Solar heat gain rate (W/m)

The solar heat gain is given by:

$$q_s = \alpha Q_{se} \sin(\theta) A' \tag{3.11}$$

where: α is the solar absorptivity; Q_{se} is the total solar and sky radiated heat flux rate elevation corrected (W/m^2); θ is the effective angle of incidence of the sun's rays (degrees); A' is the projected area of conductor per unit length (m^2/m).

The effective sun's ray incidence angle is calculated by:

$$\theta = \arccos[\cos(H_c)\cos(Z_c - Z_l)] \tag{3.12}$$

where: H_c is the altitude of the sun (degree), Z_c is the Azimuth of the sun (degree) and Z_l is the Azimuth of the line (degree).

For the conductor, the projected area per unit length is given by:

$$A' = D \tag{3.13}$$

3.2.5 Joule heat gain rate (W/m)

$$R(T_c) = R(20°C)\big(1 + \alpha_e(T_c - 20°C)\big) \tag{3.14}$$

where α_e is the temperature coefficient (%/°C).

3.3 Dynamic thermal rating of transformers

The thermal model introduced by IEEE Std C57.91-2011 [24] is used to determine the dynamic thermal ratings for transformers. Two temperatures are critical for transformer operation, top-oil temperature (TOT) as well as hottest-spot temperature (HST).

The HST of a mineral oil-immersed transformer is calculated by:

$$T_H = T_a + \Delta T_{to} + \Delta T_H \tag{3.15}$$

where T_H is the winding hottest-spot temperature (HST, °C) and ΔT_{to} is the top-oil rise over ambient temperature (°C), ΔT_H is the winding hottest-spot rise over top-oil temperature (°C).

The TOT is given by:

$$T_{to} = T_a + \Delta T_{to} \tag{3.16}$$

The TOT rise at a time following a step change in loading is given by:

$$\Delta T_{to} = \left(\Delta T_{to,U} - \Delta T_{to,i}\right)\left(1 - \exp\left(-\frac{t}{\tau_{to}}\right)\right) + \Delta T_{to,i} \tag{3.17}$$

where $\Delta T_{to,i}$ and $\Delta T_{to,U}$ are the initial and final TOT rise (°C) respectively, τ_{to} is the oil time constant (hours).

The initial and final top-oil rise is estimated by (3.18) and (3.19).

$$\Delta T_{to,i} = \Delta T_{to,R}\left[\frac{K_i^2 R+1}{R+1}\right]^n \tag{3.18}$$

$$\Delta T_{to,U} = \Delta T_{to,R}\left[\frac{K_U^2 R+1}{R+1}\right]^n \tag{3.19}$$

where $\Delta T_{to,R}$ is the top-oil rise over ambient temperature at rated load (°C) and for the considered tap position, K_i and K_U are the ratios of load before and after step change to the rated load, n is the empirically derived exponent used to calculate the variation of ΔT_{to} with changes in load and the exponent is determined by the transformer cooling type, R is the ratio of load losses at rated load to no load at considered tap setting.

The winding HST rise over top-oil temperature is estimated by:

$$\Delta T_H = \left(\Delta T_{H,U} - \Delta T_{H,i}\right)\left(1 - \exp\left(-\frac{t}{\tau_w}\right)\right) + \Delta T_{H,i} \tag{3.20}$$

where $\Delta T_{H,i}$ and $\Delta T_{H,U}$ are the initial and final HST rise over top-oil temperature (°C), τ_w is the winding time constant at hot spot location (hours).

The initial and final HST rise is given by:

$$\Delta T_{H,i} = \Delta T_{H,R} K_i^{2m} \tag{3.21}$$

$$\Delta T_{H,U} = \Delta T_{H,R} K_U^{2m} \tag{3.22}$$

where $\Delta T_{H,R}$ is the winding HST rise over top-oil temperature at rated load on the considered tap position (°C), m is the empirically derived exponent used to calculate the variation of ΔT_H with changes in load.

3.4 Problem statement

Two types of capacity allocations are usually available to DG developers: a) firm capacity, when allocated DG output power can be injected into the network under all normal operating conditions without any constraint violations, and b) "non-firm capacity", when higher than firm capacity is allocated, but it will be curtailed/reduced to the firm capacity whenever higher DG outputs result in constraint violations. The main reason for considering non-firm capacity during the allocation process is that firm capacity might be too restrictive, as the constraint violations against which assessment is performed might be non-frequent "worst case scenarios", e.g. coincidental minimum demand and maximum DG output. This is particularly true in case of wind-based DG technologies, which feature strong and inherently stochastic variations of power outputs, which should be evaluated together with daily, weekly and seasonal changes in demands and available DTRs of network components. The research presented in this chapter concentrates on the relationship between the installed DG capacity and system technical constraints, while the economics aspects are neglected.

3.4.1 Network models

Two networks shown in Figure 3.1 are used for analysis. The first is a generic MV network model from [133], representing typical rural network configuration in the UK/Scotland. It is connected to a 33 kV grid supply point via primary 33/11 kV substation. The substation has a 2.5 MVA oil natural-air natural (ONAN) cooling type transformer with OLTC control, supplying two 11 kV feeders ("Feeder A" and "Feder B"). Both feeders are made of two types of OHL conductors: "Type S" is all aluminium

alloy conductor (AAAC, 75℃) 100 mm^2 Oak AL4, while "Type T" is ACSR 54/9 mm^2 (75℃). Each feeder supplies a number of secondary 11/0.4 kV distribution transformers, through which 34 load buses are connected, with maximum and minimum P/Q demands of 1.46 MW/0.48 Mvar and 0.2434 MW/0.0800 Mvar, respectively. All 48 buses are available for connection of wind-based DG units. The second network is IEEE 33-test network, for which data and information are available in [134].

3.4.2 Variations in loading conditions

Variations in loading conditions are identified from the available hourly demand data, recorded over a period of six calendar years in an actual Scottish MV distribution network, representing demands of a predominantly residential class of customers. The corresponding daily load profiles, assumed to be the same at all load buses in the considered network, are shown in Figure 3.2. Demand data are normalised using the maximum demand recorded over the six years of monitoring.
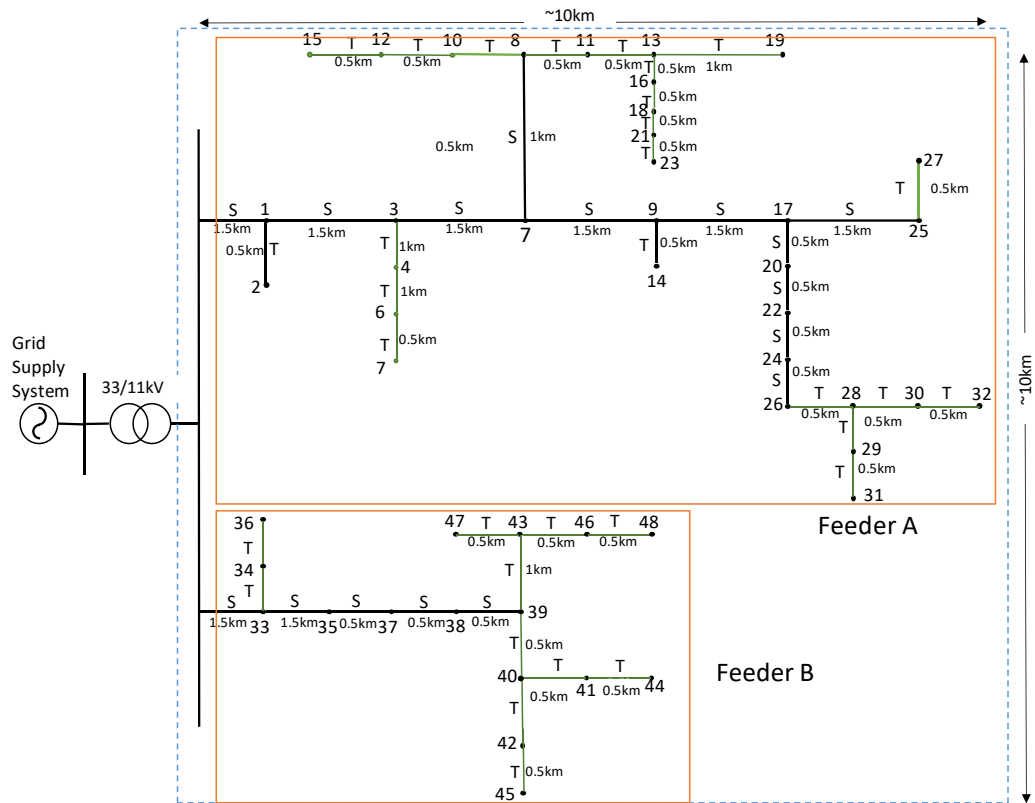
a)   Typical Scottish/UK generic rural MV distribution network
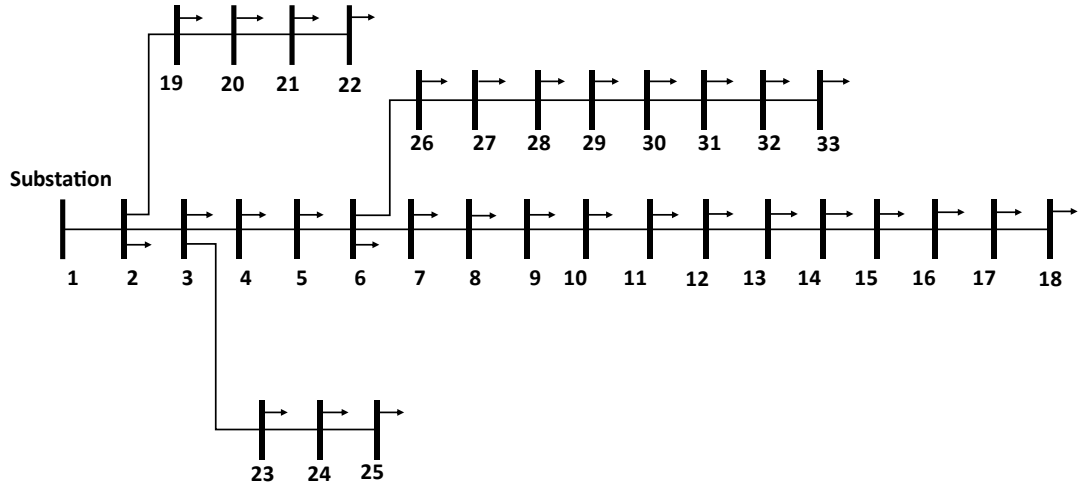
b) IEEE 33-bus test network

Figure 3.1: Two test networks used for HC analysis
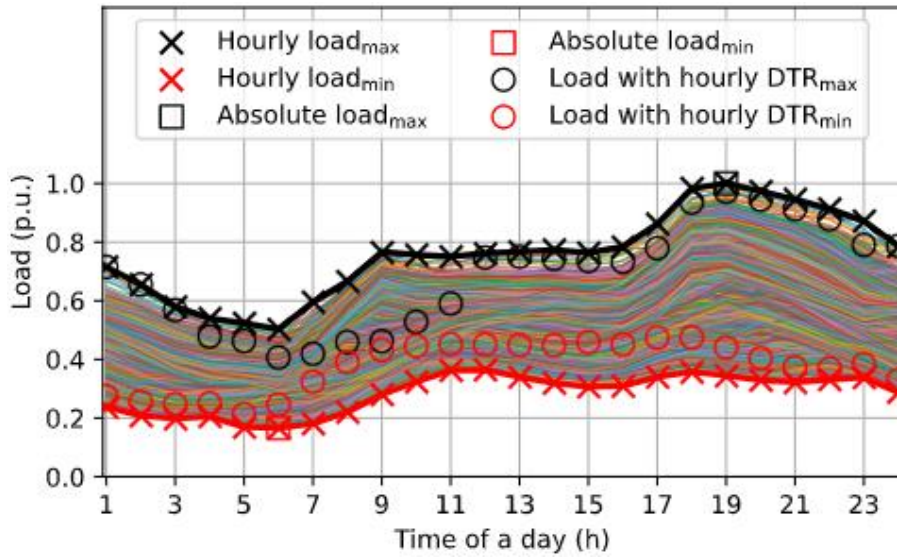
Figure 3.2: Daily load profiles of predominantly residential customers recorded over a period of six years in a Scottish distribution network

Figure 3.2 indicates three general cases for input demand data availability in deterministic scenario-based analysis: a) only absolute maximum and absolute minimum annual demands amongst all hours of the day are available (two values), b) maximum and minimum annual demands registered at each of 24 hours of the day (24 minimum and 24 maximum values), c) coincidental values of demands when maximum and minimum annual DTR values are reached at a specific hour of the day (48 values for each set of DTR values, calculated in the next sub-section). In the

42

probabilistic analysis, time-stamped hourly demand values (8760 values in a calendar year) are synchronised with hourly values of ambient parameters and DTR values.

3.4.3 Variations in power outputs of wind-based DG

Wind energy resource features strong stochastic variations, resulting in wide variations of power outputs of wind-based DG. This is illustrated in Figure 3.3 using recorded data from an actual wind farm (WF) in Scotland for six years. It can be clearly seen that at any hour of the day and for any day of the year, the power output of a wind-based DG can be anywhere between 0 and 1 pu. This is different from, e.g. PV-based DG, which is always zero during the night hours. In terms of assessing HC for wind-based DG, this simply means that the maximum 1 pu power output should be considered as possible to occur at all hours of all days of the year. Variations of wind direction are similar, i.e. wind direction at any hour of the day and on any day of the year can be anywhere in a range from 0° to 360°.
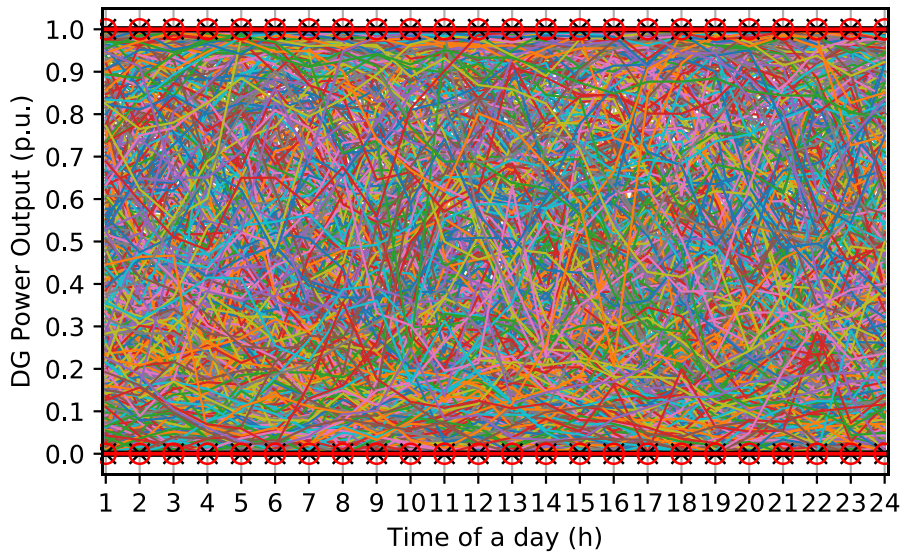
Figure 3.3: Variations of power outputs of a wind-based DG recorded at an actual wind farm in Scotland over the period of one calendar year

In terms of correlating DG power outputs with the variations in DTR values of network components, it is important to identify the range of wind speeds at which 1 pu DG power output is obtained. Based on the recorded WF data, Figure 3.4 shows the operational power curve of one wind turbine (WT). It is clear that WT will produce 1 pu power output for a relatively wide range of input wind speeds: the minimum is around 14.5 m/s, while the maximum is around 23 m/s (both are estimated from the

43

5th-95th percentile interval of all measured 1 pu WT power outputs). These two wind speed values are used for assessing variations in minimum and maximum DTR values in the next sub-section. Due to the relatively small size of the considered networks (10 km x 10 km, Figure 3.1 a)), it is assumed that maximum 1 pu. DG output in cases with two or more DG units will be produced by all connected DG units.
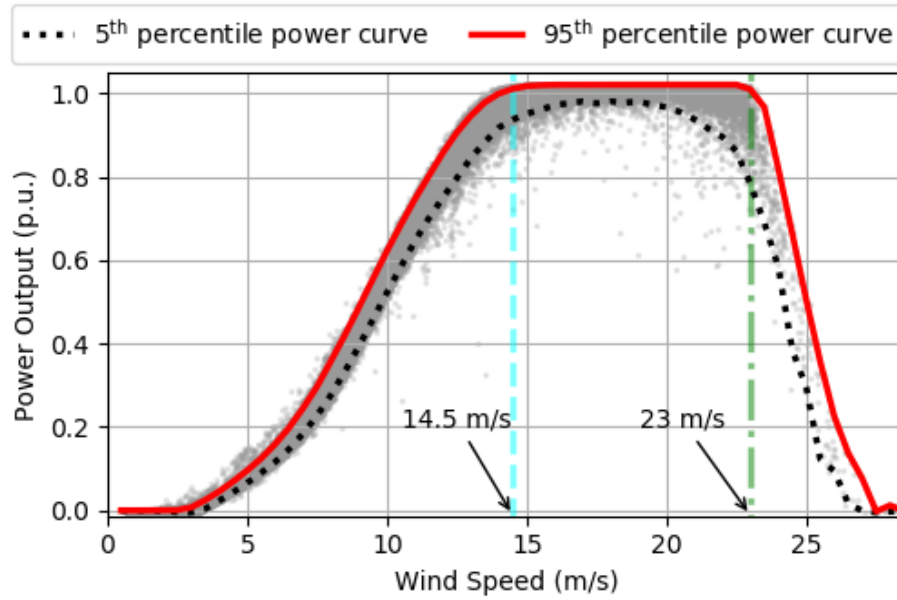
Figure 3.4: Wind speeds for which an actual WT produces 1 pu power output

3.4.4 Variations in DTR limits of network components

Essentially, DTR analysis acknowledges that thermal characteristics of network components will change with the variations of ambient parameters, which in turn will impact their maximum MVA loading. For example, and in the context of the presented analysis, high wind speed will result in the increased power outputs of wind-based DG, but it will also cool-down and decrease the temperature of overhead lines through which DG power is exported, therefore allowing higher MVA loading before the thermal limit is reached. In the considered HC analysis, this means that for calculating minimum DTR of the lines, minimum wind speed at which wind-based DG produces 1 pu power output should be used (14.5 m/s, Figure 3.4), while for calculating maximum DTR, maximum wind speed at which wind-based DG produces 1 pu power output should be used (23 m/s). Similarly, wind direction ("attacking angle") of 0° (along the line) should be used for calculating minimum DTR values, while wind direction of 90° (perpendicular to the line) should be used for calculating maximum

44

DTR values. As shown in Figure 3.3, 1 pu power output of wind-based DG could be expected at any hour of any day of the year, which means that annual variations of two other ambient parameters that have an impact on DTR values (temperature and solar irradiance) should be considered next. The variations of ambient parameters are obtained for the same six-year period for which loading conditions are shown in Figure 3.2 from datasets in [135], while DTR models of overhead lines are calculated by the thermal balance equation (3.3). The parameters for DTR calculation are available in [136].

Calculation of minimum and maximum DTR values is illustrated in Figure 3.5, where Figure 3.5a shows annual variations of temperature, Figure 3.5b shows annual variations of solar irradiance, while Figure 3.5c – Figure 3.5e show changes in DTR values for the OHL Types S and T and the 33/11 kV transformer in Figure 3.1 a).
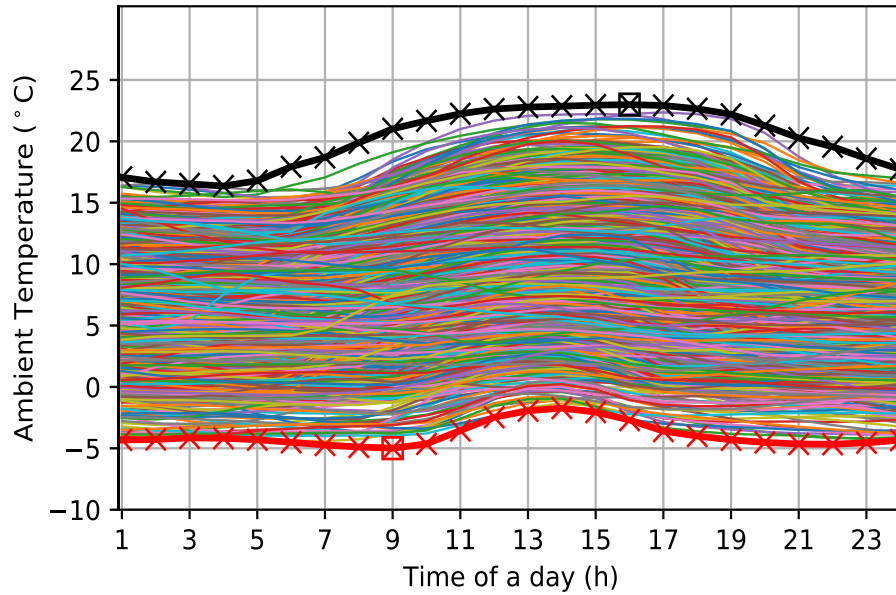
a) annual temperature variations
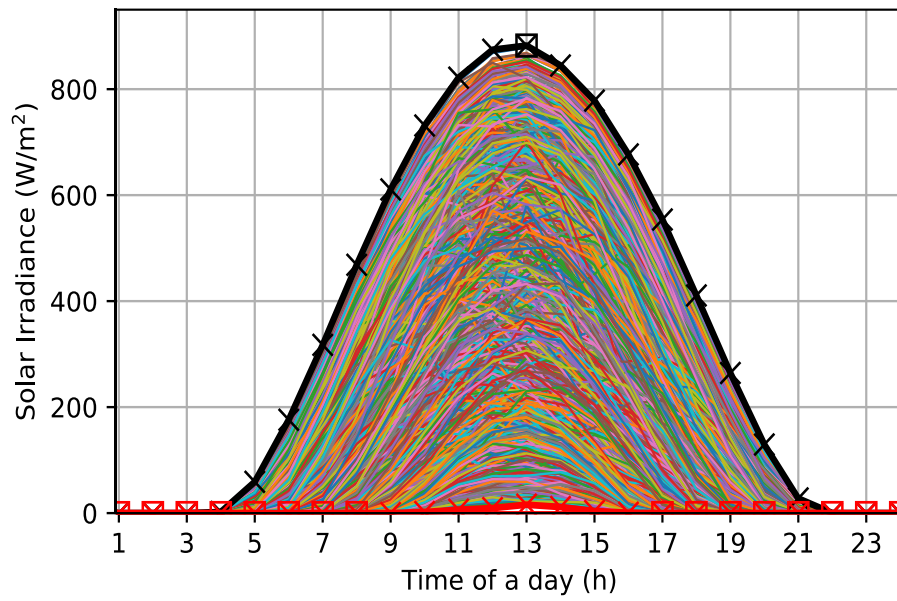
b) annual solar irradiance variations
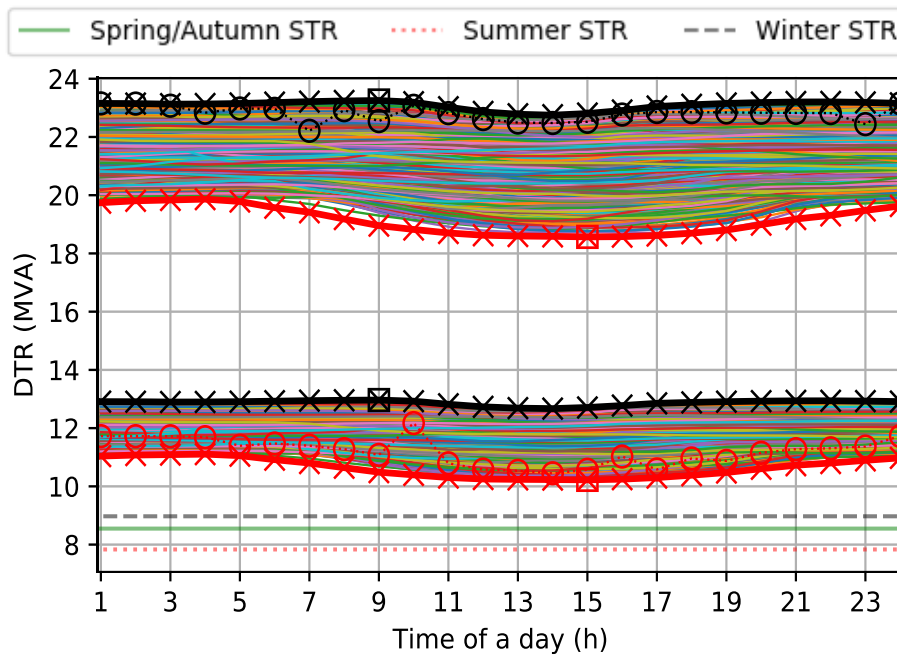
c) variations in minimum and maximum DTR values for OHL Type S for wind speeds of 14.5 m/s and 23 m/s, and wind directions of 0° and 90°
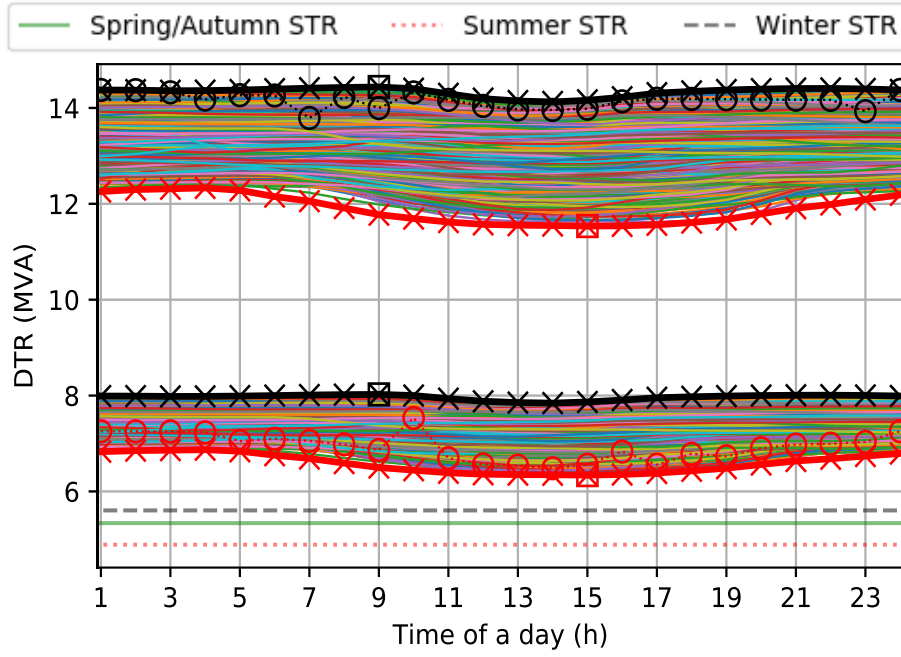
d) variations in minimum and maximum DTR values for OHL Type T for wind speeds of 14.5 m/s and 23 m/s, and wind direction of 0º and 90º
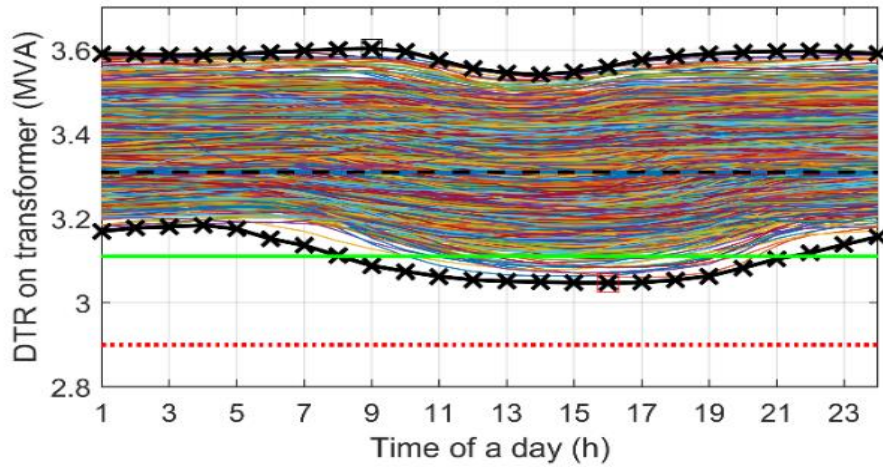
e) Variations in DTR values for 33/11 kV transformer (no impact of wind speed considered)

Figure 3.5: Calculated variations in minimum and maximum DTR values, with c) showing an example of coincidental DTR values with max/min demands

Similarly to demands, Figure 3.5 indicates three general cases for deterministic scenario-based DTR analysis: a) only absolute maximum and minimum annual DTR values amongst all hours of the day, b) maximum and minimum annual DTR values registered at each of 24 hours of the day, and c) DTR values coincidental with maximum and minimum annual demands at a specific hour of the day. In the probabilistic analysis, time-stamped calculated hourly DTR values (8760×6 values) are synchronised with hourly demand values.

3.5 Numerical results

The presented HC assessment procedure has three stages. Firstly, maximum LHC of individual buses is calculated assuming connection of a single DG unit at a considered bus in the network, giving maximum possible LHC at any individual considered bus. Then, maximum LHCs are scaled-down, and an optimisation approach is used to calculate NHC, assuming the connection of DG units at all network buses. An alternative optimisation approach, in which DG at any bus was increased from 0 to maximum value, is used for checking optimality of solutions. This stage gives minimum LHC, obtained from a proportional allocation of available NHC. Finally, calculation of bus-to-bus LHC sensitivity factors is used to determine available LHC at individual buses for any number of DG units with different installed powers and connected at arbitrary network buses.

Two approaches are implemented: a) "deterministic", in which a limited number of selected scenarios with minimum and maximum values of demands, DTR limits and DG outputs are considered as the non-coincidental and coincidental inputs for the analysis, and b) probabilistic, based on the analysis of time-series of simultaneous hourly variations of all input parameters, providing their probability distributions.

The results for LHC and NHC are presented as the ranges of values from 0% constraint violation (representing "firm capacity" allocation) to 100% constraint violation (representing the full range of possible "non-firm capacity" allocations). A simple analysis study is presented, with consideration of only overhead line and transformer DTR constraints, which can be easily extended to include additional technical, operational and other relevant constraints. The main reason for presenting ranges of 0%-100% constraint violations is that allocation of "non-firm" capacity will be determined using different criteria by both DNOs and DG developers, so the actual allocation in practice is essentially done on a "case-by-case" basis. Therefore, this chapter presents the whole ranges of possible non-firm capacity allocations, regardless of the required amount of curtailment, which is considered out of the scope of this chapter. All the network models and power flow calculations are implemented via an open source distribution system analysis tool, openDSS [137].

3.5.1 Scottish/UK generic rural MV distribution network

Stage 1 with deterministic LHC assessment

The 33/11 kV transformer's DTR values in Figure 3.5e suggest that this transformer is a main limiting component/factor for connecting DG, as its DTR values are around ½ of the DTR values of OHL Type T (Figure 3.5d) and around 1/3 of the DTR of OHL Type S (Figure 3.5c). This not only makes further HC assessment to be trivial (only loading constraints of one component should be considered) but also suggests that this transformer should be upgraded, before DNOs could connect any significant DG in this network, i.e. before they can start to allocate significant hosting capacity to DG developers. Also, in many cases, transformer upgrading is much easier, faster and with lower costs than upgrading of OHLs. Therefore, only loading constraints of OHLs are considered in further analysis and information is used for selecting the optimal size of transformer for upgrading.

LHC assessment with non-coincidental absolute maximum and minimum annual demand and DTR values:

These input values are used for evaluating LHC at individual network buses, always assuming the connection of a single DG unit in the network. They reflect practical situations in which only limited information is available, e.g. only minimum and maximum annual demands at load buses (no demand time series) or only absolute minimum and maximum DTR values of network components. Table 3.1 lists input data for this scenario, while Figure 3.6 presents results for all min-max combinations as black dashed lines.

Table 3.1: Non-coincidental scenarios

Scenario	Wind speed (m/s)	Attacking angle (degree)	Ta (°C)	Solar irradiance (W/m^2)	Load (p.u.)	DTR (MVA)
DTRmax Loadmax	23.0	90	-4.99	0	1	23.2518 (S) 14.4367 (T)
DTRmin Loadmin	14.5	0	22.9	882.2350	0.1667	10.2233 (S) 6.3405 (T)

LHC assessment with non-coincidental annual maximum and minimum demand and DTR values for each of 24 hours of the day:

When this more detailed information on variations in demands and DTR values is available, e.g. as in Figure 3.2 and Figure 3.5, it may be used to calculate corresponding non-coincidental LHC values, again assuming connection of a single DG unit in the network. Figure 3.6 shows these results as blue-coloured box-plots, constructed from the corresponding 24 maximum and 24 minimum demand and DTR values at every hour of the day.

LHC assessment with coincidental annual maximum and minimum demand and DTR values for each of 24 hours of the day:

When time-stamp information on the actual hour and day when minimum and maximum annual demands and minimum and maximum annual DTRs occur at each of 24 hours of a day, then coincidental DTR values can be obtained for minimum and maximum demands, and vice versa. These coincidental demand and DTR values (Figure 3.2 and Figure 3.5c) are realistic input data for HC assessment, as they reflect actual loading conditions in the considered network, which is generally not the case with non-coincidental data. The LHC results for this scenario are shown in Figure 3.6 as red-coloured box-plot, each constructed from the corresponding 48 values (24 demands coincidental with 24 maximum and 24 minimum DTR values, and 24 DTRs coincidental with 24 maximum and 24 minimum demands).

Stage 1 with probabilistic LHC assessment

Probabilistic LHC assessment is performed by statistical processing of time-stamped and synchronised (coincidental) hourly demands and hourly DTR values (8760 values in a calendar year for every dataset). These results are presented in Figure 3.6 as black-coloured box-plots, constructed from min/max LHC values calculated for each demand and DTR conditions. For example, deterministic LHC scenarios, which correspond to firm capacity allocation and 0% constraint violations, might occur for only a short period during a calendar year, which will then result in a too conservative allocation of LHC. This can be seen in the results for Bus 14 in Figure 3.6b, where a 5th percentile relaxation of the minimum coincidental LHC results in an increase of firm LHC of 3.11%.

Stage 2: NHC assessment

Stage 1 LHC are obtained under the assumption that there is a single DG unit connected at the considered bus and that both firm and non-firm capacity allocations (up to 100% constraint violation) are available. Assessment of NHC is a more complex problem, as NHC will change with the numbers, sizes and actual locations of connected DG. Furthermore, allocation of non-firm capacity to a number of DG developers might result in operational difficulties, as required curtailment shall be distributed in some way between a number of DG units. Therefore, the further analysis considers only firm capacity.

After Stage 1, firm NHC may be roughly assessed as the sum of maximum firm LHC for two feeders (A and B), which is 22.35 MW, or as a sum of LHCs for two DG units on Feeders A and B with the highest LHC, which is 21.33 MW. As these results are obtained for a single DG unit and do not allow to evaluate changes in operating and loading conditions, network power flows and losses for a number of connected DG units, two probabilistic optimisation methods are used next for NHC assessment.
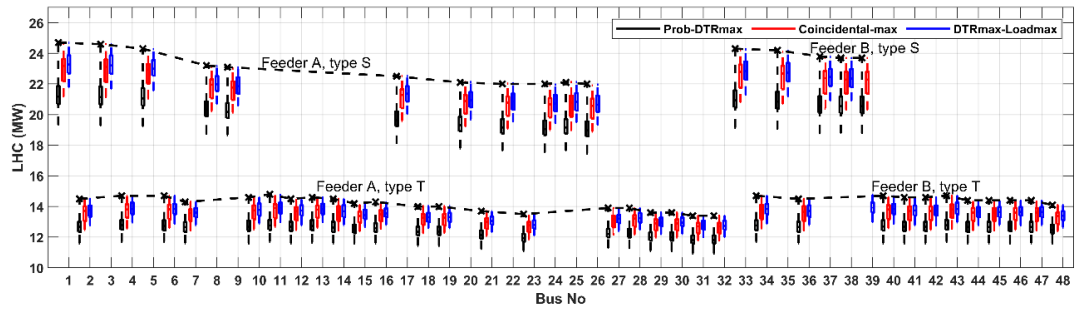
a) LHC values corresponding to non-firm capacity allocation (100% constraint violation limit)
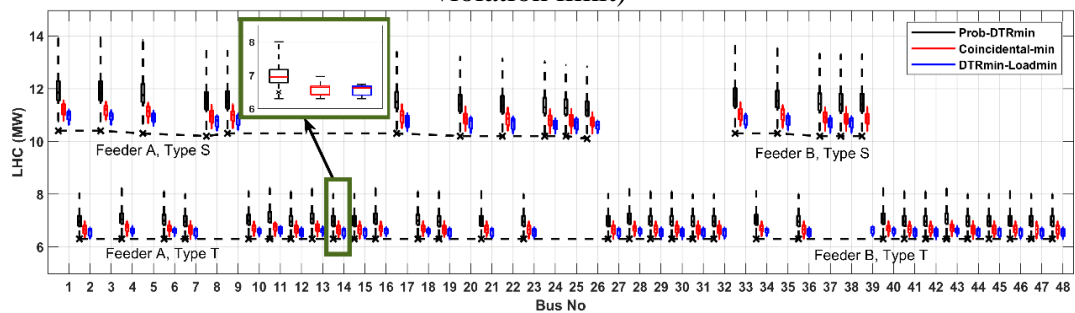
b) LHC values corresponding to firm capacity allocation (0% constraint violation limit)

Figure 3.6: Comparison of ranges of LHC values assessed by deterministic and probabilistic approaches at individual network buses (for a single DG unit connected at a considered bus)

NHC assessment with "Direct Optimisation Approach":

In this case, NHC is obtained by classical optimisation approach, assuming that DG might be connected at all 48 network buses and that optimisation starts from zero DG initially connected at each bus. The objective function is to maximise the total connected DG in the network while satisfying constraints on the loading of the lines:

$$max \sum_{i \in \mathcal{N}} p_i^g \tag{3.23}$$

$$P_j^l = P_i^l - r_{ij} \frac{\left(P_i^{l^2} + Q_i^{l^2}\right)}{|V_i|^2}, \forall (l, i, j) \in \mathcal{L} \tag{3.24}$$

$$Q_j^l = Q_i^l - x_{ij} \frac{\left(P_i^{l^2} + Q_i^{l^2}\right)}{|V_i|^2}, \forall (l, i, j) \in \mathcal{L} \tag{3.25}$$

$$P_i^l = P_j^{l-1} + p_i^g - P_{di}, \forall (l, i, j) \in \mathcal{L} \tag{3.26}$$

$$Q_i^l = Q_j^{l-1} + q_i^g - Q_{di}, \forall (l, i, j) \in \mathcal{L} \tag{3.27}$$

$$|V_j|^2 = |V_i|^2 - \frac{2\left(r_{ij}P_i^l + x_{ij}Q_i^l\right)}{|V_1|} + (r_{ij}^2 + x_{ij}^2) \frac{\left(P_i^{l^2} + Q_i^{l^2}\right)}{|V_i|^2}, \forall (l, i, j) \in \mathcal{L} \tag{3.28}$$

$$\theta_j = \theta_i - atan\left(\frac{\frac{P_i^l x_{ij} - Q_i^l r_{ij}}{|V_i|}}{|V_i| - \frac{P_i^l r_{ij} + Q_i^l x_{ij}}{|V_i|}}\right) \tag{3.29}$$

$$S_i^l = \sqrt{(P_i^{l^2} + Q_i^{l^2})}, S_j^l = \sqrt{(P_j^{l^2} + Q_j^{l^2})}, \forall (l, i, j) \in \mathcal{L} \tag{3.30}$$

$$V_i^{min} < |V_i| < V_i^{max}, \forall i \in \mathcal{N} \tag{3.31}$$

$$0 \le S_i^l \le S_l^{max}, 0 \le S_j^l \le S_l^{max}, \forall (l, i, j) \in \mathcal{L} \tag{3.32}$$

where: p_i^g is the size of DG connected at bus i for $\forall i \in \mathcal{N}$, and $\mathcal{N}$ is the set of bus indices, P_i^l, Q_i^l and P_j^l, Q_j^l are active and reactive power flows of line l measured at the *from* bus i and *to* bus j, S_i^l and S_j^l are the apparent power flow in line l measured at the *from* bus i and *to* bus j.

Total of 100 runs of this optimisation method resulted in the close values of the objective function, i.e. NHC, which varied in the range between 23.63-23.86 MW. However, almost every run provided a different solution, with wide ranges of

variations for resulting numbers, locations and sizes of DG units. Figure 3.7 shows these LHC results from 100 runs by blue box-plots.

NHC assessment with optimisation approach based on LHC values from stage 1:

In this case, NHC is obtained by a suitable proportional reduction of minimum LHC values obtained in Stage 1 for DG units connected at all buses (e.g. 10% of Stage 1 minimum LHC values), with the violations of some DTRs and some bus limits. The objective function is to minimise the reduction from initially connected DG while satisfying constraints (3.24) - (3.32).

For the selection of target buses for DG reduction, sensitivity analysis is implemented. Apparent power flow sensitivity factors and bus voltage sensitivity factors with the connected DG size are calculated with (3.33) and (3.34).

$$PISF_l^i = \frac{\partial S_l}{\partial p_i^g} = \frac{\Delta S_l}{\Delta p_i^g}, \forall (l, i, j) \in \mathcal{L}_{vio} \ and \ \forall i \in \mathcal{N} \qquad (3.33)$$

$$PVSF_i^j = \frac{\partial V_i}{\partial p_i^g} = \frac{\Delta V_i}{\Delta p_i^g}, \forall i \in \mathcal{N}_{vio}, j \in \mathcal{N} \qquad (3.34)$$

where $\mathcal{L}_{vio}$ and $\mathcal{N}_{vio}$ denote the sets of indices of overloading branches and buses with voltage violations.

The results of LHC-based optimisation are also illustrated in Figure 3.7, where they are close to the mean LHC values of 100 runs of the direct optimisation approach. The obtained NHC value is also close (23.72 MW). These results provide important information on the required upgrading of existing 33/11 kV transformer, which should be replaced by a transformer with DTR of around 25 MVA.

Stage 3: LHC for any number of DGs with different powers connected at arbitrary buses

Stage 3 tries to evaluate available firm LHC at a bus for any combination/number of DGs (with different powers) connected at arbitrary network buses. Available capacity is between boundary cases for firm LHC obtained in Stages 1 and 2 and can be

calculated by "bus-to-bus" LHC sensitivity factors of a bus i regarding installed p^g at bus j, $LHCSF_i^j$:
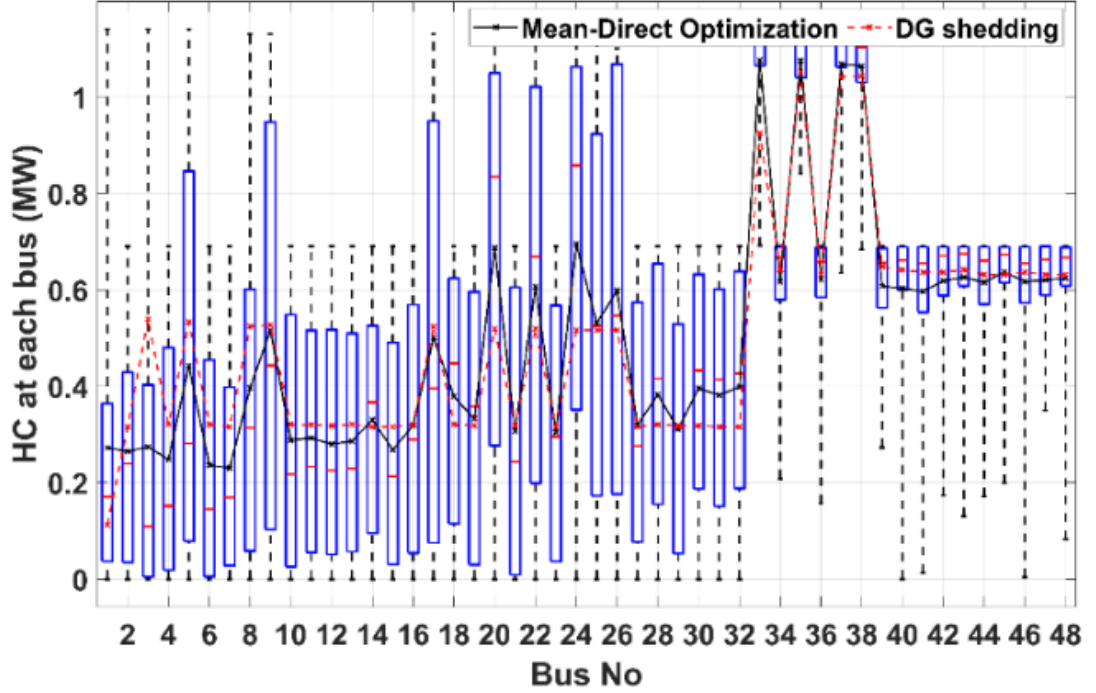
Figure 3.7: Comparison of two optimisation methods (DG at all buses) for the Typical Scottish/UK generic rural MV distribution network

$$LHCSF_i^j = \frac{\partial LHC_i}{\partial p_j^g} = \frac{\Delta LHC_i}{\Delta p_j^g} \text{ for } \forall i, j \in \mathcal{N} \qquad (3.35)$$

The results for bus-to-bus LHC sensitivity factors are shown in Figure 3.8. It can be observed that the LHC at one bus will be affected by the DG units connected to buses in the same feeder. Those sensitivity factors allow to quickly find the impact of the connection of DG units at any buses on the available LHC at other buses in the network. The proposed method is more computationally efficient as it doesn't need iterative power flow calculation. Table 3.2 presents the comparison of results for firm LHC at different buses (at the beginning, middle and end of each feeder and each line type) with accurate power flow analysis for Cases 1-4, corresponding to 5, 10, 20 and 30 DG units randomly located in the considered network. There are errors between power flow based results and results of the sensitivity-based method, because the power flow equations are nonlinear and network loss is not taken into account. The maximum error occurs at bus 26 when 5 DG units are connected. The error is 10%. This method can

be used to provide initial estimation for system operators when making the plan for DG connection.

Table 3.2: Comparison of Results for SFLHC and Power Flow (PF) for the Typical Scottish/UK generic rural MV distribution network

Case	BUS 1			BUS 9			BUS 26		
	PF	*SF*	*Error (%)*	*PF*	*SF*	*Error (%)*	*PF*	*SF*	*Error (%)*
1	4800	4382	8.71	4900	4740	3.27	5000	5502	10.0
2	6100	5716	6.30	6300	5845	7.22	6400	6339	0.95
3	6900	6557	4.97	7100	6652	6.31	7300	7037	3.61
4	5900	5532	6.24	6200	5614	9.45	6300	6017	4.49
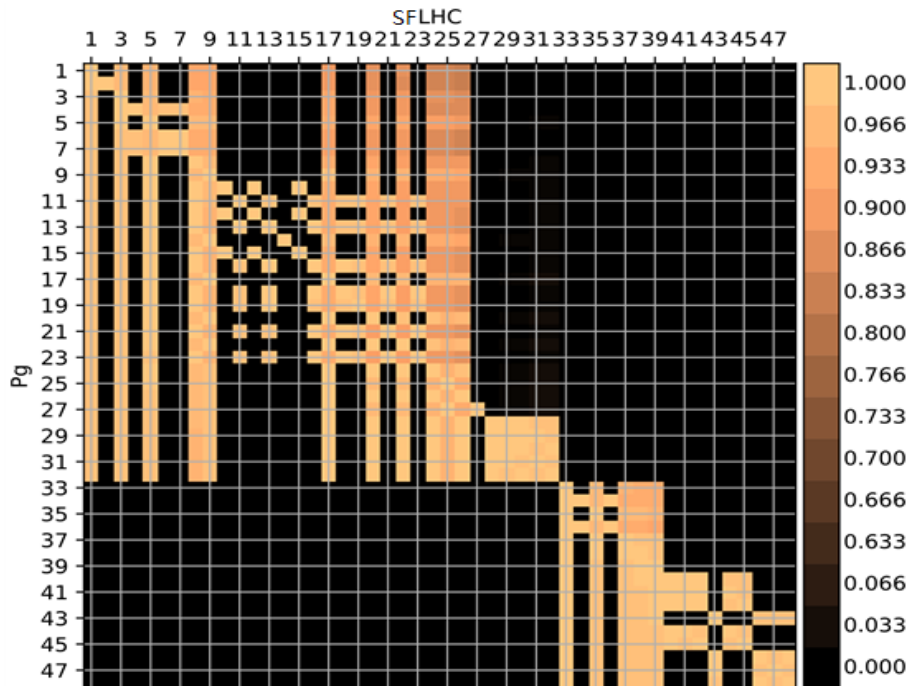
Figure 3.8: Graphical illustration of bus-to-bus LHC sensitivity factors for the Typical Scottish/UK generic rural MV distribution network

3.5.2 IEEE 33-bus network

The proposed approach is also tested on IEEE 33-bus network. The comparison between direct optimization and LHC-based optimization is presented in Figure 3.9. Two different number of DG units, 5% and 10% of the minimum LHC obtained in the first stage, are connected into the initial network initially, then optimal DG shedding is implemented at targeted buses determined by sensitivity analysis. The two analysis achieved similar NHC values of 6.8780 MW and 6.8821 MW, which are both close to the mean NHC obtained from one hundred runs of direct optimisation approach,

6.8655MW. However, the HC at each bus is different. The results obtained with 5% of LHC connected into the network initially are closer to the mean values of direct optimization results.

Bus-to-bus LHC sensitivity factors are presented in Figure 3.10, while Table 3.3 shows results for firm LHC at different buses with accurate power flow analysis and sensitivity factor method (SFLHC) for three scenarios, corresponding to 5, 10, 20 units randomly located in the considered network.
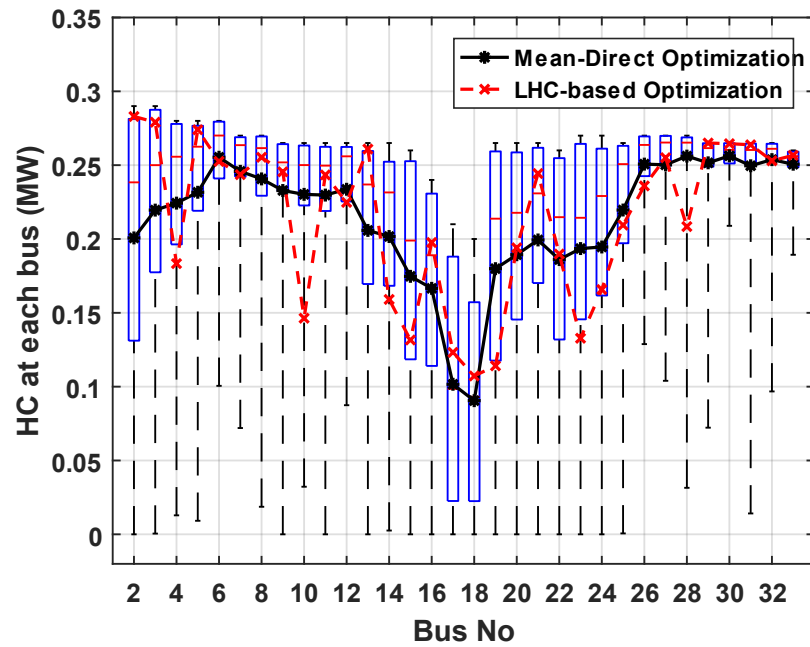
a) LHC-based optimization with the initial connection of 5% of LHC
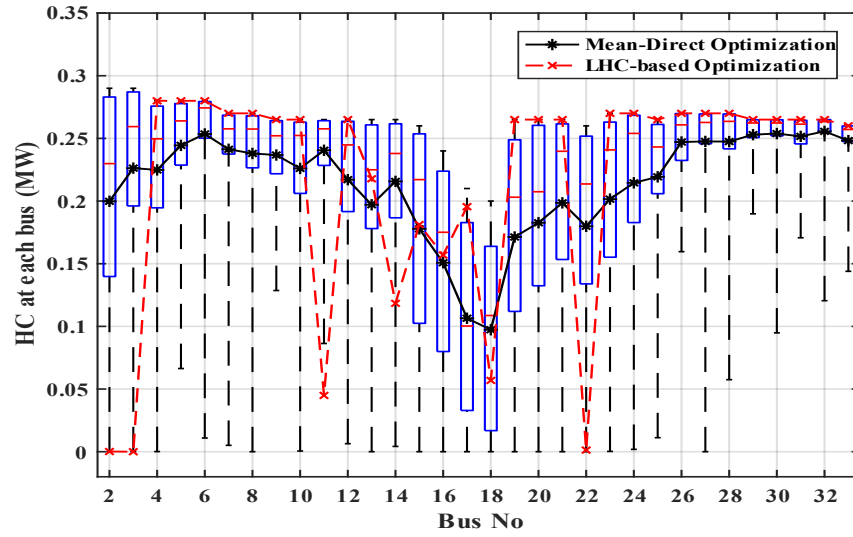
b) LHC-based optimization with the initial connection of 10% of LHC

Figure 3.9: Comparison of two optimisation methods (DG at all buses) for IEEE 33-bus test system
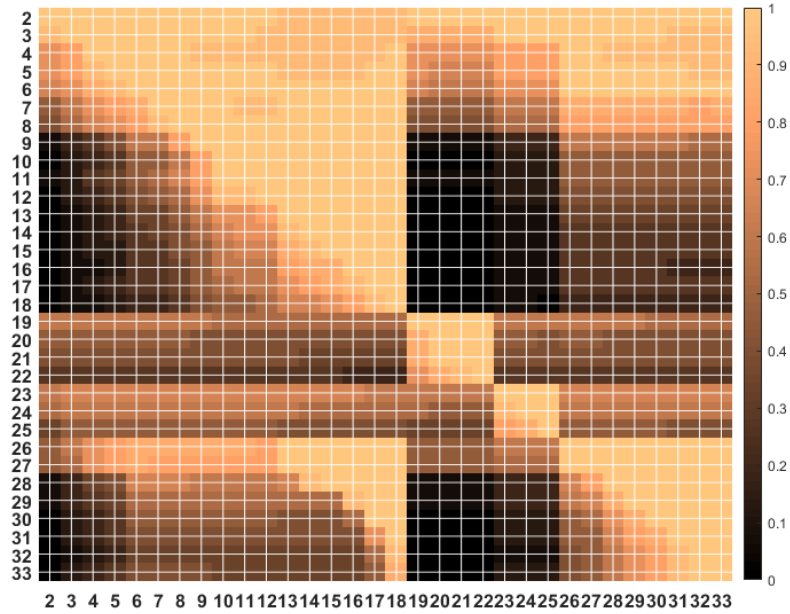
Figure 3.10: Graphical illustration of bus-to-bus LHC sensitivity factors for IEEE 33-bus test system

Table 3.3: Comparison of Results for SFLHC and Power Flow (PF) for IEEE 33-bus test system

Case	BUS 2			BUS 3			BUS 26		
	PF	SF	Error (%)	PF	SF	Error (%)	PF	SF	Error (%)
1	5400	5700	5.28	5400	5259	2.68	5400	4917	9.83
2	5400	5586	3.32	5500	5177	6.25	6500	4865	13.1
3	5400	5531	2.37	5600	5149	8.75	5600	4859	17.3

3.6 Conclusions

This chapter used deterministic and probabilistic approaches for assessing HC of distribution networks for wind-based DG, considering variations of demands and DG power outputs, as well as DTR of network components. A three-stage HC assessment approach was presented, where maximum LHC of individual buses was calculated first, assuming the connection of a single DG unit in the network. Then, maximum LHCs were used to calculate NHC, assuming that DG units were connected at all network buses. Finally, bus-to-bus LHC-sensitivity factors were calculated to determine available LHC for any number of DG units connected at arbitrary network buses. Presented analysis can be used for a systematic evaluation of available HC and as a basis for a practical procedure for a fair/proportional HC allocation.

Chapter 4
Probabilistic Models for Evaluation of Uncertainties in Power System Operation

4.1   Introduction

The previous chapter presented the hosting capacity assessment of wind-based DG in distribution networks with the application of DTRs. The increased penetration of wind-based generation, as well as implementation of DTRs, will introduce a range of new challenges for network operation and control due to the related uncertainties. The power outputs of wind generation systems are highly variable and unpredictable and therefore, cannot be controlled and dispatched as the conventional generation plants. On the other hand, DTR, which evaluates real-time available line capacity [138], can vary in wide ranges due to variations in ambient conditions and actual loading conditions. A sudden change in weather conditions ("sudden" in terms of thermal time constants of network components) may cause the fluctuations in real-time thermal ratings, which cannot be compensated by generation dispatch or load curtailment due to short response times. Another problem related to DTR uncertainties are variations in DTR values due to, e.g. different wind attacking angles on different sections of an OHL and the general problem of finding the "hot spot" temperature, which, however, are not considered in this thesis. Consequently, to integrate DTR into system operation, accurate prediction of the uncertainties in real-time thermal rating and wind-based generation is essential.

A typical approach for modelling wind generation is the use of power curves, which specify how output power of a wind turbine (WT) changes with the variations of input wind speed [139]–[142]. Power curves specified by the manufacturers are commonly used when there are no available field data, e.g. during the planning or general design phases of a wind farm (WF). However, manufacturer power curves are obtained in controlled conditions (e.g. in air-tunnels), where the effects of wind speed and wind direction variations, presence of turbulences, overall dynamics of WTs and other site and application specific factors are usually not fully and correctly represented. Consequently, if manufacturers' power curve is used for the analysis, this might result in significant errors. This is discussed in [143], where two general approaches for

59

building equivalent power curve models of the whole WF based on the field measurement data are presented. These equivalent power curve models are formulated as the averaged aggregate representation of the outputs from all WTs and are specifically aimed for the estimation of annual energy production of the considered WF.

Instead of using averaged power outputs, this chapter assesses ranges of variations of WF power outputs with the input wind speeds and formulates suitable probabilistic models using the best-fit PDF representations. The probabilistic models for wind speed and wind directions are also built up and used for the calculation of DTR values. The risk of line overloading is evaluated by MCS-based OPF analysis, which is implemented on a UK variant of IEEE 14-bus network.

4.2 Uncertainties of wind conditions

The evaluation of uncertainties in wind conditions is illustrated on the example of an actual Scottish wind farm. The wind farm contains six 3MW double-fed induction generator wind turbines, sited on relatively flat terrain. The available measurements are average 10-minute values of wind speeds, wind directions and the power outputs of six wind turbines. As the model of the wind farm requires simultaneous measurements at all individual wind turbines, the recorded data are filtered, and those measurements with missing data are discarded, as well as the corrupted data due to monitoring system faults and measurement errors.

4.2.1 Probabilistic models for wind speed

The original wind speed data are firstly grouped using the "method of bins" from [144], where wind speed values recorded with one decimal point accuracy are allocated to corresponding "bins" with a resolution of 1 m/s. Then the histogram plot of the wind speed can be obtained.

Three distribution functions, 1) a two-parameter Weibull distribution (2-pW), 2) a three-parameter Weibull distribution (3-pW) and 3) a generalized normal distribution (GND) are applied for approximating the wind speed distribution. The PDF and CDF of 2-pW are given as follows:

$$f(x) = \begin{cases} \frac{\beta}{\eta}\left(\frac{x}{\eta}\right)^{\beta-1} \exp\left(-\left(\frac{x}{\eta}\right)^{\beta}\right) & x \geq 0 \\ 0 & x < 0 \end{cases} \tag{4.1}$$

$$F(x) = \begin{cases} 1 - \exp\left(-\left(\frac{x}{\eta}\right)^{\beta}\right) & x \geq 0 \\ 0 & x < 0 \end{cases} \tag{4.2}$$

where $\beta > 0$ is the shape parameter and $\eta > 0$ is the scale parameter.

The PDF and CDF of 3-pW are presented as (3.3) and (3.4):

$$f(x) = \begin{cases} \frac{\beta}{\eta}\left(\frac{x-\gamma}{\eta}\right)^{\beta-1} \exp\left(-\left(\frac{x-\gamma}{\eta}\right)^{\beta}\right) & x \geq \gamma \\ 0 & x < \gamma \end{cases} \tag{4.3}$$

$$F(x) = \begin{cases} 1 - \exp\left(-\left(\frac{x-\gamma}{\eta}\right)^{\beta}\right) & x \geq \gamma \\ 0 & x < \gamma \end{cases} \tag{4.4}$$

where γ is the location parameter. It can be obviously observed that 2-pW is a special condition of the 3-pW with the location parameter setting to zero.

The PDF and CDF of GND are presented as (4.5) and (4.6):

$$f(x) = \frac{\phi(y)}{\eta - \beta(x - \gamma)} \tag{4.5}$$

$$F(x) = \Phi(y) \tag{4.6}$$

where γ, η and β represent the location, scale and shape parameters respectively. $\phi(y)$ and $\Phi(y)$ are the PDF and CDF of the standard normal distribution. The variable y is given by:

$$y = \begin{cases} -\frac{1}{\beta}\log\left[1 - \frac{\beta(x-\gamma)}{\eta}\right] & \beta \neq 0 \\ \frac{\beta(x-\gamma)}{\eta} & \beta = 0 \end{cases} \tag{4.7}$$

Parameter estimation method

The parameters of the PDF functions are estimated with the method of moments (MOM). This method is based solely on the law of large numbers. For a set of independent random variables following an identical distribution with the mean of μ, the mean value of this set will converge to the distribution mean μ as the size of the set increases. More generally, for a set of independent random variables $x = (x_1, x_2, \dots x_n)$ which follow the identical distribution $f(x, \chi)$ where χ is the vector of distribution parameters and $m(\cdot)$ is a real value function, if $k(\chi) = E_\chi(m(x))$ where $E_\chi(\cdot)$ is the mean of the distribution defined by χ, then

$$\frac{1}{n} \sum_{i=1}^{n} m(X_i) \to k(\chi) \ as \ n \to \infty$$

Choosing $m(x) = x^m$ and writing $\mu_m = E(X^m) = k_m(\chi)$ for the mth moment, the process of MOM can be given as follows:

1. If the model has d parameters, the first d^{th} moments can be represented by:

$$\mu_m = k_m(\chi_1, \chi_2, \dots, \chi_d), m = 1, 2, \dots, d$$

   d equations with d unknowns are obtained.

2. Solving the above equations, the representation for each parameter can be determined as:

$$\chi_m = g_m(\mu_1, \mu_2, \dots, \mu_d), m = 1, 2, \dots, d$$

3. Based on the sampling data $x = (x_1, x_2, \dots, x_n)$, the first d sample moments are:

$$\overline{x^m} = \frac{1}{n} \sum_{i=1}^{n} x_i^m, m = 1, 2, \dots, d$$

4. Replace the distribution moments μ_m in Step 2 with the sample moments, then the formulas of the method of moments estimators based on the sampling data x can be obtained:

$$\hat{\chi}_k(x) = g_k\left(\bar{x}, \overline{x^2}, \dots, \overline{x^d}\right)$$

Following the process, the parameters of 2-pW distribution can be estimated by solving the following equations:

$$\ln\Gamma\left(1 + \tfrac{2}{\beta}\right) - 2\ln\Gamma\left(1 + \tfrac{1}{\beta}\right) - \ln\left(\overline{x^2}\right) + 2\ln\bar{x} = 0 \tag{4.8}$$

$$\hat{\eta} = \frac{\bar{x}}{\Gamma\left(1 + \tfrac{1}{\hat{\beta}}\right)} \tag{4.9}$$

For GND, the location parameter γ always equals to the median. While the mean μ and variance σ^2 are defined as:

$$\mu = \gamma - \frac{\eta}{\beta}\left(\exp\left(\frac{\beta^2}{2}\right) - 1\right) \tag{4.10}$$

$$\sigma^2 = \frac{\eta^2}{\beta^2}\exp(\beta^2)\left(\exp(\beta^2) - 1\right) \tag{4.11}$$

The MOM estimators for GND are given by:

$$\hat{\eta} = median(x) \tag{4.12}$$

$$\frac{\left(\exp\left(\frac{\hat{\beta}^2}{2}\right) - 1\right)^2}{\exp\left(2\hat{\beta}^2\right) - \exp\left(\hat{\beta}^2\right)} = \frac{(\hat{\gamma} - \bar{x})^2}{\hat{\eta}^2} \tag{4.13}$$

$$\hat{\eta} = \frac{(\hat{\gamma} - \bar{x})\hat{\beta}}{\exp\left(\frac{\hat{\beta}^2}{2}\right) - 1} \tag{4.14}$$

When estimating the parameters of 3-pW, a new type of moments need to be applied, defined as:

$$\mu_{wm} = \int_0^\infty \left(1 - F(x)\right)^m dx = \gamma + \frac{\eta\Gamma\left(1 + \tfrac{1}{\beta}\right)}{m^{\tfrac{1}{\beta}}} \tag{4.15}$$

63

where $F(x)$ is the CDF of the 3-pW distribution presented by (4.4). The parameters can be expressed by:

$$\beta = \frac{ln2}{\ln(\mu_{w1} - \mu_{w2}) - \ln(\mu_{w2} - \mu_{w4})} \tag{4.16}$$

$$\gamma = \frac{\mu_{w1}\mu_{w4} - \mu_{w2}^2}{\mu_{w1} + \mu_{w4} - 2\mu_{w2}} \tag{4.17}$$

$$\eta = \frac{\mu_{w1} - \gamma}{\Gamma\left(1 + \frac{1}{\beta}\right)} \tag{4.18}$$

Given the ordered random sample $x_1 \leq x_2 \leq \cdots \leq x_n$ following the identical 3-pW distribution, the new moments can be estimated by:

$$\hat{\mu}_{wk} = \sum_{i=0}^{n-1}\left(1 - \frac{i}{n}\right)^k (x_{i+1} - x_i), x_0 = 0 \tag{4.19}$$

The parameter estimators are presented as:

$$\hat{\beta} = \frac{ln2}{\ln(\hat{\mu}_{w1} - \hat{\mu}_{w2}) - \ln(\hat{\mu}_{w2} - \hat{\mu}_{w4})} \tag{4.20}$$

$$\hat{\gamma} = \frac{\hat{\mu}_{w1}\hat{\mu}_{w4} - \hat{\mu}_{w2}^2}{\hat{\mu}_{w1} + \hat{\mu}_{w4} - 2\hat{\mu}_{w2}} \tag{4.21}$$

$$\hat{\eta} = \frac{\hat{\mu}_{w1} - \hat{\gamma}}{\Gamma\left(1 + \frac{1}{\hat{\beta}}\right)} \tag{4.22}$$

Parameter estimation results

To evaluate the performance of the three distributions, four indicators are used. The root-mean-square error (RMSE), which is used to evaluate the error between the fitted CDF and empirical CDF, is given by:

$$RMSE = \sqrt{\frac{\sum_{i=1}^{N}(\hat{y}_i - y_i)^2}{N}} \tag{4.23}$$

64

where $\hat{y}_i$ and y_i are the values of the empirical CDF function and the fitted CDF function at the middle point of the ith bin respectively. N is the total number of bins.

Besides, maximum absolute error among all bins (MAEAAB), mean absolute error (MAE) and weighted mean absolute error (WMAE) calculated as follows are used to evaluate the performance of the fits of three analytical PDFs.

$$MAEAAB = \max|\hat{P}_i - P_i|, \forall i \in \{1, \dots, N\} \tag{4.24}$$

$$MAE = \frac{\sum_{i=1}^{N}|\hat{P}_i - P_i|}{N} \tag{4.25}$$

$$WMAE = \sum_{i=1}^{N} \hat{P}_i |\hat{P}_i - P_i| \tag{4.26}$$

where $\hat{P}_i$ and P_i are the probability values within the ith bin obtained from the sampled data and fitted PDFs, N is the number of bins.

Among the above four indicators, the RMSE gives a relatively high weight to significant errors, because the errors are squared before they are averaged. It is more useful when larger errors are particularly undesirable. MAEAAB describes the largest estimation error among all bins. MAE and WMAE are similar. The slight difference is that MAE gives the same weight to all errors, while WMAE considers the impact of the errors.

The parameters of the fitted distribution functions, as well as the values of the above indicators, are presented in Table 4.1. Figure 4.1 shows the comparison of the three best-fit plots with a histogram of binned original wind speed data.

Table 4.1: Estimated parameter values and goodness-of-fit indicators

Model	Parameter values		RMSE	MAEAAB	MAE	WMAE
2-pW	*Shape η*	2.081	0.00289	0.01043	0.00155	0.00272
	Scale β	9.964				
3-pW	*Shape η*	2.053	0.00285	0.00990	0.00151	0.00272
	Scale β	9.838				
	Location γ	0.113				
GND	*Shape η*	-0.267	0.01166	0.01470	0.00283	0.00499

	Scale β	4.283				
	Location γ	8.247				
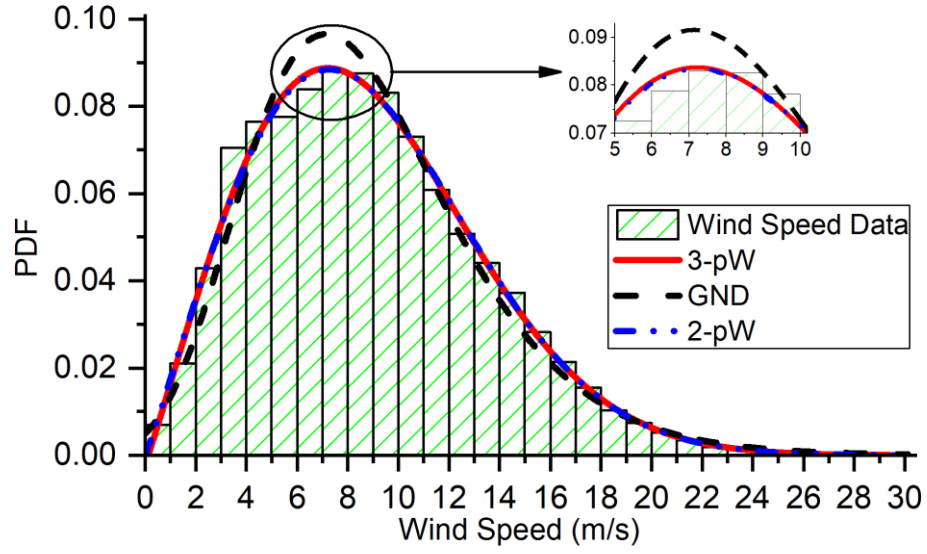
a) PDF comparison
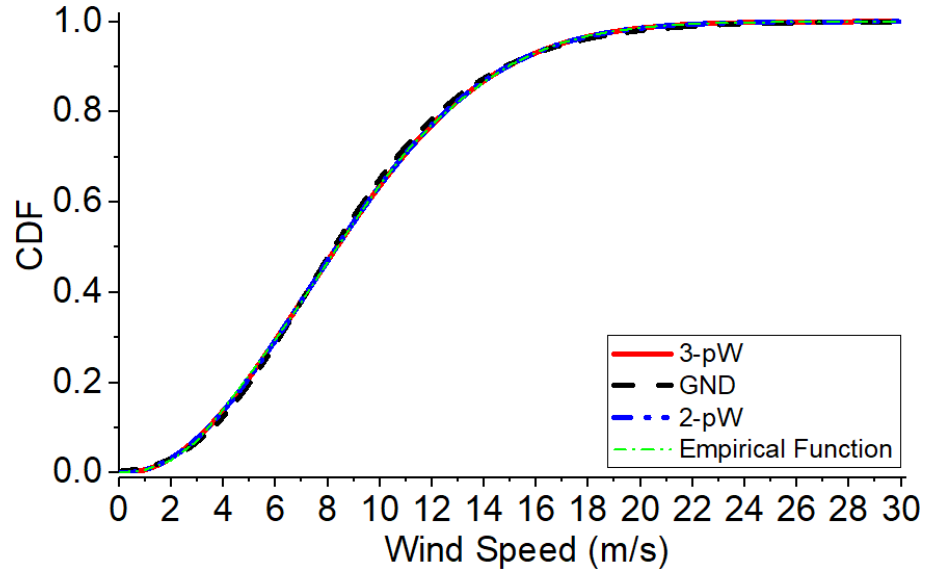
b) CDF comparison

Figure 4.1: Comparison of the best-fit PDF and CDF plots for 2p-W, 3p-W and GND
with the histogram of the binned recorded wind speed data

The results in Table 4.1 show that the recorded wind speed distribution can be more
accurately represented with both 2p-W and 3p-W distributions than with GND. The

error with 2-pW distribution is slightly higher than for 3-pW distribution. However, considering the more straightforward formulation of 2-parameter Weibull distribution, it is used for accurate modelling of wind speeds.

4.2.2 Probabilistic models for wind direction

The use of a single analytical function is not suitable for modelling multimodal distributions of wind directions recorded for each of the binned wind speeds, as there are several prevailing wind directions recorded for each wind speed bin. Therefore, a combination of a number of 3p-W distributions with different parameters, denoted as a finite mixture of Weibull (MWB) distribution, is used, as well as a similar mixture of GNDs (MGND). In addition, a finite mixture of von Mises distributions (MvM) is also used for modelling wind directions. The PDFs and CDFs of single 3-pW and GND are given above. A single von Mises distribution, which is known as a circular normal distribution, is defined by two parameters: the location parameter γ, which represents the prevailing wind direction, and the concentration parameter κ, which indicates the variance around the mean. The PDF is given by:

$$f(x) = \frac{1}{2\pi I_0(\kappa)} \exp(\kappa \cos(x - \gamma)) \tag{4.27}$$

where x is the random circular variable, $\kappa \geq 0$, $0 \leq \gamma \leq 2\pi$, $0 \leq x \leq 2\pi$ and $I_0(\kappa)$ is the modified Bessel function of the first kind and order zero:

$$I_0(\kappa) = \frac{1}{\sqrt{2\pi}} \int_0^{2\pi} \exp(\kappa \cos(x)) dx = \sum_{k=0}^{\infty} \frac{1}{(k!)^2} \left(\frac{\kappa}{2}\right)^{2k} \tag{4.28}$$

The finite mixture model of simple distributions is defined by:

$$f_M(x; \omega; \chi) = \sum_{i=1}^{k} \omega_i f_i(x; \chi_i) \tag{4.29}$$

where $f_M(\cdot)$ represents the PDF of the finite mixture model and f_i is the PDF of the ith single distribution, ω is the vector of the weights for every single distribution, $\chi = [\chi_1^T, \chi_2^T, ..., \chi_k^T]^T$ is the matrix of the parameters for the mixture model, χ_i is the vector of the parameters for the ith single distribution and ω_i is the weight of the ith

single distribution, k is the number of single distributions used in the mixture model. The weights of single distributions should satisfy the following constraints:

$$0 \leq \omega_i \leq 1 \ \forall i \in \{1, \dots, k\}, \qquad \sum_{i=1}^{k} \omega_j = 1 \qquad (4.30)$$

Parameter estimation method

To estimate the parameters of the considered finite mixture distributions, an optimization problem with the objective function presented as below is proposed:

$$\min f_{obj} = \sqrt{\frac{1}{N} \sum_{i=1}^{N} (\hat{y}_i - y_i)^2} \qquad (4.31)$$

The objective function aims to minimize the RMSE between the empirical CDF values $\hat{y}$ and the CDF values of the fitted model y_i. N is the number of total estimated points (sample size).

When estimating the parameters for MWB, the optimization variables are the weight ω, the location parameter γ, the shape parameter β, and the scale parameter η for every single 3-pW. The following constraints should be satisfied:

$$0 \leq \gamma_i \leq 2\pi, \beta_i > 0, \eta_i > 0, \forall i \in \{1, \dots, k\} \qquad (4.32)$$

For MGND, the optimization variables are the weight ω, the location parameter γ, the shape parameter β, and the scale parameter η for each single distribution. The following constraints should be met:

$$0 \leq \gamma_i \leq 2\pi, \eta_i > 0, \forall i \in \{1, \dots, k\} \qquad (4.33)$$

For MvM, the optimization variables include the weight, the location parameter γ, and the concentration parameter κ. The constraints are given as:

$$0 \leq \gamma_i \leq 2\pi, \kappa_i \geq 0 \ \forall \ i \in \{1, \dots, k\} \qquad (4.34)$$

Apart from the above constraints for specific distributions, the constraints on the weights presented as (4.30) should be met for all three distributions. As the objective function is highly nonlinear and nonconvex, this optimization problem is solved by particle swarm solver of Global Optimization Toolbox (MATLAB R2016a).

The number of single distributions in the mixture model is not treated as an optimization variable, because it is an integer and will impose additional constraints. In order to meet the balance between the model complexity and accuracy, a threshold is set for the objective function. In the beginning, the optimization problem is solved with one single distribution. If the objective value is lower than the threshold, the process stops. Otherwise, the number of separate distributions will increase by one, and the problem is solved again until the objective function is lower than the threshold.

Parameter estimation results
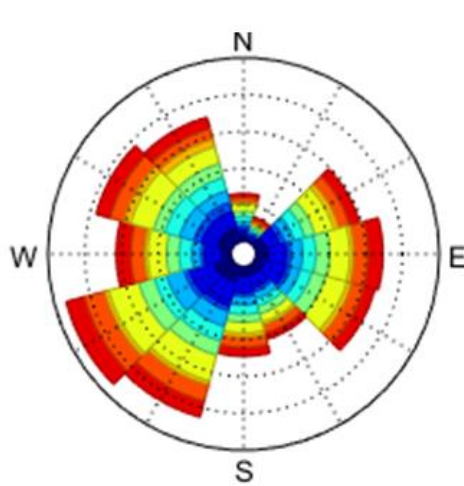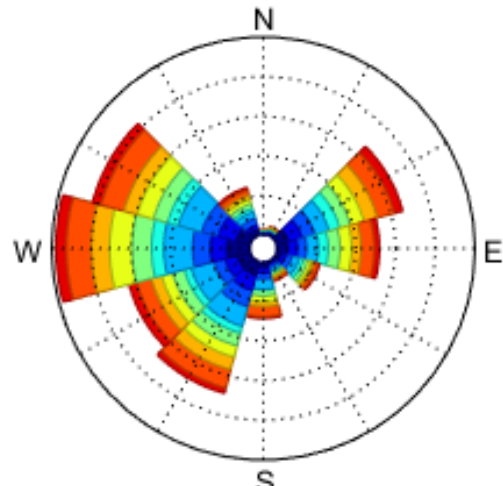
a.1) Wind speed = 6~7 m/s   a.2) Wind speed = 11~12 m/s
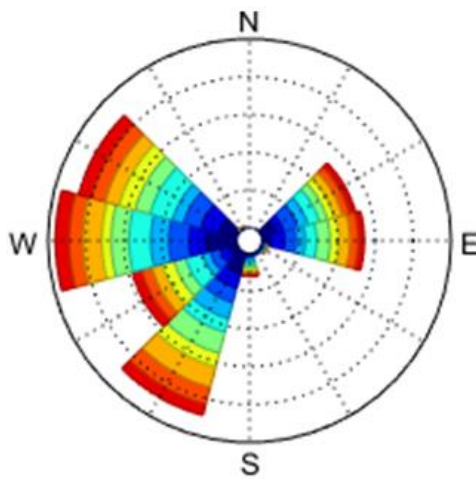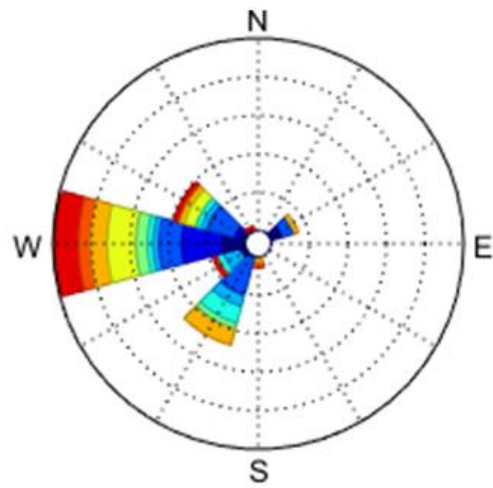
a.3) Wind speed = 17~18 m/s   a.4) Wind speed = 24~25 m/s

a) wind rose for wind speed bin (N=0 degree)
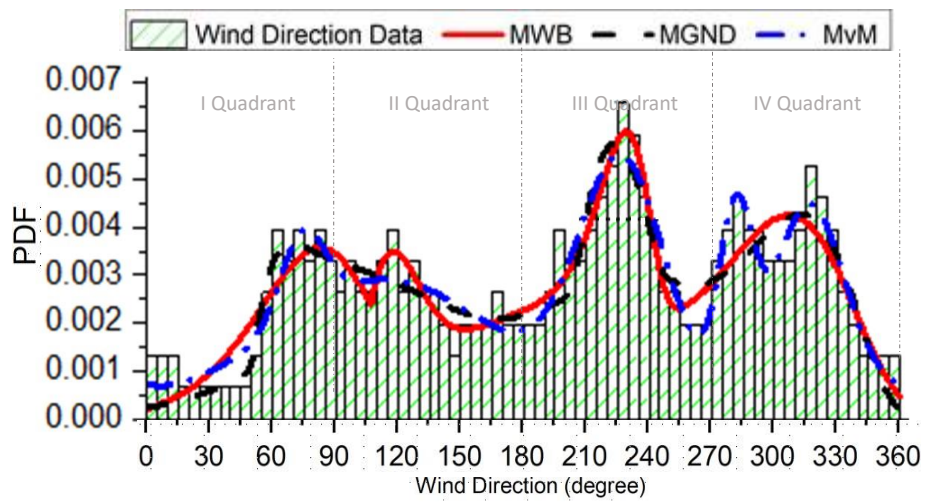
b.1) Wind speed = 6~7 m/s
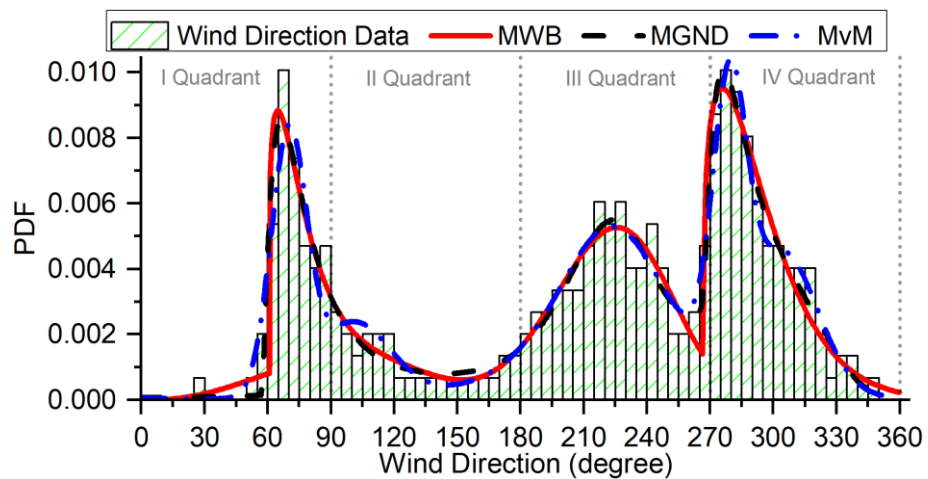
b.2) Wind speed = 11~12 m/s
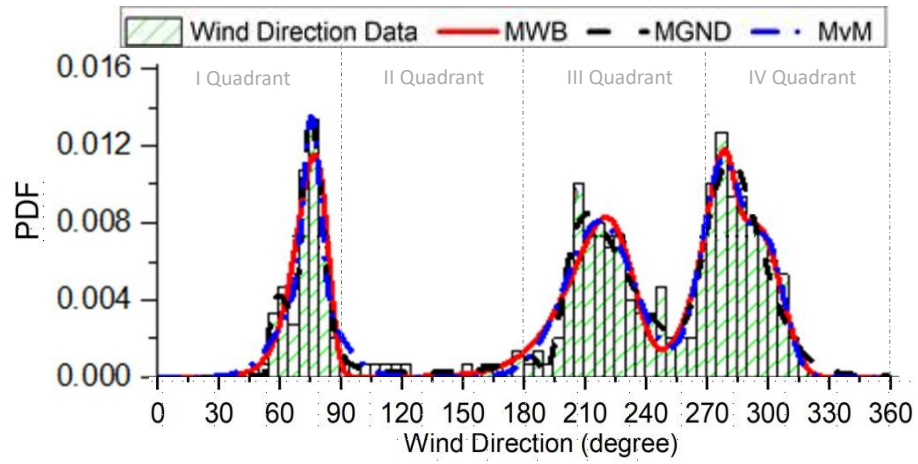
b.3) Wind speed = 17~18 m/s
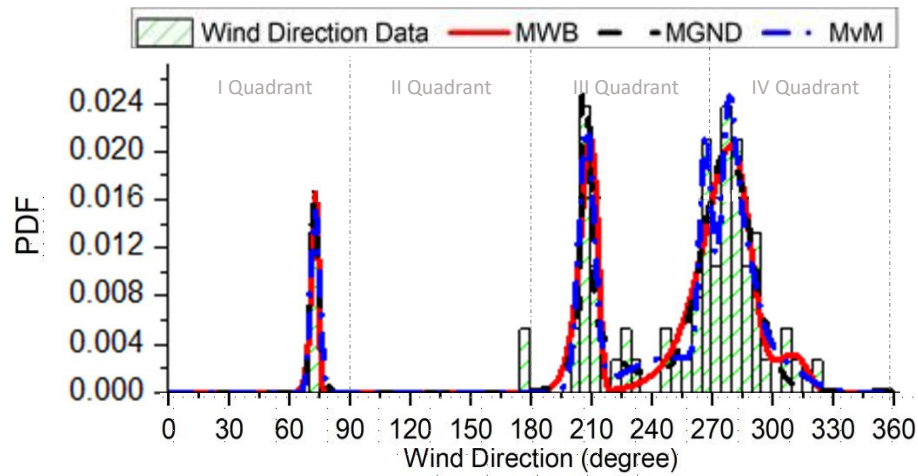
b.4) Wind speed = 24~25 m/s

b) PDFs for wind speed bins

Figure 4.2: Comparison of the three best-fit PDFs and wind roses with the recorded wind directions.

Figure 4.2 illustrates examples of the fitted PDF plots for the wind direction distribution with different wind speeds. Four wind speed bins are presented. For the convenience of the further calculation, the wind direction unit is transferred from radian to degree. The wind rose plots in Figure 4.2a show the prevailing wind directions with respect to different wind speeds. Figure 4.2b plots the histogram of the wind direction and the fitted PDFs of MWB, MGND and MvM. Tables 4.2-4.4 list the parameter values as well as the performance indicators of wind direction distributions for the wind speed bin of 11~12 m/s as an example.

Table 4.2: Parameter values for MWB (Wind Speed = 11-12m/s)

Number	Shape η	Scale β	Location γ	Weight ω	RMSE
#1	1.332	0.513	4.658	0.357	
#2	4.113	1.825	2.236	0.352	0.003
#3	1.211	0.282	1.061	0.171	
#4	2.879	1.828	0.117	0.120	

Table 4.3: Parameter values for MGND (Wind Speed = 11-12m/s)

Number	Shape η	Scale β	Location γ	Weight ω	RMSE
#1	0.187	0.336	3.822	0.184	
#2	-0.832	0.293	1.335	0.250	0.003
#3	-0.721	0.294	4.961	0.200	
#4	0.580	1.018	4.545	0.366	

Table 4.4: Parameter values for MvM (Wind Speed = 11-12m/s)

Number	Concentration κ	Location γ	Weight ω	RMSE
#1	6.595	3.784	0.139	
#2	8.768	3.977	0.106	
#3	57.101	4.847	0.163	
#4	18.114	1.777	0.071	0.002
#5	11.991	5.268	0.173	
#6	0.840	3.650	0.175	
#7	41.022	1.224	0.173	
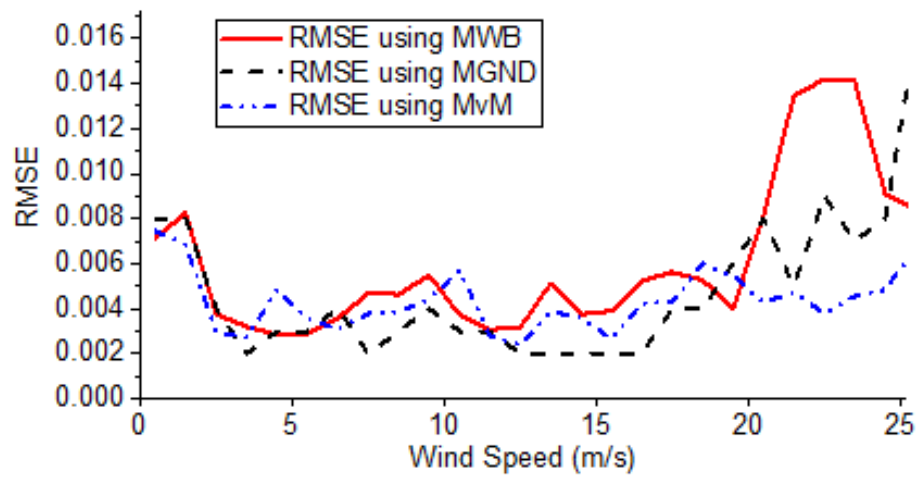
a) Fitting results comparison based on RMSE
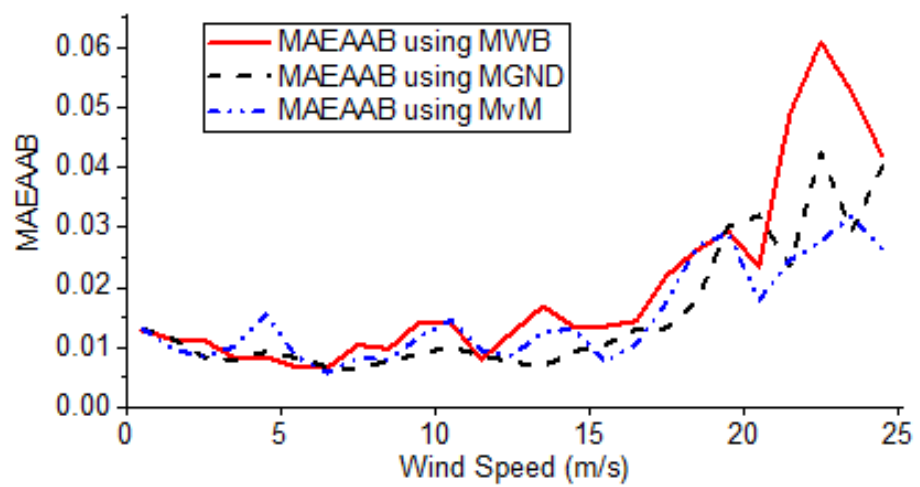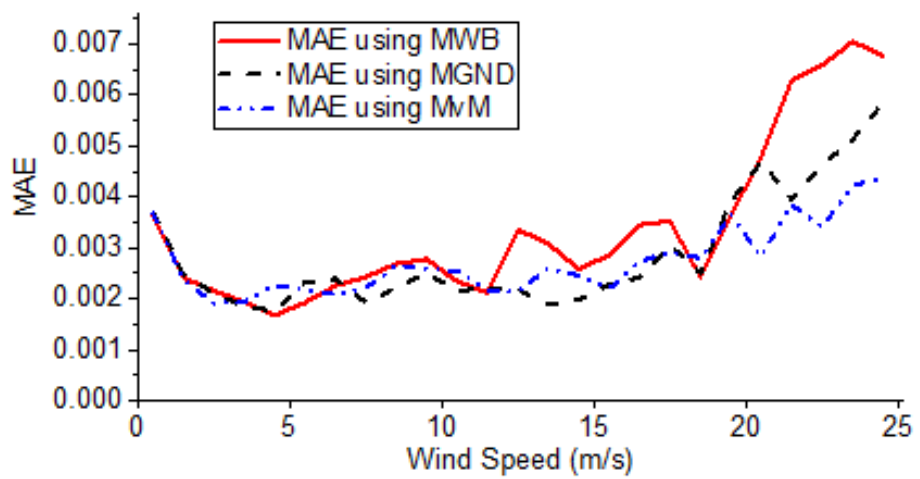
b) Fitting results comparison based on MAEAAB

c) Fitting results comparison based on MAE
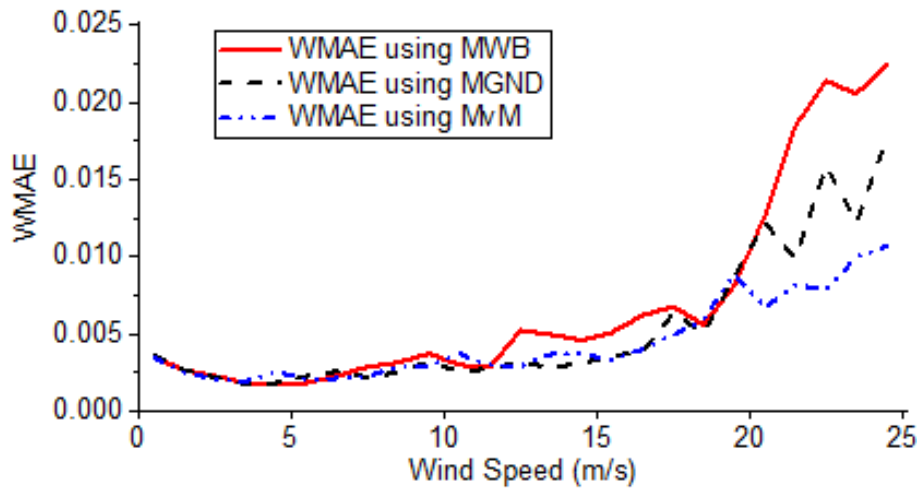
d) Fitting results comparison based on WMAE
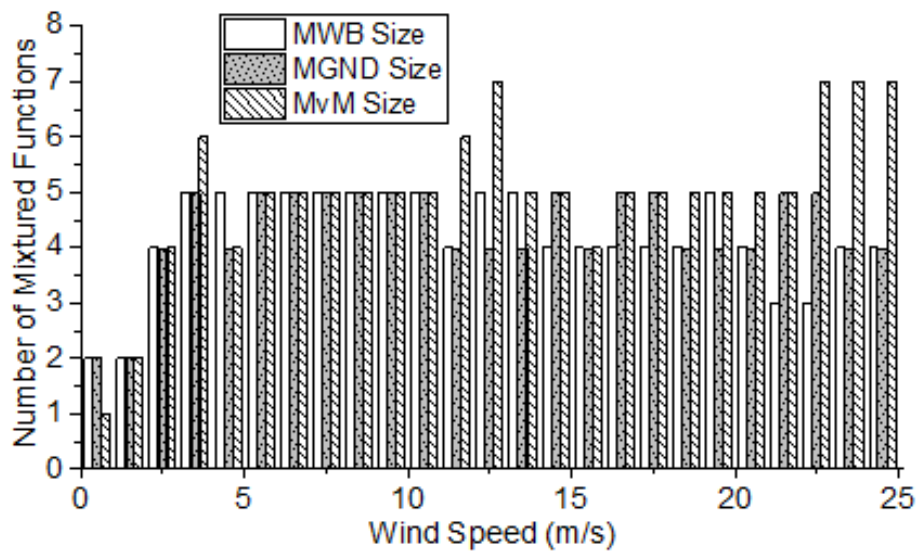
e) Fitting results comparison based on separate distribution numbers

Figure 4.3: Wind speed fitting results comparisons

Figure 4.3a – Figure 4.3d plots the errors of the fitted wind direction distributions to the wind speeds in each bin. Figure 4.3e presents the number of single distributions used for the finite mixture models. It can be observed that the three distributions all present competitive performances when the wind speed is lower than 20 m/s. However, as the wind speed increases over 20m/s, MvM is the most competitive among the three, whose CDFs are plotted as follows.
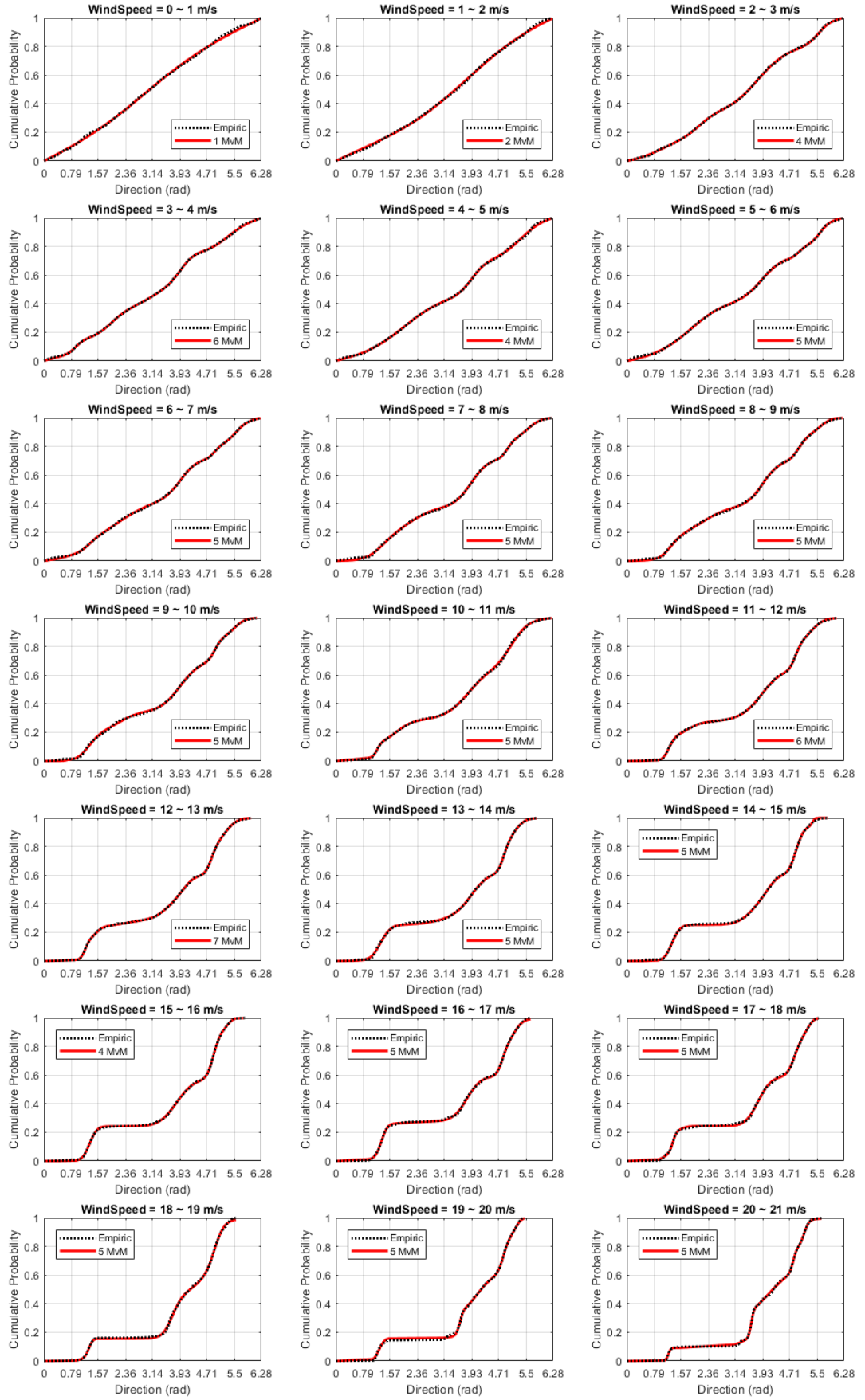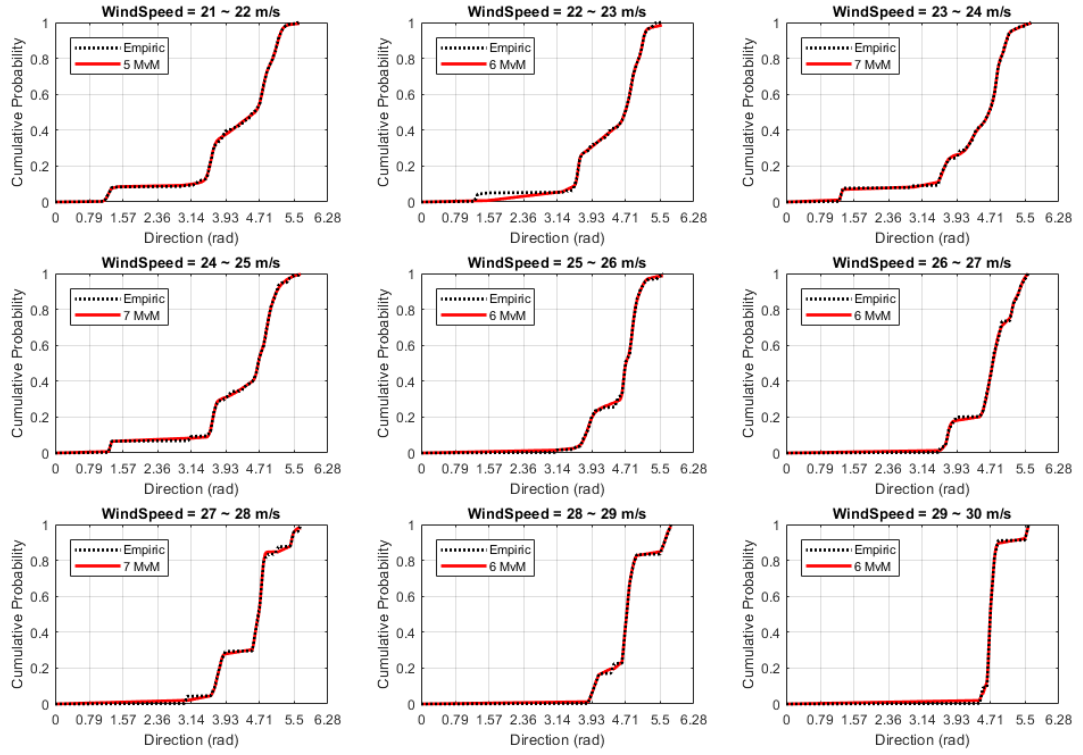
Figure 4.4: CDF of fitted MvM

4.2.3 Probabilistic models for wind power output

Due to a similar issue of multimodal distributions, the uncertainties in WF power generation are modelled using a mixture of Weibull distributions (MWB) and a mixture of GNDs (MGND). As von Mises distribution is a circular distribution, it is not used to model uncertainties in wind power outputs. The parameter values for both models are determined with the same approach presented in Section 4.2.2. Figure 4.5a shows manufacturer, recorded and average WF power outputs. For the considered wind turbine (Vestas v90 3.0 MW [145]) installed at the wind farm, the cut-in wind speed, rated wind speed and cut-out wind speed provided by manufacturer information are 4 m/s, 13 m/s and 25 m/s. The fitted results within two wind speed bins, 5-6 m/s and 11-12 m/s and 17-18 m/s, are plotted as examples in Figure 4.5b – Figure 4.5d.
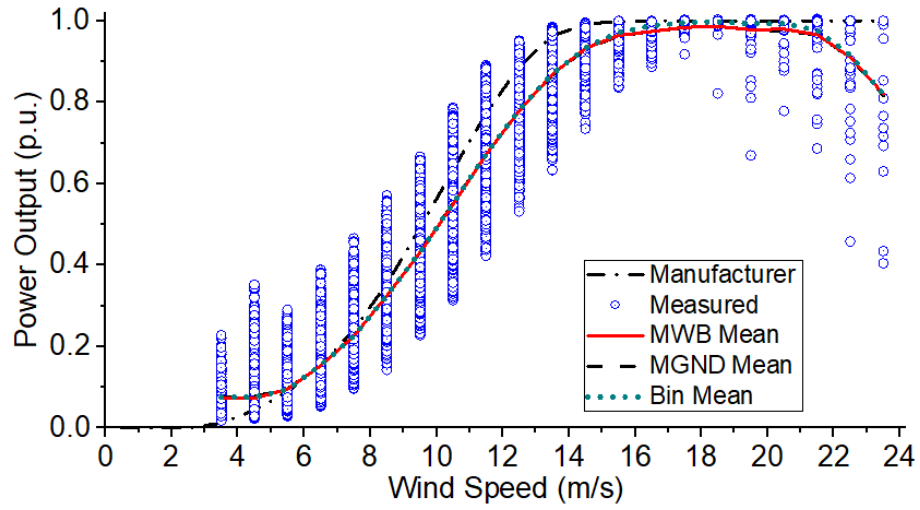
a) manufacturer curve measured data and mean MWB and MGND values
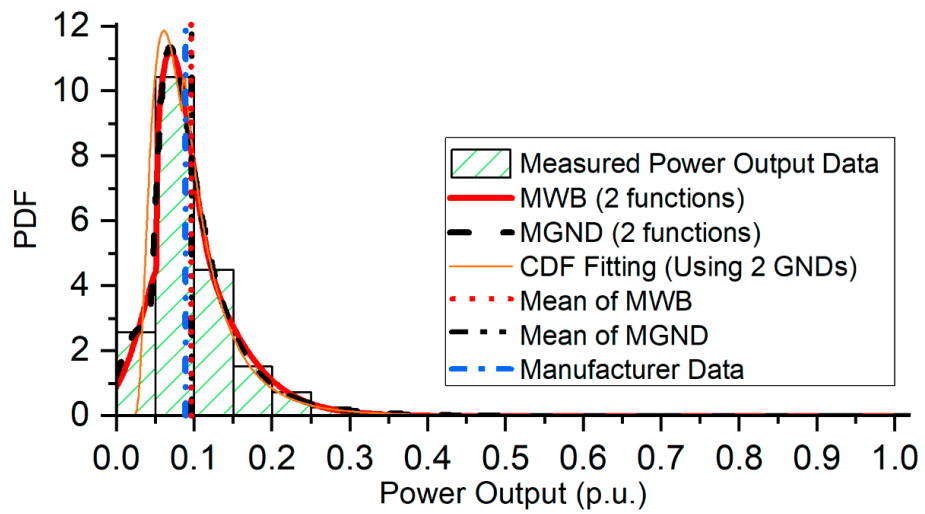
b) PDFs for 2-3 m/s wind speed bin
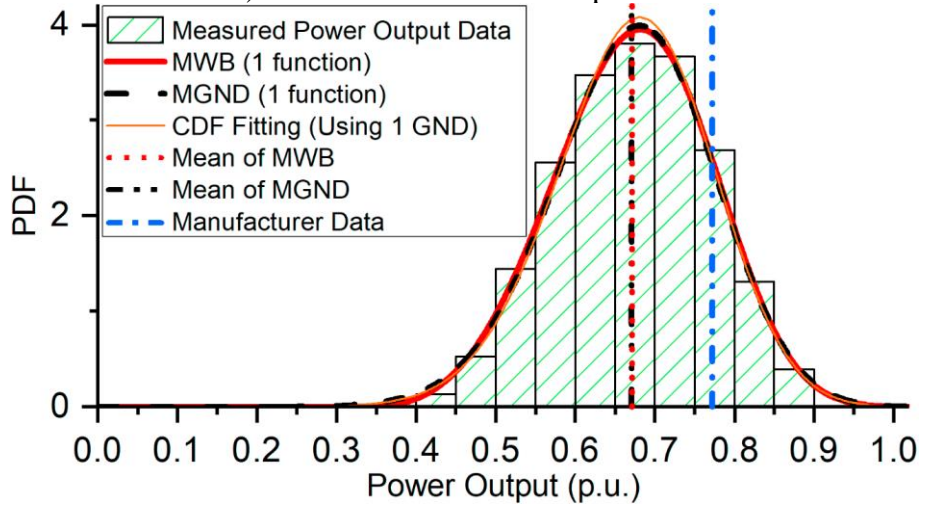
c) PDFs for 11-12 m/s wind speed bin
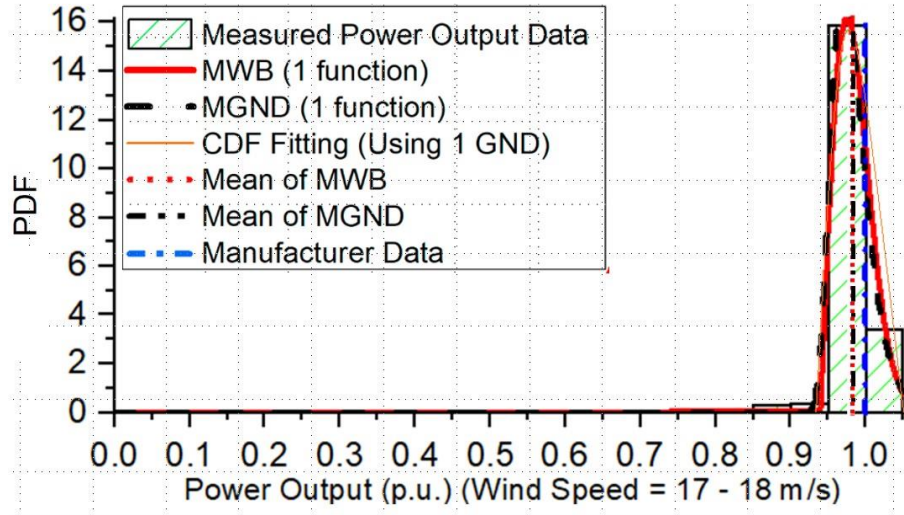
d) PDFs for 17-18 m/s wind speed bin

Figure 4.5: Comparison of PDF plots with the measured WF power outputs

To further compare the performances of MWB and MGND, the performance indicators for both distributions (RMSE, MAEAAB, MAE, and WMAE) as well as the numbers of single distributions for mixture models are plotted as below:
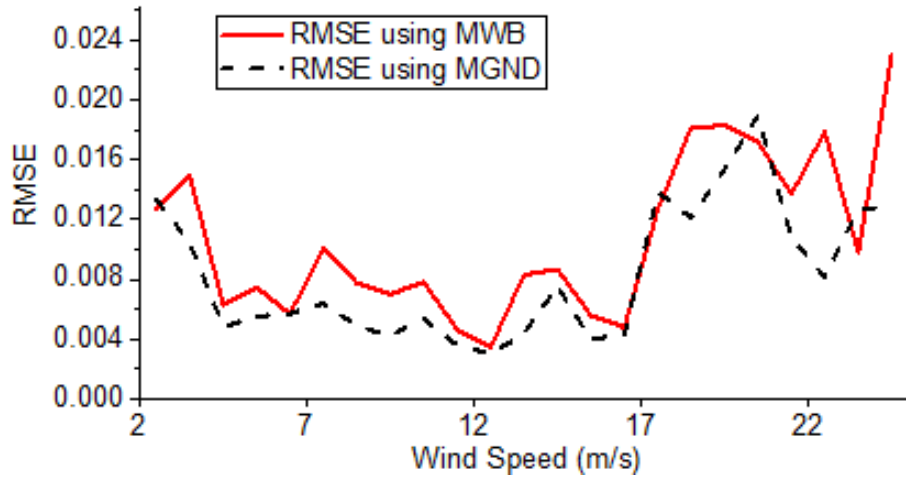
a) Fitting results comparison based on RMSE
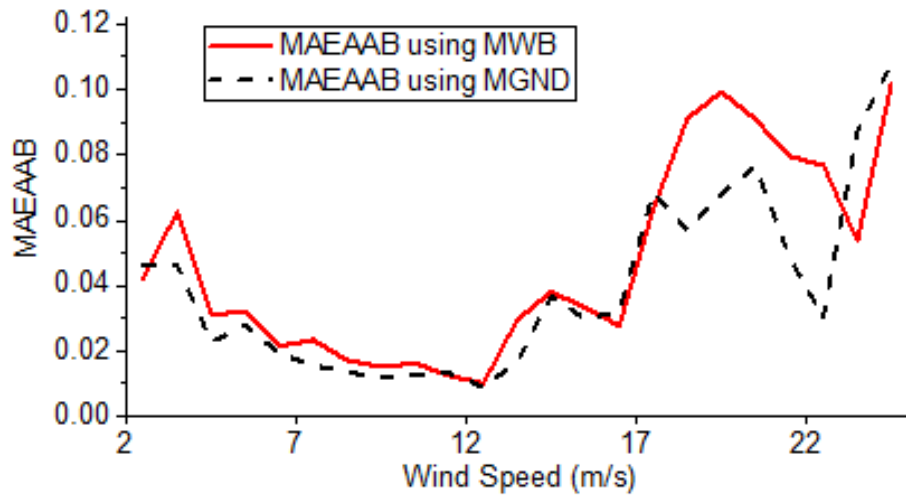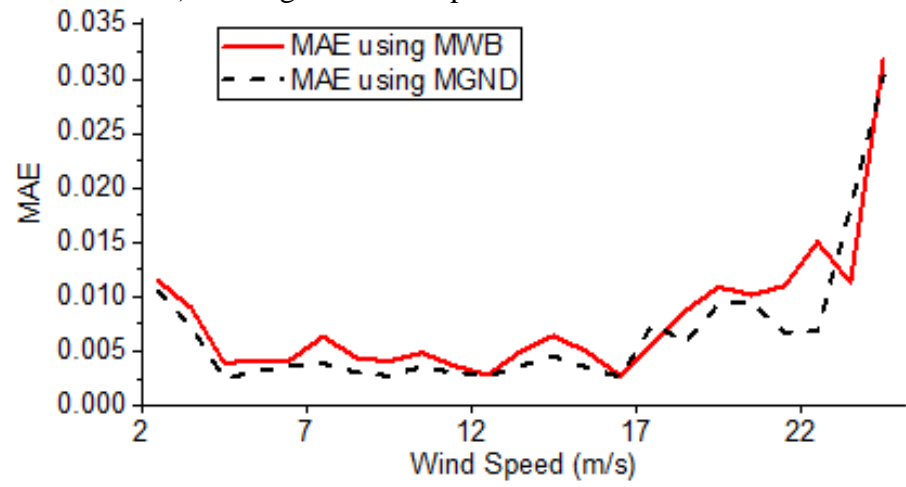
b) Fitting results comparison based on MAEAAB

c) Fitting results comparison based on MAE
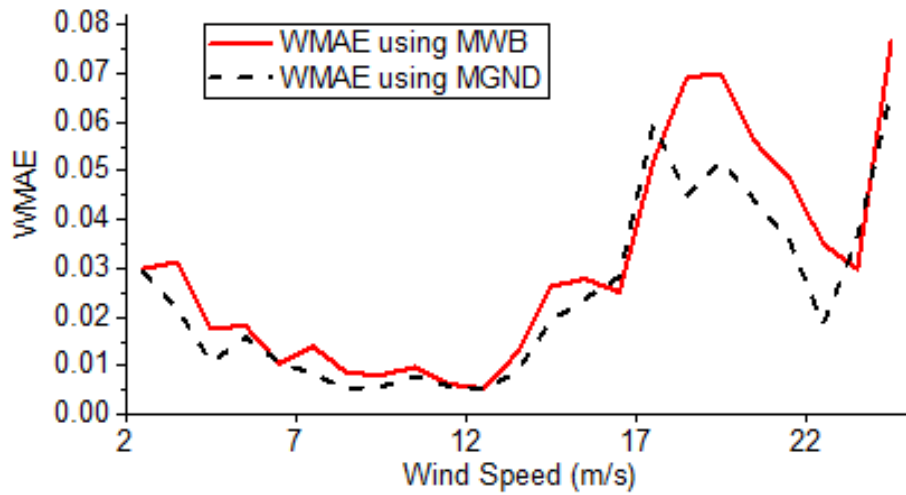
d) Fitting results comparison based on WMAE
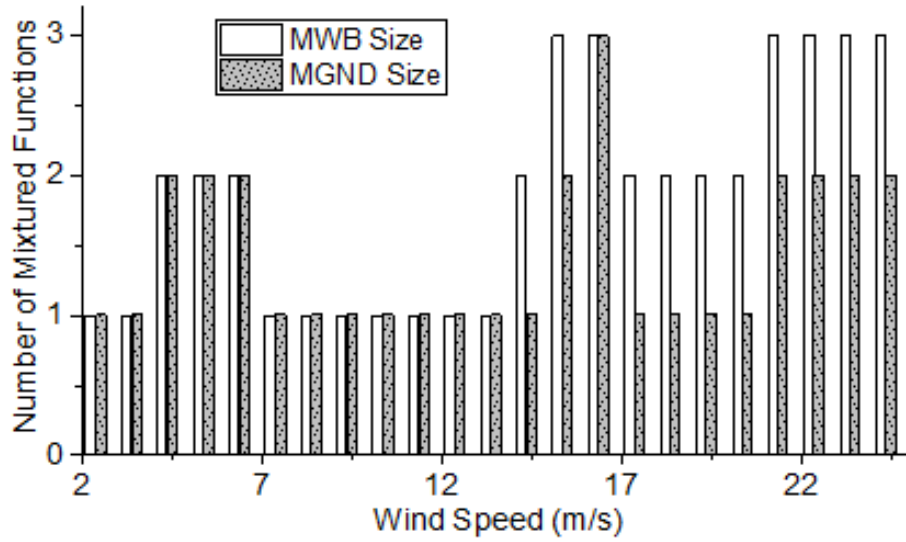
e) Fitting results comparison based on single distribution numbers

Figure 4.6: Wind power output fitting results comparisons

4.3 Probabilistic power flow analysis

The above analysis presents the PDFs for winds speeds, as well as wind directions and wind power outputs for each binned wind speed. In this part, they are used as the inputs for the Monte Carlo-based analysis to evaluate uncertainties in wind-based generation and real-time line capacities, as well as their impact on system operation. The ranges of variations are evaluated initially, and the actual risks of line overloading and wind power curtailments are calculated.

4.3.1 Network specification

The analysis is illustrated on a modified version ("UK variant") of a widely used IEEE 14-bus network, Figure 4.7 [146].
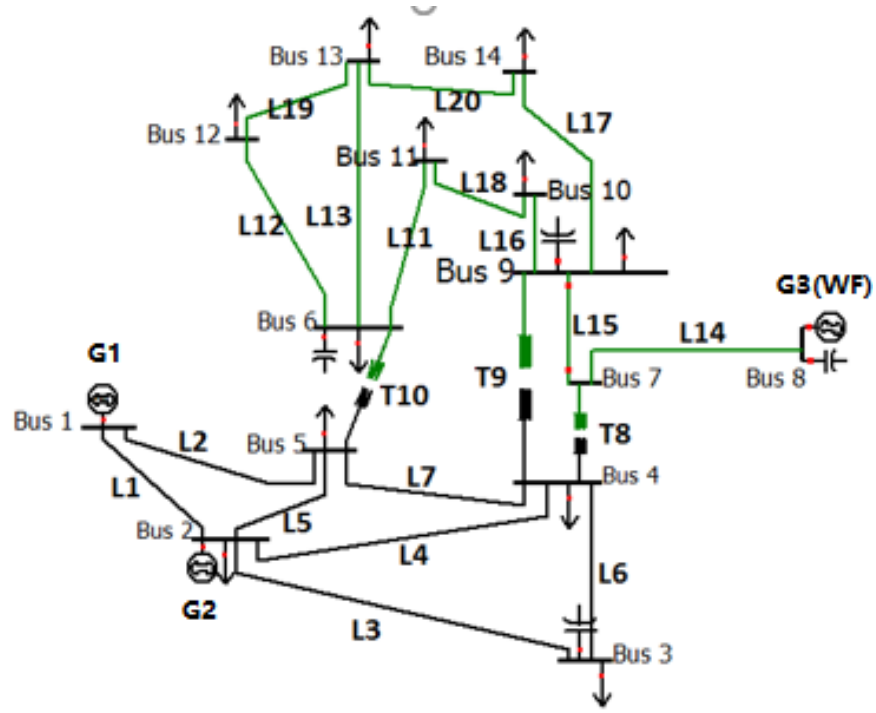
Figure 4.7: UK variant of IEEE 14-bus network

Generator G3 at Bus 8 is modelled as a WF with six 3 MW WTs, [145]. The parameters of OHLs used to estimate their thermal ratings (diameters, cross-section area, etc.) are taken from [136]. The line DTR values are estimated using recorded local temperatures from [147] (average 15.1℃ in July), while solar irradiation is calculated for the altitude and latitude of WF location. Figure 4.8 illustrates DTR values for an ACSR conductor ("242/39" from [136], with maximum operating temperature, 75℃, which is typical for ACSR-type conductors) for different wind speeds and wind directions and for two ambient temperatures: 2 ℃ and 20 ℃, representing winter and summer conditions, respectively [132]. Figure 4.8 also shows STR values for the same conductor and ambient temperatures, and wind speed of 0.5 m/s and attacking angle of 90 ° as inputs in (1) [132].
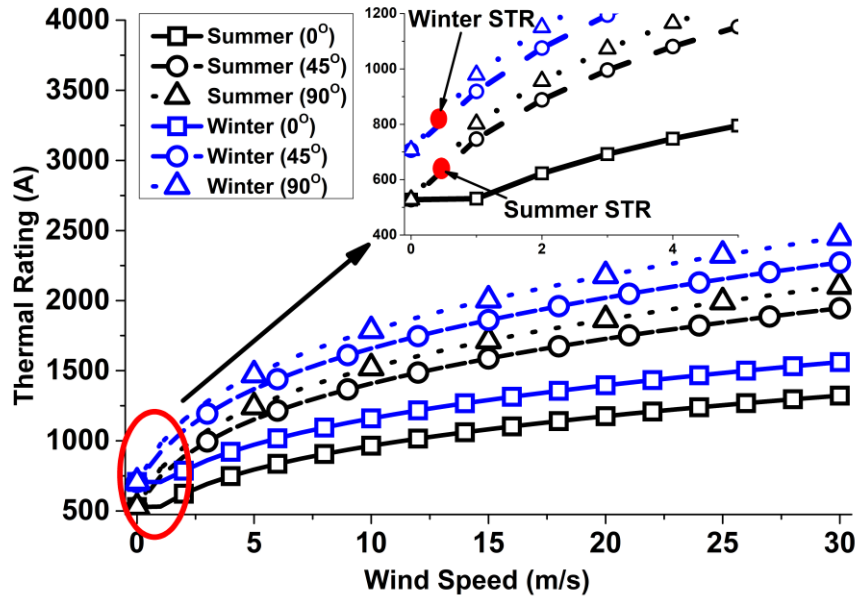
Figure 4.8: DTR of L1 (ACSR "242/39")

4.3.2 Network analysis and discussion

Evaluation of DTR impact on wind integration

First, power outputs of the wind farm at Bus 8 are estimated with the manufacturer provided power curve [145]. In this case, wind speed varies from 0 m/s to 30 m/s and two extreme wind attacking angles, 0° and 90°, are used to calculate DTR. To prevent overloading conditions, wind curtailment is necessary at specific wind conditions, plotted in Figure 4.9, which suggests that wind curtailment is necessary to mitigate the violations of STR for wind speeds between 10-25 m/s. It can be observed that the maximum wind curtailment is almost 6 MW and only 66% of available wind generation is dispatched at the same time. The application of DTR can avoid wind curtailment, as expected. Figure 4.10 plots the loading conditions of three most loaded lines, L1, L14 and L15, in which line loadings are given as the percentage ratios of line currents and STR. Pg_{man}, $Pg_{\min}$ and $Pg_{\max}$ represent the wind power outputs determined by manufacture power curve, minimum measured data and maximum measured data respectively. In Figure 4.11, conductor surface temperatures of L1, L14 and L15, when DTR is applied, are plotted. When wind speed is high, the conductor surface temperatures are relatively low due to the strong wind cooling impact. However, when the wind speed is low (close to 0m/s), L14 and L15 will be exposed to the risk of overheating. This is not related to the connection of wind generation units,

as they will produce no output for wind speeds close to 0 m/s (it is an inherent flaw in the design of the network).
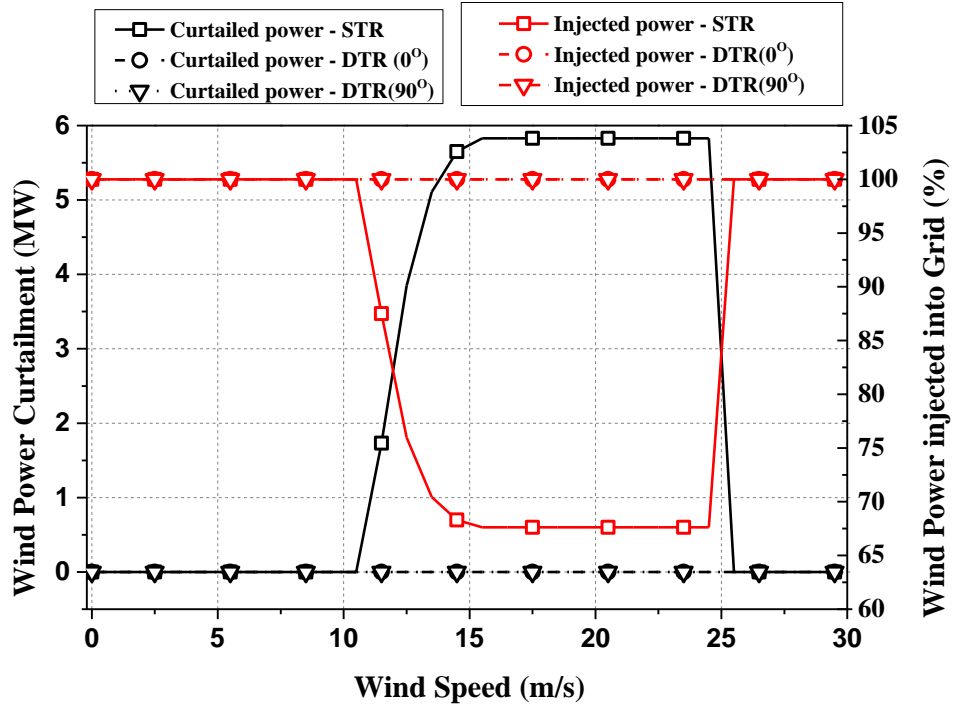
Figure 4.9: Curtailed wind power variations with wind speed and wind direction
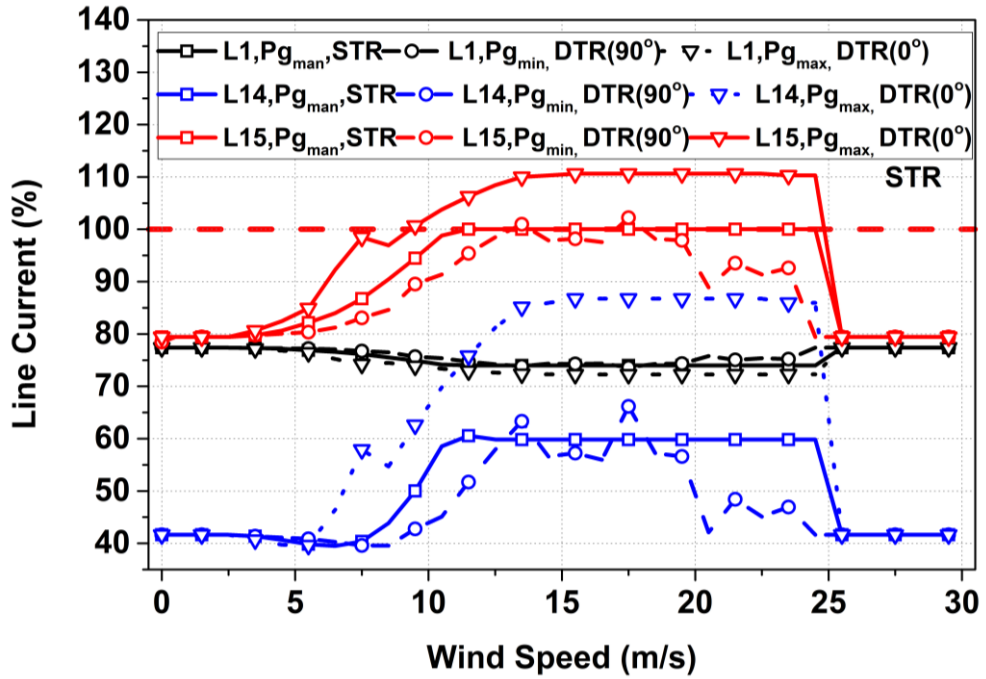
Figure 4.10: Variations of line loading with wind speed and wind direction
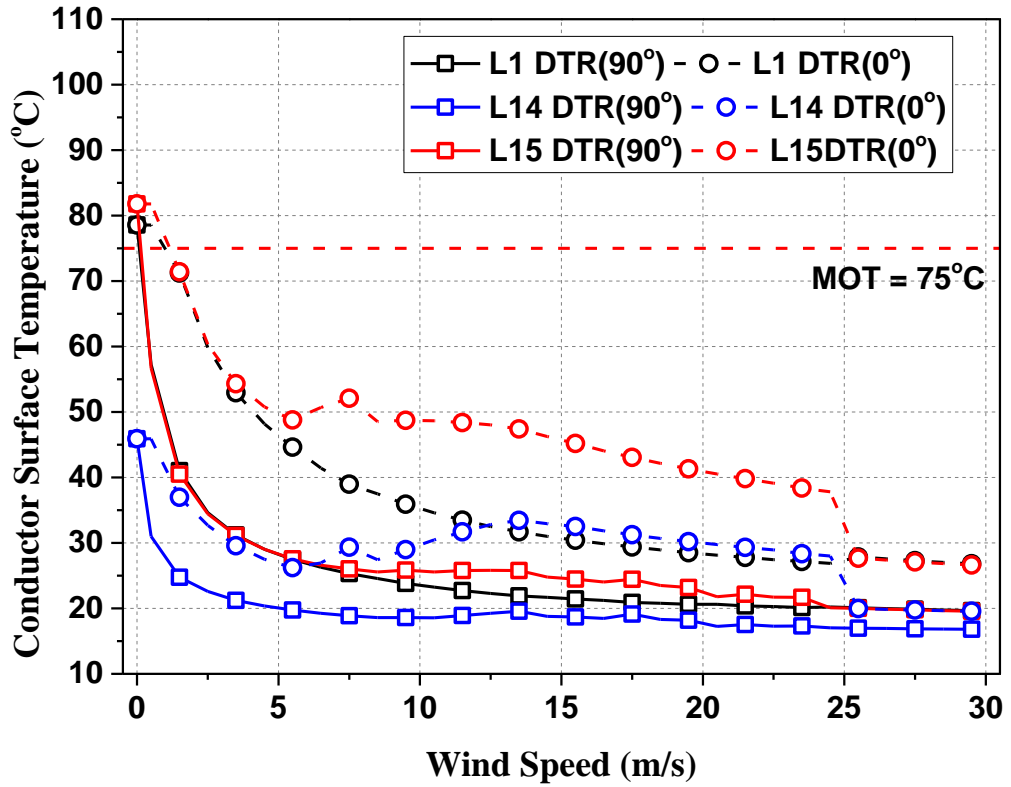
Figure 4.11: Variations of conductor surface temperatures with wind speed and wind direction

Evaluation of uncertainties from wind-based generation and DTR

First, wind speed data are generated by Monte Carlo sampling from the developed 2p-W model. For each generated wind speed value, the wind directions are sampled from corresponding MWB, GND and MvM models, while WF power outputs are sampled from associated MWB and GND models. Afterwards, DTR of each OHL is calculated for the sampled wind speed and wind direction, giving required wind power curtailment for the specific operating and ambient conditions. The total number of applied Monte Carlo simulations is set as 10,000, which means that 10,000 network operating points with different wind speeds, different wind directions and different WF power outputs are generated. Loading conditions are not varied. With respect to each scenario, the OPF problem with the objective function of wind curtailment minimization is solved. The bus voltages should be within 95% - 110% for 132kV buses and 94% - 106% for 33kV buses [148]. The power flow calculation, as well as optimal power flow, are implemented with MATPOWER [149][150] on a desktop equipped with Intel Xeon E3 processor.

Table 4.5: Wind power curtailment

Thermal Types	Wind Direction Model	Wind Power Generation Model	Curtailed Power (MW)			
			Mean	*Std*	*Max*	*Min*
STR	/	MWB	1.20	2.14	6	0
	/	MGND	1.21	2.13	6	0
DTR	MWB	MWB	0	0	0	0
		MGND	0	0	0	0
		MvM	0	0	0	0
	MGND	MWB	0	0	0	0
		MGND	0	0	0	0
		MvM	0	0	0	0
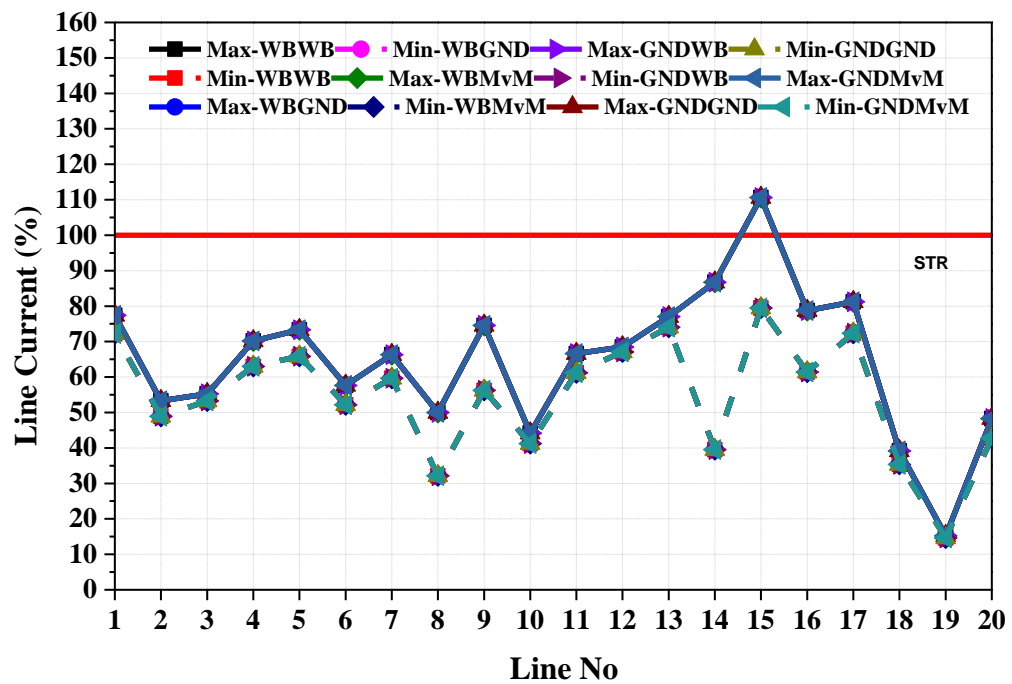
Figure 4.12: Ranges (Min/Max values) of line loading with DTR
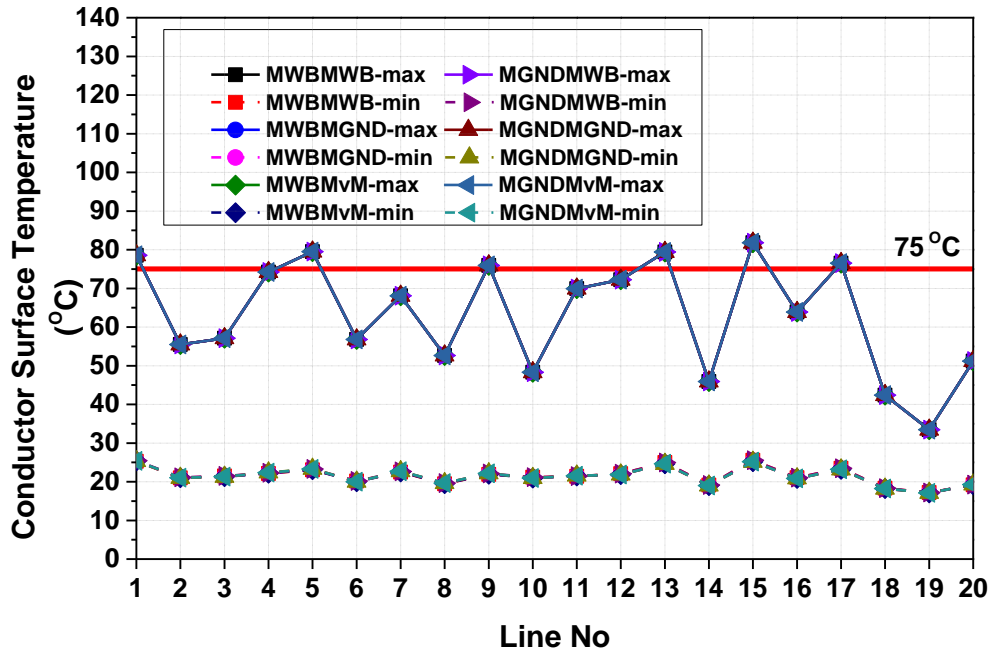
Figure 4.13: Ranges (Min/Max values) of conductor surface temperature with DTR

The presented results shown by Figure 4.12 confirm that the implementation of DTR allows using additional line capacities, as the higher current/power flows for higher wind speeds do not result in conductor temperatures above the limit. When STR is used, the mean value of wind curtailment is 1.2 MW with the standard deviation of 2.14 MW while the application of DTR can reduce the wind curtailment to zero.

In addition, Figure 4.13 shows that temperatures of Lines 1, 5, 11, 13, 15 and 17 can be higher than their maximum temperature limits. As shown by Figure 4.11, the overheating conditions occur when wind speed is low and cannot be remediated by generation dispatch or wind curtailment, as the wind power output is zero. The overheating conditions can only be detected when DTR is used as the OPF cannot find feasible solutions. Relaxing the DTR slightly to STR, the OPF will provide feasible solutions. If system operators dispatch generation according to these solutions, STR can be satisfied, but the overheating conditions will occur and may cause potential damages to line conductors. The overheat probabilities for all the lines are presented in Figure 4.14.
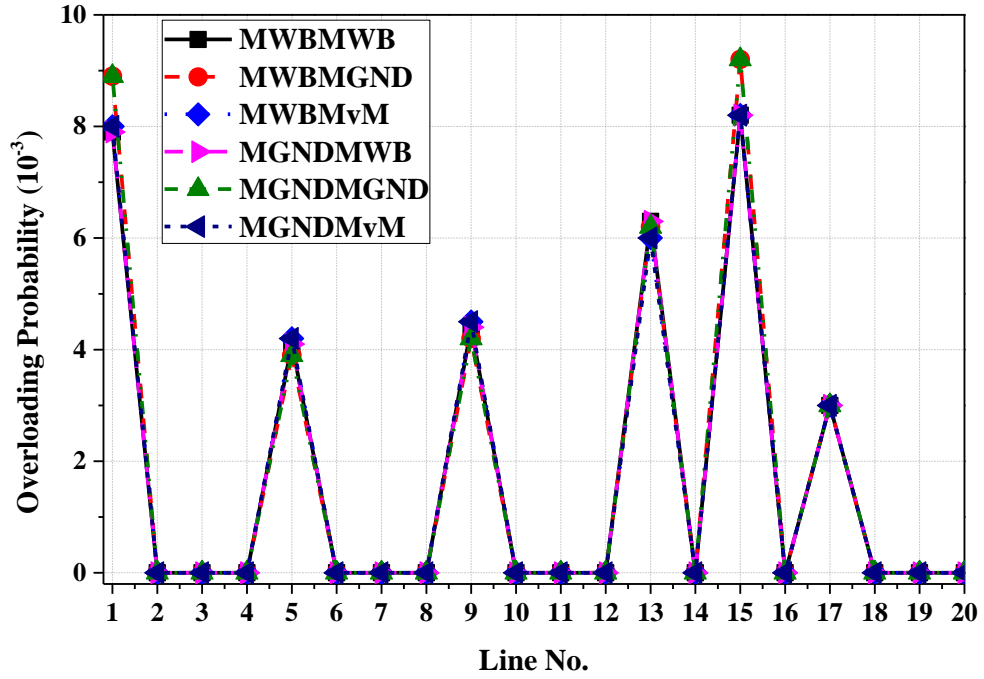
Figure 4.14: Estimated probabilities (risks) of line overloading

The MCS results show that the overheating probabilities of lines in Figure 4.13 at low wind speed are not higher than 1%. Nevertheless, the line overheating conditions may cause conductor loss of strength due to annealing and excessive line elongation (sag) and should be taken into consideration at both system planning and operational stages.

4.4 Conclusions

This chapter built up probabilistic models for wind speed, wind direction and wind-based generation based on historically recorded data from a UK wind farm located at Dalry, Scotland. A UK variant of IEEE 14-bus network was used to evaluate the impacts of DTR on the integration of wind energy resource, whose output was determined by the power curve provided by manufacturers' specifications. In addition, MCS-based analysis was implemented with the developed probabilistic models, in which the impacts of uncertainties in the wind-based generation and DTR on system operation was studied. The results presented that the application of DTR can increase the integration of wind energy and reduce energy curtailment efficiently. However, the unfavourable real-time thermal rating at low wind speed can result in unexpected overloading conditions which should be focused on system planning and operational stages.

Chapter 5

Handling Uncertainties with Affine Arithmetic and Probabilistic OPF for Increased Utilisation of Overhead Lines

5.1 Introduction

Application of dynamic thermal rating (DTR) effectively avoids costly upgrading or reinforcing of system infrastructure, as it allows for higher utilisation of network components than if their static thermal ratings (STR) are used. Previous work has shown that application of DTR can increase thermal loading of overhead lines by 5% - 15% [151], and in that way release network capacity for connecting a higher number of generation units and supplying more loads [131], [152], [153].

However, the utilisation of DTR also presents new problems for system operation due to its uncertainties. Additionally, the research presented in Chapter 4 has found that the application of DTR may result in unexpected congestions when the wind speed is low. In order to efficiently handle the large range of uncertainties introduced into power system operation, this chapter proposes a novel optimization model, which combines affine arithmetic (AA) and probabilistic optimal power flow (P-OPF) for networks with the application of DTR. The uncertainties in bus power injections, including wind generation and load, as well as in DTR limits, are initially formulated as interval values, obtained from time series generated from historically recorded data. The OPF problem with uncertainties is solved firstly with the AA approach, using Max-Min intervals of optimal objective function values, to identify optimal dispatch solutions. These AA interval solutions are usually too conservative, as they include all possible values of uncertain variables, regardless of their actual probabilities. Therefore, this chapter uses Monte Carlo Simulations (MCS') for evaluation of probabilities and uncertainties in input values (and risks in output values), based on the methods developed in Chapter 4.

Section 5.2 to Section 5.4 provide detail descriptions on affine arithmetic, affine arithmetic optimal power flow and affine formulation of DTR, which have been

presented by [10], [11] in details. Section 5.5 presents the numerical results for case studies based on three test cases.

5.2   Affine Arithmetic

Affine arithmetic (AA) is a self-validated numerical computation model, which is used to solve dependency problems in classical interval mathematic computations. It keeps track of the first-order correlations between input and computed output quantities [154][155]. Standard interval arithmetic (IA) often yields too much wider intervals than the actual (exact) ranges of the computed function, resulting in an overestimation that effectively limits the application of the IA. For instance, in chained computation, where the outputs of one step are inputs of the next step, the overestimation tends to get multiplied. This results in a cumulative error, also known as error explosion, which can be resolved by applying affine arithmetic.

Assuming that x is a variable which is subject to uncertainties, the affine form of uncertain variable, $\tilde{x}$ is:

$$\tilde{x} = x_o + x_1\varepsilon_1 + x_2\varepsilon_2 + \cdots + x_n\varepsilon_n \tag{5.1}$$

where x_o, is the central value, x_i are deviations due to the ith uncertainty, for which ε_i represents the noise symbol with the range $\mathbf{U} = [-1,1]$. The radius of $\tilde{x}$ can be expressed by $radx = \sum_{i=1}^{n} |x_i|$. $[x_l, x_u]$, when the range of $\tilde{x}$ can be given as:

$$x_l = x_o - radx, x_u = x_o + radx \tag{5.2}$$

5.2.1 Computing with affine arithmetic

Computations in affine arithmetic can be classified into two categories: affine operations and non-operations. For affine operations, the computation can be simply extended from primitive operations and functions to affine forms. However, for non-affine operations, the additional transformations are required.

Affine operations

Affine arithmetic consists of affine and non-affine operations. For two interdependent affine forms $\tilde{x} = x_o + \sum_{i=1}^{n} x_i\,\varepsilon_i$ and $\tilde{y} = y_o + \sum_{i=1}^{n} y_i\,\varepsilon_i$, the affine form $\tilde{z}$, determined by affine combinations of $\tilde{x}$ and $\tilde{y}$, is:

$$\tilde{z} = k_1\tilde{x} \pm k_2\tilde{y} \pm k_3 = (k_1 x_o \pm k_2 y_o \pm k_3) + \sum_{i=1}^{n}(k_1 x_i \pm k_2 y_i)\varepsilon_i \quad (5.3)$$

where the middle point of $\tilde{z}$ is given as $z_o = \alpha x_o \pm \beta y_o \pm \gamma$ and deviation of the ith

uncertainty is $z_i = \alpha x_i \pm \beta y_i$.

Non-affine operations

For a non-affine operation $z \leftarrow f(x, y)$, as f is not affine, z cannot be expressed exactly by affine combinations of noise symbols ε_i. An affine approximation is necessary in this case and an extra term $z_k \varepsilon_k$ should be introduced.

$$\tilde{z} = f(\tilde{x}, \tilde{y}) = f^*(\varepsilon_1, \dots, \varepsilon_n) = f^a(\varepsilon_1, \dots, \varepsilon_n) + z_k\varepsilon_k \quad (5.4)$$

where the affine approximation is represented by $f^a(\varepsilon_1, \dots, \varepsilon_n) = k_1\tilde{x} \pm k_2\tilde{y} \pm k_3$.

The error of the affine approximation should be lower than the upper bound δ.

$$\delta \geq \max_{-1 \leq \varepsilon \leq 1} \{|f^*(\varepsilon_1, \dots, \varepsilon_n) - f^a(\varepsilon_1, \dots, \varepsilon_n)|\} \quad (5.5)$$

The extra term $z_k \varepsilon_k$ represents the approximation error and the coefficient z_k equals to δ.

The noise symbol ε_k is a function of the other noise symbols $\varepsilon_1, \dots, \varepsilon_n$. However, in the preceding computations with the input of $\tilde{z}$, the relationship between ε_k and the other noise symbols would be neglected and ε_k is an independent variable. Consequently, the introduction of the non-affine term $z_k\varepsilon_k$ implied a loss of information. However, if the affine approximation is selected properly, the value of δ is usually a quadratic function with the ranges of the inputs. So the error can be decreased by shrinking the ranges of the inputs.

5.2.2 Selecting good affine approximation

As discussed above, to find a good affine approximation f^a is significant to the computation with affine arithmetic. To minimize the error and to minimize the range are the two basic ideas to find the good affine approximation for a non-affine function. In the first approach, the affine approximation that has the smallest possible error over

the given input interval is preferred. This approximation is optimal in the Chebyshev (min-max) sense. In the second approach, the affine approximation with the smallest range, that is the same range as the original function, is selected. To illustrate the difference, an example presented in [156] is given as follows. In this example, the function f is the univariate exponential function and the range of the single input is $[a, b]$. The formulation of the affine approximation is：

$$f^a(\tilde{x}) = k_1\tilde{x} + k_2 \qquad (5.6)$$

Figure 5.1 shows the affine approximations provided by two approaches. The dotted lines represent the centre values of the affine approximation, and the grey regions are the zonotopes corresponding to the error terms. It can be observed that the zonotope of Chebyshev approximation is smaller than that of minimum range approximation, which illustrates that Chebyshev approximation provides a better approximation. However, the minimum range of approximation is usually easier to obtain. In the following study, Chebyshev approximation is used to find good affine approximations for non-affine operators.
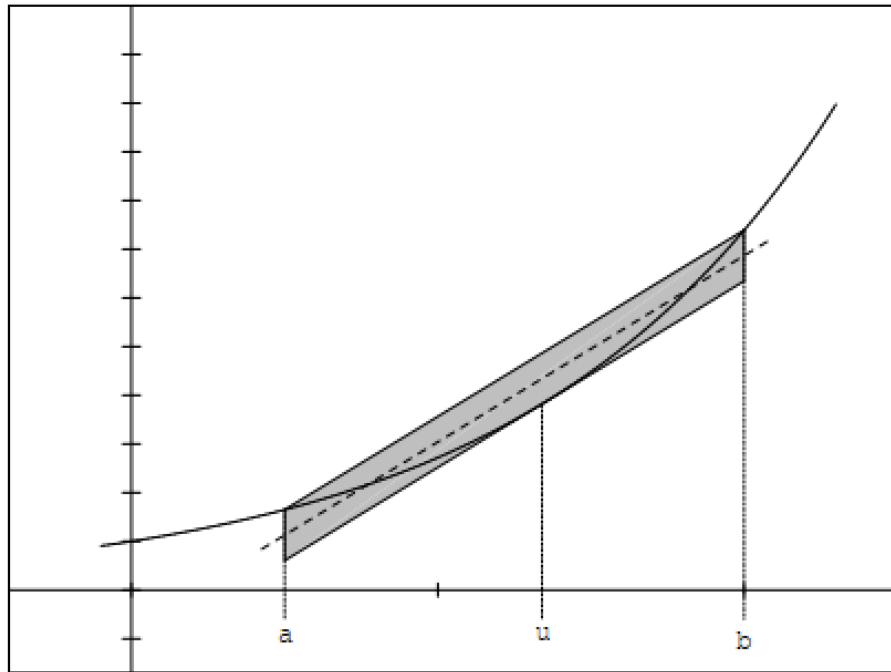
a) Chebyshev approximation

91
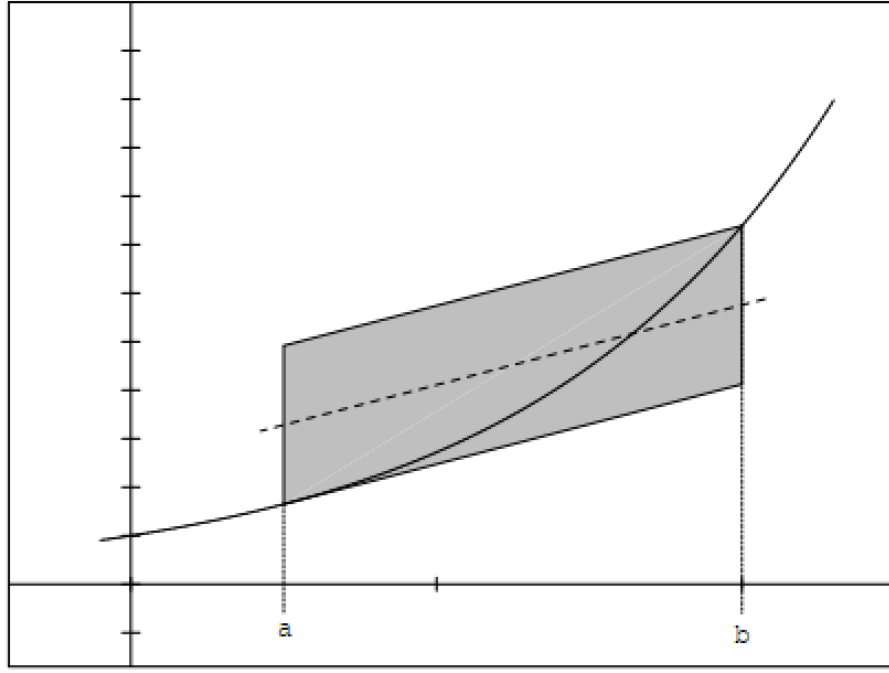
b) Minimum range approximation

Figure 5.1: Comparison between Chebyshev approximation and minimum range approximation [156]

5.2.3 Good affine approximation for some basic operations

Square root in affine arithmetic

Chebyshev approximation theory is presented as follows [156]:

Let $\mathcal{F}$ be some space of functions (polynomials, affine forms, etc.). An element of $\mathcal{F}$ that minimizes the maximum absolute difference from a given function f over some specified domain Ω is known as a *Chebyshev* (or *minimax*) $\mathcal{F}$-approximation of f over Ω.

For univariate functions, the Chebyshev approximation is characterized as follows [156]:

Theorem 1: *Let f be a bounded and continuous function from some closed and bounded interval I = [a, b] to* **R**. *Let h be the affine function that best approximates f in I under the minimax error criterion. Then, there exist three distinct points $u, v,$ and ω in I where the error $f(x) - h(x)$ has maximum magnitude; the sign of the error alternates when the three points are considered in increasing order.*

Based on **Theorem 1**, the optimum approximation can be found as follows [156]:

92

Theorem 2: *Let f be a bounded and twice differentiable function defined on some interval I = [a, b], whose second derivative f″does not change sign inside I. Let $f^a(x) = k_1 x + k_2$ be its minimax affine approximation in I, then:*

- *The coefficient α is simply $\frac{f(b)-f(a)}{b-a}$, the slope of the line r(x) that interpolates the points (a, f(a)) and (b, f(b)).*
- *The maximum absolute error will occur twice at the endpoints a and b of the range (with the same sign), and once (with the opposite sign) at an interior point u in I where $f'(u) = k_1$.*
- *The independent term γ is such that $k_1 u + k_2 = (f(u) + r(u))/2$, and the maximum absolute error is $\delta = |f(u) - r(u)|/2$.*

The affine approximation of square root is given as an example to illustrate the process provided by **Theorem 2.**

Given that $\tilde{z} = \sqrt{\tilde{x}}$ where the range of $\tilde{x}$ is [a, b], the slope of the optimal affine approximation is:

$$k_1 = \frac{\sqrt{b} - \sqrt{a}}{b - a} \tag{5.7}$$

As illustrated in **Theorem 2,** the point u is given by solving $f'(u) = \frac{1}{2\sqrt{u}} = \frac{\sqrt{b}-\sqrt{a}}{b-a}$. The value of u is:

$$u = \frac{a + b + 2\sqrt{ab}}{4} \tag{5.8}$$

The optimal independent term is:

$$k_2 = \frac{f(u) + r(u)}{2} - \alpha u = \frac{\sqrt{a} + \sqrt{b}}{8} + \frac{\sqrt{(ab)}}{2(\sqrt{a} + \sqrt{b})} \tag{5.9}$$

The maximum error is:

$$\delta = \frac{f(u) - r(u)}{2} = \frac{\left(\sqrt{b} - \sqrt{a}\right)^2}{8\left(\sqrt{a} + \sqrt{b}\right)} \tag{5.10}$$

The optimal affine form for $\tilde{z} = \sqrt{\tilde{x}}$ is

$$\tilde{z} = z_0 + z_1 \varepsilon_1 + \cdots + z_n \varepsilon_n + z_k \varepsilon_k$$

where:

$$z_0 = k_1 x_0 + k_2 \tag{5.11}$$

$$z_i = k_1 x_i \ (i = 1, \ldots, n) \tag{5.12}$$

$$z_k = \delta \tag{5.13}$$

Multiplication in affine arithmetic

Given two affine forms

$$\tilde{x} = x_0 + x_1 \varepsilon_1 + \cdots + x_n \varepsilon_n$$

$$\tilde{y} = y_0 + y_1 \varepsilon_1 + \cdots + y_n \varepsilon_n$$

Their product is

$$\tilde{x}\tilde{y} = \left(x_0 + \sum_{i=1}^{n} x_i \varepsilon_i\right)\left(y_0 + \sum_{i=1}^{n} y_i \varepsilon_i\right) = x_0 y_0 + \sum_{i=1}^{n} (x_0 y_i + x_i y_0)\,\varepsilon_i$$
$$+ \sum_{i=1}^{n} x_i\,\varepsilon_i \sum_{i=1}^{n} y_i\,\varepsilon_i$$

The affine form of the product can be written as:

$$\tilde{x}\tilde{y} = x_0 y_0 + \sum_{i=1}^{n} (x_0 y_i + x_i y_0)\,\varepsilon_i + z_k \varepsilon_k \tag{5.14}$$

where

$$|z_k| \geq \max\left(\left|\sum_{i=1}^{n} x_i\,\varepsilon_i \sum_{i=1}^{n} y_i\,\varepsilon_i\right|\right), \varepsilon_i \in \mathbf{U}$$

To simplify the computation, the upper bound for the approximation error can be [156]:

$$z_k = \left(\sum_{i=1}^{n}|x_i|\right)\left(\sum_{i=1}^{n}|y_i|\right) \tag{5.15}$$

5.3 Affine arithmetic optimal power flow

5.3.1 AA-based constrained optimization

The general formulation of AA-based optimization problem is given as (5.16)

$$\min_{\tilde{x}} \tilde{f}(\tilde{x})$$

$$s.t.\, \tilde{g}(\tilde{x}) \leq 0 \tag{5.16}$$

$$\tilde{h}(\tilde{x}) = 0$$

To solve this problem, the minimization operator and the comparison operators are also required to extend into the affine domain. As presented by [157], the similarity operator, inequality operator and the minimization operator in the affine domain are introduced.

Similarity operator for affine forms

Two affine forms $\tilde{x} = x_0 + \sum_{i=1}^{n+n_{na}} x_i\,\varepsilon_i$ and $\tilde{y} = y_0 + \sum_{i=1}^{n+n_{na}} y_i\,\varepsilon_i$ are similar with an approximation degree $\mathcal{L}_{x,y}$, i.e. $\tilde{x} \approx \tilde{y}$, if and only if:

$$\{x_i = y_i\, \forall i \in (0, \dots, n)\} \wedge \left\{\mathcal{L}_{x,y} = \sum_{i=n+1}^{n+n_{na}} |x_i| + |y_i|\right\} \tag{5.17}$$

where $\varepsilon_{n+1}, \dots, \varepsilon_{n+n_{na}}$ are the noise symbols generated by non-affine operations.

Inequality operator for affine forms

Given two affine forms $\tilde{x} = x_0 + \sum_{i=1}^{n_x} x_i\,\varepsilon_i$ and $\tilde{y} = y_0 + \sum_{i=1}^{n_y} y_i\,\varepsilon_i$, $\tilde{x} < \tilde{y}$ if and only if:

$$x_0 + \sum_{i=1}^{n_x} |x_i| < y_0 - \sum_{i=1}^{n_y} |y_i| \tag{5.18}$$

Min operator for affine forms

Given a differentiable, non-linear function $f: R \rightarrow R$ and the affine form $\tilde{x} = x_0 + \sum_{i=1}^{n} x_i \, \varepsilon_i$, the following AA-based minimization problem:

$$\min_{\tilde{x}} f(\tilde{x}) = f_0(\tilde{x}) + \sum_{i=1}^{n} f_i(\tilde{x}) \, \varepsilon_i + \sum_{i=n+1}^{n+n_{na}} f_i(\tilde{x}) \, \varepsilon_i$$

$$s.t. \, \tilde{g}(\tilde{x}) \leq 0 \tag{5.19}$$

$$\tilde{h}(\tilde{x}) = 0$$

is equivalent to the multi-objective optimization problem presented as (5.20) which aims to minimize the central value and the radius of the original objective function simultaneously. This optimization model is able to provide the solutions where both central values and deviations of affine forms for decision and state variables are given.

$$\min_{x_0,\dots,x_n} \left\{ f_0(x_0, \dots, x_n), \sum_{i=1}^{n+n_a} |f_i(x_0, \dots, x_n)| \right\}$$
$$s.t. \, \tilde{g}(\tilde{x}) \leq 0 \tag{5.20}$$
$$\tilde{h}(\tilde{x}) \approx 0$$

Considering the simplicity and the robustness of the solution, weight factors are applied to two objectives; then the optimization problem is given as:

$$\min_{x_0,\dots,x_n} \omega_1 f_0(x_0, \dots, x_n) + \omega_2 \sum_{i=1}^{n+n_a} |f_i(x_0, \dots, x_n)|$$
$$s.t. \, \tilde{g}(\tilde{x}) \leq 0 \tag{5.21}$$
$$\tilde{h}(\tilde{x}) \approx 0$$

where ω_1 and ω_2 are the weights for the centre and the radius for the original objective function, which represent the preference to determinism and robustness of solutions, respectively. The performance of the AA-based OPF solution is highly dependent on the values of the weights.

96

5.3.2 AA-based optimal power flow

Consider a power network $G(\mathcal{N}, \mathcal{L})$, with a set of network buses $\mathcal{N}$ and network branches $\mathcal{L}$, the interval of following uncertainties are modelled as (5.22) and (5.23) :

For WF maximum supplied power:

$$\widetilde{\overline{P}}_{gw} = \overline{P}_{gwo} + \overline{P}_{gw}\varepsilon_w \quad \forall w \in \mathcal{W} \tag{5.22}$$

where $\mathcal{W}$ is the set of wind farm indices.

while for load:

$$\tilde{P}_{di} = P_{dio} + P_{di}\varepsilon_i, \quad \tilde{Q}_{di} = Q_{dio} + Q_{di}\varepsilon_i \quad \forall i \in \mathcal{N} \tag{5.23}$$

where each wind generation and load have different error symbols.

The constraints of AA-OPF are listed as follows:

Power balance equations

$$\tilde{P}_{gi} + \sum_{w \in \mathcal{W}_i} \tilde{P}_w - \tilde{P}_{di} = \sum_{(l,i,j) \in \mathcal{L}_i} \tilde{P}_{lij} + \sum_{(l,i,j) \in \mathcal{L}_i^R} \tilde{P}_{lij}, \forall i \in \mathcal{N} \tag{5.24}$$

$$\tilde{Q}_{gi} + \sum_{w \in \mathcal{W}_i} \tilde{Q}_w - \tilde{Q}_{di} = \sum_{(l,i,j) \in \mathcal{L}_i} \tilde{Q}_{lij} + \sum_{(l,i,j) \in \mathcal{L}_i^R} \tilde{Q}_{lij}, \forall i \in \mathcal{N} \tag{5.25}$$

where $\tilde{P}_{gi}$ and $\tilde{Q}_{gi}$ are affine active and reactive power outputs of the generator at bus i, $\tilde{P}_w$ and $\tilde{Q}_w$ are affine active and reactive power output of wind generation indexed by w and $\mathcal{W}_i$ is the index of wind generation attached at bus i, $\tilde{P}_{di}$ and $\tilde{Q}_{di}$ are affine active and reactive demands at bus i.

Line flow equations

$$\frac{\tilde{V}_i}{t_{ij}}\left[\left(\frac{jb'_{ij}}{2} + y_{ij}\right)\frac{\tilde{V}_i}{t_{ij}} - y_{ij}\tilde{V}_j\right]^* = \tilde{P}_{lij} + j\tilde{Q}_{lij} \ \forall \ (l,i,j) \ \in \mathcal{L} \tag{5.26}$$

$$\tilde{V}_j\left[-y_{ij}\frac{\tilde{V}_i}{t_{ij}} + \left(\frac{jb'_{ij}}{2} + y_{ij}\right)\tilde{V}_j\right]^* = \tilde{P}_{lji} + j\tilde{Q}_{lji} \ \forall \ (l,i,j) \ \in \mathcal{L} \tag{5.27}$$

where b'_{ij} is the shunt susceptance of line l. For the branch $(l,i,j) \in \mathcal{L}$, $\tilde{P}_{lij}$ and $\tilde{Q}_{lij}$ are affine active and reactive power flow injected into branch l at its from end; $\tilde{P}_{lji}$ and

$\tilde{Q}_{lji}$ are affine active and reactive power flow injected into branch l at its to end. $\tilde{V}_i$ and $\tilde{V}_j$ are affine voltages at from and to ends of branch l. t_{ij} is the transformer tap ratio.

Conventional generator output

$$P_{gi}^{min} \leq \tilde{P}_{gi} \leq P_{gi}^{max}, \forall i \in \mathcal{G} \tag{5.28}$$

$$Q_{gi}^{min} \leq \tilde{Q}_{gi} \leq Q_{gi}^{max}, \forall i \in \mathcal{G} \tag{5.29}$$

Wind power output

$$0 \leq \tilde{P}_w \leq \overline{\tilde{P}}_{gw}, \forall w \in \mathcal{W} \tag{5.30}$$

Line thermal limits

$$\left|\tilde{P}_{lij} + j\tilde{Q}_{lij}\right|^2 \leq (S_l^{max})^2, \quad \left|\tilde{P}_{lji} + j\tilde{Q}_{lji}\right|^2 \leq (S_l^{max})^2, \forall (l, i, j) \in \mathcal{L} \tag{5.31}$$

Voltage magnitude limits

$$\left(V_i^{min}\right)^2 \leq \left|\tilde{V}_i\right|^2 \leq (V_i^{max})^2, \forall i \in \mathcal{N} \tag{5.32}$$

Bus voltages are represented in the rectangular form:

$$\tilde{V}_i = \tilde{e}_i + j\tilde{f}_i \tag{5.33}$$

where $\tilde{e}_i$ and $\tilde{f}_i$ are affine real and imaginary parts of the voltage at bus i.

Slack bus voltage magnitude and angle should satisfy the following constraints:

$$\tilde{e}_1 = 1, \tilde{f}_1 = 0 \tag{5.34}$$

In the following study, two objective functions are used: 1) cost minimization and 2) wind curtailment minimization. The objective functions are given as follows:

$$\min f_c\left(\tilde{P}_g\right) = \sum_{i \in \mathcal{G}} a_i * \tilde{P}_{gi}^2 + b_i * \tilde{P}_{gi} + c_i \tag{5.35}$$

where a_i, b_i and c_i are the cost coefficients of generator i.

$$\min \sum_{w \in \mathcal{W}} \tilde{P}_{curtw}^2 \tag{5.36}$$

where the curtailed wind power $\tilde{P}_{curtw}$ is given by :

$$\tilde{P}_{curtw} = \overline{\overline{P}}_{gw} - \tilde{P}_w, \forall w \in \mathcal{W} \tag{5.37}$$

Using the method described in Section 5.2, the AA-based OPF can be transformed into the formulation of deterministic optimization problem presented as (5.21).

5.4 Affine formulation of DTR

The affine formulation of DTR in this chapter considers uncertainties in wind speeds V_w and wind directions ϕ, as previously presented in [158], which can be respectively expressed by (5.38) and (5.39).

$$\widetilde{V_w} = V_{wo} + V_w \varepsilon_w \tag{5.38}$$

$$\tilde{\phi} = \phi_o + \phi \varepsilon_\phi \tag{5.39}$$

The affine form to represent DTR can be calculated as:

$$\tilde{I}_{rated} = \sqrt{\frac{\widetilde{q_c} + \widetilde{q_r} - \widetilde{q_s}}{\tilde{R}}} \tag{5.40}$$

Neglecting the term introduced by non-affine operations, the final affine form is given by:

$$\tilde{I}_{rated} = I_{rated0} + I_{ratedw} \varepsilon_w + I_{rated\phi} \varepsilon_\phi \tag{5.41}$$

where I_{rated0}, I_{ratedw}, and $I_{rated\phi}$ are the centre value, partial deviation caused by wind speed variation and partial deviation caused by wind direction variation.

5.5 Case study and numerical results

In this section, a 3-bus system available from MATPOWER [149], a 10-bus system and the IEEE 33-bus test system [134] are used to illustrate AA-OPF method and compare it with MCS solution. The proposed AA optimization model is coded with YALMIP [159]. The AA-based OPF problem is solved by IPOPT [160], while the

MCS-based approach is implemented with MATPOWER [149][150]. The values of the weight factors in (5.21) are set as 1 and 0.5 as presented in [10], [11]

5.5.1 The 3-bus system

In the 3-bus system, a load with the nominal value of 3 MW, 0.8 Mvar is located at Bus 2. The load is forecast as 0.9 pu and it varies in a $\pm 11\%$ range of the forecast value. Lines L1-2 and L2-3 are overhead lines with ACSR conductors of types Gopher and Mole, whose specific parameters for DTR calculation can be obtained from [136]. The bus voltage is 11 kV and the bus voltage limits are 0.9 pu to 1.10 pu. The capacity of the wind turbine at Bus 3 is 2MW, whose power output is determined according to the manufacture power curve of Vestas 90-2.0MW [161], shown as Figure 5.3. The range of forecast wind speed is between [8m/s, 10m/s] and the forecast wind power output is 0.625pu and the range of its variation is $\pm 28\%$ of the forecast value.
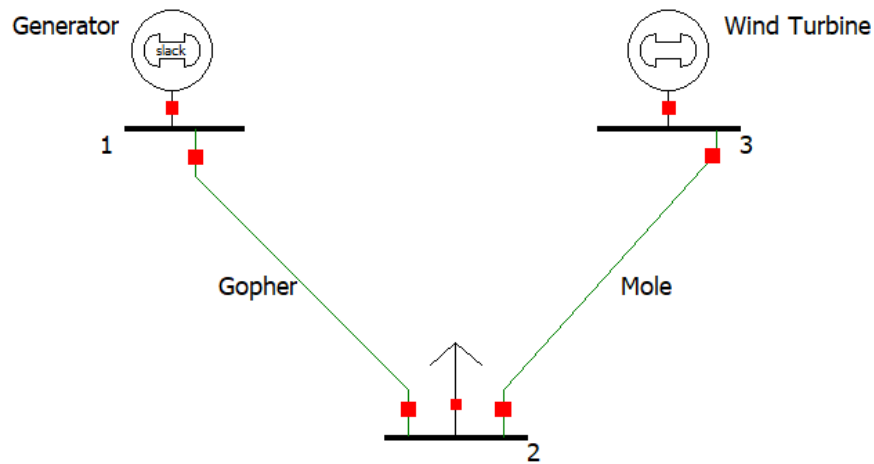
Figure 5.2: The 3-bus network configuration
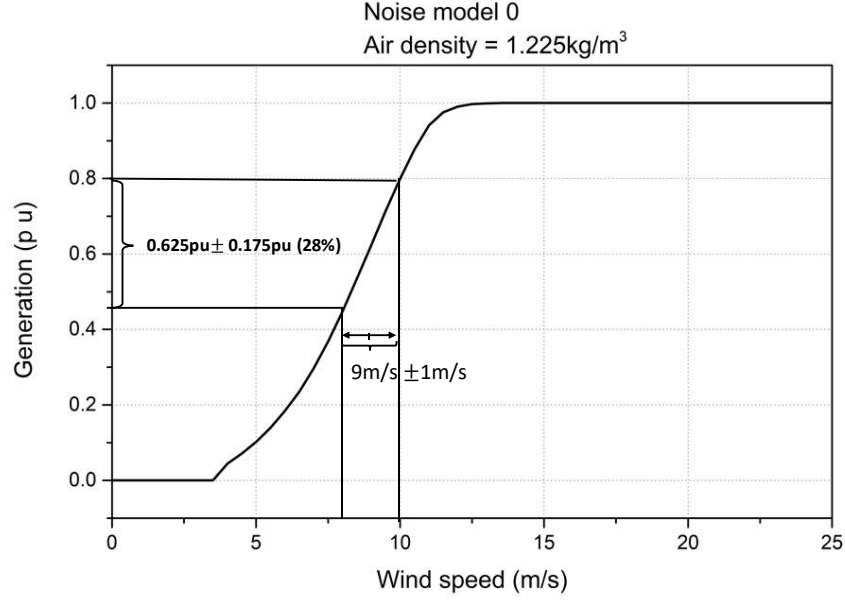
Figure 5.3: Manufacture power curve for Vestas 90-2.0MW turbine

Assuming that the wind attacking angle is fixed at 90° which can provide maximum cooling impacts for overhead lines, the affine forms of DTR on L1-2 and L2-3 can be calculated according to Section 5.4:

$$\widetilde{I_{max}^{L1-2}} = 337.8476 + 11.1464\varepsilon_{vw} + 0.1242\varepsilon_{e1} + 0.094\varepsilon_{e2} \qquad (5.42)$$

$$\widetilde{I_{max}^{L2-3}} = 187.9407 + 6.2140\varepsilon_{vw} + 0..693\varepsilon_{e1} + 0.0525\varepsilon_{e2} \qquad (5.43)$$

where ε_w is the noise symbol representing wind speed uncertainty, ε_{e1} and ε_{e2} are noise symbols introduced by non-affine operations in DTR calculation. As the deviations caused by ε_{e1} and ε_{e2} are quite small (0.1242 A and 0.094 A for L1-2, 0.693 A and 0.0525 A for L2-3), these two terms can be neglected to simplify the calculation The fuel cost function of the generator at bus 1 is given as (5.35) where a,b and c are given as 0, 14 and 0 \$/MW [149].

Implementing AA-OPF presented in Section 5.3.2, the optimal power output of conventional generator at Bus 1 (optimised to minimize fuel cost against wind and demand variations) can be obtained as:

$$\widetilde{P_g} = 1.4507 - 0.3501\varepsilon_w + 0.3002\varepsilon_D \qquad (5.44)$$

The centre value of the optimal power output P_{go} is 1.4507 MW and the deviations caused by uncertainties in wind and demand are 0.3501 MW and 0.3002 MW. According to the definition of affine arithmetic, the radius of optimal power output $radP_g$ is 0.6503 MW. The optimal dispatch interval is therefore calculated as $[Pg_o - radP_g, P_{go} + radP_g]$, which is given as [0.8004 MW, 2.1010 MW]. The intervals obtained by the MCS method are the benchmark to check the validity of the obtained AA interval. In the MCS method, all the uncertainties inputs are assumed to be independent and distributed randomly within the ranges. The MCS-based method needs 2000 iterations to converge and the further increase of MCS iterations does not change the intervals significantly. The interval provided by the MCS-based approach is [0.8133 MW, 2.0967 MW]. The error between the upper bounds is 0.205% and the lower bound error is 1.611%

Figure 5.4 depicts the intervals of bus voltage magnitudes, reactive power generation and line currents obtained by AAOPF and MCS-based OPF respectively. It can be seen that MCS-based intervals are slightly inside AA intervals, but they are quite close to each other. It demonstrates that the MCS-based method provides the exact intervals and AA intervals are too conservative in this case. For instance, AA interval of current flow on L1-2 is 60% wider than MCS results which means that the AA interval may cover power flow solutions with very low probability to occur.
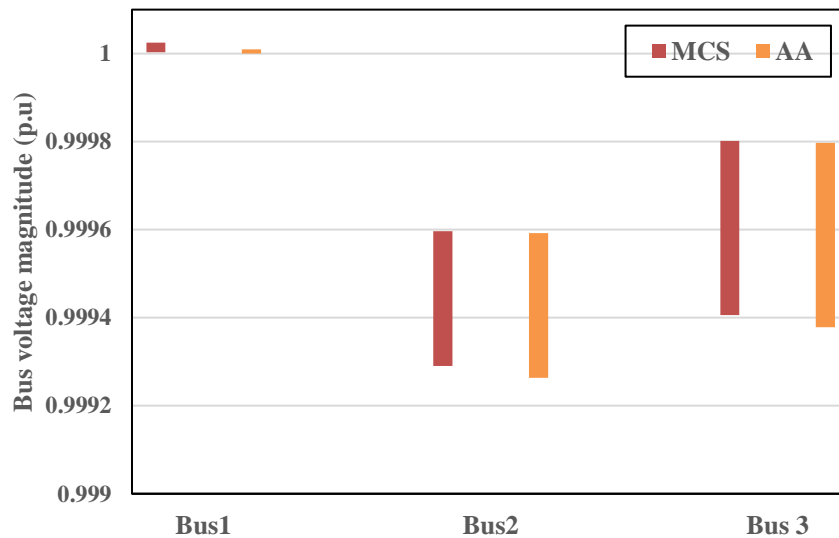
a) Bus voltage magnitude intervals
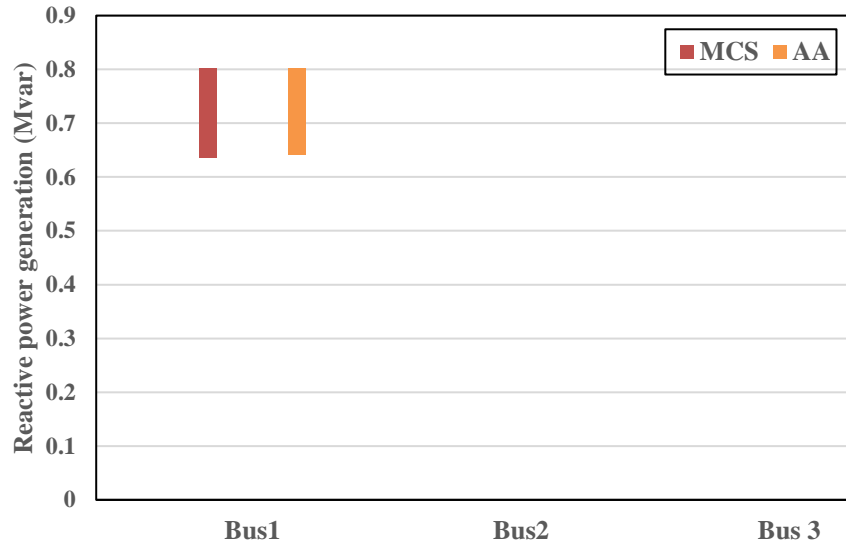
b) Reactive power generation intervals
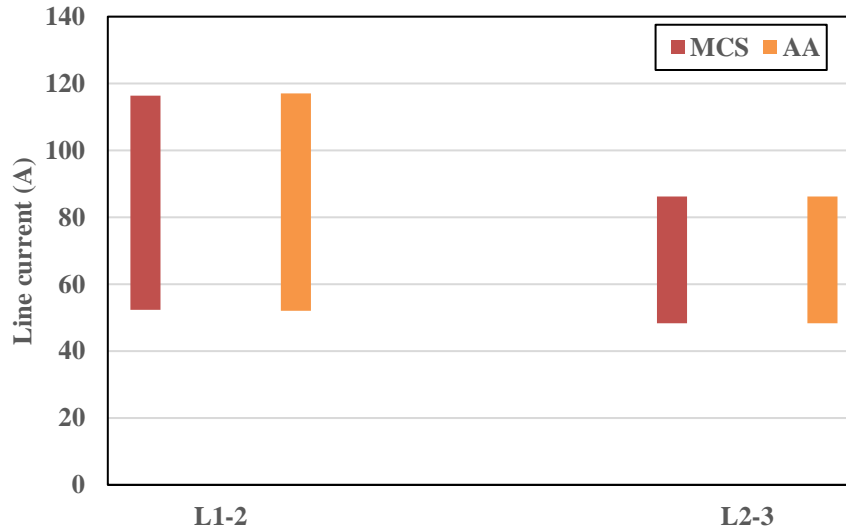
c) Line current intervals

Figure 5.4: Comparison between AA-based OPF and MCS-based OPF in 3-bus system

The results based on the 3-bus system show that AA method is able to achieve similar results as MCS-based method but AA method is much faster as the MCS method requires 2000 iterations of OPF to converge, even for a simple test network.

5.5.2 The 10-bus system

The case study is based on a real transmission network in Italy, Figure 5.5, with a high penetration of wind power, where frequent OHL congestion (i.e. overloading of OHLs in terms of their STR limits) results in wind energy curtailment. The network has 10

buses, where Bus 1 is the slack bus (connection point to HV bulk power system). The nominal bus voltage for each bus is 150 kV. There are eight wind farms, WF1 to WF8, all operating with a unity power factor and two bulk load supply points, L1 and L2, located at Bus 3 and Bus 10, with peak demands of 56 MW, 6 Mvar and 50 MW, 5 Mvar, respectively. All lines in network are OHLs, whose DTRs can be calculated according to the thermal model presented in Section 5.4. Detailed network information can be obtained from [11].
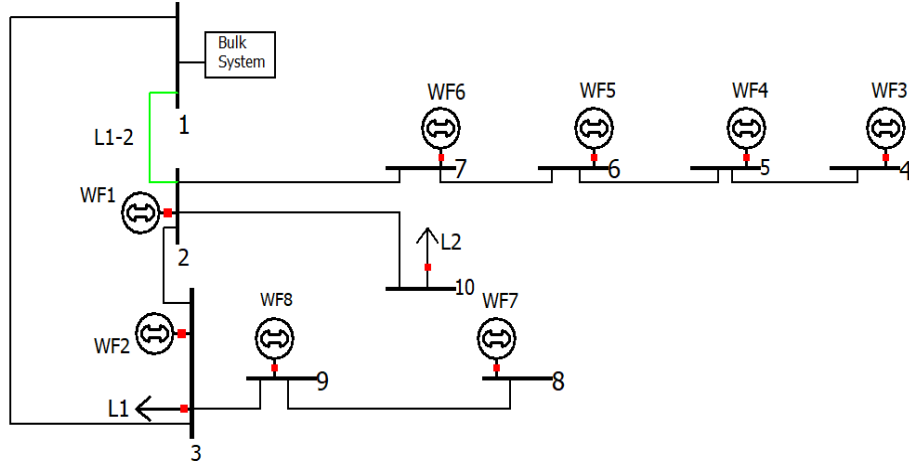
Figure 5.5: The 10-bus network configuration

Wind profiles, load profiles and their uncertainties

Two days are selected for analysis: one in summer (6th of June) and one in winter (2nd of January). To evaluate load profile uncertainties, two recorded load profiles (6 – year and the resolution of 30-minute) are used. The seconds-order Markov Chain (MC) model is applied to analyse the variations in load profiles, in which the probability of transferring from one state to the next state only depends on the two successive previous states. The model used to generate the load profiles with uncertainties is discussed in detail by [10]. Two days are selected for the following network analysis: one in summer (6th of June) and one in winter (2nd of January). The load profiles of L1 and L2 in the two days are plotted as Figure 5.6.

In order to evaluate seasonal variations in DTR limits and their impacts on wind energy integration, wind profiles are also needed for both wind farms and OHLs. Considering the number of wind farms and OHLs in the test network, 18 correlated wind speed profiles are required. However, due to the topology of the network, L1-2 is the main

limitation to the wind energy integration and the DTR limits of other OHLs will not be reached. Consequently, the wind conditions at all OHLs can be assumed to be the same to simplify the computation. Daily wind speed profiles for WF1-WF8 as well as a daily wind speed profiles for OHLs, are generated for these two days based on Copula theory [162], [163] and Markov Chain model.

Copula function is a multivariate PDF with uniformly distributed marginal probability for each variable. Considering a bivariate distribution, if the marginal distributions F_X and F_Y are known, their joint distribution F_{XY} can be written as $F_{XY}(x,y) = C(F_X(x), F_Y(y))$. If F_X and F_Y are continuous, then the Copula function C is unique. If $F_X(x) = u$ and $F_Y(y) = v$, where u and v are respectively realisations of uniformly distributed variables U and V, $C_{UV}(u,v) = F\left(F_X^{-1}(u), F_Y^{-1}(v)\right)$ can be used to build corresponding Copula function from multivariate distribution function and multivariate Gaussian Copula is applied to analyse high-dimensional correlations between wind speeds at several WFs, as well as for network OHLs.

Multivariate Gaussian Copula function has one Copula linear correlation parameter ρ_g for every bivariate dependence, so the d-dimensional Gaussian Copula can be written as:

$$C_g\left(u_1, u_2, \ldots, u_d; \boldsymbol{\rho_g}\right) = \Phi_{\boldsymbol{\rho_g}}\left(\Phi^{-1}(u_1), \Phi^{-1}(u_2), \ldots, \Phi^{-1}(u_d)\right) \tag{5.45}$$

$$c_g\left(u_1, u_2, \ldots, u_d; \boldsymbol{\rho_g}\right) = \frac{\partial^d C_g\left(u_1, u_2, \ldots, u_d; \boldsymbol{\rho_g}\right)}{\partial u_1 \partial u_2 \ldots \partial u_d}$$
$$= \left|\boldsymbol{\rho_g}\right|^{-\frac{1}{2}} \exp\left(-\frac{1}{2}\boldsymbol{\zeta_g}^{\mathrm{T}}(\boldsymbol{\rho_g}^{-1} - \mathbf{I})\boldsymbol{\zeta_g}\right) \tag{5.46}$$

$$\boldsymbol{\zeta_g} = \left(\Phi^{-1}(u_1), \Phi^{-1}(u_2), \ldots, \Phi^{-1}(u_d)\right) \tag{5.47}$$

The above equations transform marginal distributions into a uniform domain in [0,1] using marginal cumulative density function (CDF) and then transform the uniform

domain into a normal domain [164]. This approach expresses dependency between uncertain variables x_i ($i = 1, 2, 3, \ldots, d$) by the dependency between their standard normal transforms. In fitting Gaussian Copula, the parameter $\boldsymbol{\rho_g}$ is estimated using maximum likelihood estimation (MLE) method [165].

Since the correlation matrix $\boldsymbol{\rho_g}$ is a positive definite matrix, it can be applied with Cholesky factorisation: $\boldsymbol{\rho_g} = \mathbf{TT}^*$, where $\mathbf{T}$ is a lower triangular matrix and $\mathbf{T}^*$ is its conjugate transpose. The first step of sampling from a given Gaussian d-dimensional Copula is to generate a d-dimensional variable $\mathbf{Q} = [\mathbf{q}_1, \mathbf{q}_2, \ldots, \mathbf{q}_d]$, which can be uncorrelated, and every dimension of the variable $\mathbf{q}_i$ ($i = \{1, 2, \ldots, d\}$) follows the standard normal distribution. The target correlated variable $\mathbf{Y} = [\mathbf{y}_1, \mathbf{y}_2, \ldots, \mathbf{y}_d]$ can be obtained from $\mathbf{Y} = \mathbf{TQ}$. Afterwards, by applying inverse standard normal distribution, $\mathbf{Y}$ can be transferred into a correlated variable in the uniform domain in $[0, 1]$.

The available datasets for wind speeds are 3-year recordings at nine uncorrelated locations: one (L1) with synchronous/simultaneous recording of wind speed and wind direction, and eight (L2-L9) with only wind speed measurements. The synchronous wind speed/direction time series are used for wind profile at the OHLs. For L2-L9, MC models are fitted based on the historical data and new eight auto-correlated wind speed time series are obtained based on the transition matrices. To generate required cross-correlated wind speed time series, the target correlation matrix $\boldsymbol{\rho_g}$ in Table 5.1 is assumed [166]:

Table 5.1: Target correlation matrix $\boldsymbol{\rho_g}$

	L1	L2	L3	L4	L5	L6	L7	L8	L9
L1	1	0.900	0.840	0.810	0.650	0.890	0.680	0.670	0.770
L2	0.900	1	0.930	0.940	0.830	0.910	0.850	0.850	0.860
L3	0.840	0.930	1	0.940	0.820	0.840	0.860	0.850	0.800
L4	0.810	0.940	0.940	1	0.860	0.820	0.910	0.910	0.860
L5	0.650	0.830	0.820	0.860	1	0.750	0.860	0.850	0.750
L6	0.890	0.910	0.840	0.820	0.750	1	0.790	0.790	0.880
L7	0.680	0.850	0.860	0.910	0.860	0.790	1	0.980	0.860
L8	0.670	0.850	0.850	0.910	0.850	0.790	0.980	1	0.870
L9	0.770	0.860	0.800	0.860	0.750	0.880	0.860	0.870	1

Nine auto-correlated, as well as cross-correlated wind speed time series, can be obtained by the method discussed above. Table 5.2 shows the calculated correlation coefficient matrix of the simulation results.

Table 5.2: Calculated correlation matrix of simulation time series

	L1	L2	L3	L4	L5	L6	L7	L8	L9
L1	1	0.893	0.847	0.806	0.642	0.889	0.676	0.666	0.767
L2	0.893	1	0.928	0.939	0.824	0.903	0.841	0.847	0.859
L3	0.847	0.928	1	0.934	0.816	0.845	0.855	0.848	0.804
L4	0.806	0.939	0.934	1	0.852	0.812	0.893	0.904	0.860
L5	0.642	0.824	0.816	0.852	1	0.743	0.848	0.841	0.741
L6	0.889	0.903	0.845	0.812	0.743	1	0.790	0.786	0.874
L7	0.676	0.841	0.855	0.893	0.848	0.790	1	0.973	0.858
L8	0.666	0.847	0.848	0.904	0.841	0.786	0.973	1	0.871
L9	0.767	0.859	0.804	0.860	0.741	0.874	0.858	0.871	1

Wind speed and wind direction profiles for OHL L1-2 are plotted in Figure 5.7 and Figure 5.8, all for the two selected days. For a given wind speed profiles, power outputs of wind turbines (WTs) in WF can be estimated through many approaches [167]. The most common approach is to use of manufacturer power curve, which specifies the relationship between the input wind speed and WT output power. However, as discussed in the previous chapter, manufacturer power curves are obtained in controlled conditions (air-tunnels), where the impact of variations in wind speeds and wind directions, WT dynamics and application specific factors are not considered. In order to fully represent uncertainties in WF power outputs, the MGND model

developed in chapter 4 is applied to estimate WF output generation profiles and their uncertainties according to generated input wind speed profiles, with Figure 5.9 giving an example for WF1.
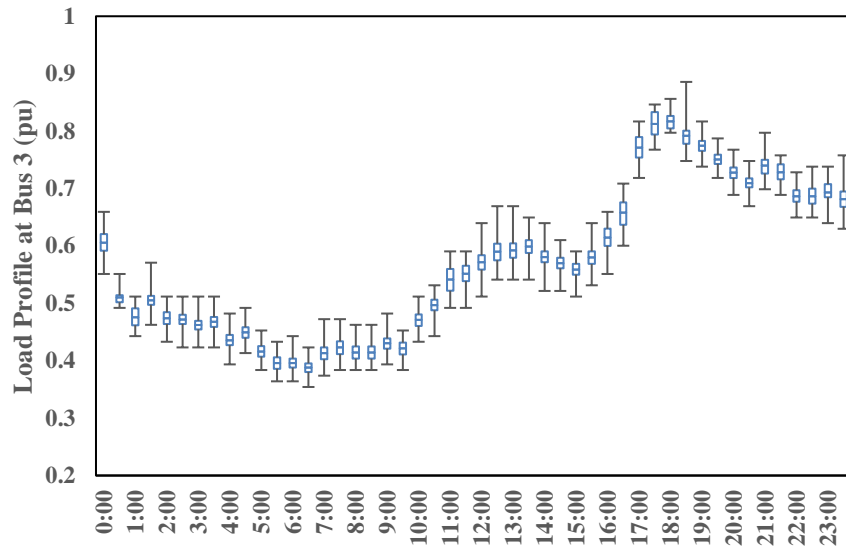
a) Load L1 at winter day
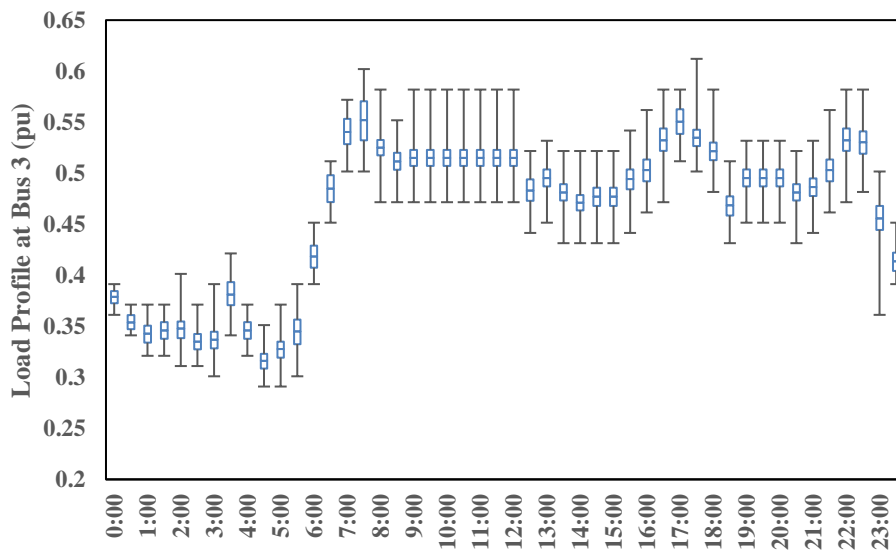
b) Load L1 at summer day
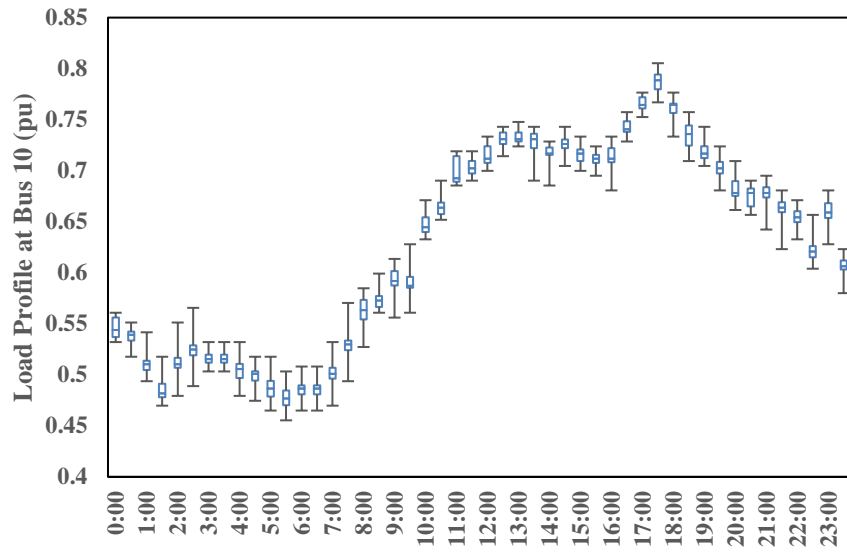
c) Load L2 at winter day
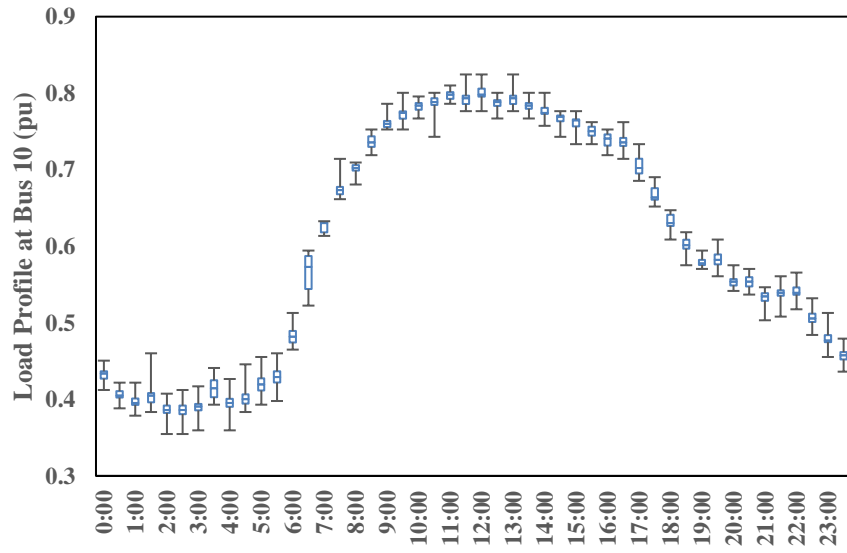
d) Load L2 at summer day

Figure 5.6: Daily load profiles and uncertainties for load L1 and L2
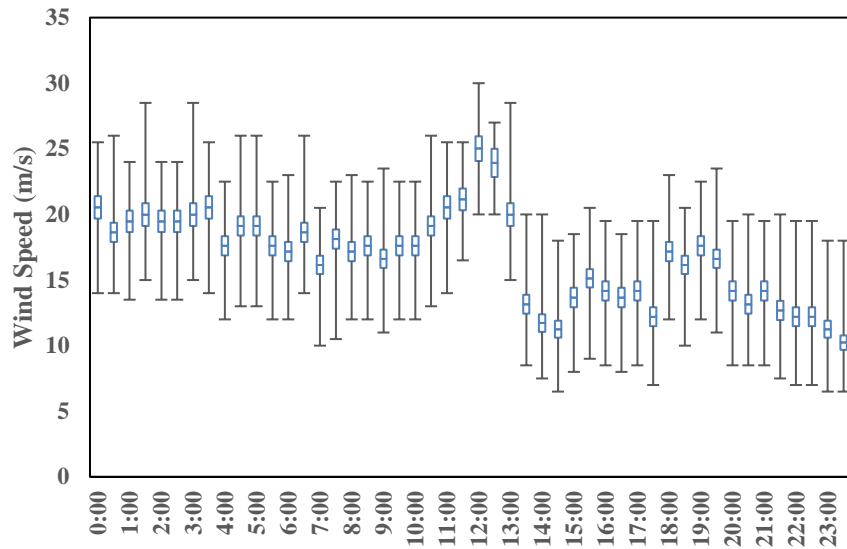
a) Wind speed variations on a selected winter day
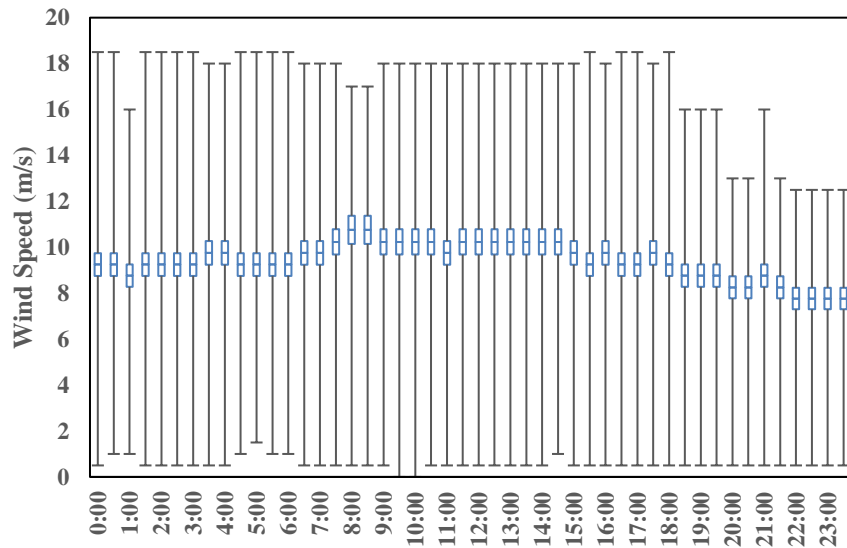
b) Wind speed variations on a selected summer day
Figure 5.7: Daily wind speed profile and uncertainties at OHL L1-2
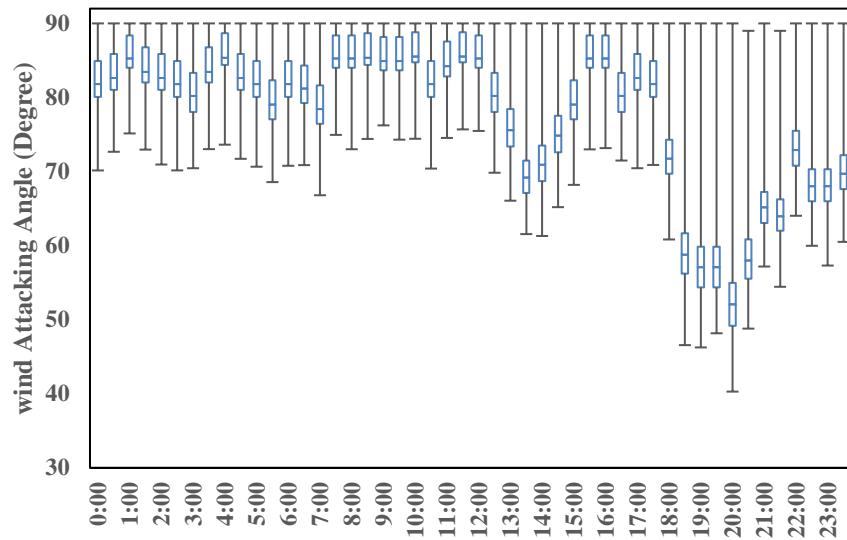
a) Wind direction variations on a selected winter day
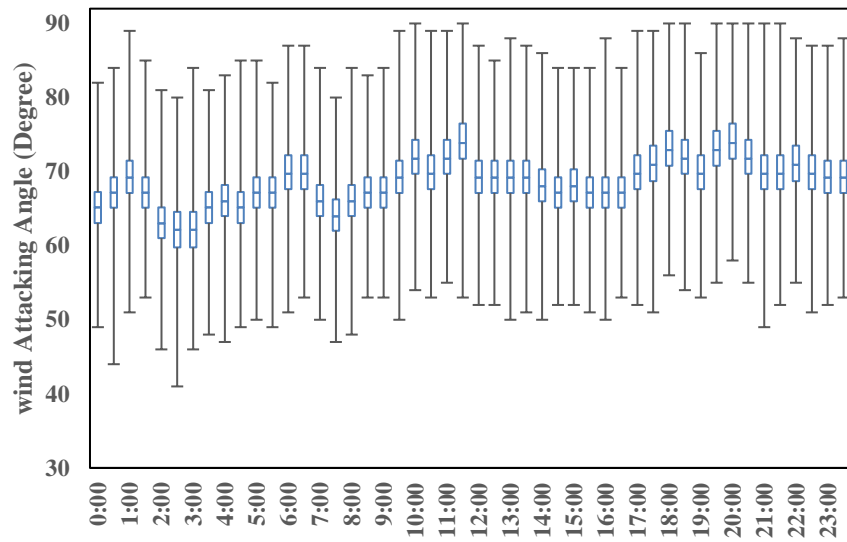
b) Wind direction variations on a selected summer day
Figure 5.8: Daily wind direction (line attacking angle) and uncertainties at OHL L1-2

111
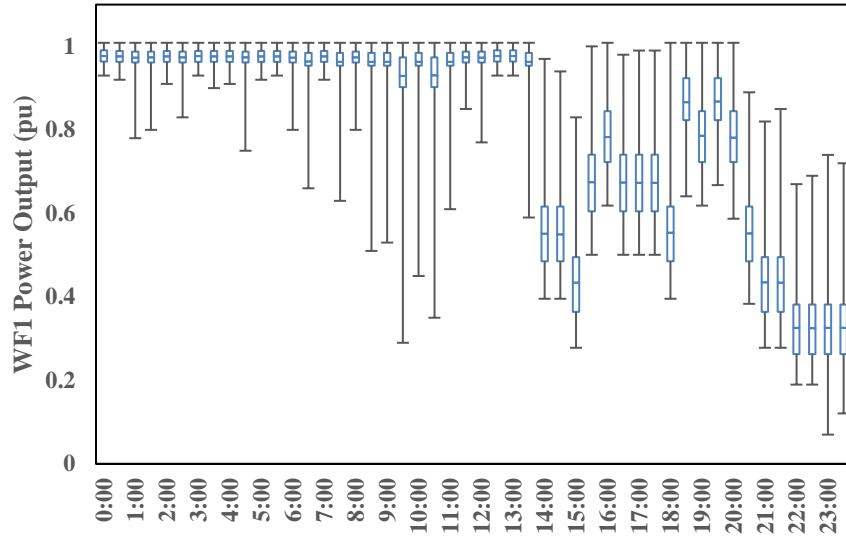
a) Power output variations for WF1 on a selected winter day
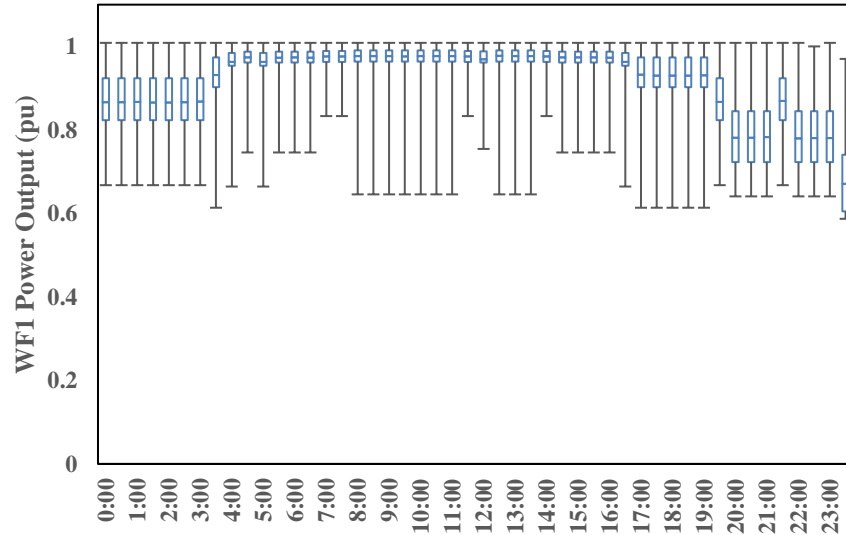
b) Power output variations for WF1 on a selected summer day
Figure 5.9: Daily power output and uncertainties for WF1

Comparison between DTR and STR values

Firstly, Min-Max ranges of DTR values, corresponding to the minimum and maximum wind speed and wind direction uncertainties (as in Figures 5.7 and 5.8), are used as input values in the AA-based OPF method. The evaluated upper and lower bounds of DTR values, as well as STR value, are plotted for the considered day and L1-2 in Figure 5.10. As the load profile is recorded with the resolution of 30 minutes, the DTR is also calculated with this resolution. The time constant of the considered OHL conductor is defined as the time duration which the conductor needs to reach 63.% of

its final steady-state temperature [168], [169]. Figure 5.11 plots time constant variation of the ACSR conductor with wind speed and wind attacking angle. The ambient temperature is 25 °C, and the initial and final currents are 200 A and 600 A. The change of the final current will cause slight variations in the time constant values. As the time constant is not higher than 25 minutes and generally lower than 5 minutes when the wind speed is high, it can be assumed that the OHL conductor will reach steady-state thermal operating condition within each 30-minute period, i.e. that thermal capacitance of the OHL conductor can be neglected.
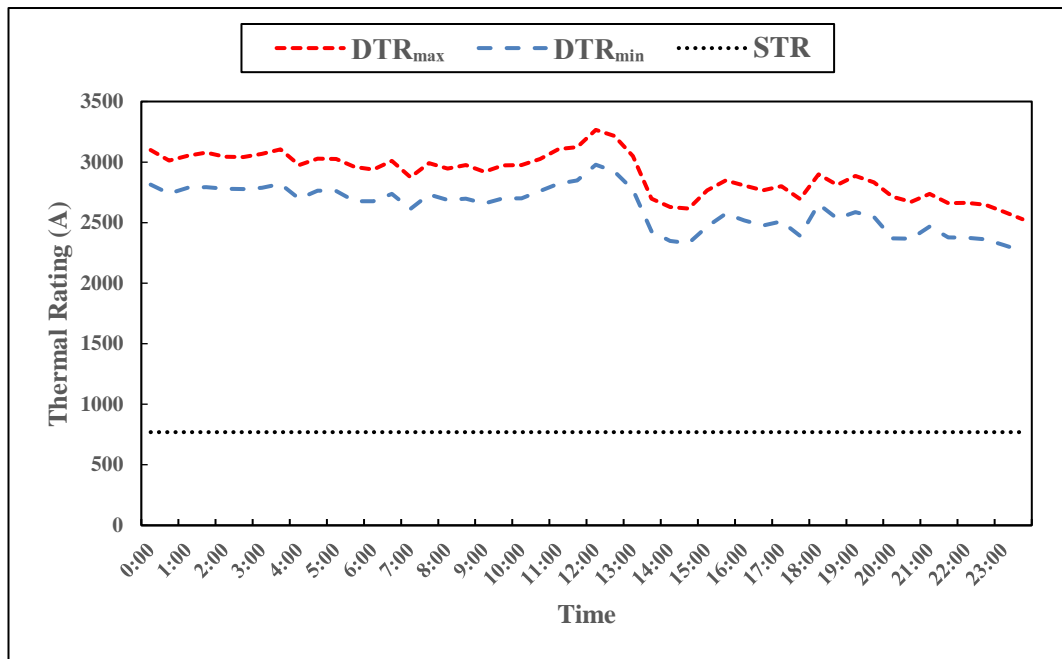
a) winter day
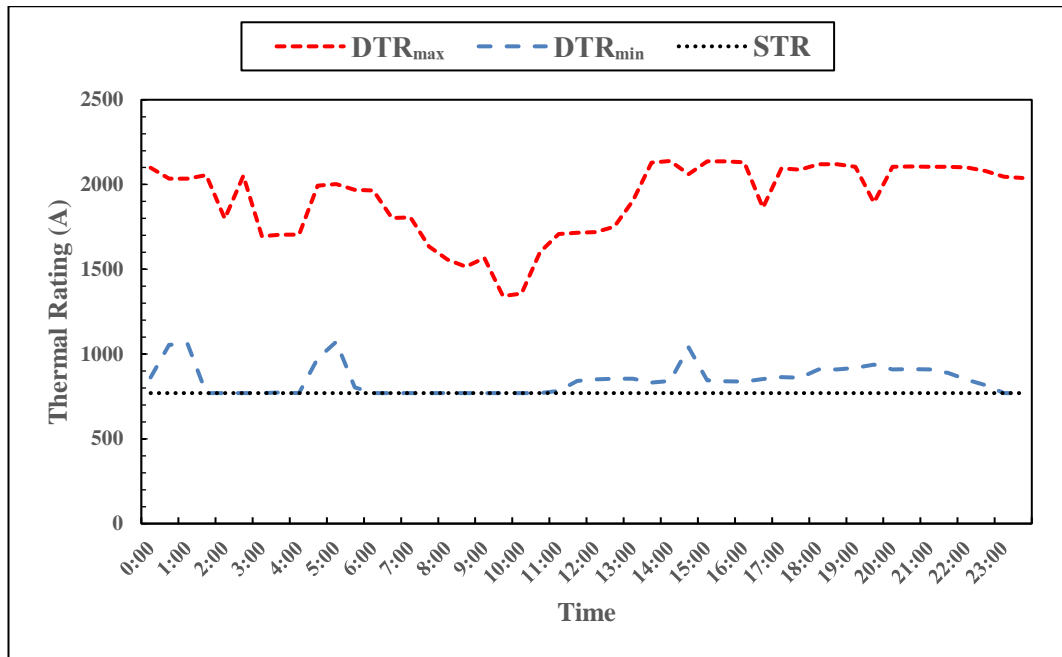
b) summer day

Figure 5.10: Comparison between STR and AA-OPF DTR values for L1-2
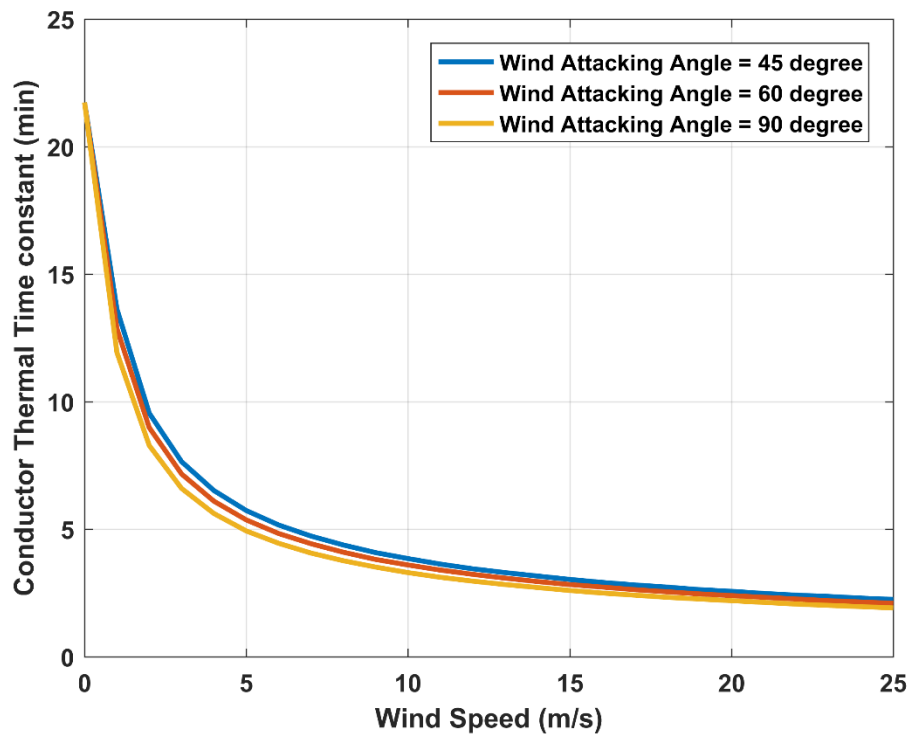
Figure 5.11: Thermal time constant of the ACSR conductor

Assuming that the demand of L1 and L2 is 0.26089 pu and 0.35471 pu (minimum loads in the summer day), the power outputs of wind generation are all at 1.0 pu and the DTRs are all 769.8 A which are the lowest value in the summer day presented as

114

Figure 5.10, the optimal wind curtailment for this deterministic scenario can give the currents on all lines as shown in Figure 5.12. This deterministic scenario presents the worst case from the perspective of wind integration as the load and DTR are the minimum while the wind generation is maximum (This is not realistic as DTR and wind generation should be correlated). The line currents presented in Figure 5.12 shows that the main limitation of wind integration is the DTR of L1-2. The currents on the other lines are far from DTR limits except from L1-3. As the L1-3 is close to L1-2 according to network configuration, the assumption that all OHLs have the same wind profiles will not cause significantly different results from the cases with different wind profiles.
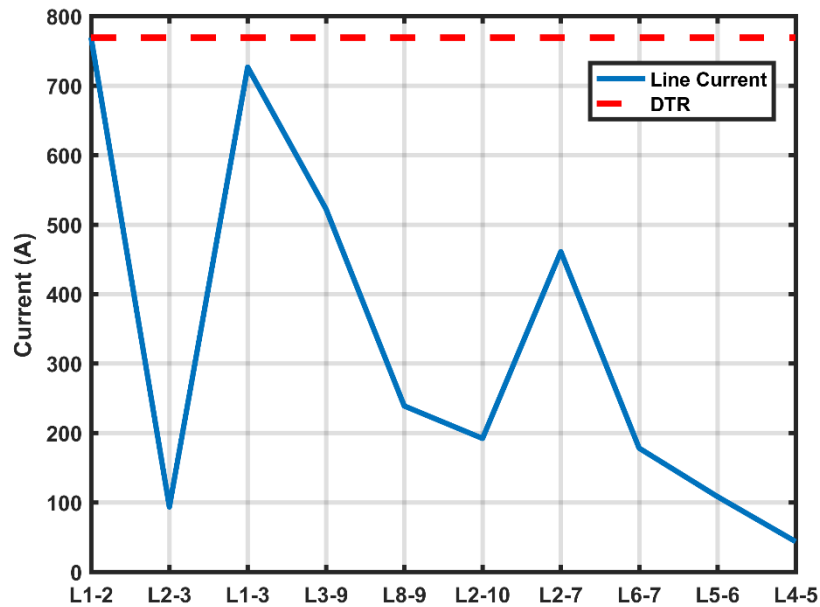
Figure 5.12: Line currents for the worst scenario – 10-bus system (Maximum wind generation, minimum load and minimum DTR)
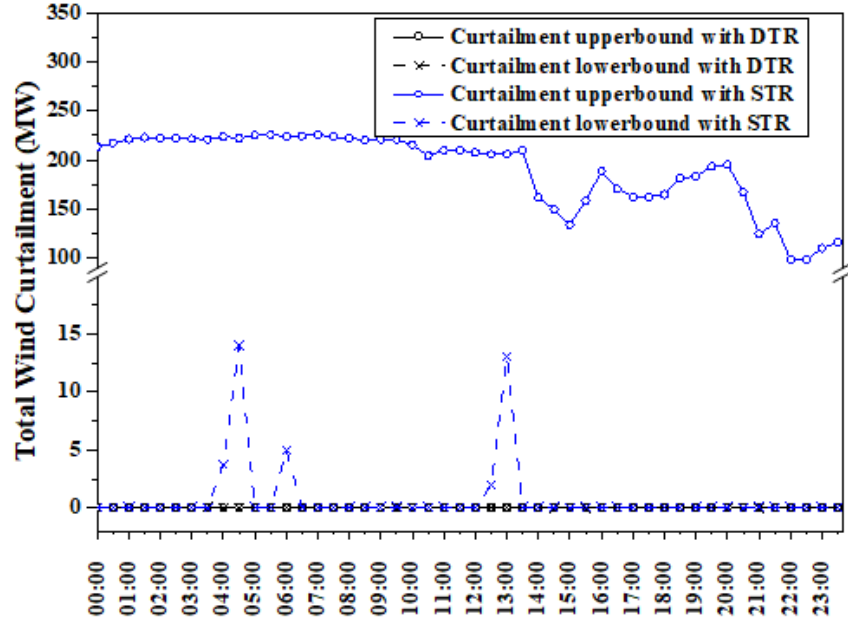
a) winter day
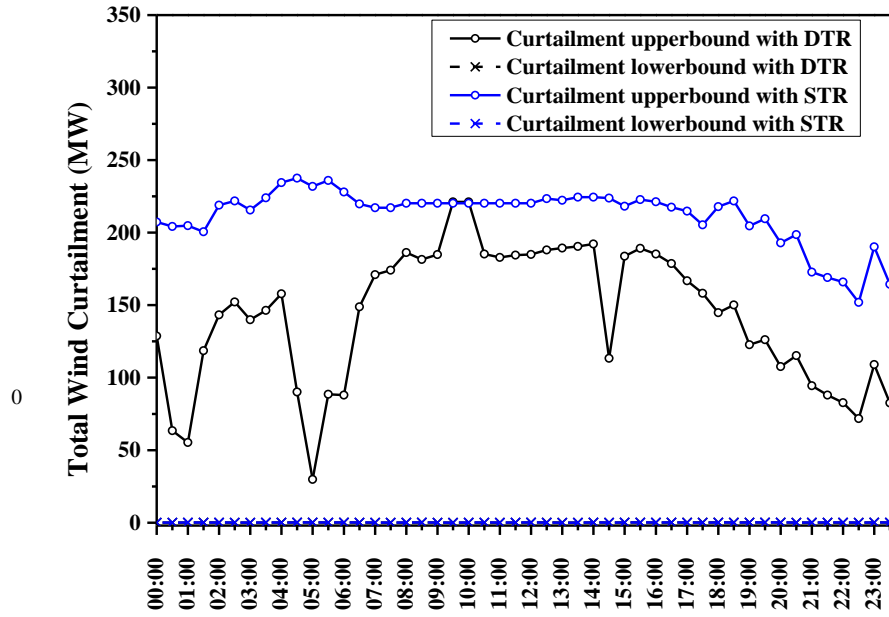
b) summer day

Figure 5.13: Comparison of wind curtailments with STR and AA-OPF DTR limits

To evaluate benefits of applying DTR limits for maximising wind power exported into the grid (and minimising wind curtailment), the AA-based OPF with DTR and STR limits are solved separately, and upper/lower bounds for the estimated total wind curtailments are plotted in Figure 5.13. DTR limits allow exporting much more generated wind power: for a winter day, as there is no curtailment at all (high-wind

and low temperature), while for a summer day, there is some curtailment (medium-wind and high temperature).

Comparison between AA-based OPF and MCS-based P-OPF

A probabilistic MCS-based OPF is then implemented to identify PDFs required for the optimal dispatch solutions in terms of the assessed curtailment risks. In this MCS-based P-OPF, generated power of each WF is sampled according to probabilistic models developed in Section 4.2. MGND are used to represent the uncertainties in wind power outputs at specific wind speeds. At the same time, loads are sampled with normal distributions, where standard deviations are estimated according to 0.95 and 0.05 quantiles in Figure 5.5. For each 30-minute time interval, 10,000 samples are generated for all uncertain variables (eight WF generations and two load demands, as well as wind speeds and wind directions at OHLs) and used as inputs to the OPF solver. 10,000 OPF solutions yield the intervals which are defined by the maximum and minimum values. The increasing of MCS iterations does not change the mean values and standard deviations of solutions significantly.

The daily maximum and minimum wind curtailments determined by MCS-based P-OPF are compared with AA-OPF results in Figure 5.14, confirming that there is no curtailment for a winter day.

a)   winter day
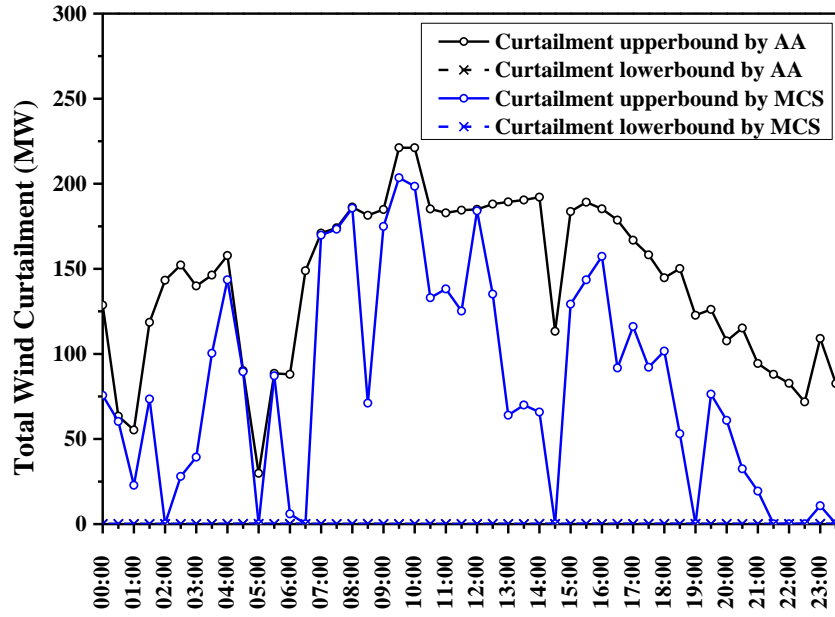
b) summer day

Figure 5.14：Comparison of wind curtailment results with MCS and AA methods

For a summer day, both MCS-OPF and AA-OPF results suggest possible substantial curtailments. But it can be observed the upper bound given by the MCS-based method is lower than that of AA method in most time of the day and the values are approaching zero sometimes. This is because AA-OPF uses the minimum and maximum values from the estimated ranges of variations, which have very low probabilities, resulting in too large ranges of uncertainties and possible inappropriate operational decisions related to wind curtailment strategies.

To evaluate the above point in more detail, six time intervals in which the MCS-based method give close to zero curtailments are selected to show the distributions of P-OPF solutions. Histograms of wind curtailment are plotted together with AA-OPF Min-Max intervals, and AA-OPF intervals obtained when variations of input variables are limited to their 0.05 to 0.95 quantiles uncertainty ranges in Figure 5.15.

a) 02:00

b) 05:00

c) 06:30

d) 14:30

e) 19:00

f) 22:30
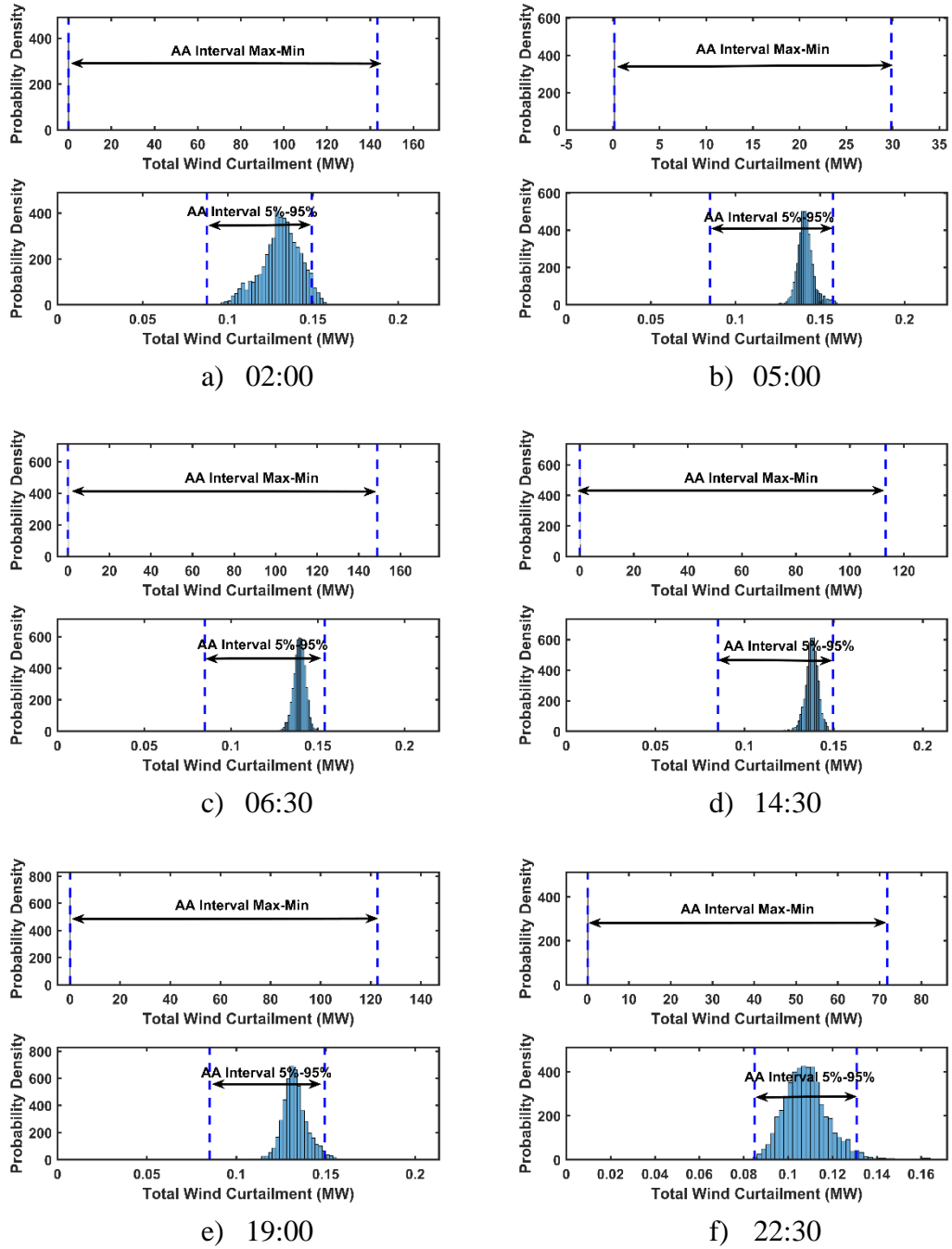
Figure 5.15：Comparison of AA-OPF and P-OPF solutions for wind curtailment

It can be observed that the AA intervals will shrink significantly if the ranges of uncertain inputs are limited to their 0.05 to 0.95 quantiles. For example, at 02:00 and 05:00 hours, AA Min-Max intervals are around [0.010 MW, 143.28 MW] and [0.059MW, 29.854 MW] while 5%-95% AA intervals reduce to [0.0877 MW, 0.1463 MW] and [0.085 MW, 0.1575 MW]. The probability (i.e. risk) that the wind curtailment will fall out of this interval is obtained from the P-OPF distributions and

in both cases is less than 2%. At 19:00 and 22:30 hours, Min-Max AA intervals are [0.085 MW, 126.169 MW] and [0.72 MW, 71.815 MW], while 5%-95% AA intervals reduce to [0.112 MW, 0.152 MW] and [0.106 MW, 0.131MW] with the probability that wind curtailment will fall out of this interval less than 1%.

5.5.3 The 33-bus Network

In the 33-bus network, there are four WTs located at Buses 13, 21, 24 and 29, each with a rated power of 2 MW and operating with unity power factor. The bus voltage level is 12.66 kV. The total peak demand is 3.7 MW and 2.3 Mvar [134][149], which is represented with two different load profiles (Region 1 and Region 2). The system comprises 32 OHLs. Similar to the 10-bus network, the ampacity of L1-2 is the main factor that results in wind curtailment. Bus 1 is connected to the bulk transmission system and the variations in wind generation and demands are balanced by importing or exporting power at Bus 1. The same wind profiles and load profiles presented in Figure 5.6, 5.7 and 5.8 are applied to wind generation, demands and DTR calculation. The loads in Region 1 would follow the load profiles presented in Figure 5.6a and Figure 5.6b, while the loads in Region 2 would follow the load profiles given by Figure 5.6c and Figure 5.6d.
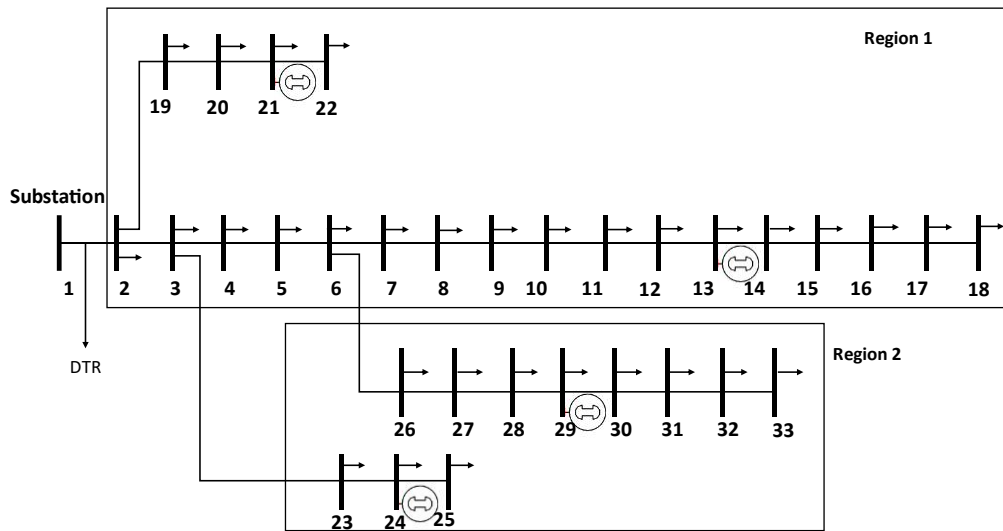
Figure 5.16：Configuration of the 33-bus Network

Comparison between DTR and STR values

In this network, the conductor type of OHLs is "Fox" [136]. The comparison between DTR and STR values for the conductor in the summer day is presented in Figure 5.17. Similar to the 10-bus network, L1-2 in this 33-bus network is also most heavily loaded (30% higher than the second) as shown in Figure 5.18. In this case, DTR is only implemented for Line L1-2 to release the bottleneck, which can increase the dispatched wind power significantly, and for other OHLs, the STR of 200 A is applied. To prevent the violation of STRs, wind curtailment is necessary. The results of the AA method present that there is no wind curtailment in the winter day and the wind curtailments in the summer day with DTR and STR are both plotted in Figure 5.19.
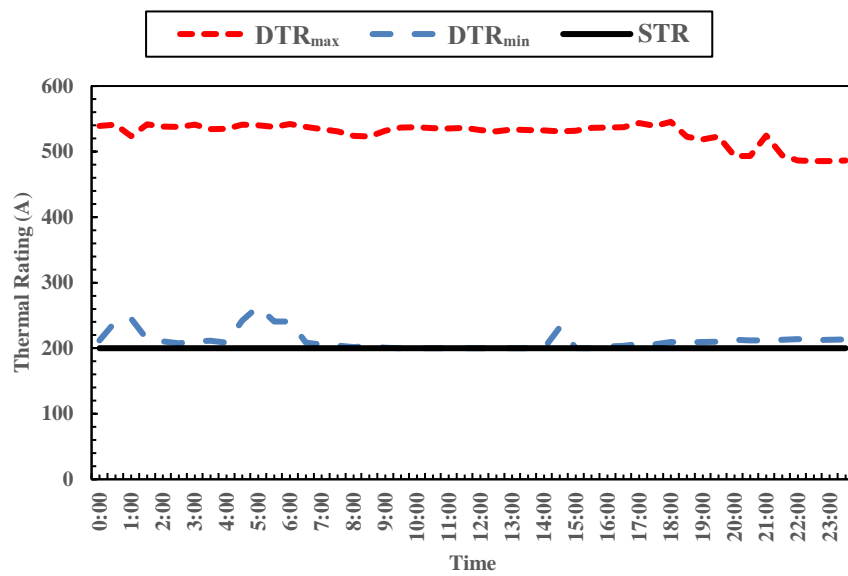
Figure 5.17: Comparison of DTR and STR values for L1-2 in the summer day (IEEE 33-bus test network)
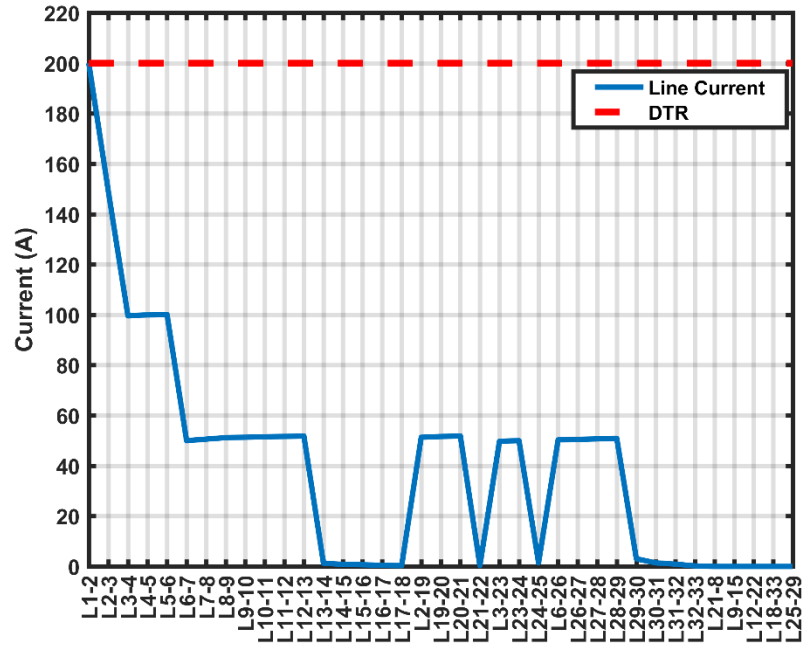
Figure 5.18: Line currents for the worst scenario – 33bus system (Maximum wind generation, minimum load and minimum DTR)
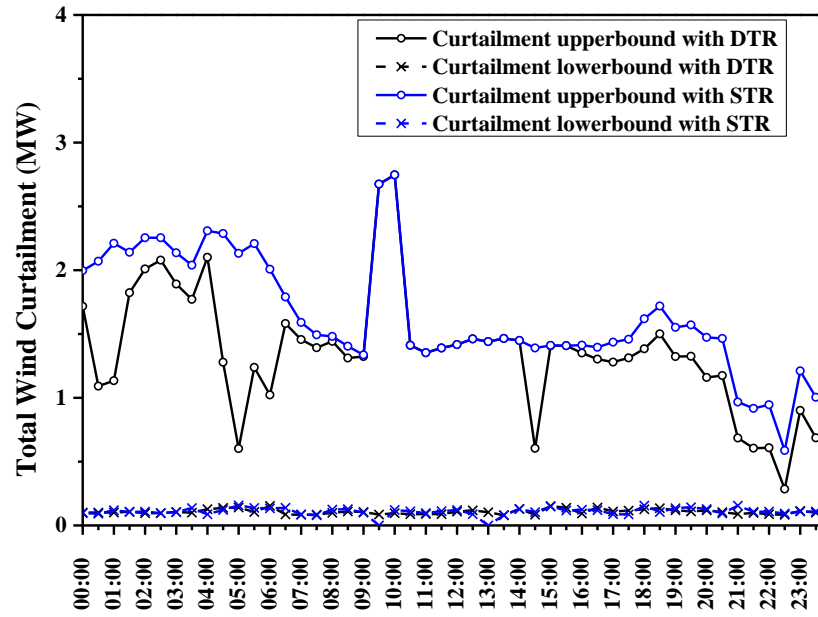
Figure 5.19: Comparison of wind curtailments with STR and AA-OPF DTR limits in the summer day (IEEE 33-bus test network)
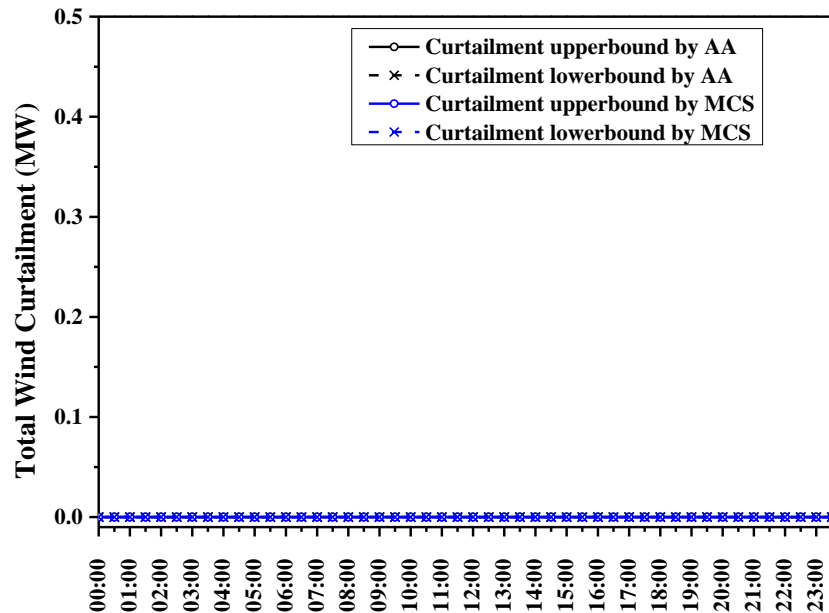
Figure 5.20：Comparison of wind curtailment results with MCS and AA methods in the summer day (IEEE 33-bus test network)

a) 8:30

b) 10:00

c) 10:30

d) 12:00

e) 13:30   f) 15:30
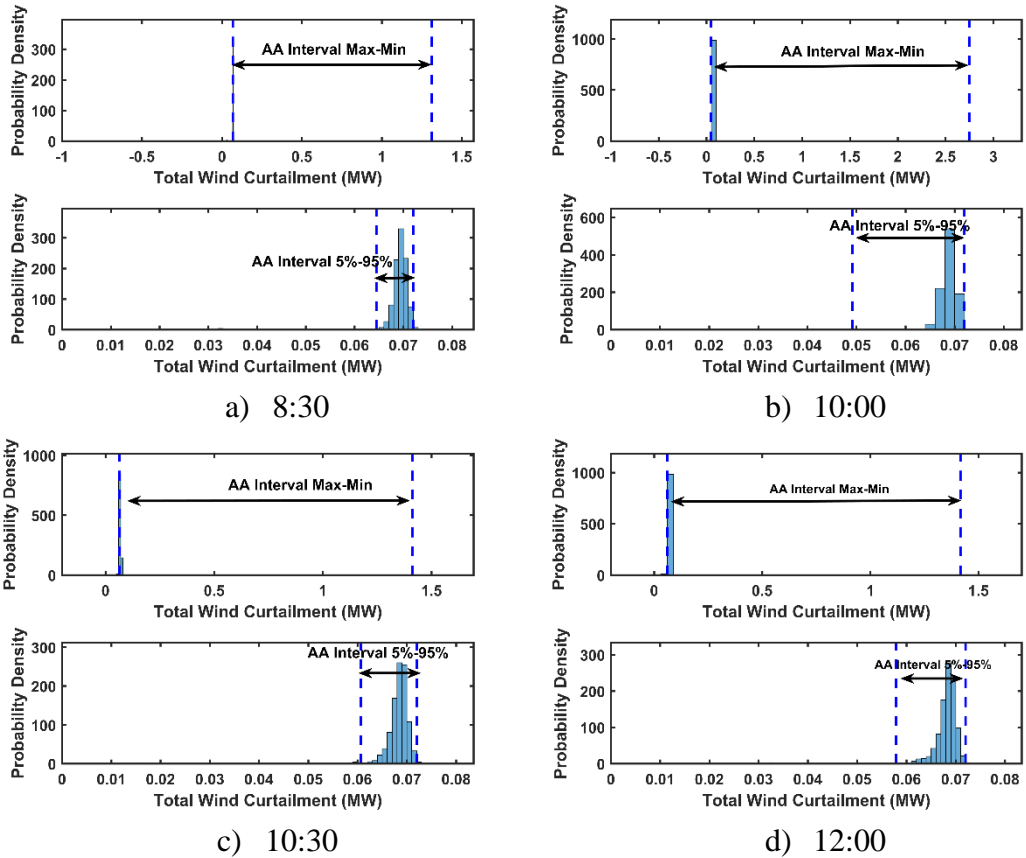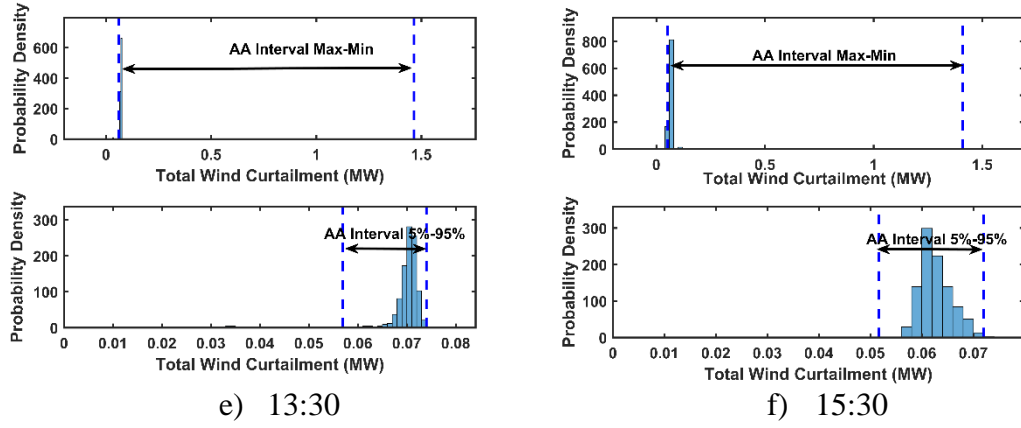
Figure 5.21：Comparison of AA-OPF and P-OPF solutions for wind curtailment in the summer day (IEEE 33-bus test network)

Maximum and minimum daily wind curtailment profiles obtained by AAOPF and MCS-based OPF are plotted in Figure 5.20. No wind curtailment is required on the winter day. However, on the summer day, significant wind curtailment might be implemented for most of the day.

The PDFs of P-OPF solutions for wind curtailment for a summer day are plotted together with AA-OPF Min-Max intervals, and AA-OPF intervals obtained when variations of input variables are limited to their 0.05 to 0.95 quantiles uncertainty ranges in Figure 5.21. At 8:30, the interval obtained by MCS-based method is [0.053 MW, 0.0766 MW] while the interval achieved by AA-OPF is [0.0321 MW, 1.311 MW]. By limiting the variations of input uncertainties into their 5th-95th percentiles, the AA interval will reduce to [0.067MW, 0.072 MW], whose lower bound and upper bound are the 4th percentile and 99th percentile of MCS results. At 10:00, the MCS interval is [0.047 MW, 2.744 MW] and the Min-Max AA interval is [0.008 MW, 2.747 MW]. The 5%-95% AA is [0.050 MW, 0.072 MW] and this interval contains 98.5% of solutions obtained by MCS.

The case studies presented above indicate that AA-based method is capable to find out the solution intervals subject to the input intervals of uncertain variables with less computational time. For the 33-bus system, AA-based method needs 36.07 seconds on average to converge for each 30-minute time interval while the MCS-based method takes over 500 seconds. However, the intervals identified by AA-based method can be too wide compared with those achieved by the MCS method, as they include solutions

related to uncertain events with very low probability. In order to achieve the proper optimal dispatch intervals, a confidence level is set for all input uncertainties, and the input intervals are shrunk to 5th -95th percentile of their original ranges. The AA solution intervals with the 5th -95th percentile ranges are very close to those obtained by MCS-based method.

5.6 Conclusions

An AA-based OPF model with DTR limits was presented for day-ahead planning of networks with high wind penetration. In this model, uncertain information was represented by intervals and affine arithmetic was used to deal with interval inputs. However, case studies showed that the results of AA-based method were too conservative, although it was more computationally efficient compared with the MCS-based method. For the case studies presented in this chapter, reducing the input intervals to the 5th percentile and 95th percentile of uncertain input variables based on their distribution functions can find AA intervals close to the MCS-based method. In the future work, the relationship between the range of input variables and width of output intervals need to be studied so that the approaches to determining proper confidence levels for input variables can be developed. Then the AA solutions can be tuned effectively without the implementation of MCS-based method.

Chapter 6
Congestion Management with Maximum Lead Time

6.1 Introduction

Network congestions occur when the transmission system is unable to accommodate the desired power flows due to the violations of one or more system operating constraints [170]. The management of system operating constraints (e.g. bus voltages and branch thermal limits) is one of the critical tasks took by operators. Due to the increasing demand, deregulated market and growing penetration of RES, modern electricity networks are extensively operated closer to their technical loading and security limits. Consequently, congestion management (CM), which aims to manage constraints (e.g. available loading limits for the post-contingency power flows) and prevent their violation, has become an efficient tool to ensure network security.

Network congestions can be caused by multiple reasons. For instance, the sudden increase of generation or demand may result in overloading conditions on specific transmission lines. Another main reason for network congestions is unexpected contingency events, such as short circuit faults and failures of network components. The management of these network congestions, involving the identification of violated constraints and selection of corrective actions, is denoted as "post-contingency congestion management".

Congestion management can be formulated as a nonlinear constrained optimization problem with the objective to find optimal control solutions that resolve all constraint violations while minimizing the cost of achieving that solution. It should be noted that this CM problem is similar to the OPF problem. The main differences between general OPF formulation and CM problem are the objective functions and the inequality constraints. In general OPF problem, the objective function is more relative to economic aspect, which aims to minimize fuel cost, or emission, or losses, considering normal operating constraints. However, CM formulation focuses on finding a feasible corrective control solution, especially for post-contingency congestion management. Normal operating constraints may result in an infeasible region when the contingency

events are severe, and the optimization problem would be infeasible in this case. To prevent the infeasibility, the normal constraints should be relaxed, and the emergency operating constraints need to be applied. For instance, in pre-contingency conditions, power flow in the network is limited by normal ratings, which can be carried by network facilities continuously without loss of life. While in post-contingency conditions, emergency ratings will be used. Emergency ratings specify the level of power flow that facilities can carry for a specific time to implement corrective actions, during which the loss of life to these facilities is acceptable.

The corrective actions taken into account by post-contingency CM can be classified into two general groups: cost-free methods and non-cost-free methods [170]. The cost-free methods include the modification of network topology, shifts of transformer taps, operation of compensation devices, etc. Those methods are at the disposal of system operators, and the involved economic cost, if any, is very low. The non-cost-free methods consist of generation re-dispatch and load curtailment. The implementation of these methods usually requires considering extra costs.

Post-contingency congestion management is more challenging than congestion management due to several reasons. Firstly, the number of available corrective actions is usually limited, and the exact sequence of multiple control actions is hard to determine. For example, operational requirements for the French EHV networks in [171] specify that, following a contingency, no corrective action can be activated within one minute, and only one corrective action (usually a pre-defined topology change) is available in the following five minutes. Another challenge is that the time available to the network operator to devise and implement appropriate corrective actions ("lead time") may be too short. Consequently, the information on lead time is very useful, as it allows the operators to correctly plan and properly implement the post-contingency corrective actions within the available lead time. For example, the overloading constraints or voltage limit violations can be remediated in time, before protection system trips additional components, and potential cascade failures can be prevented. In the worst case, if load shedding is inevitable, the amount of available load to be shed and their locations are also determined by the available lead time. Therefore, including lead time constraints into congestion management procedures is

especially important during severe contingency events. However, the integration of lead time constraints into the CM model was considered in very few previous references. An optimization model is proposed in [172] for CM with dynamic line ratings, while an optimal real-time CM algorithm was proposed in [173], [174]. A security-constrained OPF model (SCOPF) to compute optimal controls for maximizing congestion clearing times is developed in [12], [18], with suitable penalties applied and solved by PSO method.

The maximum operating temperature is a critical factor to guarantee the secure operation of both transmission lines and transformers. In the normal operating state, the line loadings are restricted by the thermal ratings with respect to the maximum operating temperatures under given ambient conditions. Following a severe contingency event, e.g., the simultaneous occurrence of two faults in an N-1 secure system, it is likely that several lines and transformers will be overloaded. Considering the thermal inertia of overloaded components, there would be a specific time interval before the overloading components reach its maximum operating temperature. This time interval, which depends on both pre- and post-contingency component loading conditions, is viewed as the lead time for system operators to manage the corresponding congestions, generally determined as the shortest time to reach the maximum temperature among all overloaded components.

In this chapter, a multi-stage optimization model is built up to identify the correct actions for post-contingency congestion management, taking into account maximum lead time. At the first stage, optimal settings of volt-var controls, such as OLTC transformers and shunt capacitors are selected, taking into account voltage-dependent load models. The second stage provides optimal generation re-dispatch, supported by fast-start generators. At the third and ultimate stage, optimal load shedding is implemented to clear all remaining constraint violations. The OPF problem is solved by a hybrid metaheuristics method and illustrated on a modified IEEE 14-bus network (Not the same as that in Chapter 4). Obtained results demonstrate that all violated constraints can be efficiently resolved within the MLT available to network operators.

6.2 Dynamic thermal ratings and maximum lead time calculation

Loading limits of overhead lines and transformers are important physical constraints that have to be considered in power system analysis. Violating the loading limit of an overhead line will result in excessively high temperature which may cause the elongation and sagging of the conductor, i.e. reduced safety clearance distances, as well as conductor annealing. Similarly, overloading of a transformer can cause an increase in its operation temperature, which has a significant impact on the ageing of transformers. Consequently, in order to prevent potential damages and safety hazards resulted from overheating conditions, both overhead line conductors and transformers should operate with the loading conditions that will prevent thermal overloading.

As presented in Section 3.2, the thermal balance equation (3.1) describes the relationship between the current carried by a conductor, I, and the conductor's surface temperature, T_c. The relationship between the steady-state conductor temperature and its current is illustrated in Figure 6.1 with the standard ACSR conductor, "Sparrow 6/1" from [136]. The wind speed and the wind attacking angle are assumed to be 0.5 m/s and 90 degrees. For ACSR, a default temperature of 75 °C is used to determine normal rating (NR) and this temperature was used as the maximum design temperature by several power companies for their transmission lines. The long-term emergency rating (LTER) is calculated with 90 °C, which is the maximum continuous operating temperature. The temperature of the conductor to specify the short-term emergency rating (STER) is defined with 100 °C [175]. The currents corresponding to the three steady-state conductor temperatures are also labelled in Figure 6.1.
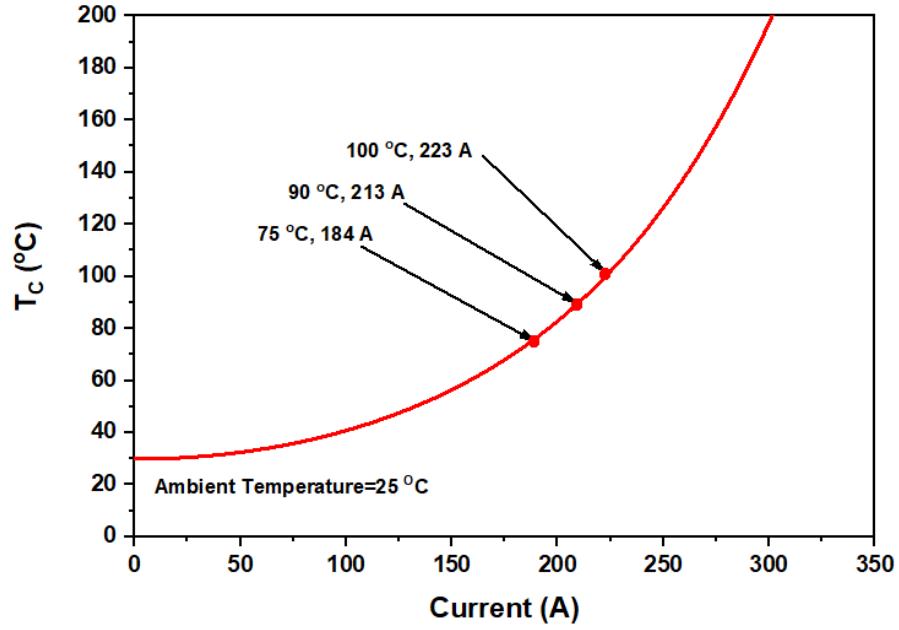
Figure 6.1：Conductor surface temperature T_c as a function of its current for specific fixed ambient conditions

Emergency ratings are determined with both limiting temperature and fault duration. LTER is the rating with the fault duration measured in hours, while STER is the rating for the conductor to operate safely within a shorter fault duration times measured in minutes (5~15 minutes) [175]. Considering the thermal time constant of the overhead line conductor, the calculation of LTER can be based on the steady-state thermal balance equation (the transient term $\frac{dT_c}{dt} = 0$), while the STER should be considered taking into account the transient thermal characteristics of the conductor.

When a contingency event occurs, if the post-contingency current is higher than the pre-contingency current, the conductor temperature will start to increase according to (3.1), based on the pre-contingency current/temperature and the ambient conditions, as plotted in Figure 6.2. Upon reaching the maximum allowable operating temperature, thermal protection will be activated. The protection equipment in modern power system is designed based on the emergency ratings with specific fault durations. The overloading conditions caused by post-contingency currents have to be corrected within the specific durations, so as to prevent the overheating of conductors; otherwise, the overloaded lines will be tripped. In the proposed congestion management algorithm, the maximum allowed overloading time (OVT) for a conductor is defined with the following criteria:

130

1) If the final steady-state conductor temperature with the post-contingency current is between 75 °C and 90°C, i.e. the post-contingency current violates NR but it is still lower than LTER, the OHL will be allowed to operate for no longer than 30 minutes. It should be noted that although the protection system may tolerate this current for up to several hours, it is assumed that system operators will aim to recover the system to the normal operating state as soon as possible, typically within 30 minutes, so the OVT in this condition is given as 30 minutes, rather than several hours.

2) If the final steady-state conductor temperature with the post-contingency current is between 90 °C and 100 °C, i.e. the post-contingency current is between LTER and STER, the OHL will be allowed to operate for no longer than 5 minutes. The duration of 5 minutes is selected because STER is commonly given with the allowed duration of overloading conditions between 5~15 minutes.

3) If the final steady-state conductor temperature with the post-contingency current is higher than 100 °C, which is generally the maximum allowable temperature of the ACSR, the OVT is defined as the time for which the conductor temperature will reach 100 °C.

The OVT for a conductor is calculated as:

$$OVT = \begin{cases} \infty & T_{cf} \leq 75°C \\ t_{NR} + 1800 & 75°C < T_{cf} \leq 90°C \\ t_{LTER} + 300 & 90°C < T_{cf} \leq 100°C \\ t_{STER} & T_{cf} \geq 100°C \end{cases} \qquad (6.2)$$

where t_{NR}, t_{LTER} and t_{STER} are the time intervals that conductor temperature takes to reach 75°C, 90°C and 100°C after contingencies occur, T_{cf} is conductor temperature many time constants after the step-change of loading conditions.

Figure 6.2 illustrates OVT calculation based on the maximum allowable conductor temperature of 100° C and pre-contingency temperature of 40° C (corresponding to a pre-contingency current of I_0=100 A). The ambient temperature is 25 C, and the wind speed and wind attacking angle are 0.5 m/s and 90 degrees. Figure 6.2a shows the

131

variation of OHL conductor temperature with a contingency event occurs at 1500sec. It is assumed that the system will reach a viable steady-state after the contingency event. The post-contingency current is 250A. Figure 6.2b presents the transient temperature variation between 1440s and 1800 s. The time intervals that the conductor temperature takes to reach the thermal limits are labelled. It can be observed that the thermal protection will react when the conductor temperature reaches 100° C, giving OVT value of 207s, about 3.5min. Figure 6.3 plots the relationship between OVT and pre- and post-contingency currents.
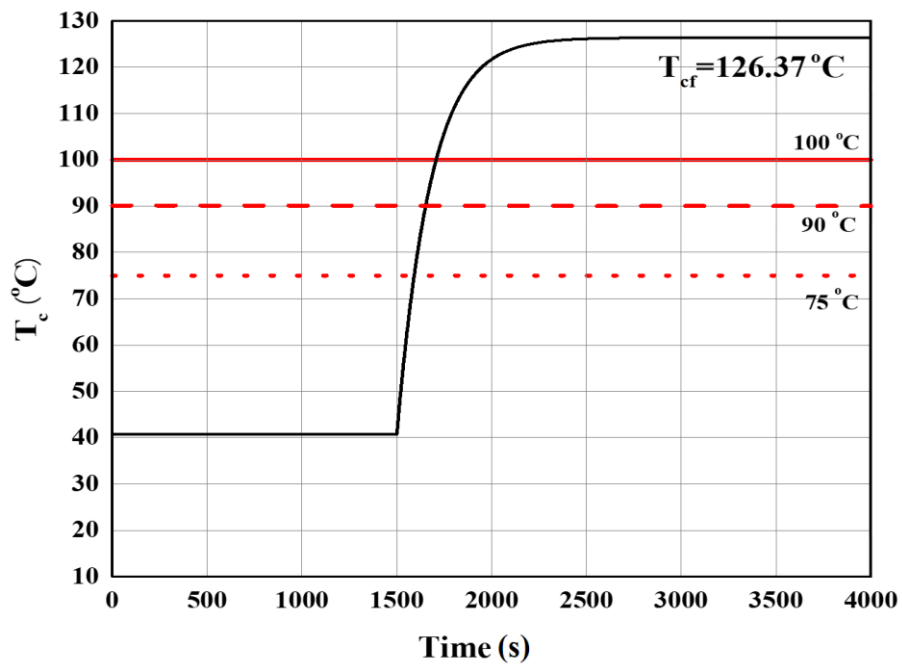
a) Variation of conductor temperature
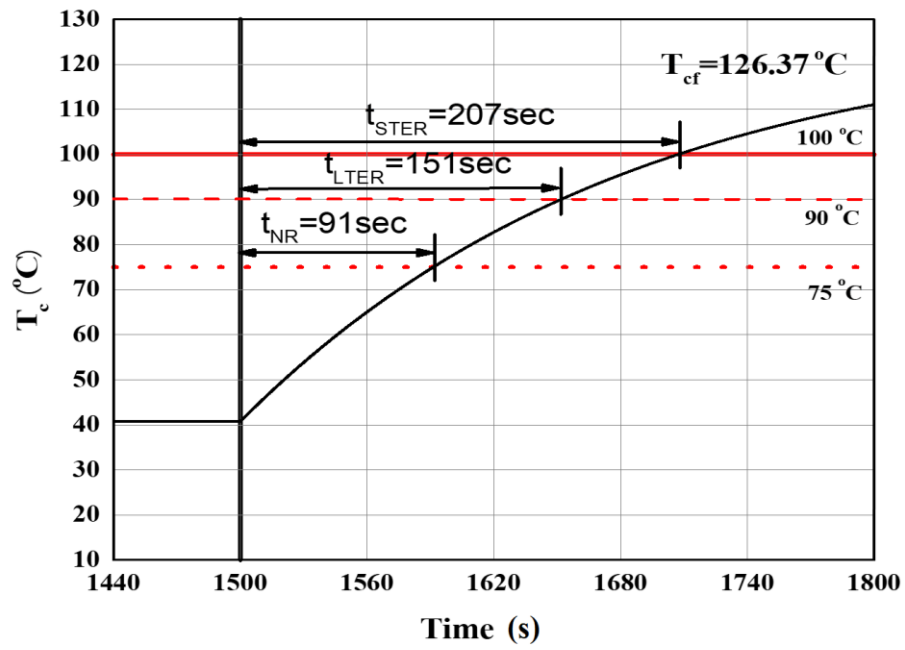
b) Transient temperature variation between 1440 sec and 1800 sec

Figure 6.2: Illustration of OVT calculation
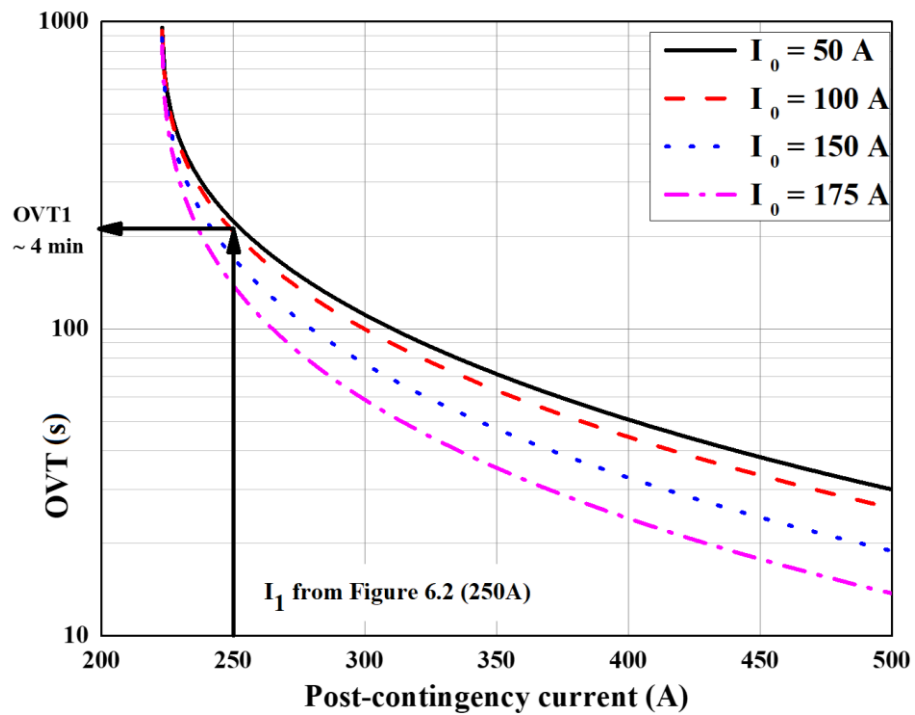
Figure 6.3: OVT variation with post-contingency current

The OVT calculation for the transformer is similar to the calculation of OHL. The NR, LTER and STER are defined with respect to 120°C, 130°C and 160°C for transformer winding hottest-spot temperature (HST) [24]. When the final steady-state HST is between 120°C and 130°C, the transformer is allowed to operate for 4 hours. If the

temperature is between 130°C and 160°C, the time is 30 minutes. The OVTs for PTs are defined as:

$$OVT = \begin{cases} \infty & T_{Hf} \leq 120°C \\ t_{NR} + 3600 * 4 & 120°C < T_{Hf} \leq 130°C \\ t_{LTER} + 1800 & 130°C < T_{Hf} \leq 160°C \\ t_{STER} & T_{Hf} > 130°C \end{cases} \quad (6.3)$$

The description of transformer thermal model used to calculate transformer OVT is provided by Chapter 3.

As the tripping of any overloaded line will only worsen the post-contingency operating conditions, the minimum OVT of all overloaded components represents the time available for devising appropriate corrective actions by network operators, denoted as maximum lead time (MLT). After the first corrective action is taken, loading of the network components is again calculated and minimum OVT of all remaining overloaded components is the next MLT, and so on until there is no overloading.

6.3 Proposed post-contingency congestion management (CM) method

6.3.1 Proposed post-contingency CM algorithm

A multi-stage optimization model is proposed to find the optimal corrective actions. At the first stage, the optimization model aims to maximize MLT by finding the optimal settings of fast response control actions, including generator automatic voltage regulators, transformer tap ratios and reactive power compensators, which are denoted as "volt-var controls". These control actions are at the disposal of system operators and cost-free. At the second stage, the optimization problem is solved to find the amount of generation re-dispatch and connection of reserve generation to manage the congestions. The ramping up/down rates of connected generators, as well as the times required for connecting fast-start generators, are considered. If the generation re-dispatch is not enough for congestion management, load shedding is inevitable. At the third and ultimate stage, optimal load shedding is implemented to resolve any remaining constraint violations.

In this algorithm, the time required to implement corrective actions has been considered. For example, it is assumed that volt/var control actions need 10 seconds to activate, while the generation re-dispatch is implement minute by minute. These values may vary in practical situations and are used here only as indicative values, without affecting the implementation of the proposed methodology. The branch flows and bus voltages are assumed to be constant during the time required to implement corrective actions. Furthermore, the corrective actions will cause a step-change in branch flows once they are activated. These time intervals are considered to estimate real-time temperatures of branches, and the algorithm will try to prevent the temperature rise that will result in violating maximum allowable operating temperatures during the CM process.

If the corrective actions are efficient, the network security can be improved by relieving overloading conditions or reducing the number of voltage limit violations, and the MLT is expected to be prolonged after each corrective actions until all post-contingency constraints are removed. However, the corrective actions may not always be available in the same order. For example, when the volt-var control or generation re-dispatch cannot relieve overloading conditions, the CM algorithm will decide whether to wait until the reserve provided by fast-start generators is available to be dispatched or to immediately implement load shedding based on the MLT.

6.3.2 Formulation of post-contingency CM

For each stage, the optimization problem is formulated as:

$$\min f(x_0, x_c, u_0, u_c)$$

$$s.t. \quad G(x_0, x_c, u_0, u_c) = 0 \tag{6.4}$$

$$H(x_0, x_c, u_0, u_c) \leq 0, c \in C = \{0,1,2,\dots N_c\}$$

where x, u are state and control variables, c is contingency index (zero for base case), C is the set of considered contingencies, $f(\cdot)$ represents the objective function, $G(\cdot)$ and $H(\cdot)$ are the equality and inequality constraints. Specifically, the equality constraints consist of AC power flow equations, while the inequality constraints are network secure operating limits.

Stage 1 –Optimal volt/var control

At the first stage, the objective function is computed to maximize the maximum lead time for system operators:

$$\min f_T = \frac{A}{MLT} \tag{6.5}$$

where A is a positive constant which is used to transfer the maximization of MLT to a minimum problem, and MLT is the maximum lead time (in seconds) calculated with specific corrective actions.

Equality constraints consist of nodal balance equations and AC power flow equations presented by (2.27) and (2.28) in Chapter 2. The inequality constraints represent network operating limits such as voltage limits and generator reactive power outputs are shown as (2.30). Apart from those, limits on shunt capacitor banks and OLTC tap positions should also be included:

$$b_i^{min} \leq b_i' \leq b_i^{max}, \forall i \in N_{shunt} \tag{6.6}$$

$$t_{ij}^{min} \leq t_{ij} \leq t_{ij}^{max}, \forall (l,i,j) \in \mathcal{L}_{\mathrm{T}} \tag{6.7}$$

where b_i' is the shunt capacitor at Bus i, t_{ij} represents the tap ratio of the transformer (l,i,j), N_{shunt} is the set of shunt capacitor indices and $\mathcal{L}_{\mathrm{T}}$ is the set of transformer indices.

The volt-var control can eliminate the voltage violations and the power flow will be changed at the same time. So the overload conditions may also be relieved. In the optimization problem, discrete variables, including OLTC positions and capacitor bank settings, are assumed to be continuous.

Most of the electrical loads exhibit voltage-dependent changes in power demands. Considering the significant impacts of volt-var control on the load, the voltage-dependent load models are applied in the optimization problem. The well-known ZIP model is adopted for each load. The active power and reactive power for a load i at given voltage magnitude V_i are shown as (6.8) and (6.9):

$$P_{di} = P_{di}^0 \left[Z_i^P \left(\frac{V_i}{V_{0i}} \right)^2 + I_i^P \left(\frac{V_i}{V_{0i}} \right) + P_i^P \right] \forall i \in \mathcal{N}_{PQ} \qquad (6.8)$$

$$Q_{di} = Q_{di}^0 \left[Z_i^Q \left(\frac{V_i}{V_{0i}} \right)^2 + I_i^Q \left(\frac{V_i}{V_{0i}} \right) + P_i^Q \right] \forall i \in \mathcal{N}_{PQ} \qquad (6.9)$$

where P_{di}^0 and Q_{di}^0 represent the active and reactive power at the nominal voltage magnitude V_{0i}, respectively. The general ZIP model consists of constant impedance Z_i^P and Z_i^Q, constant current I_i^P and I_i^Q, and constant power P_i^P and P_i^Q terms.

Stage 2 – Optimal generation re-dispatch

In the second stage, optimal generation re-dispatch is implemented to relieve congestions. The tap ratios and reactive power compensators are fixed at the optimal settings given by the first-stage evaluation. At this stage, the primary objective is also to maximize maximum lead time, which is the same as at the first stage. The nodal balance equations, including generation re-dispatch, are given as (6.10) and (6.11).

$$P_{gi0} + \Delta P_{gi} - P_{di} - g_i'|V_i|^2 = \sum_{(l,i,j)\in\mathcal{L}_i} P_{lij} + \sum_{(l,j,i)\in\mathcal{L}_i^R} P_{lji}, \forall i \in \mathcal{N} \qquad (6.10)$$

$$Q_{gi0} + \Delta Q_{gi} - Q_{di} - b_i'|V_i|^2 = \sum_{(l,i,j)\in\mathcal{L}_i} Q_{lij} + \sum_{(l,j,i)\in\mathcal{L}_i^R} Q_{lji}, \forall i \in \mathcal{N} \qquad (6.11)$$

where P_{gi0} and Q_{gi0} are the initial values of active and reactive power outputs from the generator at bus i, ΔP_{gi} and ΔQ_{gi} are the variations of generator outputs due to generation re-dispatch. The power flow on branches should be constrained by MVA limits:

$$\left(P_{lij} \right)^2 + \left(Q_{lij} \right)^2 \leq (S_l^{max})^2, \left(P_{lji} \right)^2 + \left(Q_{lji} \right)^2 \leq (S_l^{max})^2, \forall (l, i, j) \in \mathcal{L} \qquad (6.12)$$

where S_l^{max} is the MVA limit on branch l, which can be either STR determined with assumed ambient conditions given by standards or engineering recommendations such as [132], or DTR calculated with real-time ambient conditions. For both STR and DTR, the thermal limit here is 75 °C (Normal rating).

Constraints on generation-re-dispatch and generator power outputs are given as (6.13) - (6.15).

$$-Ramp_{DOWN}^i * MLT \leq \Delta P_{gi} \leq Ramp_{UP}^i * MLT, i \in \mathcal{G} \qquad (6.13)$$

$$P_{gi}^{min} \leq P_{goi} + \Delta P_{gi} \leq P_{gi}^{max}, i \in \mathcal{G} \qquad (6.14)$$

$$Q_{gi}^{min} \leq Q_{goi} + \Delta Q_{gi} \leq Q_{gi}^{max}, i \in \mathcal{G} \qquad (6.15)$$

where ΔP_{gi} represents the amount of generation re-dispatch for generator i and $Ramp_{DOWN}^i$ and $Ramp_{UP}^i$ are the ramp-down and ramp-up rates. At the beginning of the second stage, the MLT in (6.13) is determined by the power flow when the volt-var control is finished. The available amount of generation re-dispatch is determined according to the MLT and ramp rates shown as (6.13). Meanwhile, the allowed generation active and reactive power outputs are represented by (6.14) and (6.15).

Stage 3 –Optimal load shedding

If the generation re-dispatch results provided by the second-stage optimization problem is not able to manage the congestions, load shedding, as the "last resort" corrective action, is inevitable. The target buses to implement load shedding are selected based on their sensitivities to affect power flows in the overloading branches and bus voltages at the undervoltage/overvoltage buses. Two sensitivity factors, PISF and QVSF, are calculated as (6.16) and (6.17). The buses that have the highest absolute PISF and QVSF values with respect to critically overloaded branches and OV/UV buses are selected as target buses.

$$PISF_l^i = \frac{\partial S_l}{\partial P_i} = \frac{\Delta S_l}{\Delta P_i} \ \forall i \in \mathcal{N} \ and \ \forall (l, i, j) \in \mathcal{L} \qquad (6.16)$$

$$QVSF_l^i = \frac{\partial V_i}{\partial Q_j} = \frac{\Delta V_i}{\Delta Q_j} \ \forall i, j \in \mathcal{N} \qquad (6.17)$$

where $\mathcal{N}$ is the set of bus indices and $\mathcal{L}$ is the set of branch indices, ΔP_i is the variation in active power injection at bus i, ΔS_l represents the variation in apparent power flow on branch l due to ΔP_i, ΔV_i is the variation in bus voltage at bus i and ΔQ_j is the variation in reactive power injection at bus j.

At this stage, the optimization model is solved to provide a solution to manage congestions by optimal load shedding at target buses.

$$\min\left(\sum_{i=1}^{\mathcal{G}} C_{redispatch}\left(\Delta P_{gi}\right) + \sum_{j=1}^{N_{target}} C_{loadshedding}\left(P_{LS_j}\right)\right) \quad (6.18)$$

where N_{target} is the set of the target bus indices and P_{LS_j} is the amount of load shedding at bus j. $C_{redispatch}(\cdot)$ and $C_{loadshedding}(\cdot)$ are the cost functions for generation re-dispatch and load shedding. To balance the reduced load, coordinate control of generation should also be implemented, so the cost of generation re-dispatch is also included in the objective function to find the economic generation re-dispatch. As the generation fuel cost at P_{gio} is given by $aP_{gio}^2 + bP_{gio} + c$, the re-dispatch cost from P_{gio} with the amount of ΔP_{gi} is calculated by $(2aP_{gio} + b)|\Delta P_{gi}|$. In order to reduce the amount of load shedding, it is assumed that the cost rate of load shedding is the same as the maximum cost rate of generation redispatch:

$$C_{loadshedding}\left(P_{LS_j}\right) = \max_{i \in \mathcal{G}}(2aP_{gio} + b) * P_{LS_j} \quad (6.19)$$

The amount of load shedding is limited by:

$$0 \leq P_{LSi} \leq P_{di}^0 - P_{di}^{min}, \forall i \in N_{target} \quad (6.20)$$

where P_{di}^0 is the load at bus i at the nominal voltage and P_{di}^{min} is the minimum load to supply at bus i. The amount of load which is actually supplied, denoted as P_{dsi} and Q_{dsi}, are given by:

$$P_{dsi} = (P_{di}^0 - P_{LSi})\left[Z_i^P \left(\frac{V_i}{V_{0i}}\right)^2 + I_i^P \left(\frac{V_i}{V_{0i}}\right) + P_i^P\right] \forall i \in N_{target} \quad (6.21)$$

$$Q_{dsi} = (Q_{di}^0 - P_{LSi}\tan\phi_i)\left[Z_i^P \left(\frac{V_i}{V_{0i}}\right)^2 + I_i^P \left(\frac{V_i}{V_{0i}}\right) + P_i^P\right] \forall i \in N_{target} \quad (6.22)$$

where ϕ_i is the power factor angle of the load at bus i.

The nodal balance equations at the target buses to implement load shedding are presented as:

$$P_{gi0} + \Delta P_{gi} - P_{dsi} - g_i'|V_i|^2 = \sum_{(l,i,j)\in\mathcal{L}_i} P_{lij} + \sum_{(l,j,i)\in\mathcal{L}_i^R} P_{lji}, \forall i \in \mathcal{N} \qquad (6.23)$$

$$Q_{gi0} + \Delta Q_{gi} - Q_{dsi} + b_i'|V_i|^2 = \sum_{(l,i,j)\in\mathcal{L}_i} Q_{lij} + \sum_{(l,j,i)\in\mathcal{L}_i^R} Q_{lij}, \forall i \in \mathcal{N} \qquad (6.24)$$

Apart from the above equality constraints, the operating limits (2.30) and (6.13) – (6.15) should also be satisfied.

The flowchart of the proposed post-contingency CM algorithm has been shown in Figure 6.4. Once the contingency events occur, the post-contingency branch power flows and operating temperatures, bus voltages, as well as ambient conditions are obtained from the monitor system, and the number of security constraint violations are calculated. If any congestions or voltage limit violations caused by the contingency event have been identified, this algorithm will be used to identify the optimal actions for post-contingency CM. The optimal volt-var control will be given by the algorithm. If the optimal volt-var control actions are able to relieve the congestions, i.e. MLT is extended or number of constraint violations are reduced, system operators will implement these actions which take 10 seconds. Otherwise, the algorithm will go to stage 2 without the implementation of volt-var controls. At the beginning of the second stage, the MLT is evaluated. If the MLT is larger than 60 seconds, the algorithm starts to calculate and implement the optimal generation re-dispatch minute by minute. Otherwise, the algorithm will go to stage 3 directly as the generation re-dispatch could hardly manage loading conditions due to two reasons: 1) MLT < 60 seconds means that the contingency event is severe, 2) the ranges for generation re-dispatch are too small due to the ramp-up and ramp-down rates.
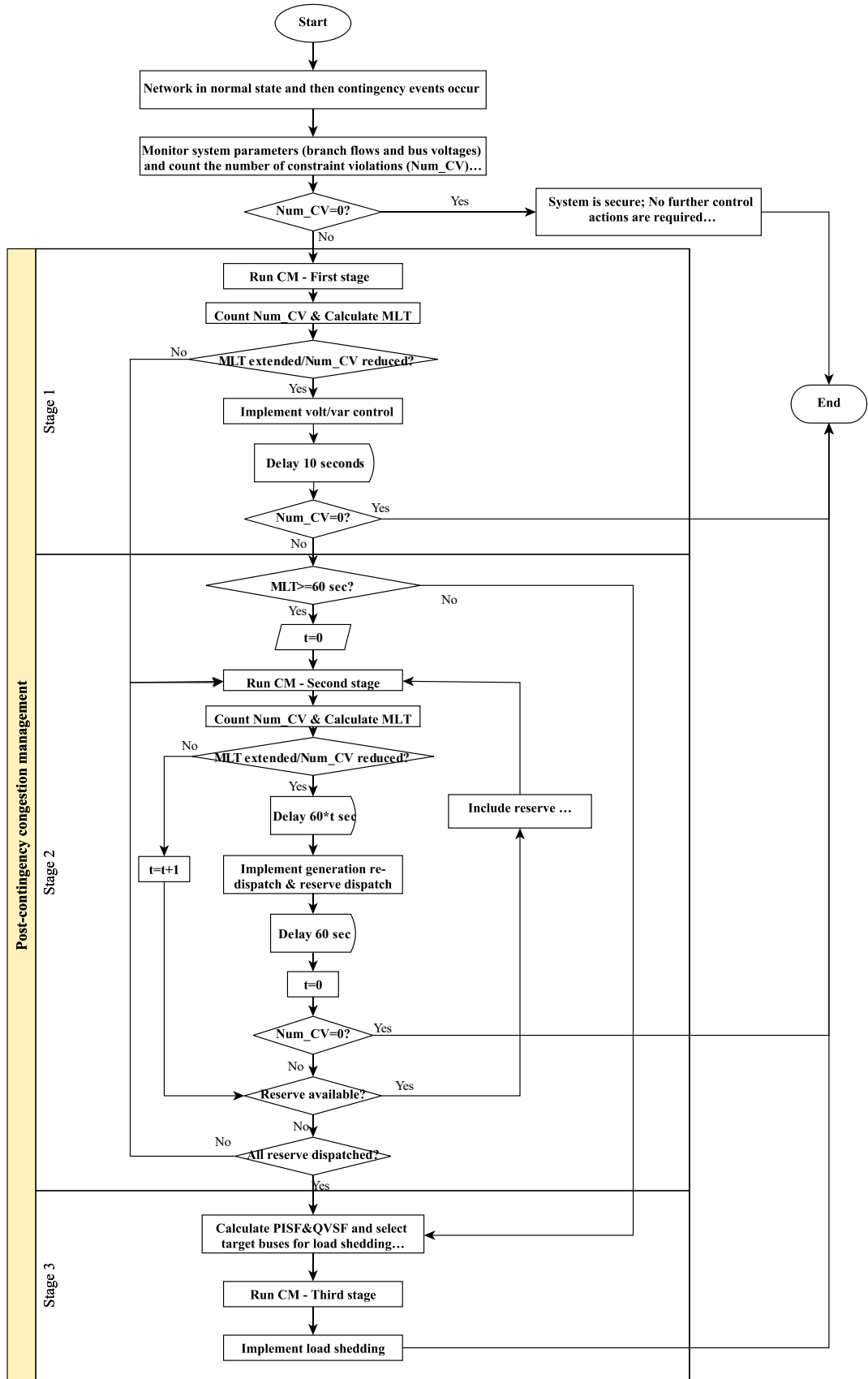
Figure 6.4: Post-contingency CM algorithm

6.3.3 Solution method - Canonical Differential Evolutionary Particle Swarm Optimization (C-DEEPSO)

The proposed optimization model is solved by Canonical differential evolutionary particle swarm optimization (C-DEEPSO), which is a hybrid metaheuristic approach that combines particle swarm optimization (PSO) with evolutionary computation and differential evolution (DE) [176].

This algorithm improves the overall fitness iteratively through repeated mutation, recombination and selection over a population of solutions to generate new solutions until the final stopping criteria is satisfied. Generation of new candidate solutions in C-DEEPSO is based on successive recombination operations applied on current and past solutions. The recombination is given by (6.25) and (6.26):

$$V_t = \omega_I^* \times V_{t-1} + \omega_A^* \times (X_{st} - X_{t-1}) + \omega_c^* \times C \times (X_{gb}^* - X_{t-1}) \qquad (6.25)$$

$$X_t = X_{t-1} + V_t \qquad (6.26)$$

where t is the index of generation, X_t and X_{t-1} represents the solution in the current generation and last generation, X_{st} is an individual generated by a specific strategy by the DE algorithm and X_{gb} is the best solution found so far, ω_I, ω_A and ω_C are weights on the inertia, memory and communication in C-DEEPSO while $*$ indicates that the parameter is subject to the mutation process, C is a diagonal matrix of random variables sampled at each iteration which follows a Bernoulli distribution with success probability P, V is the velocity of solutions.

The strategy used to generate X_{st} is denoted as *current-to-best*, which can be expressed by:

$$X_{st} = X_r + F(X_{best} - X_r) + F(X_{r1} - X_{r2}) \qquad (6.27)$$

where X_r denotes an individual different from X_{t-1} that can be generated by specific sample rules, X_{r1} and X_{r2} are randomly sampled solutions, F is a number that belongs to the interval [0, 2], aiming to control the amplification of differential variation, X_{best} is the best solution that ever found by this individual.

The sample rules for X_r have five options:

1) S_g: sampled from all individuals in the current generation;

2) P_b: sampled from a Memory B of the best individual found so far:

3) $S_g - rnd$: sampled as uniform recombination from the individuals of the current generation;

4) $P_b - rnd$: sampled as uniform recombination within Memory B;

5) $SgPb - rnd$: sampled as uniform recombination of the individuals from the current generation and Memory B.

The mutation rule of the weight factors for an individual solution is given by:

$$\omega^* = \omega + \tau \times N(0,1) \tag{6.28}$$

where τ is the mutation rate set by users and $N(0,1)$ represents the random number which follows the standard normal distribution. The values of weight factors should be within the range of $[0,1]$.

To prevent the population from being trapped around local optima, the attracting position X_{gb} for each candidate solution also need to mutate slightly. The mutation rule is given by:

$$X_{gb}^* = X_{gb}[1 + \tau \times N(0,1)] \tag{6.29}$$

The pseudo-code for C-DEEPSO is given as follows in which $MaxGen$ is the maximum number of generations, NP is the population size, MB is memory B size, P is communication probability rate [176]. The stopping criteria are: 1) the algorithm will stop when the number of generations is larger than $MaxGen$; 2) The fitness of the best candidate solution does not change within the past 100 generations.

Algorithm: Pseudo-code of C-DEEPSO

```
Begin
    INITIALIZE MaxGen, NP, MB, P and τ
    EVALUATE NP
    UPDATE X_gb and MB
    while (stopping criterion is not satisfied) {
        for (all individuals in the population) {
            COMPUTE X_r using S_gP_b − rnd
            COPY X_t
            MUTATE weights
            COMPUTE velocity and UPDATE X_t
            EVALUATE X_t and its copy
            SELECT X_best to be part of the new NP
        }
        UPDATE X_gb and MB
    }
end
```

The test presented in [176] shows that this algorithm has an efficient and competitive performance in solving large-scale OPF problems. The standard PSO algorithm is not able to find feasible solutions to this CM model based on the author's experience.

6.4 Numerical results

A modified IEEE 14-bus network in Figure 6.5 is used to demonstrate the multi-stage CM model. The network configuration, as well as the related parameters, are taken from [177] and [178]. The fuel cost functions for generators are represented by (2.31) and fuel cost coefficients are presented in Table 6.1. The values for these coefficients are obtained from [178]. The total on-line generation capacity is 390 MW and -40 Mvar to 105 Mvar. The ramp-up and ramp-down rates for each generator are 20% of the total capacity per minute. The total demand at nominal voltage is 259 MW and 73.5 Mvar. Two fast start-up generators (each rated 24.5 MW) are located at Bus 9 and Bus 13 as the reserve, with post-contingency response times of 5 minutes and 10 minutes, respectively [179]. Each transformer is with OLTC functionality and continuous tap ratio within the range of [0.9-1.1 pu]. Three shunt capacitors are located at Buses 6, 8 and 9, with capacities of 24 Mvar, 24 Mvar and 19 Mvar, respectively, at nominal voltage.

Table 6.1: Fuel cost coefficients for IEEE 14-bus system

Gen No	Bus No	a	b	c
G1	1	0.00375	2.00	0
G2	2	0.0175	1.75	0
G3	3	0.0625	1.00	0
Reserve 1 (R1)	9	0.025	3.00	0
Reserve 2 (R2)	13	0.025	3.00	0
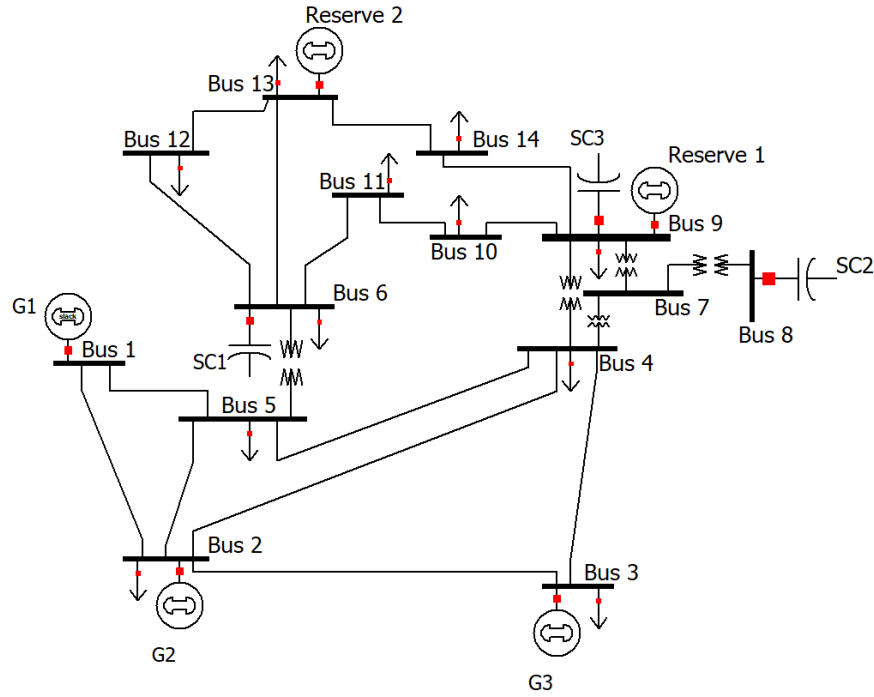
Figure 6.5: Modified IEEE 14-bus test network

This section compares results for four different load types: constant P, constant I, constant Z and for load model developed from load profiles recorded in a real network, for which model parameters $[Z^P, I^P, P^P]$ and $[Z^Q, I^Q, P^Q]$ are: [0.38, 0.11, 0.51] and [0.58, -0.15, 0.57], respectively.

To analyse the impacts of different line rating calculation strategies, the CM approach is implemented with both static thermal rating (STR) and DTR. The MVA limits provided by [177] is used as STR. The specific parameters of OHLs can be obtained from [136], and the conductor types which present the same ampacities as the STR with the summer ambient conditions in [132] are selected to represent the OHLs in the network. Then DTRs for the selected OHLs as well as transformers can be calculated

according to the assumed real-time ambient conditions: ambient temperature of 25℃, wind speed of 0.7 m/s and attacking angle of 90º and this ambient condition is assumed to be constant during the CM process. The ambient conditions which provide DTR values only slightly higher than the STR values are selected for two reasons: 1) the benefits of DTR that can increase line capacities can be shown, and 2) the DTR values are not too high so that the contingency events can cause overloading conditions that need to implement congestion management.

The optimization problem is solved by C-DEEPSO, and the system modelling and power flow calculation are implemented with MATPOWER [149][150].

6.4.1 Pre-Contingency State

Two pre-contingency operating conditions are determined by two corresponding OPF solutions minimising fuel costs and active transmission loss, respectively. The voltage limits in pre-contingency conditions are set to $100\pm6\%$. Figure 6.6 and Figure 6.7 show the MVA flows and bus voltage profiles in the pre-contingency state. In the first scenario with the objective function of fuel cost minimization, the power flows on L4-5, T4-7 and T7-9 are approaching STR. The application of DTR can significantly increase the safety margin on these branches. However, the Branch L2-3 is heavily loaded with both STR and DTR. This branch is highly likely to be overloaded when the contingency events occur. In the scenario with the objective function of loss minimization, the loading condition on L1-2, L1-5 and L2-3 are significantly reduced. When the load type is constant P and real, the power flow on T4-7 reaches STR and the application of DTR will relax this constraint. For constant I and constant Z, the power flow is lower than STR for all the transmission components.
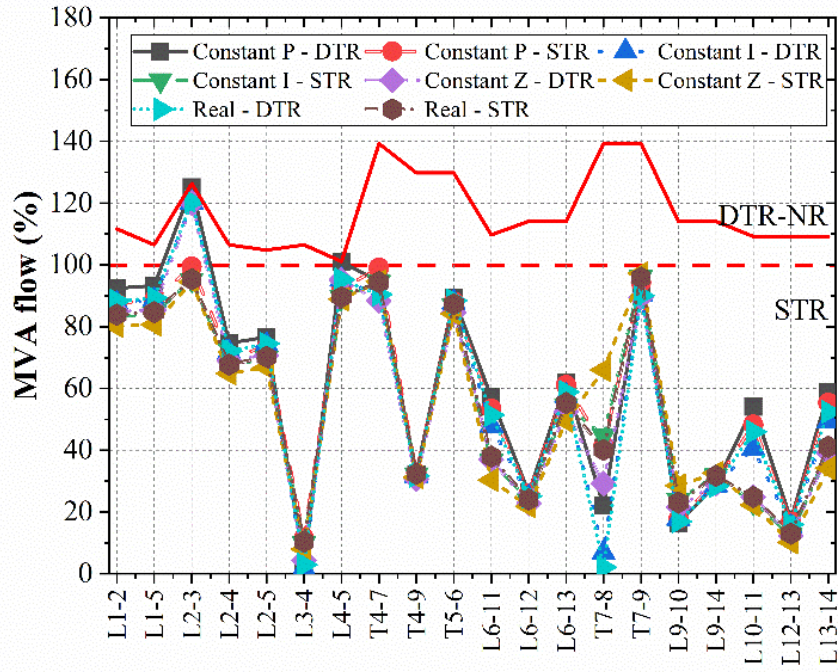
a)   Cost minimization
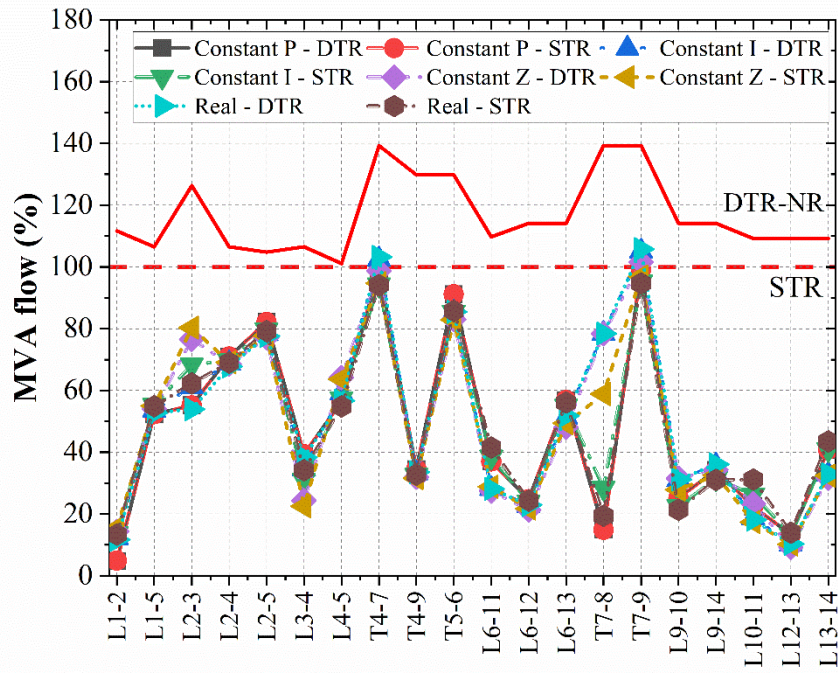
b)   Loss minimization

Figure 6.6: Branch power flow in the pre-contingency state

147
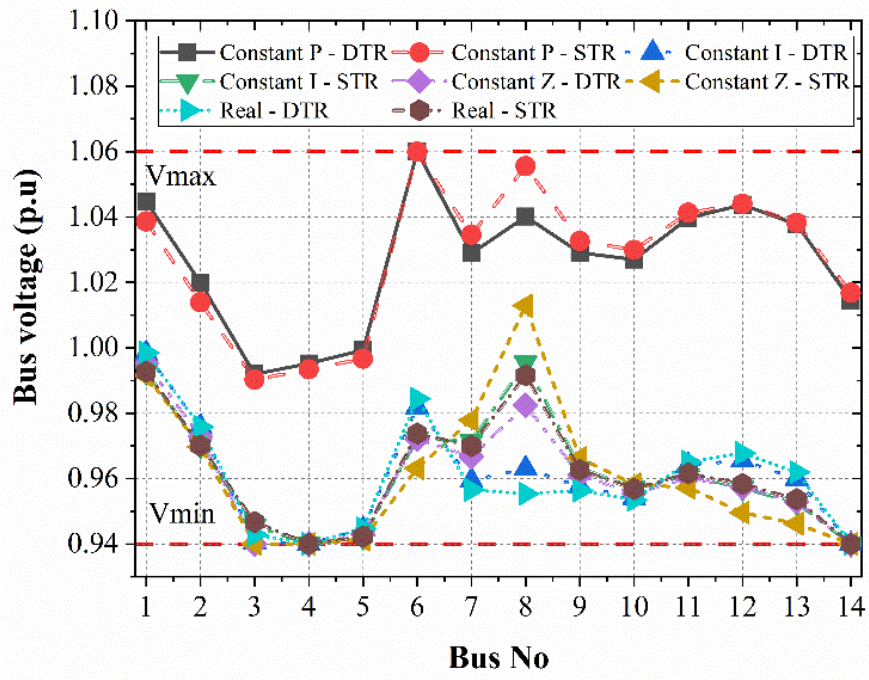
a) Cost minimization
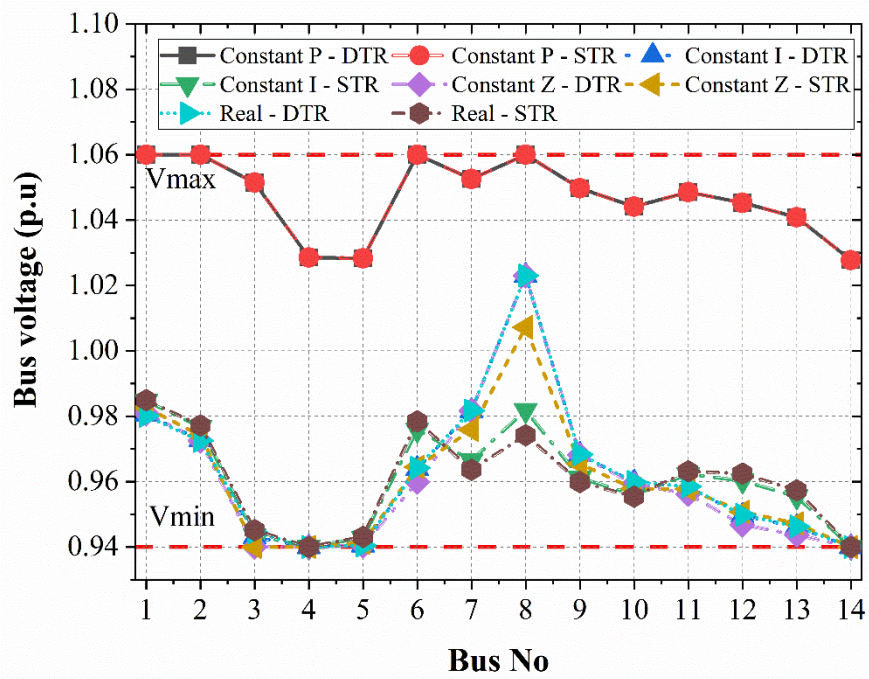
b) Loss minimization

Figure 6.7: Voltage profiles in the pre-contingency state

Table 6.2: Pre-contingency optimization results

Load type	Constant P		Constant I		Constant Z		Real	
Rating	DTR	STR	DTR	STR	DTR	STR	DTR	STR
Cost ($/h)	771	848	717	788	652	709	728	800
Loss (MW)	4.110	5.057	4.330	4.330	4.083	4.083	4.297	4.301

The plots in Figure 6.6 and Figure 6.7, as well as results in Table 6.2, indicate the strong dependency of demands of different load types on bus voltages, which then results in different optimization results. The optimal solutions present significantly higher voltages for constant P load than those for the other three load types, as higher than 1pu voltage results in lower than 1pu demand for this load type; the same reduction in demands is obtained for three other load types by reducing bus voltages (known as "conservation voltage reduction"). Compared with STR, implementation of DTRs can further significantly reduce fuel costs for all load types and provide slightly lower transmission loss for constant P and real load type, as this allows for additional power flows on the branches where the STRs are reached. However, it will not change the transmission loss when the load type is constant I and constant Z because the power flow on all branches is lower than STR.

6.4.2 Contingency (Double Fault) T4-9 & L6-13

Immediate post-contingency state

The analysed contingency event is a simultaneous double-fault of Transformer T4-9 and Line L6-13, which causes forced outages of these two branches. It is assumed that the system will not lose stability and will reach a steady-state after the occurrence of contingencies. In post-contingency state, the voltage constraints are relaxed to [0.90, 1.10] from the interval [0.94, 1.06].

Table 6.3 lists the overloaded branches with respect to both STR and DTR, as well as different pre-contingency conditions. The critical overloaded branches which have the shortest OVTs, giving MLT for analysis, are marked in bold. The MLTs for different scenarios are also presented. For the scenarios with pre-contingency of cost minimization, the numbers of overloading branches with DTR are less than those with STR. However, from the perspective of MLT, the congestions are more severe when DTR is implemented. This is because DTR will allow some components to be more

loaded in the pre-contingency state. Accordingly, the post-contingency power flow with DTR on these branches are higher than those with STR. It should be noticed that for the scenario with constant Z load type, and STR, the STRs of T4-7 and T4-9 are violated. However, considering the assumed ambient conditions, the temperature limits are still maintained, so the MLT is given as infinite according to (6.3). Compared with loss minimization, the scenarios with cost minimization generally have more severe overloading conditions, especially when the load type is constant P. For these scenarios (with STR & DTR), the Branch L12-13 is significantly overloaded, giving the OVT of around 10 minutes. Figure 6.8 shows the post-contingency power flow on each branch in detail.

Table 6.3: Immediate post-contingency constraint violations (T4-9 & L6-13)

Pre-contingency state		Cost minimization		Loss minimization	
Load Type	Rating	Overloaded branches	MLT (s)	Overloaded branches	MLT (s)
Constant P	DTR	T7-9, **L12-13**	567	T4-7, T7-9, **L12-13**	2090
	STR	T4-7, T7-9, **L12-13**	690	T4-7, T7-9, **L12-13**	2090
Constant I	DTR	L12-13	750	T4-7, **T7-9**	2218
	STR	T4-7, T7-9, **L12-13**	2103	T4-7, **T7-9**, L12-13	2088
Constant Z	DTR	L12-13	2521	T7-9	15029
	STR	T4-7, **T7-9**	Inf	T4-7, **T7-9**	Inf
Real	DTR	**L12-13**	652	T4-7, **T7-9**	2163
	STR	L2-3, T4-7, T7-9, **L12-13**	1021	T4-7, T7-9, **L12-13**	871

Inf: Final steady-state temperature is lower than the temperature corresponding to NR, MLT is infinite
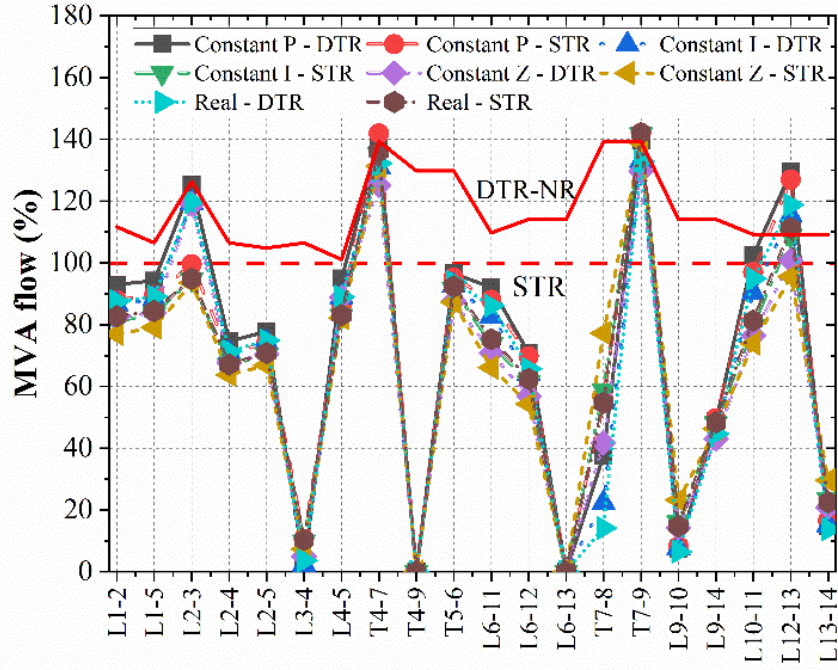
a) Pre-contingency condition: cost minimization
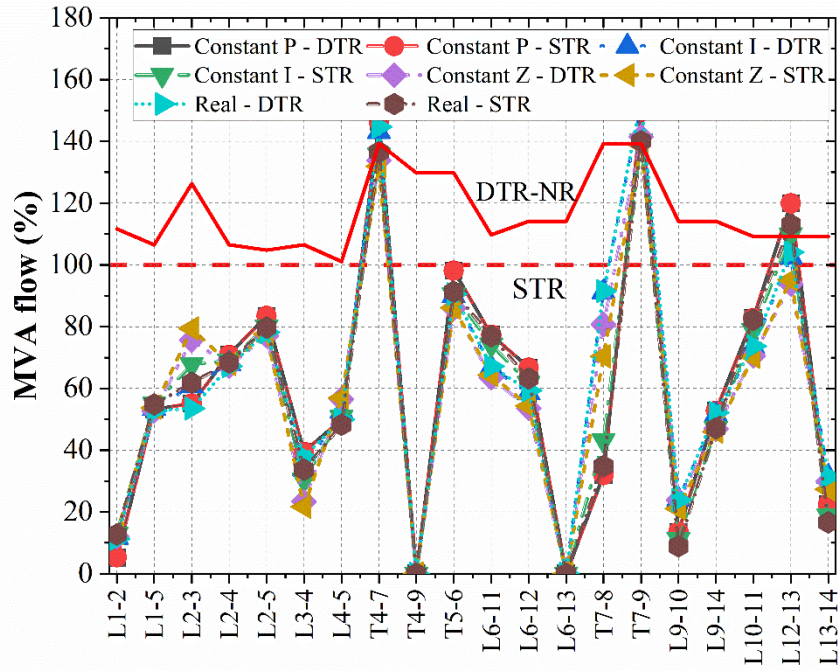
b) Pre-contingency condition: loss minimization

Figure 6.8: Immediate post-contingency branch power flow

Congestion management results

In order to resolve the post-contingency congestions, the proposed multi-stage CM method is implemented. The optimal volt-var control actions listed in Table 6.4 and

Table 6.5 are taken at the first stage, assuming that the response time is 10 seconds. These actions relieve overloading conditions for all cases significantly, especially for the scenario with constant Z load and DTR. In this scenario, the congestions are cleared solely by volt-var control actions.

Table 6.4: Post-contingency CM results (pre-contingency condition: cost minimization, T4-9 & L6-13) – Stage 1

CM Actions		Constant P		Constant I		Constant Z		Real	
		DTR	STR	DTR	STR	DTR	STR	DTR	STR
Tap ratio	T4-7	1.04	0.95	0.95	0.98	0.94	0.98	0.95	0.93
	T5-6	1.04	0.90	0.94	1.00	1.00	0.95	0.93	0.99
	T7-8	0.99	0.98	0.91	0.91	1.00	1.00	0.91	0.91
	T7-9	0.90	0.91	0.94	1.01	1.03	0.99	0.94	0.95
Shunt capacitor (Mvar)	SC1	24	24	10.7	0	22.1	9.57	0	24
	SC2	19.5	19.5	6.73	6.70	4.21	15.1	17.5	3.57
	SC3	19	19	18.6	19	12.6	12.5	14.2	19
MLT (s)		2397	2527	2474	2484	inf	inf	2223	2427

Table 6.5: Post-contingency CM results (pre-contingency condition: loss minimization, T4-9 & L6-13) – Stage 1

CM Actions		Constant P		Constant I		Constant Z		Real	
		DTR	STR	DTR	STR	DTR	STR	DTR	STR
Tap ratio	T4-7	0.96	0.95	0.96	1.03	0.98	0.98	0.94	0.93
	T5-6	0.93	0.94	0.99	1.06	0.94	0.95	0.98	0.99
	T7-8	1.00	1.00	1.05	0.95	1.01	1.00	1.05	0.91
	T7-9	0.95	0.98	0.96	1.01	1.00	0.99	0.96	0.95
Shunt capacitor (Mvar)	SC1	8.82	12.8	22.2	6.55	14.5	10.9	16.5	24.0
	SC2	6.60	5.25	7.12	12.0	21.8	12.72	4.15	3.57
	SC3	19	19	19	19.0	17.9	12.5	19	19
MLT (s)		2495	2493	2415	2490	Inf	inf	2351	2463

The optimal generation re-dispatch results of three on-line generators in the second stages are listed in Table 6.6 and Table 6.7 on a minute by minute basis. The response time of the first reserve generation (R1) at Bus 9 is 5 minutes, which clear congestions at all branches except for the case with realistic load type and STR.

Table 6.6: Post-contingency CM results (pre-contingency condition: cost minimization，T4-9 & L6-13) – Stage 2

CM Actions	Constant P		Constant I		Constant Z		Real	
	DTR	*STR*	*DTR*	*STR*	*DTR*	*STR*	*DTR*	*STR*
Generation re-dispatch (1 min)								
ΔP_{G1} (MW)	0	0	-6.93	0	-	4.89	-12.07	4.60
ΔP_{G2} (MW)	0	-2.32	3.62	0	-	-4.72	4.54	-9.33
ΔP_{G3} (MW)	0	2.97	2.52	0	-	0	2.70	2.59
$\sum|\Delta P_G|$ (MW)	0	5.76	13.1	0	-	9.61	19.3	16.5
Reserve 1 (MW)	X	X	X	X	-	X	X	X
Reserve 2 (MW)	X	X	X	X	-	X	X	X
Cost ($/h)	0	35.7	51.2	0	-	29.6	72.5	65.8
MLT (s)	2337	2468	2415	2424	inf	inf	2163	2367
Generation re-dispatch (2 min)								
ΔP_{G1} (MW)	0.99	0	0	0	-	-7.33	-12.07	-2.32
ΔP_{G2} (MW)	-1.72	0	0	0	-	2.15	4.54	-0.04
ΔP_{G3} (MW)	0.42	0	0	0	-	-1.08	2.70	0.50
$\sum|\Delta P_G|$ (MW)	3.12	0	0	0	-	10.6	0	2.86
Reserve 1 (MW)	X	X	X	X	-	X	X	X
Reserve 2 (MW)	X	X	X	X	-	X	X	X
Cost ($/h)	12.0	0	0	0	-	37.69	72.51	12.12
MLT (s)	2286	2408	2355	2364	-	inf	2103	2308
Generation re-dispatch (3 min)								
ΔP_{G1} (MW)	0	0	0	0	-	0	0	0
ΔP_{G2} (MW)	0	0	0	0	-	0	0	0
ΔP_{G3} (MW)	0	0	0	0	-	0	0	0
$\sum|\Delta P_G|$ (MW)	0	0	0	0	-	0	0	0
Reserve 1 (MW)	X	X	X	X	-	X	X	X
Reserve 2 (MW)	X	X	X	X	-	X	X	X
Cost ($/h)	0	0	0	0	-	0	0	0
MLT (s)	2226	2348	2295	2304	-	inf	2043	2248
Generation re-dispatch (4 min)								
ΔP_{G1} (MW)	0	0	0	-21.81	-	0	0	0
ΔP_{G2} (MW)	0	0	0	1.72	-	0	0	0
ΔP_{G3} (MW)	0	0	0	17	-	0	0	0
$\sum|\Delta P_G|$ (MW)	0	0	0	40.5	-	0	0	0
Reserve 1 (MW)	X	X	X	X	-	X	X	X
Reserve 2 (MW)	X	X	X	X	-	X	X	X
Cost ($/h)	0	0	0	224.1	-	0	0	0
MLT (s)	2166	2288	2235	2245	-	inf	1983	2188
Generation re-dispatch (5 min) + Reserve Generation 1 (R1)								
ΔP_{G1} (MW)	-23.62	-32.40	-32.79	-28.33	-	-37.49	-6.39	-12.72
ΔP_{G2} (MW)	8.37	2.92	11.17	5.00	-	18.31	0.82	-1.43
ΔP_{G3} (MW)	-1.01	3.15	-0.64	1.27	-	5.52	-4.35	-13.48
$\sum|\Delta P_G|$ (MW)	33	38.5	44.6	34.6	-	61.3	11.6	24.7
Reserve 1 (MW)	14.71	23.75	20.07	24.50	-	15.68	22.00	24.50
Reserve 2 (MW)	X	X	X	X	-	X	X	X
Cost ($/h)	157	214.5	207.0	190.0	-	259.6	120.0	200.3
MLT (s)	Inf	inf	inf	inf	-	inf	inf	inf
Generation re-dispatch (10 min) + Reserve Generation 1 (R1) + Reserve Generation 2 (R2)								
ΔP_{G1} (MW)	-	-	-	-	-	-	-	-2.93
ΔP_{G2} (MW)	-	-	-	-	-	-	-	-3.13
ΔP_{G3} (MW)	-	-	-	-	-	-	-	-2.35
$\sum|\Delta P_G|$ (MW)	-	-	-	-	-	-	-	8.41
Reserve 1 (MW)	-	-	-	-	-	-	-	24.50
Reserve 2 (MW)	-	-	-	-	-	-	-	7.73
Cost ($/h)	-	-	-	-	-	-	-	61.26

X: Control actions are not available

-: CM is finished & No actions are needed

Inf: Final steady-state temperature is lower than the temperature corresponding to NR, MLT is infinite

Table 6.7: Post-contingency CM results (pre-contingency condition: loss minimization，T4-9 & L6-13) – Stage 2

CM Actions	Constant P		Constant I		Constant Z		Real	
	DTR	*STR*	*DTR*	*STR*	*DTR*	*STR*	*DTR*	*STR*
Generation re-dispatch (1 min)								
ΔP_{G1} (MW)	-14.39	0	0	0	-	13.82	0	0
ΔP_{G2} (MW)	14.56	0	0	0	-	-21.16	0	0
ΔP_{G3} (MW)	-0.08	0	0	0	-	2.99	0	0
$\sum \lvert \Delta P_G \rvert$ (MW)	29.03	0	0	0	-	37.97	0	0
Reserve 1 (MW)	X	X	X	X	-	X	X	X
Reserve 2 (MW)	X	X	X	X	-	X	X	X
Cost ($/h)	123.1	0	0	0	-	186.2	0	0
MLT (s)	2435	2433	2355	2430	-	inf	2310	2403
Generation re-dispatch (2 min)								
ΔP_{G1} (MW)	0	15.33	0	0	-	0	0	0
ΔP_{G2} (MW)	0	-15.23	0	0	-	0	0	0
ΔP_{G3} (MW)	0	0	0	0	-	0	0	0
$\sum \lvert \Delta P_G \rvert$ (MW)	0	30.55	0	0	-	0	0	0
Reserve 1 (MW)	X	X	X	X	-	X	X	X
Reserve 2 (MW)	X	X	X	X	-	X	X	X
Cost ($/h)	0	128.1	0	0	-	0	0	0
MLT (s)	2375	2373	2295	2370	-	inf	2250	2343
Generation re-dispatch (3 min)								
ΔP_{G1} (MW)	0	0	-10.37	0	-	0	0	0
ΔP_{G2} (MW)	0	0	0.19	0	-	0	0	0
ΔP_{G3} (MW)	0	0	9.24	0	-	0	0	0
$\sum \lvert \Delta P_G \rvert$ (MW)	0	0	19.8	0	-	0	0	0
Reserve 1 (MW)	X	X	X	X	-	X	X	X
Reserve 2 (MW)	X	X	X	X	-	X	X	X
Cost ($/h)	0	0	0	0	-	0	0	0
MLT (s)	2315	2313	2235	2310	-	inf	2190	2283
Generation re-dispatch (4 min)								
ΔP_{G1} (MW)	27.13	0	0	0	-	0.17	0	0
ΔP_{G2} (MW)	-20.46	0	0	0	-	-0.19	0	0
ΔP_{G3} (MW)	-6.53	0	0	0	-	-0.03	0	0
$\sum \lvert \Delta P_G \rvert$ (MW)	54.12	0	0	0	-	0.39	0	0
Reserve 1 (MW)	X	X	X	X	-	X	X	X
Reserve 2 (MW)	X	X	X	X	-	X	X	X
Cost ($/h)	282.8	0	0	0	-	1.754	0	0
MLT (s)	2256	2253	2175	2250	-	inf	2130	2223
Generation re-dispatch (5 min) + Reserve Generation 1 (R1)								
ΔP_{G1} (MW)	-0.49	8.11	-22.05	-30.39	-	-34.96	-0.15	15.33
ΔP_{G2} (MW)	-13.02	-23.36	17.42	24.00	-	10.88	5.07	-24.00
ΔP_{G3} (MW)	6.61	-9.36	-8.19	-9.62	-	2.25	-12.90	-16.99
$\sum \lvert \Delta P_G \rvert$ (MW)	20.12	40.83	47.66	64.01	-	48.09	18.11	56.32
Reserve 1 (MW)	6.472	24.50	24.50	24.50	-	20.49	10.92	24.50
Reserve 2 (MW)	X	X	X	X	-	X	X	X
Cost ($/h)	181.2	349.5	334.1	403.0	-	226.3	231.3	458.9
MLT (s)	Inf	inf	inf	inf	-	inf	inf	inf
Total Cost ($/h)	**587.1**	**477.6**	**334.1**	**403.0**	**-**	**414.3**	**231.3**	**458.9**

X: Control actions are not available

-: CM is finished & No actions are needed

Inf: Final steady-state temperature is lower than the temperature corresponding to NR, MLT is infinite

Figure 6.9 plots the variations of power flows and operating temperatures of L12-13 and T7-9 during the CM process for the case with STR and realistic load type. It can be observed the temperatures on both components are prevented from violating the maximum allowable operating temperatures. In the immediate post-contingency condition, L12-13 is most heavily loaded with the MLT of 1021 seconds. The optimal volt-var control relieves the overloading condition of L12-13 but the power flow on T7-9 increases. However, as the thermal time constant of the transformer (around 2 hours) is much larger than that of L12-13 (around 3 minutes), the MLT is extended to 2427 seconds. The dispatch of the first reserve generation removes the violation of STR at L12-13 and reduces the power flow on T7-9 significantly, with which the hottest-spot temperature of T7-9 starts to decrease and will not violate the temperature limit (120 °C). However, the power flow is still above the STR. The violation of STR at T7-9 will be eliminated when the second reserve generation dispatch is available.

a) L12-13

155
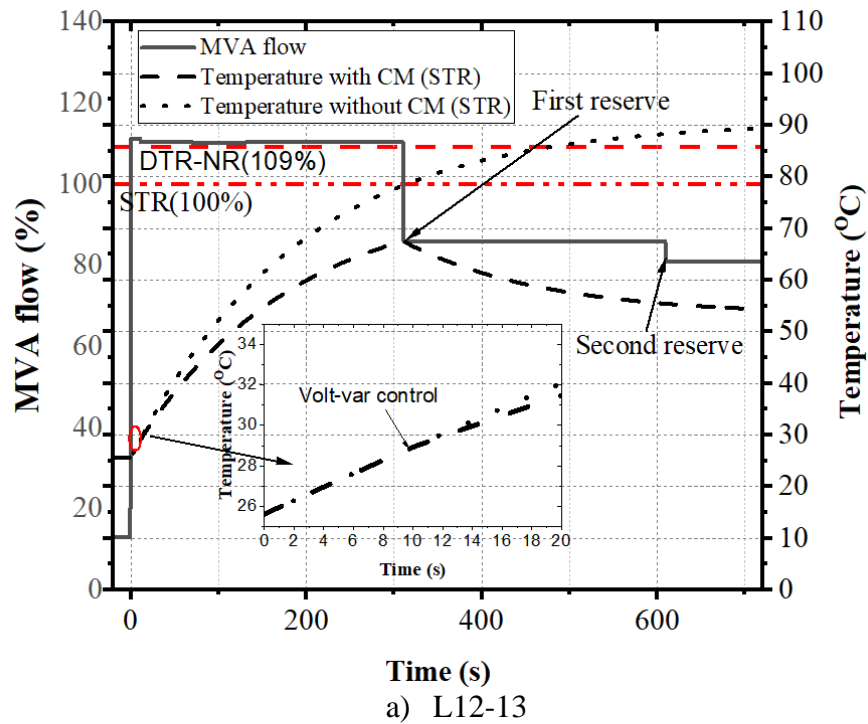
Figure 6.9: Component loading and temperature variations during CM process. (T4-9
& L9-14, Pre-contingency condition: cost minimization, load type: Real, STR)

6.4.3 Contingency (Double Fault) L6-13 & L9-14

Immediate post-contingency state

The second contingency event to be analysed is a simultaneous double-fault of Lines
L6-13 & L9-14. Compared with the previous contingency event, this event results in
much severe post-contingency conditions, for which the overloading branches,
undervoltage buses and MLTs are listed in Table 6.8. For most scenarios, the MLTs
are less than 60 seconds, which are too short of implementing enough generation re-
dispatch and reserve dispatch to relieve constraint violations, considering the ramp-up
and ramp-down rates of on-line generators and the response times of reserve
generation.

156

Table 6.8: Immediate post-contingency constraint violations (L6-13 & L9-14)

Pre-contingency state		Cost minimization			Loss minimization		
Load Type	Rating	Overloaded Components	UV buses	MLT (s)	Overloaded Components	UV buses	ML T (s)
Constant P	DTR	L2-3, L6-12, **L12-13**, L13-14	13, 14	18	L6-12, **L12-13**, L13-14	13, 14	28
	STR	L2-3, L5-6, L6-12, **L12-13**, L13-14	12,13, 14	23	T5-6, L6-12, **L12-13**, L13-14	12, 13, 14	18
Constant I	DTR	L12-13	13, 14	48	L12-13	13, 14	48
	STR	L6-12, **L12-13**, L13-14	13, 14	48	L6-12, **L12-13**, L13-14	13, 14	48
Constant Z	DTR	L12-13	13, 14	73	L12-13	13, 14	73
	STR	L12-13	13, 14	73	L12-13	13, 14	73
Real	DTR	**L12-13**, L13-14	13, 14	42	**L12-13**, L13-14	13, 14	42
	STR	L6-12, **L12-13**, L13-14	13, 14	42	L6-12, **L12-13**, L13-14	13, 14	42

a) Pre-contingency condition: cost minimization
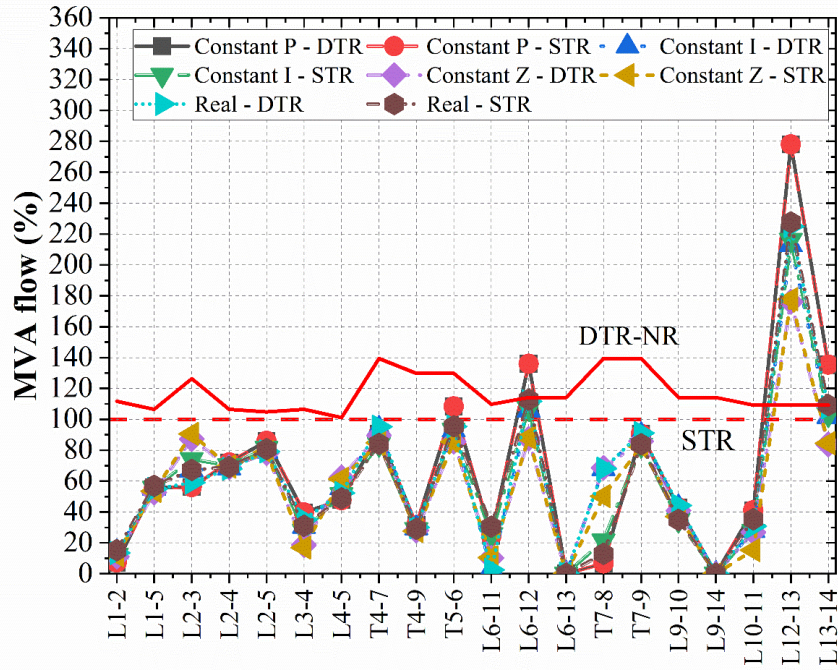
b) Pre-contingency condition: loss minimization

Figure 6.10: Immediate post-contingency branch power flow (L6-13 & L9-14)

Congestion management results

Table 6.9 and Table 6.10 list the optimal settings provided by the first-stage CM algorithm, showing that these control actions can hardly extend MLTs. The bus voltages after volt/var control are plotted in Figure 6.11, which demonstrates that even after the volt-var control actions are implemented, there will be overvoltage conditions at Bus 6 and Bus 7, with only slightly improved undervoltage conditions at Bus 13. Considering the MLTs and numbers of bus voltage limit violations, the available volt-var control is not efficient for this contingency event. Due to the short periods of OLTs (≤ 60 seconds), the CM algorithm decides to implement optimal load shedding immediately after the contingency event occurs. Based on the values of sensitivity factors calculated as (6.22) and (6.23), Bus 13 and Bus 14 are selected as the target buses to implement load shedding. The optimal load shedding results, as well as the coordinated control of generations provided by the third-stage CM model, are given by Table 6.10. It can be observed that the CM cost for the scenarios with DTR are generally lower, which presents the benefits of the application of DTR. Among the four load types, Constant Z load gives the lowest CM cost with both pre-contingency conditions. Figure 6.12 plots the variations in MVA loading and conductor surface temperature of L12-13 for the case with realistic load type and STR.

Table 6.9: Post-contingency CM results (pre-contingency condition: cost minimization, L6-13 & L9-14) – Stage 1

CM Actions		Constant P		Constant I		Constant Z		Real	
		DTR	*STR*	*DTR*	*STR*	*DTR*	*STR*	*DTR*	*STR*
Tap ratio	*T4-7*	0.97	1.03	0.93	0.98	0.98	1.04	1.02	0.90
	T4-9	1.05	1.06	1.08	0.97	1.01	1.08	0.97	0.98
	T5-6	0.90	0.90	0.90	0.93	0.94	0.90	0.90	0.90
	T7-8	1.10	1.06	1.03	1.00	1.00	1.05	1.03	1.00
	T7-9	1.06	0.90	0.94	1.00	1.06	0.91	0.97	0.90
Shunt capacitor (Mvar)	*SC1*	10.0	2.97	18.7	24	19	9.45	18.9	19.0
	SC2	16.1	21.2	16.5	13	8.52	17.5	7.64	9.74
	SC3	7.90	4.49	17.3	19	19	7.06	19.0	15.7
MLT (s)		27	29	38	38	69	56	36	35

Table 6.10: Post-contingency CM results (pre-contingency condition: loss minimization, L6-13 & L9-14) – Stage 1

CM Actions		Constant P		Constant I		Constant Z		Real	
		DTR	*STR*	*DTR*	*STR*	*DTR*	*STR*	*DTR*	*STR*
Tap ratio	*T4-7*	0.94	1.06	1.02	1.02	0.90	0.99	0.99	0.99
	T4-9	1.02	1.10	0.90	0.90	0.90	0.98	0.98	1.02
	T5-6	0.90	0.90	0.93	0.93	0.90	0.96	0.90	0.90
	T7-8	1.10	1.10	1.02	1.02	0.95	1.02	0.93	0.93
	T7-9	1.10	1.04	0.96	0.96	0.92	1.00	0.93	0.93
Shunt capacitor (Mvar)	*SC1*	3.98	23.6	19.0	19.0	10.8	19.0	3.02	11.2
	SC2	8.66	23.6	9.42	9.42	11.0	8.12	0	2.44
	SC3	17.6	19.0	11.1	11.1	0	18.8	0	4.59
MLT (s)		24	20	38	38	56	69	35	36
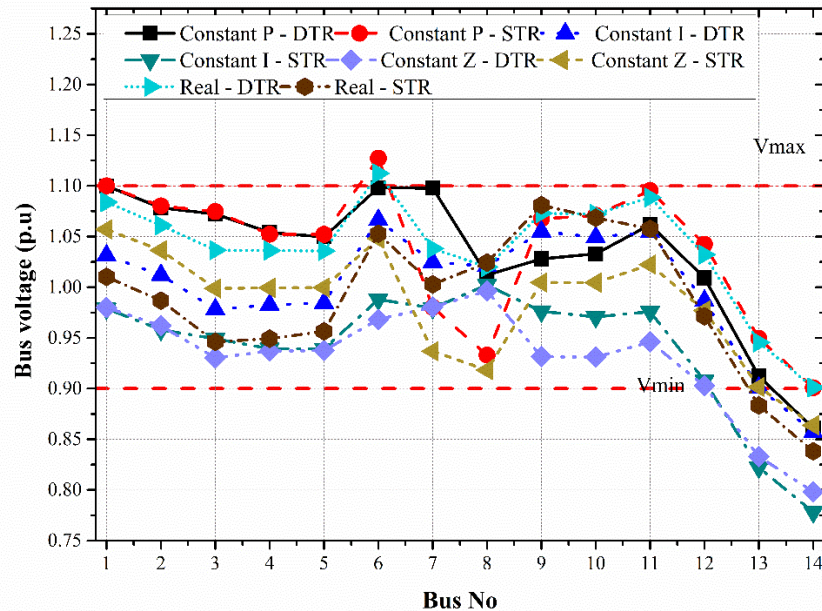
a) Pre-contingency condition: cost minimization

159
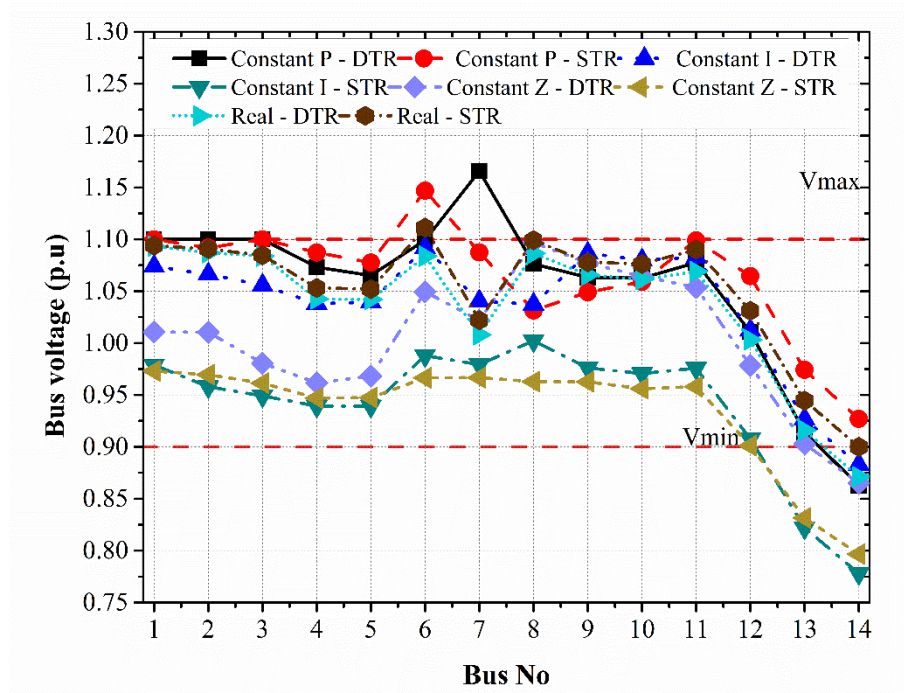
b) Pre-contingency condition: loss minimization
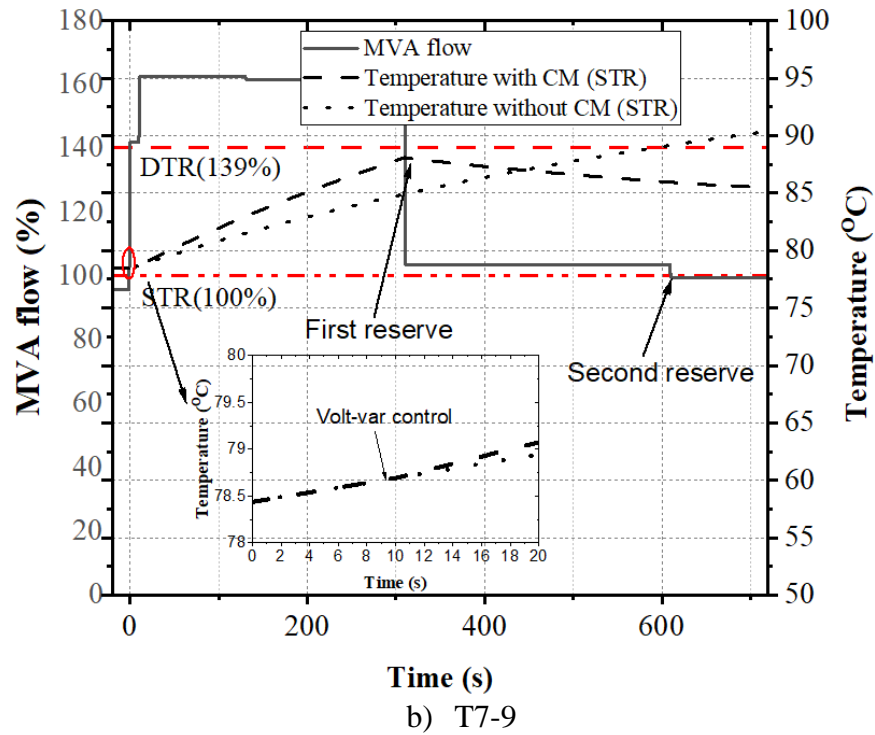
Figure 6.11: Bus voltages after first-stage CM
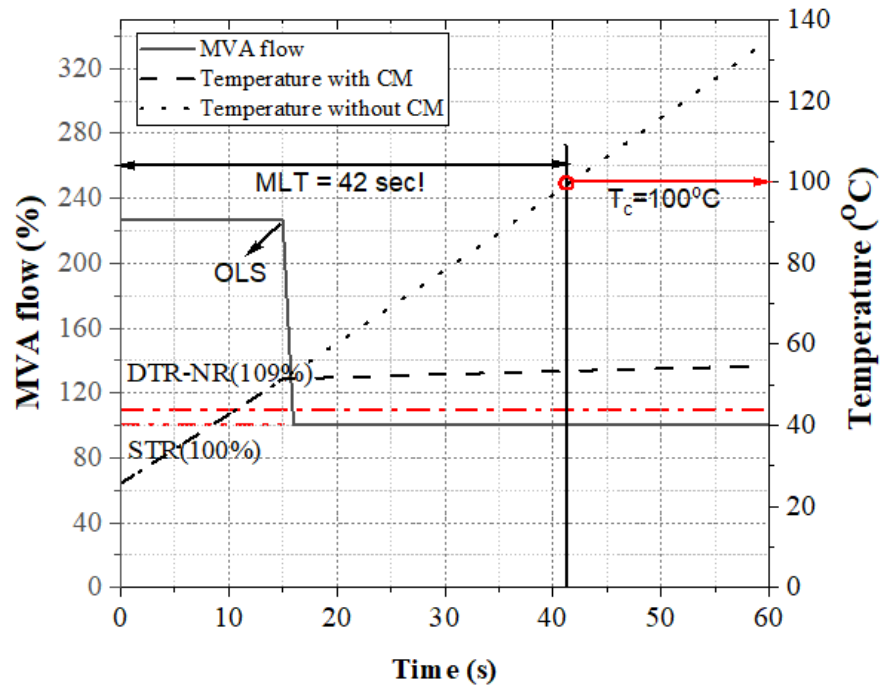
Figure 6.12: Component loading and temperature variations during the CM process. (L6-13 & L9-14, Pre-contingency condition: cost minimization, load type: Real, STR)
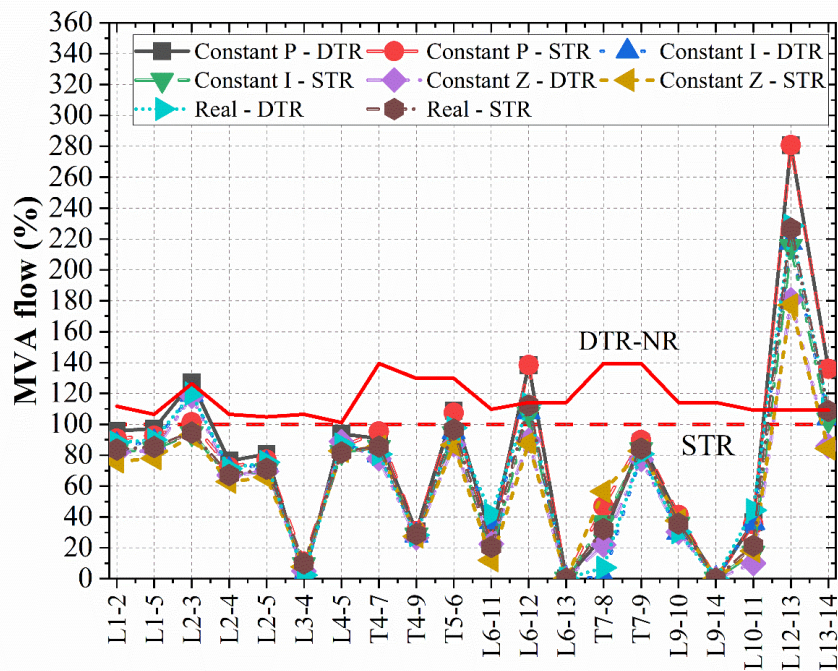
Table 6.11: Post-contingency CM results – Stage 3

CM actions	Constant P		Constant I		Constant Z		Real	
Fuel cost minimization								
	DTR	*STR*	*DTR*	*STR*	*DTR*	*STR*	*DTR*	*STR*
ΔP_{G1} (MW)	-12.35	-13.65	-1.99	-0.03	-3.84	-0.04	-0.13	0.00
ΔP_{G2} (MW)	-11.20	-11.20	-0.85	-1.95	0.01	-0.13	-6.95	-5.96
ΔP_{G3} (MW)	0.00	0.00	-0.08	0.05	0.02	10.04	-0.01	0.00
Reserve 1 (MW)	X	X	X	X	X	X	X	X
Reserve 2 (MW)	X	X	X	X	X	X	X	X
Selected buses	13, 14	13, 14	13, 14	13, 14	13, 14	13, 14	13, 14	13, 14
P_{LS} at Bus 13 (MW)	6.52	2.16	12.35	10.55	12.58	9.75	11.04	3.61
P_{LS} at Bus 14 (MW)	9.46	14.90	3.67	6.56	2.11	6.33	5.12	13.73
$\sum |P_{LS}|$ (MW)	15.98	17.06	16.02	17.11	14.69	16.08	16.16	17.34
Total cost ($)	1211.36	1636.54	1083.06	1497.75	850.82	1344.74	1125.93	1551.36
Active transmission loss minimization								
	DTR	*STR*	*DTR*	*STR*	*DTR*	*STR*	*DTR*	*STR*
ΔP_{G1} (MW)	-22.10	-23.18	0.00	0.01	-1.75	-1.39	0.00	7.42
ΔP_{G2} (MW)	0.00	0.00	0.00	0.03	0.00	0.01	0.00	0.00
ΔP_{G3} (MW)	0.00	0.00	0.00	-0.02	0.00	0.00	0.00	0.00
Reserve 1 (MW)	X	X	X	X	X	X	X	X
Reserve 2 (MW)	X	X	X	X	X	X	X	X
Selected buses	13, 14	13, 14	13, 14	13, 14	13, 14	13, 14	13, 14	13, 14
P_{LS} at Bus 13 (MW)	1.52	5.57	13.47	7.36	2.37	12.45	11.52	11.60
P_{LS} at Bus 14 (MW)	14.56	11.40	2.51	9.86	12.69	3.54	4.57	5.47
$\sum |P_{LS}|$ (MW)	16.08	16.97	15.98	17.22	15.06	15.99	16.09	17.11
Total cost ($)	2221.50	2345.44	1972.24	2033.49	1517.13	1562.74	2115.07	2153.13

6.5 Conclusions

This chapter presented a novel multi-stage OPF-based approach for efficient management of severe contingency events. It detailed the development of dynamic thermal models for power transformers and overhead lines, which were required to correctly estimate the maximum lead time (MLT) available to network operators for corrective actions.

The presented multi-stage congestion management (CM) method takes into account: a) volt-var controls, which do involve any high costs and have fast response time (first stage), b) re-dispatch of on-line generators, taking into account their ramping up/down times on a minute-by-minute basis, and activation of reserve generation, which has

prescheduled response times (second stage), and c) optimal load shedding, which is implemented in the final third stage as the "last resort" measure to ensure that all remaining congestions are resolved.

Another benefit of the presented CM approach is that it can provide network operators with information on the costs of available corrective actions, so their response can be based on techno-economic optimization. The presented results for different load types (constant power, constant current, constant impedance and realistic load models) highlights the importance of including the correct load model in the analysis. Comparison of results for STRs and DTRs on the two example contingency events demonstrates that DTRs allow network operators to utilize the additional capacity of network components for a more cost-efficient resolving of violated constraints.

Chapter 7
Conclusions and Future Work

7.1 Thesis summary

Modern power system operating conditions are closer to their technical limits due to ageing infrastructure, deregulated electricity market, increased integration of renewable generation, etc. Furthermore, the growing penetration of renewable generation, the application of DTR and new technologies on the load side (e.g. demand-side management) have all significantly increased the level of uncertainties in power system operation. To ensure high levels of system security and techno-economic performance, it is necessary to develop advanced computational tools for system operators to improve their decision-making capability in a highly uncertain environment.

Chapter 2 presented an overview of approaches for power system security control. It introduced the three main functions of power systems security and the classification of system operating states. In addition, a literature review of methods to manage uncertainties in power system was provided. Those methods can be classified into three categories, probabilistic, possibilistic and hybrid approaches based on the different formulations of uncertainty models. This chapter also presented an introduction to the OPF problem and three approximated formulations.

Chapter 3 evaluated the hosting capacity for wind-based distributed generation of a distribution network with the application of DTR. Both deterministic and probabilistic approaches were applied, and variations of demands and DG power outputs, as well as DTR of network components, were considered. The HC assessment has three steps. In the first step, maximum locational HC was calculated, assuming that only one DG unit is connected in the network. Then, assuming that DG units were calculated at all buses, the hosting capacity of the whole network (NHC) were calculated based on maximum LHCs obtained in the first step. Finally, bus-to-bus LHC-sensitivity factors were calculated to determine the variations of available LHCs after the connection of additional DG units at arbitrary network buses.

This work considers the uncertainty impacts in the planning stage. To analyse the uncertainty impacts in the operation stage, more accurate probabilistic models are necessary. Chapter 4 used several distributions, including 2-p WB, MvM and MGND to model the uncertainties due to wind energy: uncertainties in wind speed, wind direction, as well as variations in outputs of wind generation systems. Based on these probabilistic models, MCS-based analysis was implemented to analyse the impacts of DTR on wind energy integration. The results demonstrated the benefits of DTR application. A significant amount of wind curtailment can be avoided when the wind speed is high. However, the unfavourable real-time thermal rating at low wind speed can result in unexpected overloading conditions which should also be considered, although outputs of wind generation are zero for the low/zero wind conditions.

To manage the operational risk arising from multiple uncertainties and improve system security, a novel OPF-based model which combines affine arithmetic and MCS-based approach was presented in Chapter 5. In this approach, uncertainties from different sources, such as input wind energy, output wind generation and load variations were initially represented by intervals and the model was solved with the AA approach at first. The AA-based results can provide the intervals of optimal dispatch solution corresponding to the Max-Min intervals of input uncertainties. However, the AA-based results may be too conservative, as they include extreme events, such as the maximum and minimum values of uncertain variables, which are rarely occurring. Consequently, the MCS-based approach was implemented to generate the output sample results for uncertain input variables, based on the developed probabilistic models and to obtain the actual probabilities of optimal solutions. Compared to the MCS-based approach, the presented AA-P-OPF method is much more efficient in terms of the required computational times, as it does not need to solve the OPF problem for each sample repeatedly. It can also resolve the issue with too wide solution ranges obtained by AA-OPF method with Min-Max intervals and take into account probability distributions of input uncertainties. The presented method can be used by system operators for optimal generation dispatch and the selection of low-risk wind curtailment strategies, where the risk level is directly related to the specified confidence level in the evaluated uncertainty ranges.

The presented method can provide system operators with economically efficient dispatch solutions while maintaining system security level under normal operating conditions. However, the impacts of disturbances, such as contingencies, on system operation, have not been considered so far. Therefore, Chapter 6 proposed a multi-stage OPF-based approach for the efficient management of severe contingency events. The presented multi-stage congestion management (CM) method took into account both cost-free and non-cost-free congestion management actions, which include volt-var controls, generation re-dispatch and load shedding. The volt-var control was implemented firstly due to the short response time. Then, the generation re-dispatch was used in the second stage to mitigate the violations of branch thermal limits and bus voltages. As the response time of generation re-dispatch is relatively long, to prevent permanent damages to the equipment caused by post-contingency currents, the maximum lead time for system operators to implement corrective actions, estimated by dynamic thermal models of transmission lines and transformers, are included into the optimization model as constraints. Load shedding was used in the last stage to manage the remaining constraint violations. Four different load types (constant power, constant current, constant impedance, and realistic load models) were applied in the analysis, and the results demonstrate the importance to use accurate load model in post-contingency congestion management. Comparison of results for STR and DTR demonstrates that the use of DTR allows network operators to utilize the additional capacity of network components for more cost-efficient corrective actions to remediate constraint violations.

7.2   Research implications

The research presented by this thesis firstly introduced approaches to evaluate hosting capacity for wind-based generation in distribution networks with DTR application. Then a framework was proposed to handle uncertainties in network operation, introduced by the variations of wind generation, DTR, and load conditions. An affine arithmetic based optimization model, which combines both interval and probabilistic information of uncertainties, was developed. It can be a useful tool for system operators to identify optimal generation dispatch and select wind curtailment strategies with low risk for a network with high wind penetration. After introducing the AA-P-OPF model for system optimal operation under normal operating conditions, this thesis

also proposed a framework for post-contingency CM, in which the optimal remedial actions are selected to mitigate branch overloading conditions and bus voltage violations within the maximum lead time. The response times for different actions were considered, and the remedial actions were determined in three stages, considering the limiting lead time av. Volt-var control is used to relieve congestion management at first due to its quick response, then generation re-dispatch and reserve dispatch are implemented. If the congestions cannot be removed by generation re-dispatch, load shedding is selected in the last step.

This thesis has provided the required theoretical backgrounds and several approaches for improving system performance in both economic and security aspects subject to uncertainties at a high level. The presented methods can effectively extend the state-of-the-art in power system optimization with uncertainties, which is expected to be of significant value to both system planners and operators. Those approaches improve the decision-making capability for system control centres to overcome challenges in the context of modern power systems.

7.3 Limitations of the research and future work

The proposed frameworks were implemented on the test networks or practical networks, which were all a relatively small size. To further examine the applicability of the presented methods, practical networks of larger sizes should be used. However, from the perspective of the author, the proposed methods should be applicable to larger networks in the presented form directly.

The AA-P-OPF model proposed in Chapter 5 was based on the original formulation of the ACOPF problem, which is nonconvex and NP-hard. The complexity of the model will increase significantly as the number of uncertain variables increases. For instance, the number of constraints in AA-P-OPF with five uncertain variables, such as wind speed, wind direction, wind power output, dynamic thermal rating and load, will be almost six times of those in the original OPF formulation. In future work, principal component analysis or machine learning-based method should be implemented to reduce the number of uncertain resource to simplify the optimization model. Another promising direction is to develop a convex relaxed formulation for the

AA-P-OPF model. Compared with the nonconvex model solved by nonlinear solvers, such as Interior Point Optimizer (IPOPT), the convex model may achieve better solutions potentially with lower computational efforts.

Furthermore, AA-P-OPF only included continuous variables. However, in power system operation, some control variables are discrete in nature, such as the setting of OLTC tap ratios, the switching of transmission lines in different configurations, discrete-step capacitor banks and the charging/discharging control of energy storage systems. In future work, these discrete variables and related control actions should be integrated into the convex relaxed model. To solve the mixed-integer nonlinear programming problem with linear integer parts and convex continuous parts, generalized benders decomposition or distributed optimization algorithms, such as alternating direction method of multipliers can be applied.

The post-contingency CM model proposed in Chapter 6 was solved by a metaheuristic algorithm, which took longer computational time. The main reason to use the metaheuristic algorithm is that the CM model with MLT constraints involves some non-smooth or non-differentiable functions (e.g. component temperatures, MLT), which effectively limit the application of conventional gradient-based solver methods. To overcome these problems, proper linearization and approximations would be applied to smooth these functions. In addition, the sequence of corrective actions is predefined in the post-contingency CM model. The operators are suggested to use volt-var control actions at first, then apply generation re-dispatch and connection of reserve generation. If these actions cannot mitigate congestions, load shedding is implemented in the end. However, in practical applications, the sequence can be more flexible. For instance, the operators may apply volt-var controls during generation re-dispatch, or apply control over the demand-manageable portion of the load, or "partial/contracted load shedding" before generation re-dispatch to prevent unwanted dynamics. To overcome this problem, dynamic programming, model predictive control and reinforcement learning may be promising options.

Finally, system stability response has become more sensitive to small disturbances, as the displacement of synchronous generators with wind turbines has reduced system inertia. Consequently, dynamic security assessment plays an increasingly important

role in security analysis. In the future work, dynamic security constraints should be integrated into the post-contingency CM model to ensure not only steady-state system security, but also transient or dynamic system security.

Bibliography

[1] CIGRE/CIRED Working Group C4.24, "Power quality and EMC issues with future electricity networks," CIGRE, 2018.

[2] D. Xenias, C. Axon, N. Balta-Ozkan, L.M. Cipcigan, P. Connor, R. Davidson, A. Spence, G. Taylor and L.E. Whitmarsh, "Scenarios for the Development of Smart Grids in the UK: Literature Review," *UKERC Working Paper*, 2014.

[3] P. Kundur, J. Paserba, V. Ajjarapu, G. Andersson, A. Bose, C. Canizares, N. Hatziargyriou, D. Hill, A. Stankovic, C. Taylor, T. Van Cutsem, and V. Vittal, "Definition and Classification of Power System Stability," *IEEE Trans. Power Syst.*, vol. 19, no. 2, pp. 1387–1401, 2004.

[4] E. L. Miguelez, L. R. Rodriguez, T. G. S. Roman, F. M. E. Cerezo, M. I. N. Fernandez, R. C. Lafarga, and G. L. Camino, "A practical approach to solve power system constraints with application to the Spanish electricity market," *IEEE Trans. Power Syst.*, vol. 19, no. 4, pp. 2029–2037, 2004.

[5] F. Yu and F. Tu, "A real-time constraint management approach through constraint similarity and pattern recognition in power system," *IEEE Trans. Smart Grid*, vol. 4, no. 4, pp. 1743–1750, Dec. 2013.

[6] F. Capitanescu, J. L. Martinez Ramos, P. Panciatici, D. Kirschen, A. Marano Marcolini, L. Platbrood, and L. Wehenkel, "State-of-the-art, challenges, and future trends in security constrained optimal power flow," *Electr. Power Syst. Res.*, vol. 81, pp. 1731–1741, Aug. 2011.

[7] B. Stott, O. Alsac, and A. J. Monticelli, "Security analysis and optimization," *Proc. IEEE*, vol. 75, no. 12, pp. 1623–1644, Dec. 1987.

[8] P. B. Eriksen, T. Ackermann, H. Abildgaard, P. Smith, W. Winter, and J. M. Rodriguez Garcia, "System operation with high wind penetration," *IEEE Power Energy Mag.*, vol. 3, no. 6, pp. 65–74, Nov. 2005.

[9] T. J. Hammons, "Integrating renewable energy sources into European grids," *Int. J. Electr. Power Energy Syst.*, vol. 30, no. 8, pp. 462–475, Oct. 2008.

[10] D. Fang, M. Zou, G. Coletta, A. Vaccaro, and S. Z. Djokic, "Handling

uncertainties with affine arithmetic and probabilistic OPF for increased utilisation of overhead transmission lines," *Electr. Power Syst. Res.*, vol. 170, pp. 364–377, May 2019.

[11] G. Coletta, A. Vaccaro, D. Villacci, D. Fang, and S. Z. Djokic, "Affine arithmetic for efficient and reliable resolution of weather-based uncertainties in optimal power flow problems," *Int. J. Electr. Power Energy Syst.*, vol. 110, pp. 713–724, Sep. 2019.

[12] J. Gunda, D. Fang, S. Z. Djokic, and M. Lehtonen, "Identification and Handling of Critical Constraints in Time-Constrained SCOPF Analysis of Power Systems," in *IREP Symposium X Bulk Power Systems Dynamics and Control Symposium (IREP)*, Portugal, 2017, pp. 1–10.

[13] D. Fang, J. Gunda, S. Z. Djokic, and A. Vaccaro, "Security-and time-constrained OPF applications," in *2017 IEEE Manchester PowerTech, Powertech 2017*, Manchester, UK, 2017.

[14] D. Fang, M. Zou, and S. Djokic, "Probabilistic OPF incorporating uncertainties in wind power outputs and line thermal ratings," in *2018 IEEE International Conference on Probabilistic Methods Applied to Power Systems (PMAPS)*, Boise, ID, 2018, pp. 1-6.

[15] M. Zou, D. Fang, S. Z. Djokic, and S. Hawkins, "Equivalent Power Curves and Short-term Forecasting of Power Outputs of an Off-shore Wind Farm Based on a Multi-state Operational Model," in *4th Int. Conf. on Offshore Renewable Energy (CORE 2019)*, Glasgow, 2019.

[16] M. Zou, J. Gu, D. Fang, G.P Harrison, S. Z. Djokic, X. Wang, C. Zhang, "Comparison of Three Methods for a Weather Based Day-Ahead Load Forecasting," *2019 IEEE PES Innovative Smart Grid Technologies Europe (ISGT-Europe)*, Bucharest, Romania, 2019, pp. 1-5.

[17] S. Z. Djokic, M. Zou, D. Fang, V. Di Giorgio, R. Langella, and A. Testa, "On the Importance of Correlating Wind Speed and Wind Direction for Evaluating Uncertainty in Wind Turbine Power Output," *2019 International Conference on Clean Electrical Power (ICCEP)*, Otranto, Italy, 2019, pp. 36-45.

[18] D. Fang, J. Gunda, M. Zou, G. Harrison, S. Z. Djokic, and A. Vaccaro,

"Dynamic thermal rating for efficient management of post-contingency congestions," *2019 IEEE Milan PowerTech*, Milan, Italy, 2019, pp. 1-6.

[19]   M. Zou, D. Fang, G. Harrison, and S. Djokic, "Weather Based Day-Ahead and Week-Ahead Load Forecasting using Deep Recurrent Neural Network," *2019 IEEE 5th International forum on Research and Technology for Society and Industry (RTSI)*, Florence, Italy, 2019, pp. 341-346.

[20]   D. Fang, M. Zou, G. P Harrison, S. Z. Djokic, I. Hernando-Gil, M. Ndawula, J. Gunda, and X. Xu, "Deterministic and Probabilistic Assessment of Distribution Network Hosting Capacity for Wind-Based Renewable Generation," in *2020 IEEE International Conference on Probabilistic Methods Applied to Power Systems (PMAPS)*, Liege, Belgium, to be published, pp. 1–6.

[21]   D. Fang, M. Zou, G. P. Harrison, S. Z. Djokic, and A. Vaccaro, "Multi-Stage Congestion Management Considering Maximum Lead Time and Voltage-Dependent Load Models," in *2020 IEEE PES Innovative Smart Grid Technologies Europe (ISGT-Europe)*, The Hague, The Netherlands, 2020, pp. 1–6.

[22]   M. Zou, D. Fang, S. Hawkins, and S. Z. Djokic, "Assessment of Wind Energy Resources and Identification of Outliers in On-Shore and Off-Shore Wind Farm Measurements," in *3rd Int. Conf. on Offshore Renewable Energy (CORE 2018)*, Glasgow, UK, 2018.

[23]   "IEEE Standard for Calculating the Current-Temperature Relationship of Bare Overhead Conductors," in *IEEE Std 738-2012 (Revision IEEE Std 738-2006 - Inc. IEEE Std 738-2012 Cor 1-2013)*, pp. 1–72, 12 Dec 2013.

[24]   "IEEE Guide for Loading Mineral-Oil-Immersed Transformers and Step-Voltage Regulators," in *IEEE Std C57.91-2011 (Revision IEEE Std C57.91-1995)*, pp. 1–172, 2012.

[25]   A. J. Wood and B. F. Wollenberg, *Power Generation, Operation and Control*, 2nd ed. New York: John Wiley & Sons, 1996.

[26]   D. P. Kothari and I. J. Nagrath, *Modern Power System Analysis*. New Delhi: Tata McGraw-Hill, 2003.

[27]   P. Kundur, *Power System Stability and Control*. New York: McGraw-Hill, 1994.

[28] L. Wehenkel and M. Pavella, "Preventive vs. emergency control of power systems," in *2004 IEEE PES Power Systems Conference and Exposition*, 2004, New York, NY, 2004, pp. 1665-1670 vol. 3.

[29] T. E. Dy Liacco, "The Adaptive Reliability Control System," *IEEE Trans. Power Appar. Syst.*, vol. PAS-86, no. 5, pp. 517–531, 1967.

[30] L. H. Fink and K. Carlsen, "Operating under stress and strain.," *IEEE Spectr.*, vol. 15, no. 3, pp. 48–53, 1978.

[31] I. Genc, R. Diao, V. Vittal, S. Kolluri, and S. Mandal, "Decision tree-based preventive and corrective control applications for dynamic security enhancement in power systems," *IEEE Trans. Power Syst.*, vol. 25, no. 3, pp. 1611–1619, Aug. 2010.

[32] J. Zhu, "Uncertainty Analysis in Power Systems," in *OPTIMIZATION OF POWER SYSTEM OPERATION*, 2nd ed., Hoboken, New Jersey: John Wiley & Sons, Inc, 2015, pp. 529–578.

[33] P. B. Eriksen, T. Ackermann, H. Abildgaard, P. Smith, W. Winter, and J. M. Rodriguez Garcia, "System operation with high wind penetration," *IEEE Power and Energy Magazine*, vol. 3, no. 6, pp. 65–74, 2005.

[34] J. Zhu, "Application of Renewable Energy," in *Optimization of Power System Operation*, 2nd ed., Hoboken, New Jersey: John Wiley & Sons, Inc, 2015, pp. 407–436.

[35] A. Soroudi and T. Amraee, "Decision making under uncertainty in energy systems: State of the art," *Renewable and Sustainable Energy Reviews*, vol. 28. pp. 376–384, Dec 2013.

[36] M. Hemmati, B. Mohammadi-Ivatloo, and A. Soroudi, "Uncertainty management in decision-making in power system operation," in *Decision Making Applications in Modern Power Systems*, New York, NY, USA: Elsevier, 2020, pp. 41–62.

[37] A. Soroudi, M. Aien, and M. Ehsan, "A probabilistic modeling of photo voltaic modules and wind power generation impact on distribution networks," *IEEE Syst. J.*, vol. 6, no. 2, pp. 254–259, 2012.

[38] D. A. Bechrakis, J. P. Deane, and E. J. McKeogh, "Wind resource assessment

of an area using short term data correlated to a long term data set," *Sol. Energy*, vol. 76, no. 6, pp. 725–732, Jun. 2004.

[39] Z. Liu, F. Wen, and G. Ledwich, "Optimal siting and sizing of distributed generators in distribution systems considering uncertainties," *IEEE Trans. Power Deliv.*, vol. 26, no. 4, pp. 2541–2551, Oct. 2011.

[40] R. A. Jabr, "Adjustable robust OPF with renewable energy sources," *IEEE Trans. Power Syst.*, vol. 28, no. 4, pp. 4742–4751, 2013.

[41] Y. Lv, L. Guan, Z. Tang, and Q. Zhao, "A Probability Model of PV for the Middle-term to Long-term Power System Analysis and Its Application," in *Energy Procedia*, 2016, vol. 103, pp. 28–33.

[42] N. M. Nor, A. Ali, T. Ibrahim, and M. F. Romlie, "Battery Storage for the Utility-Scale Distributed Photovoltaic Generations," *IEEE Access*, vol. 6, pp. 1137–1154, Nov. 2017.

[43] V. K. Jadoun, V. C. Pandey, N. Gupta, K. R. Niazi, and A. Swarnkar, "Integration of renewable energy sources in dynamic economic load dispatch problem using an improved fireworks algorithm," *IET Renew. Power Gener.*, vol. 12, no. 9, pp. 1004–1011, Jul. 2018.

[44] A. R. Jordehi, "How to deal with uncertainties in electric power systems? A review," *Renew. Sustain. Energy Rev.*, vol. 96, pp. 145–155, Nov. 2018.

[45] R. Hemmati, R. A. Hooshmand, and N. Taheri, "Distribution network expansion planning and DG placement in the presence of uncertainties," *Int. J. Electr. Power Energy Syst.*, vol. 73, pp. 665–673, Jun. 2015.

[46] J. H. Zhao, F. Wen, Z. Y. Dong, Y. Xue, and K. P. Wong, "Optimal dispatch of electric vehicles and wind power using enhanced particle swarm optimization," *IEEE Trans. Ind. Informatics*, vol. 8, no. 4, pp. 889–899, 2012.

[47] H. Kamankesh, V. G. Agelidis, and A. Kavousi-Fard, "Optimal scheduling of renewable micro-grids considering plug-in hybrid electric vehicle charging demand," *Energy*, vol. 100, pp. 285–297, Apr. 2016.

[48] S. Alaee, R.-A. Hooshmand, and R. Hemmati, "Stochastic transmission expansion planning incorporating reliability solved using SFLA meta-heuristic optimization technique," *CSEE J. Power Energy Syst.*, vol. 2, no. 2, pp. 79–86,

Jun. 2016.

[49] R. Hemmati, R. A. Hooshmand, and A. Khodabakhshian, "Market based transmission expansion and reactive power planning with consideration of wind and load uncertainties," *Renewable and Sustainable Energy Reviews*, vol. 29. pp. 1–10, 2014.

[50] A. Shapiro, D. Dentcheva, and A. Ruszczynski, *Lectures on Stochastic Programming Modeling and Theory*. Philadelphia, PA: SIAM, 2009.

[51] A. Shapiro and A. Philpott, "A tutorial on stochastic programming," 2007. [Online]. Available:www2.isye.gatech.edu/people/faculty/Alex_Shapiro/TutorialSP.pdf.

[52] J. R. Birge and F. Louveaux, *Introduction to Stochastic Programming*, 2nd ed. New York: Springer-Verlag, 2006.

[53] A. Papavasiliou, S. S. Oren, and R. P. O'Neill, "Reserve requirements for wind power integration: A scenario-based stochastic programming framework," *IEEE Trans. Power Syst.*, vol. 26, no. 4, pp. 2197–2206, Nov. 2011.

[54] A. Narayan and K. Ponnambalam, "Risk-averse stochastic programming approach for microgrid planning under uncertainty," *Renew. Energy*, vol. 101, pp. 399–408, Feb. 2017.

[55] V. Mohan, J. G. Singh, and W. Ongsakul, "An efficient two stage stochastic optimal energy and reserve management in a microgrid," *Appl. Energy*, vol. 160, pp. 28–38, 2015.

[56] I. L. R. Gomes, H. M. I. Pousinho, R. Melício, and V. M. F. Mendes, "Stochastic coordination of joint wind and photovoltaic systems with energy storage in day-ahead market," *Energy*, vol. 124, pp. 310–320, 2017.

[57] H. Heitsch and W. Römisch, "Scenario reduction algorithms in stochastic programming," *Comput. Optim. Appl.*, vol. 24, pp. 187–206, Feb. 2003.

[58] N. Gröwe-Kuska, H. Heitsch, and W. Römisch, "Scenario reduction and scenario tree construction for power management problems," *2003 IEEE Bologna Power Tech Conference Proceedings*, Bologna, Italy, 2003, pp. 1-7 pp. Vol.3.

[59] J. M. Morales, S. Pineda, A. J. Conejo, and M. Carrión, "Scenario reduction for

futures market trading in electricity markets," *IEEE Trans. Power Syst.*, vol. 24, no. 2, pp. 878–888, 2009.

[60] S. Pineda and A. J. Conejo, "Scenario reduction for risk-averse electricity trading," *IET Gener. Transm. Distrib.*, vol. 4, no. 6, pp. 694–705, Jan. 2010.

[61] H. P. Hong, "An efficient point estimate method for probabilistic analysis," *Reliab. Eng. Syst. Saf.*, vol. 59, no. 3, pp. 261–267, 1998.

[62] S. M. Mohseni-Bonab, A. Rabiee, B. Mohammadi-Ivatloo, S. Jalilzadeh, and S. Nojavan, "A two-point estimate method for uncertainty modeling in multi-objective optimal reactive power dispatch problem," *Int. J. Electr. Power Energy Syst.*, vol. 75, pp. 194–204, Feb. 2016.

[63] M. Mehrtash, M. Raoofat, M. Mohammadi, and H. Zareipour, "Fast stochastic security-constrained unit commitment using point estimation method," *Int. Trans. Electr. Energy Syst.*, vol. 26, no. 3, pp. 671–688, Mar. 2016.

[64] S. S. Reddy, "Optimal scheduling of thermal-wind-solar power system with storage," *Renew. Energy*, vol. 101, pp. 1357–1368, Feb. 2017.

[65] Q. Gong, J. Lei, H. Qiao, and J. Qiu, "Risk assessment for distribution systems using an improved PEM-based method considering wind and photovoltaic power distribution," *Sustain.*, vol. 9, no. 4, Mar. 2017.

[66] M. Sedghi, A. Ahmadian, and M. Aliakbar-Golkar, "Optimal storage planning in active distribution network considering uncertainty of wind power distributed generation," *IEEE Trans. Power Syst.*, vol. 31, no. 1, pp. 304–316, Jan. 2016.

[67] L. A. Zadeh, "Fuzzy sets," *Inf. Control*, vol. 8, no. 3, pp. 338–353, 1965.

[68] H.-J. Zimmermann, *Fuzzy Set Theory — and Its Applications*. New York: Springer, 1985.

[69] G. Alefeld and G. Mayer, "Interval analysis: Theory and applications," *J. Comput. Appl. Math.*, vol. 121, no. 1–2, pp. 421–464, 2000.

[70] H. Zhang and D. Liu, *Fuzzy Modeling and Fuzzy Control*. Boston, MA: Birkhäuser, 2006.

[71] M. A. Matos and E. M. Gouveia, "The fuzzy power flow revisited," *IEEE Trans. Power Syst.*, vol. 23, no. 1, pp. 213–218, Feb. 2008.

[72]   D. K. Mohanta, P. K. Sadhu, and R. Chakrabarti, "Fuzzy reliability evaluation of captive power plant maintenance scheduling incorporating uncertain forced outage rate and load representation," *Electr. Power Syst. Res.*, vol. 72, no. 1, pp. 73–84, Nov. 2004.

[73]   B. Venkatesh, P. Yu, H. B. Gooi, and D. Choling, "Fuzzy MILP unit commitment incorporating wind generators," *IEEE Trans. Power Syst.*, vol. 23, no. 4, pp. 1738–1746, 2008.

[74]   P. Attaviriyanupap, H. Kita, E. Tanaka, and J. Hasegawa, "A fuzzy-optimization approach to dynamic economic dispatch considering uncertainties," *IEEE Trans. Power Syst.*, vol. 19, no. 3, pp. 1299–1307, Aug. 2004.

[75]   V. Miranda and P. S. Hang, "Economic dispatch model with fuzzy wind constraints and attitudes of dispatchers," *IEEE Trans. Power Syst.*, vol. 20, no. 4, pp. 2143–2145, 2005.

[76]   L. Wang and C. Singh, "Balancing risk and cost in fuzzy economic dispatch including wind power penetration based on particle swarm optimization," *Electr. Power Syst. Res.*, vol. 78, no. 8, pp. 1361–1368, Aug. 2008.

[77]   R. E. Moore, R. B. Kearfott, and M. J. Cloud, *Introduction to Interval Analysis*. Philadelphia, PA: SIAM, 2009.

[78]   Z. Wang and F. L. Alvarado, "Interval Arithmetic in Power Flow Analysis," *IEEE Trans. Power Syst.*, vol. 7, no. 3, pp. 1341–1349, 1992.

[79]   A. T. Sarić and A. M. Stanković, "An application of interval analysis and optimization to electric energy markets," *IEEE Transactions on Power Systems*, vol. 21, no. 2. pp. 515–523, May-2006.

[80]   Y. Wang, Q. Xia, and C. Kang, "Unit commitment with volatile node injections by using interval optimization," *IEEE Trans. Power Syst.*, vol. 26, no. 3, pp. 1705–1713, 2011.

[81]   P. Zhang, W. Li, and S. Wang, "Reliability-oriented distribution network reconfiguration considering uncertainties of data by interval analysis," *Int. J. Electr. Power Energy Syst.*, vol. 34, no. 1, pp. 138–144, Jan. 2012.

[82]   D. Bertsimas, D. B. Brown, and C. Caramanis, "Theory and applications of robust optimization," *SIAM Rev.*, vol. 53, no. 3, pp. 464–501, Aug. 2011.

[83] R. Jiang, J. Wang, and Y. Guan, "Robust unit commitment with wind power and pumped storage hydro," *IEEE Trans. Power Syst.*, vol. 27, no. 2, pp. 800–810, May 2012.

[84] D. Bertsimas, E. Litvinov, X. A. Sun, J. Zhao, and T. Zheng, "Adaptive robust optimization for the security constrained unit commitment problem," *IEEE Trans. Power Syst.*, vol. 28, no. 1, pp. 52–63, 2013.

[85] A. Charnes and W. W. Cooper, "Chance-Constrained Programming," *Manage. Sci.*, vol. 6, no. 1, pp. 73–79, Oct. 1959.

[86] D. Bienstock, M. Chertkov, and S. Harnett, "Chance-constrained optimal power flow: Risk-aware network control under uncertainty," *SIAM Rev.*, vol. 56, no. 3, pp. 461–495, Aug. 2014.

[87] L. Roald and G. Andersson, "Chance-Constrained AC Optimal Power Flow: Reformulations and Efficient Algorithms," *IEEE Trans. Power Syst.*, vol. 33, no. 3, pp. 2906–2918, May 2018.

[88] K. Margellos, P. Goulart, and J. Lygeros, "On the road between robust optimization and the scenario approach for chance constrained optimization problems," *IEEE Trans. Automat. Contr.*, vol. 59, no. 8, pp. 2258–2263, 2014.

[89] M. Vrakopoulou, B. Li, and J. L. Mathieu, "Chance Constrained Reserve Scheduling Using Uncertain Controllable Loads Part I: Formulation and Scenario-based Analysis," *IEEE Trans. Smart Grid*, vol. 3053, no. c, pp. 1–10, 2017.

[90] H. Zhang and P. Li, "Chance Constrained Programming for Optimal Power Flow Under Uncertainty," *IEEE Trans. Power Syst.*, vol. 26, no. 4, pp. 2417–2424, 2011.

[91] A. Nemirovski and A. Shapiro, "Convex approximations of chance constrained programs," *SIAM J. Optim.*, vol. 17, no. 4, pp. 959–996, 2006.

[92] A. Venzke, L. Halilbasic, U. Markovic, G. Hug, and S. Chatzivasileiadis, "Convex Relaxations of Chance Constrained AC Optimal Power Flow," *IEEE Trans. Power Syst.*, pp. 1–13, 2017.

[93] L. Halilbasic, P. Pinson, and S. Chatzivasileiadis, "Convex Relaxations and Approximations of Chance-Constrained AC-OPF Problems," *IEEE Trans.*

Power Syst., vol. 34, no. 2, pp. 1559–1570, Mar. 2019.

[94] N. Rezaei, A. Ahmadi, A. E. Nezhad, and A. Khazali, "Information-gap decision theory: Principles and fundamentals," in *Robust Optimal Planning and Operation of Electrical Energy Systems*, Springer International Publishing, 2019, pp. 11–33.

[95] A. Rabiee, A. Soroudi, and A. Keane, "Information Gap Decision Theory Based OPF with HVDC Connected Wind Farms," *IEEE Trans. Power Syst.*, vol. 30, no. 6, pp. 3396–3406, Nov. 2015.

[96] M. Majidi, B. Mohammadi-Ivatloo, and A. Soroudi, "Application of information gap decision theory in practical energy problems: A comprehensive review," *Applied Energy*, vol. 249. Elsevier Ltd, pp. 157–165, 01-Sep-2019.

[97] M. Pourahmadi-Nakhli, A. R. Seifi, and R. Taghavi, "A nonlinear-hybrid fuzzy/probabilistic load flow for radial distribution systems," *Int. J. Electr. Power Energy Syst.*, vol. 47, no. 1, pp. 69–77, 2013.

[98] A. Soroudi, "Possibilistic-scenario model for DG impact assessment on distribution networks in an uncertain environment," *IEEE Trans. Power Syst.*, vol. 27, no. 3, pp. 1283–1293, 2012.

[99] J. Carpentier, "Contribution a l'etude du dispaching economique," *Bull. la Soc. Fr. des Electr.*, vol. 3, no. 8, 1962.

[100] M. Cain, R. O'Neill, and A. Castillo, "History of Optimal Power Flow and Formulations (OPF Paper 1)," Tech. Rep., US FERC, December. pp. 1–36, 2012.

[101] R. Bacher and H. Glavitsch, "Network Topology Optimization with security constraints," *IEEE Trans. Power Syst.*, vol. 1, no. 4, pp. 103–111, 1986.

[102] E. B. Fisher, R. P. O'Neill, and M. C. Ferris, "Optimal transmission switching," *IEEE Trans. Power Syst.*, vol. 23, no. 3, pp. 1346–1355, 2008.

[103] K. W. Hedman, R. P. O'Neill, E. B. Fisher, and S. S. Oren, "Optimal transmission switching with contingency analysis," *IEEE Trans. Power Syst.*, vol. 24, no. 3, pp. 1577–1586, 2009.

[104] D. Romero-Quete and C. A. Canizares, "An Affine Arithmetic-Based Energy Management System for Isolated Microgrids," in *IEEE Transactions on Smart*

Grid, vol. 10, no. 3, pp. 2989-2998, May 2019.

[105] A. K. Kazerooni and J. Mutale, "Transmission Network Planning under Security and Environmental Constraints," *IEEE Trans. Power Syst.*, vol. 25, no. 2, pp. 1169–1178, May 2010.

[106] J. Lavaei and S. H. Low, "Zero Duality Gap in Optimal Power Flow Problem," *IEEE Trans. Power Syst.*, vol. 27, no. 1, pp. 92–107, 2012.

[107] S. H. Low, "Convex Relaxation of Optimal Power Flow—Part I: Formulations and Equivalence," *IEEE Trans. Control Netw. Syst.*, vol. 1, no. 1, pp. 15–27, 2014.

[108] S. H. Low, "Convex Relaxation of Optimal Power Flow, Part II: Exactness," *IEEE Trans. Control Netw. Syst.*, vol. 1, no. 2, pp. 177–189, 2014.

[109] B. Kocuk, S. S. Dey, and X. Andy Sun, "Strong SOCP relaxations for the optimal power flow problem," *Oper. Res.*, vol. 64, no. 6, pp. 1177–1196, Nov. 2016.

[110] P. N. Yasasvi, S. Chandra, A. Mohapatra, and S. C. Srivastava, "An Exact SOCP Formulation for AC Optimal Power Flow," in *2018 20th National Power Systems Conference, NPSC 2018*, 2018.

[111] R. A. Jabr, "A Conic Quadratic Format for the Load Flow Equations of Meshed Networks," *IEEE Trans. Power Syst.*, vol. 22, no. 4, pp. 2285–2286, Nov. 2007.

[112] R. Madani, S. Sojoudi, and J. Lavaei, "Convex Relaxation for Optimal Power Flow Problem: Mesh Networks," *IEEE Trans. Power Syst.*, vol. 30, no. 1, pp. 199–211, Jan. 2015.

[113] M. Rylander, J. Smith, and W. Sunderman, "Streamlined Method for Determining Distribution System Hosting Capacity," in *IEEE Transactions on Industry Applications*, vol. 52, no. 1, pp. 105-111, Jan.-Feb. 2016

[114] S. Stanfield and S. Safdi, "Optimizing the Grid: A Regulator's Guide to Hosting Capacity Analyses for Distributed Energy Resources," IREC, USA, Dec. 2017.

[115] A. Arshad, V. Püvi, and M. Lehtonen, "Monte Carlo-Based Comprehensive Assessment of PV Hosting Capacity and Energy Storage Impact in Realistic Finnish Low-Voltage Networks," *Energies*, vol. 11, no. 6, p. 1467, Jun. 2018.

[116] E. Mulenga and M. H. J. Bollen, "Impact of Service and Feeder Cable Upgrade

on Hosting Capacity for Single Phase Connected Photovoltaics," *2018 18th International Conference on Harmonics and Quality of Power (ICHQP)*, Ljubljana, 2018, pp. 1-6.

[117] A. M. El-Zonkoly, "Optimal Placement of Multi-distributed Generation Units including Different Load Models using Particle Swarm Optimization," *Swarm Evol. Comput.*, vol. 1, no. 1, pp. 50–59, Mar. 2011.

[118] N. Etherden and M. H. J. Bollen, "Increasing the Hosting Capacity of Distribution Networks by Curtailment of Renewable Energy Resources," *2011 IEEE Trondheim PowerTech*, Trondheim, 2011, pp. 1-7.

[119] N. Etherden, M. Bollen, S. Ackeby, and O. Lennerhag, "The Transparent Hosting Capacity Approach Overview, Applications and Developments," *Proc. 23rd Int. Conf. Exhib. Electr. Distrib.*, Lyon, France. 2015, pp. 1–5.

[120] E. Sáiz-Marín, E. Lobato, and I. Egido, "Local Hosting Capacity Increase by Means of Wind Farm Voltage Control Provision," *IEEE Trans. Power Syst.*, vol. 29, no. 4, pp. 1731–1738, 2014.

[121] D. Mende, Y. T. Fawzy, D. Premm, and S. Stevens, "Increasing the Hosting Capacity of Distribution Networks for Distributed Generation Using Reactive Power Control - Potentials and Limits," in *2nd International Workshop on Integration of Solar Power into Power Systems*, Lisbon, Portugal, 2012.

[122] L. F. Ochoa, C. J. Dent, and G. P. Harrison, "Distribution Network Capacity Assessment: Variable DG and Active Networks," *IEEE Trans. Power Syst.*, vol. 25, no. 1, pp. 87–95, Feb. 2010.

[123] W. Sun and G. P. Harrison, "Wind-solar Complementarity and Effective Use of Distribution Network Capacity," *Appl. Energy*, vol. 247, pp. 89–101, Aug. 2019.

[124] A. Rabiee and S. M. Mohseni-Bonab, "Maximizing Hosting Capacity of Renewable Energy Sources in Distribution Networks: A Multi-objective and Scenario-based Approach," *Energy*, vol. 120, pp. 417–430, Feb. 2017.

[125] D. A. Quijano, J. Wang, M. R. Sarker, and A. Padilha-Feltrin, "Stochastic Assessment of Distributed Generation Hosting Capacity and Energy Efficiency in Active Distribution Networks," *IET Gener. Transm. Distrib.*, vol. 11, no. 18, pp. 4617–4625, Dec. 2017.

[126] X. Xu, J. Gunda, R. Dowling, and S. Djokic, "A Two-stage Approach for Renewable Hosting Capacity Assessment," *2019 IEEE PES Innovative Smart Grid Technologies Europe (ISGT-Europe)*, Bucharest, Romania, 2019, pp. 1-5.

[127] R. Adapa and D. A. Douglass, "Dynamic thermal ratings: Monitors and calculation methods," *2005 IEEE Power Engineering Society Inaugural Conference and Exposition in Africa*, Durban, 2005, pp. 163-167.

[128] C. J. Wallnerstrom, Y. Huang, and L. Soder, "Impact from Dynamic Line Rating on Wind Power Integration," *IEEE Trans. Smart Grid*, vol. 6, no. 1, pp. 343–350, 2015.

[129] A. K. Kazerooni, J. Mutale, M. Perry, S. Venkatesan, and D. Morrice, "Dynamic Thermal Rating Application to Facilitate Wind Energy Integration," in *2011 IEEE PES Trondheim PowerTech*, Trondheim, 2011.

[130] B. Xu, A. Ulbig, and G. Andersson, "Impacts of Dynamic Line Rating on Power Dispatch Performance and Grid Integration of Renewable Energy Sources," *IEEE PES ISGT Europe 2013*, Lyngby, 2013, pp. 1-5.

[131] M. Z. Degefa, M. Humayun, A. Safdarian, M. Koivisto, R. J. Millar, and M. Lehtonen, "Unlocking Distribution Network Capacity through Real-time Thermal Rating for High Penetration of DGs," *Electr. Power Syst. Res.*, vol. 117, pp. 36–46, Dec. 2014.

[132] "Current Rating Guide for High Voltage Overhead Lines Operating in the UK Distribution System." ER P27, 1986.

[133] I. Hernando-Gil, "Integrated Assessment of Quality of Supply in Future Electricity Networks," University of Edinburgh, Edinburgh, UK, 2014.

[134] M. E. Baran and F. F. Wu, "Network Reconfiguration in Distribution Systems for Loss Reduction and Load Balancing," *IEEE Trans. Power Deliv.*, vol. 4, no. 2, pp. 1401–1407, 1989.

[135] A. Molod, L. Takacs, M. Suarez, and J. Bacmeister, "Development of the GEOS-5 Atmospheric General Circulation Model: Evolution from MERRA to MERRA2," *Geosci. Model Dev.*, vol. 8, no. 5, pp. 1339–1356, May 2015.

[136] "Aluminium Conductors| ACSR | Eland Cables." [Online]. Available: https://www.elandcables.com/media/38193/acsr-astm-b-aluminium-

conductor-steel-reinforced.pdf. [Accessed: 14-Jun-2020].

[137] "The Open Distribution System Simulator OpenDSS." [Online]. Available: https://www.epri.com/pages/sa/opendss. [Accessed: 29-Jun-2020].

[138] Ofgem, "Implementation of Real-Time Thermal Ratings," 2013.

[139] M. Aien, A. Hajebrahimi, and M. Fotuhi-Firuzabad, "A Comprehensive Review on Uncertainty Modeling Techniques in Power System Studies," *Renewable and Sustainable Energy Reviews*, vol. 57. Elsevier Ltd, pp. 1077–1089, 01-May-2016.

[140] C. Carrillo, A. F. Obando Montano, J. Cidras, and E. Diaz-Dorado, "Review of Power Curve Modelling for Wind Turbines," *Renew. Sustain. Energy Rev.*, vol. 21, pp. 572–581, 2013.

[141] V. Sohoni, S. C. Gupta, R. K. Nema, V. Sohoni, S. C. Gupta, and R. K. Nema, "A Critical Review on Wind Turbine Power Curve Modelling Techniques and Their Applications in Wind Based Energy Systems," *J. Energy*, vol. 2016, no. region 4, pp. 1–18, 2016.

[142] V. Thapar, G. Agnihotri, and V. K. Sethi, "Critical Analysis of Methods for Mathematical Modelling of Wind Turbines," *Renew. Energy*, vol. 36, no. 11, pp. 3166–3177, 2011.

[143] B. P. Hayes, I. S. Ilie, A. Porpodas, S. Z. Djokic, and G. Chicco, "Equivalent power curve model of a wind farm based on field measurement data," *2011 IEEE Trondheim PowerTech*, Trondheim, 2011, pp. 1-7.

[144] "*Wind turbines. Part 12-1 Power performance measurements of electricity producing wind turbines*". in IEC 61400-12-1, pp. 1-96, 2006.

[145] Vestas, "General Specification V90 - 3.0 MW," Vestas Wind Systems A/S, Report 950010.R1, 2013.

[146] I. Hernando-Gil, F. Li, A. Collin and S. Djokic, "Development of sub-transmission network equivalents and after-diversity-demand values: Case study of the UK residential sector," *2016 18th Mediterranean Electrotechnical Conference (MELECON)*, Lemesos, 2016, pp. 1-6.

[147] "World Temperatures — Weather Around The World." [Online]. Available: https://www.timeanddate.com/weather/. [Accessed: 15-Jun-2020].

[148] National Grid, "National Electricity Transmission System Security and Quality of Supply Standard,", Version 2.3, pp. 1–93, Feb 2017.

[149] "MATPOWER – Free, open-source tools for electric power system simulation and optimization." [Online]. Available: https://matpower.org/. [Accessed: 15-Jun-2020].

[150] R. D. Zimmerman, C. E. Murillo-Sánchez, and R. J. Thomas, "MATPOWER: Steady-state Operations, Planning, and Analysis Tools for Power Systems Research and Education," *IEEE Trans. Power Syst.*, vol. 26, no. 1, pp. 12–19, Feb. 2011.

[151] D. A. Douglass and A. A. Edris, "Real-time Monitoring and Dynamic Thermal Rating of Power Transmission Circuits," *IEEE Trans. Power Deliv.*, vol. 11, no. 3, pp. 1407–1415, 1996.

[152] J. Yang, X. Bai, D. Strickland, L. Jenkins, and A. M. Cross, "Dynamic Network Rating for Low Carbon Distribution Network Operation-A U.K. Application," *IEEE Trans. Smart Grid*, vol. 6, no. 2, pp. 988–998, 2015.

[153] A. Safdarian, M. Z. Degefa, M. Fotuhi-Firuzabad, and M. Lehtonen, "Benefits of Real-Time Monitoring to Distribution Systems: Dynamic Thermal Rating," *IEEE Trans. Smart Grid*, vol. 6, no. 4, pp. 2023–2031, Jul. 2015.

[154] L. H. De Figueiredo and J. Stolfi, "Affine arithmetic: Concepts and applications," *Numer. Algorithms*, vol. 37, no. 1-4 SPEC. ISS., pp. 147–158, 2004.

[155] J. Stolfi and L. H. De Figueiredo, "An Introduction to Affine Arithmetic," *TEMA. Mat. Apl. Comput.*, vol. 4, no. 3, pp. 297–312, 2003.

[156] J. Stolfi, L. H. de Figueiredo, and Jorge Stolfi and Luiz Henrique De Figueiredo, "Self-validated Numerical Methods and Applications," *Proc. Monogr. 21st Brazilian Math. Colloquium, Citeseer*, 1997.

[157] A. Vaccaro and C. A. Canizares, "An Affine Arithmetic-Based Framework for Uncertain Power Flow and Optimal Power Flow Studies," *IEEE Trans. Power Syst.*, vol. 32, no. 1, pp. 274–288, 2017.

[158] A. Piccolo, A. Vaccaro, and D. Villacci, "Thermal Rating Assessment of Overhead Lines by Affine Arithmetic," *Electr. Power Syst. Res.*, vol. 71, no. 3, pp. 275–283, 2004.

[159] "YALMIP : A Toolbox for Modeling and Optimization in MATLAB - YALMIP." [Online]. Available: https://yalmip.github.io. [Accessed: 15-Jun-2020].

[160] A. Wächter and L. T. Biegler, "On the Implementation of An Interior-point Filter Line-search Algorithm for Large-scale Nonlinear Programming," *Math. Program.*, vol. 106, no. 1, pp. 25–57, May 2006.

[161] Vestas, "General Specification V90-1.8/2.0 MW 50 Hz VCS," Vestas Wind Systems A/S, Report 0004-6207 V05, 2010.

[162] G. Papaefthymiou and B. Klöckl, "MCMC for Wind Power Simulation," *IEEE Trans. Energy Convers.*, vol. 23, no. 1, pp. 234–240, Mar. 2008.

[163] Y. Pan, L. Shi, and Y. Ni, "Modelling of Multiple Wind Farms Output Correlation based on Copula Theory," *J. Eng.*, vol. 2017, no. 13, pp. 2303–2308, Jan. 2017.

[164] G. Papaefthymiou and D. Kurowicka, "Using Copulas for Modeling Stochastic Dependence in Power System Uncertainty Analysis," *IEEE Trans. Power Syst.*, vol. 24, no. 1, pp. 40–49, 2009.

[165] A. Shemyakin and A. Kniazev, *Introduction to Bayesian Estimation and Copula Models of Dependence*, Hoboken, New Jersey: Wiley-Blackwell, May 2017..

[166] B. P. Hayes, "Distributed Generation and Demand Side Management : Applications to Transmission System Operation," University of Edinburgh, Edinburgh, 2013.

[167] M. Lydia, S. S. Kumar, A. I. Selvakumar, and G. E. Prem Kumar, "A Comprehensive Review on Wind Turbine Power Curve Modeling Techniques," *Renew. Sustain. Energy Rev.*, vol. 30, pp. 452–460, 2014.

[168] W. Z. Black and W. R. Byrd, "Real-time Ampacity Model for Overhead Lines," *IEEE Trans. Power Appar. Syst.*, vol. PAS-102, no. 7, pp. 2289–2293, 1983.

[169] J. Fu, S. Abbott, B. Fox, D. . Morrow, and S. Abdelkader, "Wind Cooling Effect on Dynamic Overhead Line Ratings," *45th International Universities Power Engineering Conference UPEC2010*, Cardiff, Wales, 2010, pp. 1-6.

[170] A. Pillay, S. Prabhakar Karthikeyan, and D. P. Kothari, "Congestion Management in Power Systems - A Review," *Int. J. Electr. Power Energy Syst.*,

vol. 70, pp. 83–90, Sep. 2015.

[171] B. Delourme, A. Lasnier, H. Lefevbre, and G. Simeant, "Minimizing the cost of generation re-dispatching taking into account remedial actions." in *Proc. CIGRE Conf.*, France, 2006, paper C2-103.

[172] F. Qiu and J. Wang, "Distributionally Robust Congestion Management with Dynamic Line Ratings," *IEEE Trans. Power Syst.*, vol. 30, no. 4, pp. 2198–2199, Jul. 2015.

[173] M. M. Esfahani and G. R. Yousefi, "Real Time Congestion Management in Power Systems Considering Quasi-Dynamic Thermal Rating and Congestion Clearing Time," *IEEE Trans. Ind. Informatics*, vol. 12, no. 2, pp. 745–754, 2016.

[174] M. Mahmoudian Esfahani, A. Sheikh, and O. Mohammed, "Adaptive real-time congestion management in smart power systems using a real-time hybrid optimization algorithm," *Electr. Power Syst. Res.*, vol. 150, pp. 118–128, Sep. 2017.

[175] S. D. Kim, S. R. Kim, and M. M. Morcos, "Application and Evaluation of Short-term Emergency Ratings for Double-circuit Transmission Lines Application and Evaluation of Short-term Emergency Ratings for Double-circuit Transmission Lines," *Electr. Power Components Syst.*, vol. 40, no. 7, pp. 729–740, 2012.

[176] C. G. Marcelino, P. E. M. Almeida, E. F. Wanner, L. M. Carvalho, and V. Miranda, "Fundamentals of the C-DEEPSO algorithm and its application to the reactive power optimization of wind farms," *2016 IEEE Congress on Evolutionary Computation (CEC)*, Vancouver, BC, 2016, pp. 1547-1554.

[177] "IEEE 14-Bus Test Network." [Online]. Available: https://labs.ece.uw.edu/pstca/pf14/pg_tca14bus.htm. [Accessed: 15-Jun-2020].

[178] J. Gunda, "Analysis and Management of Security Constraints in Overstressed Power Systems.", the University of Edinburgh, Edinburgh, 2018.

[179] E. Ela, M. Milligan, and B. Kirby, Operating Reserves and Variable Generation, Tech. Rep., NREL/TP-5500-51928, Aug. 2011.